

ABSTRACT

Search for Supersymmetric Top Quarks in the CMS Run 2 Data Set

Caleb James Smith, Ph.D.

Advisor: Jay R. Dittmann, Ph.D.

Elementary particle physics is described very accurately by the Standard Model. With the discovery of the Higgs boson at CERN by ATLAS and CMS in 2012, the full set of fundamental particles in the Standard Model has been confirmed to exist by experimentation. The LHC and the CMS detector continue to probe physics at higher energies to determine if additional fundamental particles exist that are not present in the Standard Model. An analysis of the CMS Run 2 data set collected during the years 2016–2018 at center-of-mass energy 13 TeV corresponding to an integrated luminosity of 137.0 fb^{-1} is presented. This analysis searches for supersymmetric top quarks in the all-hadronic final state. The search targets multiple simplified SUSY models. Custom algorithms are used to identify top quarks and W bosons. The leading Standard Model background processes are $t\bar{t}$, $W(\rightarrow \ell\nu)+\text{jets}$, $Z(\rightarrow \nu\bar{\nu})+\text{jets}$, QCD, and $t\bar{t}Z$. A complete description of the $Z(\rightarrow \nu\bar{\nu})+\text{jets}$ data-driven background prediction is given. The results are interpreted for several simplified SUSY models, and limits are placed on the masses of the supersymmetric top

quark (up to 1.3 TeV), the gluino (up to 2.3 TeV), and the lightest supersymmetric particle (up to 1.4 TeV).

Search for Supersymmetric Top Quarks in the CMS Run 2 Data Set

by

Caleb James Smith, M.A., B.S.

A Dissertation

Approved by the Department of Physics

Dwight P. Russell, Ph.D., Interim Chairperson

Submitted to the Graduate Faculty of
Baylor University in Partial Fulfillment of the
Requirements for the Degree
of
Doctor of Philosophy

Approved by the Dissertation Committee

Jay R. Dittmann, Ph.D., Chairperson

Kenichi Hatakeyama, Ph.D.

Walter Wilcox, Ph.D.

Lorin Matthews, Ph.D.

Jon Harrison, Ph.D.

Accepted by the Graduate School
December 2020

J. Larry Lyon, Ph.D., Dean

Copyright © 2020 by Caleb James Smith

All rights reserved

TABLE OF CONTENTS

LIST OF ACRONYMS	viii
LIST OF FIGURES	xii
LIST OF TABLES	xvii
ACKNOWLEDGMENTS	xix
DEDICATION	xx
CHAPTER ONE	
Introduction	1
CHAPTER TWO	
High Energy Physics	3
2.1 The Standard Model of Particle Physics	3
2.1.1 The Electromagnetic Interaction	9
2.1.2 The Weak Interaction	10
2.1.3 The Strong Interaction	10
2.1.4 The Higgs Boson Interaction	10
2.2 Supersymmetry	15
CHAPTER THREE	
The CMS Experiment	21
3.1 The Large Hadron Collider	21
3.2 The Compact Muon Solenoid	23
3.3 CMS Phase 1 Upgrades	28
CHAPTER FOUR	
Event Reconstruction	29
4.1 Muons	29
4.2 Electrons	30
4.3 Photons	30
4.4 Hadrons	30
4.5 Jets	30
CHAPTER FIVE	
Searching for Supersymmetry	33
5.1 Overview	33
5.2 Object Identification	35
5.2.1 Electrons	35

5.2.2	Muons	35	
5.2.3	Taus	36	
5.2.4	Isolated Tracks	36	
5.2.5	Photons	37	
5.2.6	Jets	37	
5.2.7	b-tagging	37	
5.2.8	Soft b-tagging	38	
5.2.9	Boosted Top- and W-tagging	39	
5.2.10	Resolved Top-tagging	40	
5.2.11	ISR-tagging	42	
5.2.12	Missing Transverse Energy.....	43	
5.2.13	Level-1 Trigger Prefiring Inefficiency	43	
5.2.14	HEM 15/16 Failure	44	
5.3	Search Strategy	45	
5.3.1	Triggers	47	
5.3.2	Event Selection	48	
5.3.3	Search Region Selection	54	
5.3.4	Validation Region Selection	55	
5.4	Standard Model Backgrounds	59	
5.4.1	Lost Lepton Background	61	
5.4.2	Z Invisible Background	63	
5.4.3	QCD Background	68	
5.4.4	$t\bar{t}Z$ and Rare Backgrounds.....	69	
5.5	Uncertainties	74	
5.6	Results.....	77	
5.6.1	Validation Bins	77	
5.6.2	Search Bins	77	
5.6.3	Limits	79	
CHAPTER SIX			
	Z Invisible Background	88	
6.1	Overview	88	
6.2	Method	89	
6.3	Normalization Factor	91	
6.4	Shape Factor	99	
6.5	Combining Eras	107	
6.6	Uncertainties	109	
6.7	Results.....	115	
CHAPTER SEVEN			
	Conclusion.....	120	
APPENDICES.....			122
APPENDIX A			
	Decay Rate Calculations.....	123	

APPENDIX B	
Event Displays	131
APPENDIX C	
Background Predictions.....	138
APPENDIX D	
Z Invisible Predictions.....	146
BIBLIOGRAPHY	154

LIST OF ACRONYMS

ALICE	A Large Ion Collider Experiment
APD	Avalanche Photodiode
ASIC	Application Specific Integrated Circuit
BDT	Boosted Decision Tree
BPIX	Barrel Pixel
BSB	Baylor Science Building
BSM	Beyond the Standard Model
CERN	European Organization for Nuclear Research
CKM	Cabibbo-Kobayashi-Maskawa
CL	Confidence Level
CMS	Compact Muon Solenoid
COM	center-of-mass
CP	Charge Parity
CR	Control Region
CSC	Cathode Strip Chamber
CTF	Combinatorial Track Finder
DM	Dark Matter
DNN	Dense Neural Network
DT	Drift Tube
ECAL	Electromagnetic Calorimeter
FNAL	Fermi National Accelerator Laboratory
FPGA	Field Programmable Gate Array
FPIX	Forward Pixel
FPR	False Positive Rate
FSR	Final-State Radiation

GR	Gradient Reversal
GSF	Gaussian Sum Filter
GUT	Grand Unified Theory
HB	Hadron Calorimeter Barrel
HCAL	Hadron Calorimeter
HE	Hadron Calorimeter Endcap
HF	Hadron Calorimeter Forward
HLT	High Level Trigger
HO	Hadron Calorimeter Outer
HPD	Hybrid Photodiode
IP	Interaction Point
IRC	Infrared and Collinear
ISR	Initial-State Radiation
IVF	Inclusive Vertex Finder
JEC	Jet Energy Correction
JES	Jet Energy Scale
L1	Level 1
LEP	Large Electron-Positron
LHCb	Large Hadron Collider beauty
LHC	Large Hadron Collider
LINAC	Linear Accelerator
LL	Lost Lepton
LPC	LHC Physics Center
LSP	Lightest Supersymmetric Particle
MC	Monte Carlo
MET	Missing Transverse Energy
MSSM	Minimal Supersymmetric Standard Model
NLL	Next-to-Leading Logarithmic

NLO	Next-to-Leading Order
PDF	Probability Distribution Function
PF	Particle Flow
PMNS	Pontecorvo-Maki-Nakagawa-Sakata
PMT	Photomultiplier Tube
POG	Physics Object Group
POI	Parameter Of Interest
PS	Proton Synchrotron
PSB	Proton Synchrotron Booster
PU	Pileup
PV	Primary Vertex
QCD	Quantum Chromodynamics
QED	Quantum Electrodynamics
QIE	Charge Integrator and Encoder
RNN	Recurrent Neural Network
ROC	Receiver Operating Characteristic
RPC	Resistive Plate Chamber
RPV	R-Parity Violating
SF	Scale Factor
SiPM	Silicon Photomultiplier
SM	Standard Model
SPS	Super Proton Synchrotron
SR	Search Region
SSR	Silicon Strip Tracker
SUSY	Supersymmetry
SV	Secondary Vertex
SY Y	Stealth SUSY with SY Y coupling
TDR	Technical Design Report

TEC	Tracker Endcap
TF	Transfer Factor
TIB	Tracker Inner Barrel
TID	Tracker Inner Disks
TOB	Tracker Outer Barrel
TP	Trigger Primitive
TPR	True Positive Rate
VEV	Vacuum Expectation Value
VPT	Vacuum Phototriode
WIMP	Weakly Interacting Massive Particle
WP	Working Point

LIST OF FIGURES

Figure 2.1.	The elementary particles in the Standard Model	4
Figure 2.2.	Standard Model interactions expressed as Feynman diagram vertices ..	5
Figure 2.3.	Inverted couplings in the SM as a function of energy scale for the electromagnetic, weak, and strong forces.....	6
Figure 2.4.	Evidence of the Higgs boson in the diphoton invariant mass distribution at CMS.....	12
Figure 2.5.	The potential $V(\phi)$ from Eq. (2.7) with $\mu^2 > 0$ and $\mu^2 < 0$	13
Figure 2.6.	Inverted couplings in the MSSM as a function of energy scale for the electromagnetic, weak, and strong forces.....	17
Figure 2.7.	The SM particles and SUSY particles	18
Figure 3.1.	The CERN accelerator complex.....	23
Figure 3.2.	An illustration of the CMS detector and subdetectors	25
Figure 3.3.	A transverse slice of CMS with subdetectors and illustrative particles originating at the collision point.....	25
Figure 3.4.	One end of the CMS detector during an LHC shutdown period.....	26
Figure 4.1.	Clustering jets using the anti- k_T algorithm with the distance parameter $R = 1$	32
Figure 5.1.	Event diagrams for the direct squark production scenarios considered in this study	34
Figure 5.2.	Event diagrams for the direct gluino production scenarios considered in this study	34
Figure 5.3.	Top quark and W boson tagging efficiencies as a function of top quark p_T and W boson p_T for the merged and resolved tagging algorithms ..	42
Figure 5.4.	The m_T^b distribution for SM backgrounds and some mass points for the T2tt and T1tttt signal models	46

Figure 5.5. MET trigger efficiency in the baseline region as a function of p_T^{miss} ...	49
Figure 5.6. Electron and muon trigger efficiencies in the lepton control region as a function of lepton p_T	49
Figure 5.7. Photon trigger efficiency in the photon control region as a func- tion of photon p_T and η using the JetHT data set	50
Figure 5.8. Background composition from data-driven background predictions...	62
Figure 5.9. Comparison of the data and MC as a function of p_T^{miss} in the single lepton CR for each era in the low Δm inclusive region	64
Figure 5.10. Comparison of the data and MC as a function of p_T^{miss} in the single lepton CR for each era in the high Δm inclusive region	65
Figure 5.11. Comparisons of the transfer factors for each era of MC in the low and high Δm regions	66
Figure 5.12. Comparisons of the transfer factors for each era of MC in the low and high Δm regions	67
Figure 5.13. Validation of simulation in the QCD control region for the low Δm and high Δm selections as a function of p_T^{miss} and H_T	70
Figure 5.14. The predicted rate of QCD in the validation bins.....	70
Figure 5.15. The predicted rate of QCD in the search bins.....	71
Figure 5.16. Dominant leading-order Feynman diagram for $t\bar{t}Z$ production at the LHC	71
Figure 5.17. $t\bar{t}Z$ validation in the three-lepton channel from Single Muon and Single Electron data	73
Figure 5.18. Data, background prediction, and ratio in low Δm and high Δm validation bins	78
Figure 5.19. Data, background prediction, and pull in low Δm and high Δm validation bins	78
Figure 5.20. Observed data yields, predicted SM background, and example signal models in the low Δm bins 0–52 and high Δm bins 53–104.....	80
Figure 5.21. Observed data yields, predicted SM background, and example signal models in the high Δm bins 105–152 with $N_b = 2$ and high Δm bins 153–182 with $N_b \geq 3$	81

Figure 5.22. Observed data yields, postfit SM background prediction, and example signal models in the low Δm bins 0–52 and high Δm bins 53–104	82
Figure 5.23. Observed data yields, postfit SM background prediction, and example signal models in the high Δm bins 105–152 with $N_b = 2$ and high Δm bins 153–182 with $N_b \geq 3$	83
Figure 5.24. The 95% CL upper limit on the production cross section of the T2tt, T2bW, and T2tb simplified models as a function of the top squark and LSP masses	85
Figure 5.25. The 95% CL upper limit on the production cross section of the T2ttC, T2bWC, and T2cc simplified models as a function of the top squark mass and the difference between the top squark and LSP masses	86
Figure 5.26. The 95% CL upper limit on the production cross section of the T1tttt, T1ttbb, and T5ttcc simplified models as a function of the gluino and LSP masses	87
Figure 6.1. The dilepton p_T for the electron and muon control regions	93
Figure 6.2. The dilepton mass for the electron and muon control regions for Run 2 with low Δm baseline applied.....	95
Figure 6.3. The dilepton mass for the electron and muon control regions for Run 2 with low Δm baseline applied.....	96
Figure 6.4. The dilepton mass for the electron and muon control regions for Run 2 with low Δm baseline applied.....	97
Figure 6.5. The dilepton mass for the electron and muon control regions for Run 2 with high Δm baseline applied	98
Figure 6.6. Modified $p_T^{\text{miss}(\gamma)}$ distributions in the photon control region with low Δm and high Δm baseline selections applied and the QCD simulation separated by photon category	103
Figure 6.7. H_T distributions in the photon control region with the high Δm baseline selection applied and the QCD simulation separated by photon category.....	104
Figure 6.8. Modified $p_T^{\text{miss}(\gamma)}$ shape distributions in the photon control region with low Δm and high Δm baseline selections applied.....	105
Figure 6.9. H_T shape distributions in the photon control region with the high Δm baseline selection applied.....	106

Figure 6.10. The modified $p_T^{\text{miss}(\gamma)}$ for the photon control region for Run 2 with low Δm baseline applied	108
Figure 6.11. The modified $p_T^{\text{miss}(\gamma)}$ for the photon control region for Run 2 with low Δm baseline applied	109
Figure 6.12. The modified $p_T^{\text{miss}(\gamma)}$ for the photon control region for Run 2 with high Δm baseline applied	110
Figure 6.13. Normalization factors, R_Z , for different Run 2 years for events passing low Δm baseline	111
Figure 6.14. Normalization factors, R_Z , for different Run 2 years for events passing low Δm baseline	112
Figure 6.15. Normalization factors, R_Z , for different Run 2 years for events passing high Δm baseline	113
Figure 6.16. Shape factors, S_γ , for different Run 2 eras for events passing the low Δm baseline and with different N_b and N_j selections	114
Figure 6.17. Shape factors, S_γ , for different Run 2 eras for events passing the low Δm baseline and with different N_b and N_j selections	115
Figure 6.18. Shape factors, S_γ , for different Run 2 eras for events passing the high Δm baseline selection and with different N_b and N_j selections	116
Figure 6.19. A comparison of the modified p_T^{miss} distributions for the low Δm and high Δm lepton and photon control regions	117
Figure 6.20. The $Z \rightarrow \nu\bar{\nu}$ simulation and Z invisible prediction in the low Δm and high Δm validation bins for Run 2	118
Figure 6.21. The $Z \rightarrow \nu\bar{\nu}$ simulation and Z invisible prediction in the low Δm and high Δm search bins for Run 2	119
Figure B.1. Event display of event 471815433, which is a data event in search bin 145 and has two tagged merged top quarks	133
Figure B.2. Event display of event 448246125, which is a data event in search bin 180 and has two tagged resolved top quarks	134
Figure B.3. Event display of event 371464374, which is a data event in search bin 140 and has one tagged merged top quark and one tagged resolved top quark	135

Figure B.4. Event display of event 621760811, which is a data event in search bin 119 and has one tagged W boson	136
Figure B.5. Event display of event 1887015358, which is a data event in search bin 46 and has one ISR jet.....	137

LIST OF TABLES

Table 2.1. Standard Model particles and corresponding SUSY particles for the MSSM.....	18
Table 2.2. Unphysical states and corresponding physical states in SUSY for the MSSM.....	19
Table 5.1. Working points used for DeepCSV to tag b quarks in corresponding years	38
Table 5.2. The soft b-tagging data/MC scale factors and fullsim/fastsim scale factors for each year of data-taking.....	39
Table 5.3. Working points used for DeepAK8 to tag top quarks and W bosons in corresponding years	40
Table 5.4. Summary of the preselection requirements (baseline selection) on the reconstructed physics objects for this search, as well as the low Δm and high Δm baseline selections	53
Table 5.5. Summary of the 53 search bins that mainly target low Δm signal models.....	55
Table 5.6. Summary of the 130 search bins that mainly target high Δm signal models.....	56
Table 5.7. Summary of the 19 validation bins for low Δm	57
Table 5.8. Summary of the 24 validation bins for high Δm	58
Table 6.1. The Z boson branching ratios for “standard” decays	89
Table 6.2. The normalization values R_Z calculated for various N_b and N_{SV} selections in low and high Δm	99
Table A.1. Fermion couplings to the Z boson	129
Table C.1. Observed number of events and SM background predictions in search bins 0–27	139
Table C.2. Observed number of events and SM background predictions in search bins 28–52.....	140

Table C.3. Observed number of events and SM background predictions in search bins 53–80.....	141
Table C.4. Observed number of events and SM background predictions in search bins 81–107	142
Table C.5. Observed number of events and SM background predictions in search bins 108–136.....	143
Table C.6. Observed number of events and SM background predictions in search bins 137–161.....	144
Table C.7. Observed number of events and SM background predictions in search bins 162–182.....	145
Table D.1. Prediction for the Z invisible background ($N_{\text{pred}}^{Z \rightarrow \nu\bar{\nu}}$) with statistical uncertainty in low Δm search bins 0–27	147
Table D.2. Prediction for the Z invisible background ($N_{\text{pred}}^{Z \rightarrow \nu\bar{\nu}}$) with statistical uncertainty in low Δm search bins 28–52	148
Table D.3. Prediction for the Z invisible background ($N_{\text{pred}}^{Z \rightarrow \nu\bar{\nu}}$) with statistical uncertainty in high Δm search bins 53–80.....	149
Table D.4. Prediction for the Z invisible background ($N_{\text{pred}}^{Z \rightarrow \nu\bar{\nu}}$) with statistical uncertainty in high Δm search bins 81–107	150
Table D.5. Prediction for the Z invisible background ($N_{\text{pred}}^{Z \rightarrow \nu\bar{\nu}}$) with statistical uncertainty in high Δm search bins 108–136.....	151
Table D.6. Prediction for the Z invisible background ($N_{\text{pred}}^{Z \rightarrow \nu\bar{\nu}}$) with statistical uncertainty in high Δm search bins 137–161.....	152
Table D.7. Prediction for the Z invisible background ($N_{\text{pred}}^{Z \rightarrow \nu\bar{\nu}}$) with statistical uncertainty in high Δm search bins 162–182.....	153

ACKNOWLEDGMENTS

I am very thankful for those who have helped me along my path. I am nothing apart from Jesus Christ, my Creator, my Lord, and my Savior. Thank you for your amazing mercy, grace, and love. I am blessed by my family, my mom, Moira, my dad, Greg, and my sister, Kylie. I am grateful for my extended family, my grandparents, aunts, uncles, and cousins. I am thankful for the friends I made along the way at universities and laboratories. Thanks to my mom for teaching me mathematics. Thanks to Dawn Morrow for teaching me how to write. Thanks to Jeremy Cipiti for introducing me to physics. Thanks to Ken Kiers for teaching me modern physics and inspiring me to be a theorist. Thanks to Jay Dittmann for encouraging me during difficult times, for enabling me to teach an introductory physics course, for welcoming me into experimental physics, for showing me how to be an experimentalist, and for being a caring and dedicated advisor. Thanks to Kenichi Hatakeyama for your tireless work ethic, your significant help in analysis, and your drive to achieve the expected results. Thanks to Joe Pastika for training me to work on detector upgrades and analysis, for teaching me to drive manual transmission, and for many laughs. Thanks to Chris Madrid for the engaging discussions and debates on physics, mathematics, programming, philosophy, faith, finances, etc. and for many laughs. Thanks to Andrew and Emma Evans for being true friends when I was far from home. Thanks to my roommates along the way, Aaron Cassidy and Brandon Anderson, for sticking with me.

*For my Lord and Savior Jesus Christ,
whose name is above every name.
To you be all glory, now and forever!*

CHAPTER ONE

Introduction

Physics is the study of physical reality. Mathematical descriptions to model nature are developed and then tested by experiment to determine their validity. Experiments yield new results, which are then described by new theories. The iterative process of the scientific method holds great power for advancing knowledge in physics.

High energy physics studies fundamental forces and particles at high energy scales. The Standard Model (SM) was developed over the last century to describe the known fundamental particles and forces. When compared to data from many different high energy physics experiments, the SM gives very precise and accurate predictions.

There are many theoretical and phenomenological motivations for physics beyond the standard model (BSM). There are questions such as the hierarchy problem, neutrino oscillations, and dark matter that are not explained by the SM. Some of these questions can be answered by BSM physics theories. High energy physics experiments search for evidence of BSM physics in data.

Supersymmetry (SUSY) is a well motivated extension of the SM. SUSY postulates that every SM fermion has a bosonic superpartner, and every SM boson has a fermionic superpartner. These superpartners introduce new terms to calculations such as the Higgs boson mass calculation. In the Higgs boson mass calculation, SUSY terms exactly cancel with SM terms, which allows the summation to converge to the finite Higgs boson mass without the requirement of fine-tuning.

This dissertation presents a search for SUSY using the CMS Run 2 data set. Chapter Two introduces the theory of high energy physics, both for the SM and for SUSY. Chapter Three describes the Large Hadron Collider (LHC) and the Compact Muon Solenoid (CMS). Chapter Four provides details on CMS event reconstruction. Chapter Five discusses the data analysis searching for SUSY and the results. Chapter Six presents the background prediction of the $Z(\rightarrow \nu\bar{\nu})+\text{jets}$ process that is used in the SUSY search. Chapter Seven gives the conclusions drawn from the results.

CHAPTER TWO

High Energy Physics

2.1 The Standard Model of Particle Physics

High energy elementary particle physics is encapsulated by the Standard Model (SM) [1]. A table of the particles present in the SM is shown in Fig. 2.1. The quark flavors are up, down, charm, strange, top, and bottom. The leptons are the electron, muon, and tau, and these each have corresponding neutrinos. The vector bosons are the gluon, the W, the Z, and the photon. The only scalar boson is the Higgs boson. All charged particles have antiparticles that have equal-magnitude opposite-sign electric charge.

There are four fundamental forces in nature: gravity, the electromagnetic force, the weak force, and the strong force. Gravity is not described by the SM, and no particle mediator of gravity (e.g. graviton) has been discovered. The electromagnetic force (discussed in Section 2.1.1) is mediated by the photon, and the related charge is electric charge. The weak force (discussed in Section 2.1.2) is mediated by the Z and W bosons, and the charge for the weak interaction is called isospin. The strong force (discussed in Section 2.1.3) is mediated by the gluon, and the associated charge is customarily represented by color. Figure 2.2 shows the Feynman diagrams of the allowed interactions in the SM.

The gauge symmetry of the SM is $U(1)_Y \times SU(2)_L \times SU(3)$ [4]. The gauge symmetry $U(1)_Y \times SU(2)_L$ is for the unified electroweak force, where Y is the weak hypercharge and L indicates left-chiral fermions. The gauge symmetry $SU(3)$ is for

Standard Model of Elementary Particles

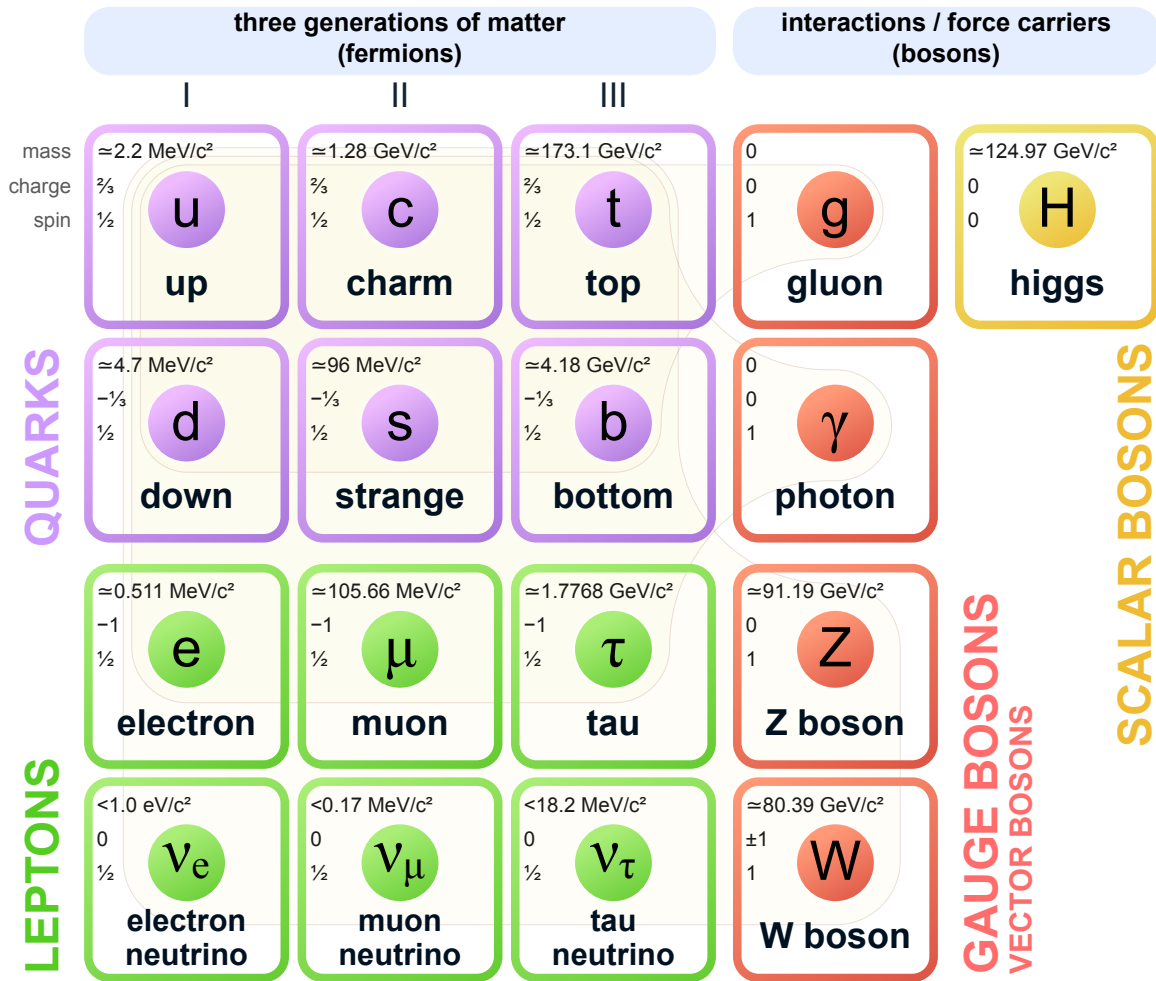


Figure 2.1: The elementary particles in the Standard Model [1, 2]. The Standard Model is composed of quarks (shown in purple), leptons (shown in green), vector bosons (shown in red), and scalar bosons (shown in yellow). The quarks and leptons are fermions. There are three generations of fermions from left to right, and particle masses increase as generation increases. The vector bosons account for the strong, weak, and electromagnetic interactions. The only scalar boson is the Higgs boson, which accounts for particle masses via the Higgs mechanism.

Standard Model Interactions (Forces Mediated by Gauge Bosons)

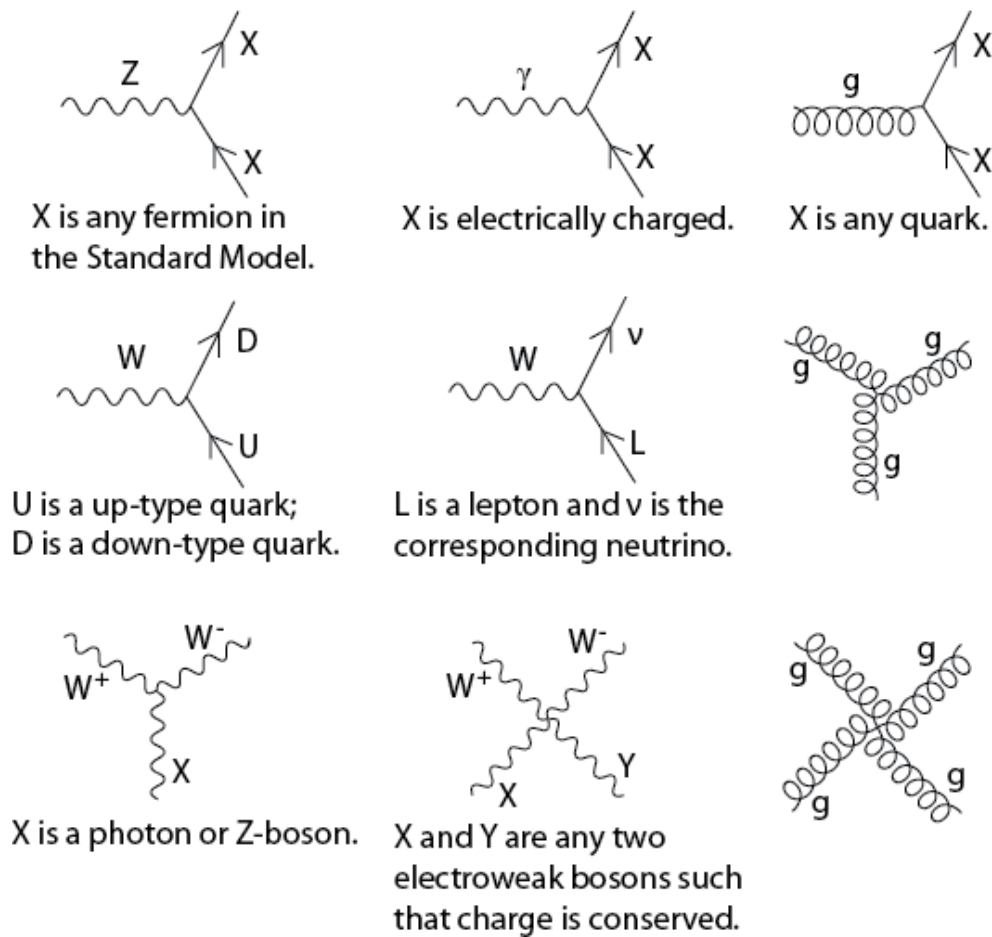


Figure 2.2: Standard Model interactions expressed as Feynman diagram vertices [1,3].

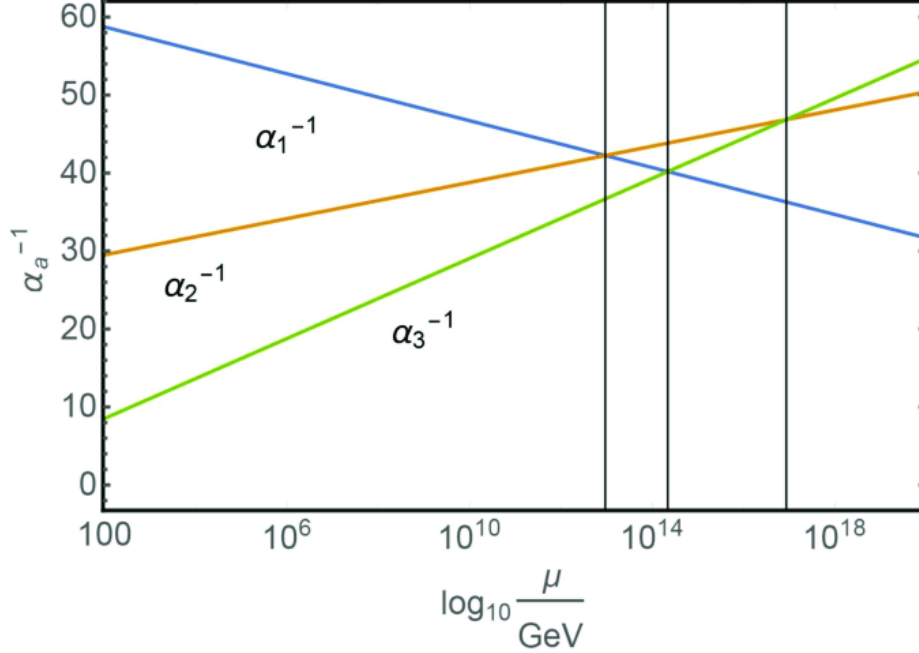


Figure 2.3: Inverted couplings in the SM as a function of energy scale for the electromagnetic (blue), weak (orange), and strong (green) forces [5]. The inverted couplings do not all intersect at the same point at high energy scales, which suggests that the SM does not predict the unification of the forces at high energies.

the strong force. The group $U(1)$ is the unitary group of degree one with 1×1 unitary matrices. The groups $SU(2)$ and $SU(3)$ are the special unitary groups of degree two and three, with 2×2 and 3×3 unitary matrices with determinant 1, respectively.

The running of the inverted couplings in the SM as a function of energy scale for the electromagnetic, weak, and strong forces are shown in Fig. 2.3. The inverted couplings do not all intersect at the same point at high energy scales. Grand Unified Theories (GUT) predict that the SM forces merge into a single force at high energies (implying one unified coupling), and this motivates theories that extend the SM to achieve this.

Assuming that neutrinos are Dirac fermions and including the strong charge parity (CP) violation phase, the SM has 26 free parameters:

- 12 fermion masses (6 quark masses and 6 lepton masses)
- 3 coupling constants for gauge interactions
- 2 Higgs boson parameters (the Higgs boson mass and vacuum expectation value)
- 8 mixing angles for the Pontecorvo-Maki-Nakagawa-Sakata (PMNS) and Cabibbo-Kobayashi-Maskawa (CKM) matrices
- 1 strong CP violation phase

The Lagrangian density of the Standard Model is comprised of many terms to fully describe the fermions and bosons in the SM along with their masses and interactions. The terms in the SM Lagrangian density (\mathcal{L}_{SM}) are organized into the four terms on the right hand side of Eq. (2.1).

$$\mathcal{L}_{\text{SM}} = \mathcal{L}_{\text{gauge}} + \mathcal{L}_{\text{leptons}} + \mathcal{L}_{\text{quarks}} + \mathcal{L}_{\text{Higgs}} \quad (2.1)$$

The first term $\mathcal{L}_{\text{gauge}}$ has gauge terms for the $U(1)$, $SU(2)$, and $SU(3)$ gauge groups (Eq. (2.2)). The second term $\mathcal{L}_{\text{leptons}}$ encapsulates lepton dynamics and masses (Eq. (2.3)). The third term $\mathcal{L}_{\text{quarks}}$ defines quark dynamics and masses (Eq. (2.4)). The final term $\mathcal{L}_{\text{Higgs}}$ describes the Higgs boson dynamics and mass (Eq. (2.5)).¹

$$\mathcal{L}_{\text{gauge}} = -\frac{1}{4}B_{\mu\nu}B^{\mu\nu} - \frac{1}{8}\text{tr}(W_{\mu\nu}W^{\mu\nu}) - \frac{1}{2}\text{tr}(G_{\mu\nu}G^{\mu\nu}) \quad (2.2)$$

¹ In these equations, (h.c.) denotes the Hermitian conjugate terms.

$$\begin{aligned}
\mathcal{L}_{\text{leptons}} = & \begin{pmatrix} \bar{\nu}_L & \bar{e}_L \end{pmatrix} \tilde{\sigma}^\mu i D_\mu \begin{pmatrix} \nu_L \\ e_L \end{pmatrix} + \bar{e}_R \sigma^\mu i D_\mu e_R + \bar{\nu}_R \sigma^\mu i D_\mu \nu_R + (\text{h.c.}) \\
& - \frac{\sqrt{2}}{v} \left[\begin{pmatrix} \bar{\nu}_L & \bar{e}_L \end{pmatrix} \phi M^e e_R + \bar{e}_R \bar{M}^e \bar{\phi} \begin{pmatrix} \nu_L \\ e_L \end{pmatrix} \right] \\
& - \frac{\sqrt{2}}{v} \left[\begin{pmatrix} -\bar{e}_L & \bar{\nu}_L \end{pmatrix} \phi^* M^\nu \nu_R + \bar{\nu}_R \bar{M}^\nu \phi^T \begin{pmatrix} -e_L \\ \nu_L \end{pmatrix} \right]
\end{aligned} \tag{2.3}$$

$$\begin{aligned}
\mathcal{L}_{\text{quarks}} = & \begin{pmatrix} \bar{u}_L & \bar{d}_L \end{pmatrix} \tilde{\sigma}^\mu i D_\mu \begin{pmatrix} u_L \\ d_L \end{pmatrix} + \bar{u}_R \sigma^\mu i D_\mu u_R + \bar{d}_R \sigma^\mu i D_\mu d_R + (\text{h.c.}) \\
& - \frac{\sqrt{2}}{v} \left[\begin{pmatrix} \bar{u}_L & \bar{d}_L \end{pmatrix} \phi M^d d_R + \bar{d}_R \bar{M}^d \bar{\phi} \begin{pmatrix} u_L \\ d_L \end{pmatrix} \right] \\
& - \frac{\sqrt{2}}{v} \left[\begin{pmatrix} -\bar{d}_L & \bar{u}_L \end{pmatrix} \phi^* M^u u_R + \bar{u}_R \bar{M}^u \phi^T \begin{pmatrix} -d_L \\ u_L \end{pmatrix} \right]
\end{aligned} \tag{2.4}$$

$$\mathcal{L}_{\text{Higgs}} = \bar{\phi} \bar{D}_\mu D^\mu \phi - \frac{1}{2} \left(\frac{m_h}{v} \right)^2 \left(\bar{\phi} \phi - \frac{v^2}{2} \right) \tag{2.5}$$

The derivatives in Eq. (2.3), Eq. (2.4), and Eq. (2.5) are defined in Eq. (2.6).

$$\begin{aligned}
D_\mu \begin{pmatrix} \nu_L \\ e_L \end{pmatrix} &= \left[\partial_\mu - \frac{ig_1}{2} B_\mu + \frac{ig_2}{2} W_\mu \right] \begin{pmatrix} \nu_L \\ e_L \end{pmatrix} \\
D_\mu \begin{pmatrix} u_L \\ d_L \end{pmatrix} &= \left[\partial_\mu + \frac{ig_1}{6} B_\mu + \frac{ig_2}{2} W_\mu + igG_\mu \right] \begin{pmatrix} u_L \\ d_L \end{pmatrix} \\
D_\mu \nu_R &= \partial_\mu \nu_R \\
D_\mu e_R &= [\partial_\mu - ig_1 B_\mu] e_R \\
D_\mu u_R &= \left[\partial_\mu + \frac{2ig_1}{3} B_\mu + igG_\mu \right] u_R \\
D_\mu d_R &= \left[\partial_\mu - \frac{ig_1}{3} B_\mu + igG_\mu \right] d_R \\
D_\mu \phi &= \left[\partial_\mu + \frac{ig_1}{2} B_\mu + \frac{ig_2}{2} W_\mu \right] \phi
\end{aligned} \tag{2.6}$$

2.1.1 The Electromagnetic Interaction

In the nineteenth century, James Clerk Maxwell united electrical and magnetic forces into the electromagnetic force and developed the unified theory of electromagnetism. The quanta of light, photons, were discovered in the twentieth century. In the SM, the photon is the mediator of the electromagnetic force as described by quantum electrodynamics (QED). The photon is a massless vector boson. Photons can interact with all electrically charged particles, but photons themselves are electrically neutral. Antiparticles have opposite electric charge compared to charged particles. Parity is conserved in QED, and U(1) is the local gauge symmetry of QED. In the SM, the electromagnetic interaction is combined with the weak interaction to form the electroweak interaction as discussed in Section 2.1.2.

2.1.2 *The Weak Interaction*

The electromagnetic and weak forces were unified into the electroweak force by Glashow, Weinberg, and Salam in the 1960s [6, 7]. The local gauge symmetry of the electroweak force is $U(1)_Y \times SU(2)_L$. The weak force mediators in the SM are the electrically charged W^+ and W^- bosons and the electrically neutral Z boson. The W and Z bosons are vector bosons that have large masses and short lifetimes. Parity is not conserved in the weak interaction as only left handed chiral particles and right handed chiral antiparticles couple to the charged W^\pm bosons. The neutral Z boson couples to both left handed chiral and right handed chiral particles and antiparticles. Calculations of W and Z boson decay rates and the Z to neutrinos branching ratio are presented in Appendix A. The Z to neutrinos branching ratio has particular interest as it relates directly to the “ Z invisible” process investigated in Chapter Six.

2.1.3 *The Strong Interaction*

Quantum chromodynamics (QCD) describes the strong force. The local gauge symmetry of the strong force is $SU(3)$, and parity is conserved in QCD. The gluon is the mediator of the strong force, and it is a massless vector boson. There are eight gluons in QCD that correspond to the eight generators of the $SU(3)$ local gauge symmetry. Gluons interact with quarks and with other gluons as both quarks and gluons carry the charge of the strong force (often referred to as color). Antiquarks carry opposite color charge compared to quarks.

2.1.4 *The Higgs Boson Interaction*

The Higgs boson was the last missing puzzle piece to be discovered in the SM. On July 4, 2012, the ATLAS and CMS collaborations announced the discovery

of a particle with properties matching those of the theorized Higgs boson [8]. The $H \rightarrow \gamma\gamma$ and $H \rightarrow ZZ$ decay channels have the best mass resolution and gave the largest significance for discovery. The diphoton invariant mass distribution from CMS is shown in Fig. 2.4. There is a clear excess in data over the background prediction near 125 GeV that is consistent with the Higgs boson.

The Higgs boson interaction results in fundamental particles obtaining mass. This Higgs mechanism describes the spontaneous symmetry breaking introduced by the Higgs boson whereby the W and Z bosons obtain mass.

Following the approach from [4], consider a scalar field ϕ with the potential

$$V(\phi) = \frac{1}{2}\mu^2\phi^2 + \frac{1}{4}\lambda\phi^4 \quad (2.7)$$

and the Lagrangian

$$\mathcal{L} = \frac{1}{2}(\partial_\mu\phi)(\partial^\mu\phi) - \frac{1}{2}\mu^2\phi^2 - \frac{1}{4}\lambda\phi^4. \quad (2.8)$$

Requiring the potential $V(\phi)$ to have finite minima implies $\lambda > 0$. To find the minima, the derivative is set to zero:

$$V'(\phi) = 0$$

$$\mu^2\phi + \lambda\phi^3 = 0.$$

The minima are

$$\phi = \begin{cases} 0 \\ +\sqrt{\frac{-\mu^2}{\lambda}} \\ -\sqrt{\frac{-\mu^2}{\lambda}}. \end{cases}$$

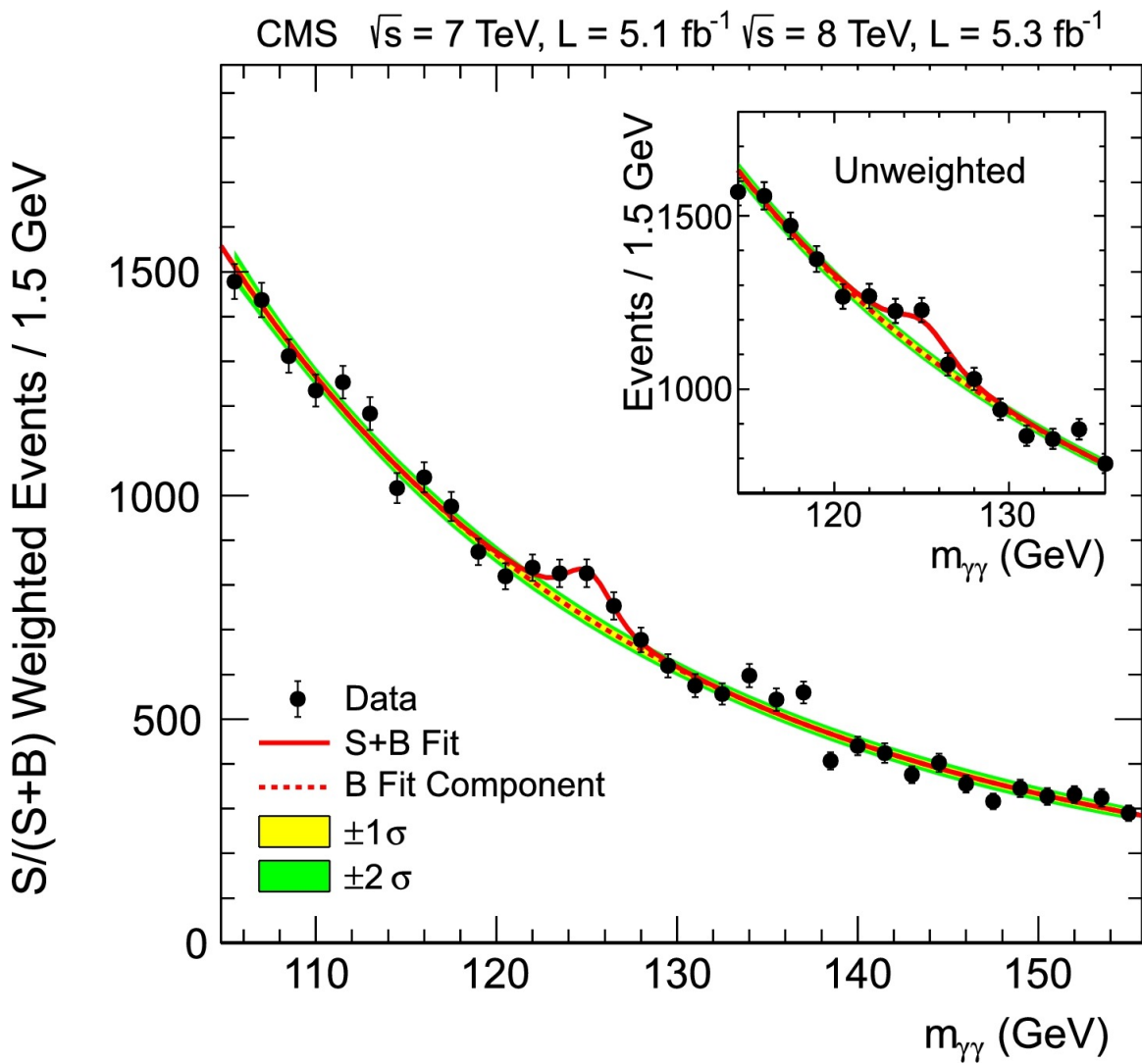


Figure 2.4: Evidence of the Higgs boson in the diphoton invariant mass distribution at CMS [8]. The background fit (dashed red line), signal plus background fit (solid red line), and data (black points) are shown. The yellow and green bands represent the $\pm 1\sigma$ and $\pm 2\sigma$ standard deviation uncertainties for the background prediction, respectively.

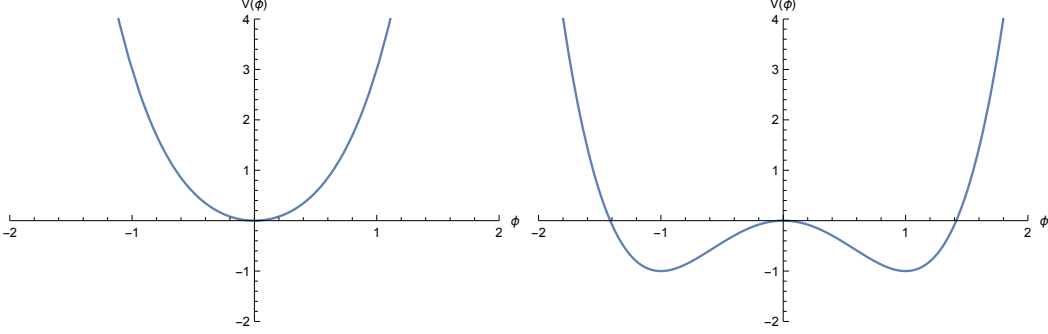


Figure 2.5: The potential $V(\phi)$ from Eq. (2.7) with $\mu^2 > 0$ (left) and $\mu^2 < 0$ (right). Both plots have $\lambda > 0$ so that the potential has finite minima.

For $\lambda > 0$, the minima $\pm\sqrt{\frac{-\mu^2}{\lambda}}$ are real and nonzero if $\mu^2 < 0$ as shown in Fig. 2.5.

The vacuum expectation value (VEV), $v > 0$, is defined as

$$v = \sqrt{\frac{-\mu^2}{\lambda}},$$

and the allowed minima of the potential are then $\phi = \pm v$. There are two possible vacuum states corresponding to the two minima for the potential $\phi = \pm v$, and the potential is symmetric about $\phi = 0$. This ϕ symmetry is broken when the system moves to one of the available minima, either $\phi = +v$ or $\phi = -v$, and acquires a nonzero VEV; this process is referred to as spontaneous symmetry breaking.

For the SM Higgs boson, four degrees of freedom are required for the W^+ , W^- , Z , and Higgs bosons. Two complex scalar fields are used to provide four degrees of freedom. One field is charged, denoted as ϕ^+ , and the other is neutral, denoted as ϕ^0 . These fields can be written in terms of real fields ϕ_i with $i = 1, 2, 3, 4$:

$$\begin{aligned}\phi^+ &= \frac{1}{\sqrt{2}} (\phi_1 + i\phi_2) \\ \phi^0 &= \frac{1}{\sqrt{2}} (\phi_3 + i\phi_4).\end{aligned}$$

The charged and neutral fields can be combined to form the weak isospin doublet ϕ :

$$\phi = \begin{pmatrix} \phi^+ \\ \phi^0 \end{pmatrix}$$

$$\phi = \frac{1}{\sqrt{2}} \begin{pmatrix} \phi_1 + i\phi_2 \\ \phi_3 + i\phi_4 \end{pmatrix}.$$

The Higgs boson potential is

$$V(\phi) = \mu^2 \phi^\dagger \phi + \lambda (\phi^\dagger \phi)^2.$$

The Lagrangian with this Higgs boson potential is then

$$\mathcal{L} = (\partial_\mu \phi)^\dagger (\partial^\mu \phi) - V(\phi)$$

$$\mathcal{L} = (\partial_\mu \phi)^\dagger (\partial^\mu \phi) - \mu^2 \phi^\dagger \phi - \lambda (\phi^\dagger \phi)^2.$$

The minima of the Higgs boson potential are determined by setting the derivative to zero:

$$\partial_\mu V(\phi) = 0$$

$$\mu^2 ((\partial_\mu \phi^\dagger) \phi + \phi^\dagger \partial_\mu \phi) + 2\lambda \phi^\dagger \phi ((\partial_\mu \phi^\dagger) \phi + \phi^\dagger \partial_\mu \phi) = 0$$

$$(\mu^2 + 2\lambda \phi^\dagger \phi) ((\partial_\mu \phi^\dagger) \phi + \phi^\dagger \partial_\mu \phi) = 0.$$

This relation will be satisfied if either term is zero, which gives

$$(\partial_\mu \phi^\dagger) \phi + \phi^\dagger \partial_\mu \phi = 0$$

$$\phi = 0$$

and

$$\begin{aligned}\mu^2 + 2\lambda\phi^\dagger\phi &= 0 \\ \phi^\dagger\phi &= -\frac{\mu^2}{2\lambda} \\ \frac{1}{2}(\phi_1^2 + \phi_2^2 + \phi_3^2 + \phi_4^2) &= \frac{v^2}{2} \\ \phi_1^2 + \phi_2^2 + \phi_3^2 + \phi_4^2 &= v^2,\end{aligned}$$

where

$$v^2 = -\frac{\mu^2}{\lambda}$$

has been used. In the unitary gauge, the Higgs boson doublet is

$$\phi(x) = \frac{1}{\sqrt{2}} \begin{pmatrix} 0 \\ v + h(x) \end{pmatrix}$$

such that ϕ^0 has a nonzero vacuum expectation value v and $h(x)$ is the Higgs field that is expanded about the minimum value of the potential v . The mass of the Higgs boson can be written in terms of λ and v as

$$m_H = \sqrt{2\lambda}v.$$

2.2 Supersymmetry

The SM has achieved agreement with experiment to very high precision after many years of scrutiny. The SM requires 26 free parameters that must be measured by experiment and input to the theory. This motivates the search for other theories with fewer free parameters that can explain the relationship between the SM parameters. The SM describes the electromagnetic, strong, and weak forces but does not include gravity. There may be a Grand Unified Theory (GUT) that unifies the fundamental forces at high energies and is able to explain all known physics including quantum

mechanics and general relativity. Furthermore, particle physics still has a number of open questions including neutrino oscillations, matter-antimatter asymmetry, the hierarchy problem [9], and the nature of dark matter (DM) [10].

Supersymmetry (SUSY) [11–16] is a theory that addresses some of the open questions regarding the SM. SUSY is an extension of the SM that posits the existence of additional particles, called superpartners, corresponding to the SM particles. SM fermions have bosonic superpartners, and SM bosons have fermionic superpartners. When calculating certain quantities (e.g. the Higgs boson mass), this fermion-boson pairing introduced by SUSY results in cancellations of higher order radiative quantum loop corrections as the fermionic loops are negative [17, 18]. SUSY thereby addresses the hierarchy problem without fine-tuning higher-order terms to result in precise cancellations; instead quantum loop cancellations occur due to a physical symmetry. Furthermore, SUSY modifies the running of the couplings of the SM forces. Figure 2.6 shows the inverted couplings for the minimal supersymmetric standard model (MSSM) as a function of energy scale for the electromagnetic, weak, and strong forces. The MSSM predicts that at high energies, the fundamental forces have equal strength and are unified into one force.

The SM and SUSY particles are shown in Fig. 2.7 and listed in Tables 2.1 and 2.2 for the minimal supersymmetric standard model (MSSM). Each SM particle has one or more supersymmetric partners. The SM spin- $\frac{1}{2}$ chiral fermions, quarks, leptons, and neutrinos are paired with spin-0 scalar bosons, squarks, sleptons and sneutrinos, respectively. The SM spin-1 gauge bosons, the gluon, photon, Z boson, and W boson, are paired with spin- $\frac{1}{2}$ gauginos, the gluino, photino, zino, and wino, respectively. The SM spin-0 scalar Higgs boson is paired with spin- $\frac{1}{2}$ weak isospin

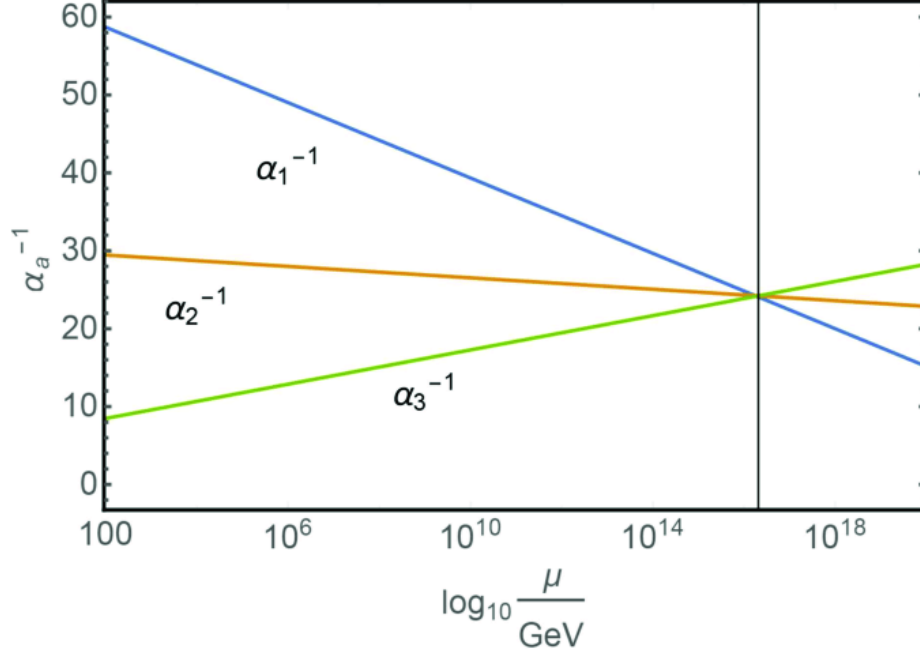


Figure 2.6: Inverted couplings in the MSSM as a function of energy scale for the electromagnetic (blue), weak (orange), and strong (green) forces [5]. The inverted couplings all intersect at the same point at high energy scales. The MSSM predicts the unification of the forces at high energies.

doublet Higgsinos. The gauginos and Higgsinos are not necessarily physical states. Rather, mixtures of gauginos and Higgsinos are combined to form the neutralinos $\tilde{\chi}^0$ and charginos $\tilde{\chi}^\pm$, which are predicted physical states in the MSSM (Table 2.2).

In unbroken supersymmetry, the supersymmetric particles have identical masses with their SM counterparts. However, unbroken supersymmetry is not physical; if it were, then supersymmetric particles would have been observed in past and current experiments as they would be accessible at the same energy scales as SM particles, and to date no supersymmetric particles have been observed. Therefore, for supersymmetry to be physical, it must be a broken symmetry in which supersymmetric particles have larger masses than their SM partners. With respect to the hierarchy problem and the Higgs boson mass calculation, the size of the contributions to this

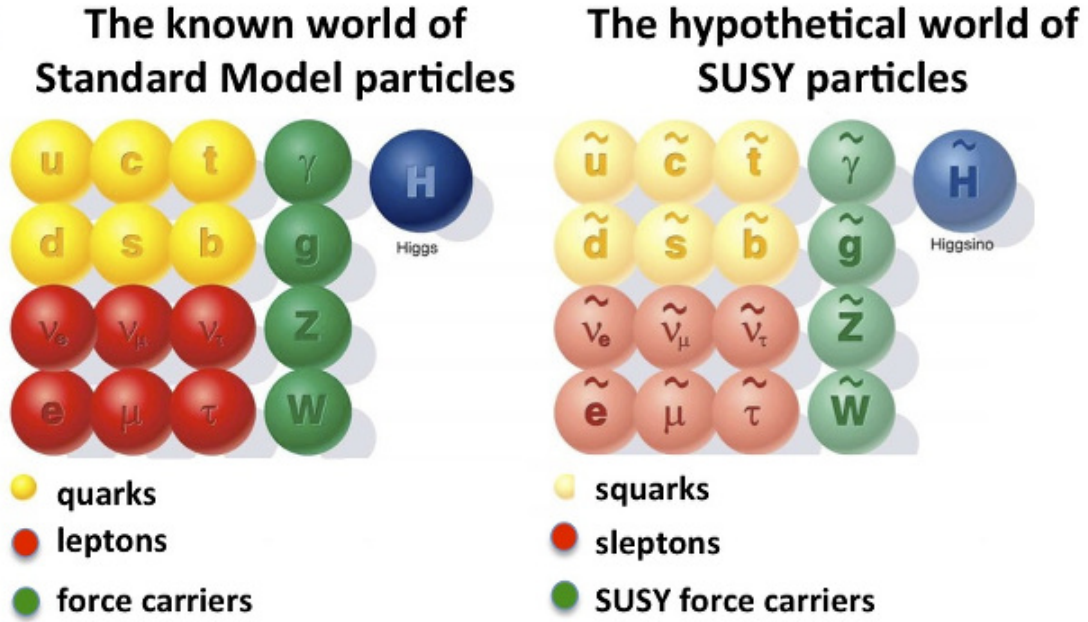


Figure 2.7: The SM particles (left) and SUSY particles (right) [19,20]. SUSY predicts that each SM particle has a superpartner. The names of fermion superpartners are created by adding an “s” to the beginning. The electron superpartner is the selectron. The names of boson superpartners are created by using “ino” as a suffix. The Higgs boson superpartner is the Higgsino. Superpartners are denoted by adding a tilde. For example, the superpartner of the up quark “u” is the up squark “ \tilde{u} ”.

Table 2.1: SM particles and corresponding SUSY particles for the MSSM [4]. The gauginos (gluino, photino, zino, and wino) and Higgsinos are not necessarily physical states. Instead, gauginos and Higgsinos are combined into physical states known as neutralinos and charginos (see Table 2.2).

Particle	Symbol	Spin	Superparticle	Symbol	Spin
Quark	q	$\frac{1}{2}$	Squark	\tilde{q}_L, \tilde{q}_R	0
Lepton	ℓ^\pm	$\frac{1}{2}$	Slepton	$\tilde{\ell}_L^\pm, \tilde{\ell}_R^\pm$	0
Neutrino	ν	$\frac{1}{2}$	Sneutrino	$\tilde{\nu}_L, \tilde{\nu}_R$	0
Gluon	g	1	Gluino	\tilde{g}	$\frac{1}{2}$
Photon	γ	1	Photino	$\tilde{\gamma}$	$\frac{1}{2}$
Z boson	Z	1	Zino	\tilde{Z}	$\frac{1}{2}$
W boson	W^\pm	1	Wino	\tilde{W}^\pm	$\frac{1}{2}$
Higgs boson	H	0	Higgsino	$\tilde{H}_1^0, \tilde{H}_2^0, \tilde{H}^\pm$	$\frac{1}{2}$

Table 2.2: Unphysical states and corresponding physical states in SUSY for the MSSM [4]. The physical states, neutralinos and charginos, are combinations of the unphysical states, gauginos and Higgsinos.

Unphysical states	Symbols	Spin	Physical states	Symbols	Spin
Neutral gauginos and Higgsinos	$\tilde{\gamma}, \tilde{Z}, \tilde{H}_1^0, \tilde{H}_2^0$	$\frac{1}{2}$	Neutralinos	$\tilde{\chi}_1^0, \tilde{\chi}_2^0, \tilde{\chi}_3^0, \tilde{\chi}_4^0$	$\frac{1}{2}$
Charged gauginos and Higgsinos	$\tilde{W}^\pm, \tilde{H}^\pm$	$\frac{1}{2}$	Charginos	$\tilde{\chi}_1^\pm, \tilde{\chi}_2^\pm$	$\frac{1}{2}$

calculation depend on particle mass. The top quark, the heaviest particle in the SM, has the largest contribution to the Higgs boson mass calculation. This motivates the search for the superpartner of the top quark, the top squark, in order to suppress the top quark term in the Higgs boson mass calculation.

A symmetry called ‘‘R-parity’’ is often applied to the MSSM, and it has important implications for collider searches for SUSY. R-parity is defined by

$$(-1)^R = (-1)^{3(B-L)+2S}, \quad (2.9)$$

where B is baryon number, L is lepton number, and S is spin. Under R-parity, all SM particles are even with an R-parity of $+1$, and all SUSY particles are odd with an R-parity of -1 . R-parity invariance implies that the lightest supersymmetric particle (LSP) must be stable. By definition, there are no lighter supersymmetric particles for the LSP to decay to, and if the LSP could decay purely to SM particles, this would violate R-parity. In addition, for experiments that collide SM particles, R-parity invariance implies that SUSY particles must be pair produced and must decay to R-parity odd states that contain at least one SUSY particle.

In many supersymmetric models that conserve R-parity, the lightest neutralino is the LSP and is neutral, weakly interacting, and stable. In this case the LSP is a weakly interacting massive particle (WIMP) candidate and a DM candidate. Collider searches for R-parity invariant SUSY typically involve models with pair-produced SUSY particles that decay to the LSP and have missing energy final states. The data analysis presented in Chapter Five looks for evidence of simplified SUSY models with top squark and gluino pair production that decay to the LSP. The analysis uses all-hadronic final states that have missing energy and is sensitive to top squark, gluino, and LSP masses up to $\approx 1\text{--}2$ TeV.

CHAPTER THREE

The CMS Experiment

Studying the SM particles and interactions in detail requires a source for high energy particles and a detector to observe the final states of interactions. Particle colliders provide a reliable, controlled, and consistent source of high energy particle collisions. Particle detectors record data from high energy particle collisions, which are used to reconstruct the final state particles from a collision event. Over time, the high energy physics community has built colliders with increasing center-of-mass collision energy in order to access fundamental particles and forces that are present at higher energies. The Large Electron-Positron (LEP) collider at the European Organization for Nuclear Research (CERN) operated from 1989 to 2000 and collided electrons with positrons at center-of-mass energies up to 209 GeV. The Tevatron at the Fermi National Accelerator Laboratory (FNAL) operated from 1983 to 2011 and collided protons with antiprotons at center-of-mass energies up to 1 TeV. The Large Hadron Collider (LHC) at CERN began operating in 2008 and collides protons at center-of-mass energies up to 13 TeV.

3.1 The Large Hadron Collider

The Large Hadron Collider (LHC) is on the French-Swiss border near Geneva, Switzerland, not far from some excellent fondue restaurants. The LHC was built from 1998 to 2008. The LHC is a circular proton collider that is 100 m underground (on average) and 26.7 km in circumference. There are four detectors around the LHC ring, which are the Compact Muon Solenoid (CMS), ATLAS, Large Hadron Collider

beauty (LHCb), and A Large Ion Collider Experiment (ALICE). CMS and ATLAS are general purpose detectors. ALICE investigates quark-gluon plasma, and LHCb targets b quark physics. The LHC proton-proton collision energy for Run 2 was 13 TeV. Protons travel very near the speed of light around the LHC with an orbit period of 88.9 μs and an orbit frequency of 11.2 kHz. Proton collisions are spaced in 25 ns intervals, and the collision frequency is 40 MHz. Protons are grouped into bunches, where each bunch contains 1.15×10^{11} protons. There are 3557 available bunch slots spaced in 25 ns intervals for one LHC orbit, but not all slots are filled, and there are “orbit gaps.” There are 2808 bunch slots filled, which is about 79% of the available slots. In total, the two LHC proton beams contain 6.46×10^{14} protons during operation. Taking the product of the the proton-proton cross section at $\sqrt{s} = 14$ TeV ($\sigma = 100 \text{ mb} = 10^{-25} \text{ cm}^2$) and the design instantaneous luminosity ($\mathcal{L} = 10^{34} \text{ cm}^{-2} \text{ s}^{-1}$) yields the collision rate $\mathcal{R} = \sigma\mathcal{L} = 10^9 \text{ s}^{-1}$, i.e. one billion proton-proton collisions per second.

The CERN accelerator complex [21] in Fig. 3.1 is composed of multiple stages to accelerate protons to their final collision energy. To begin, hydrogen atoms are obtained from a bottle of hydrogen gas. An electric field is used to remove electrons from the hydrogen atoms, which are then simply protons. The first stage of acceleration is Linac 2, which accelerates protons up to 50 MeV. Next, protons enter the Proton Synchrotron Booster (PSB) where they reach 1.4 GeV. Following this is the Proton Synchrotron (PS), which accelerates protons up to 26 GeV. Protons are then sent to the Super Proton Synchrotron (SPS) and reach 450 GeV. Finally, the protons are injected into the Large Hadron Collider (LHC) and are accelerated to 6.5 TeV. The LHC has two proton beams circling in opposite directions, and protons in both

CERN's Accelerator Complex

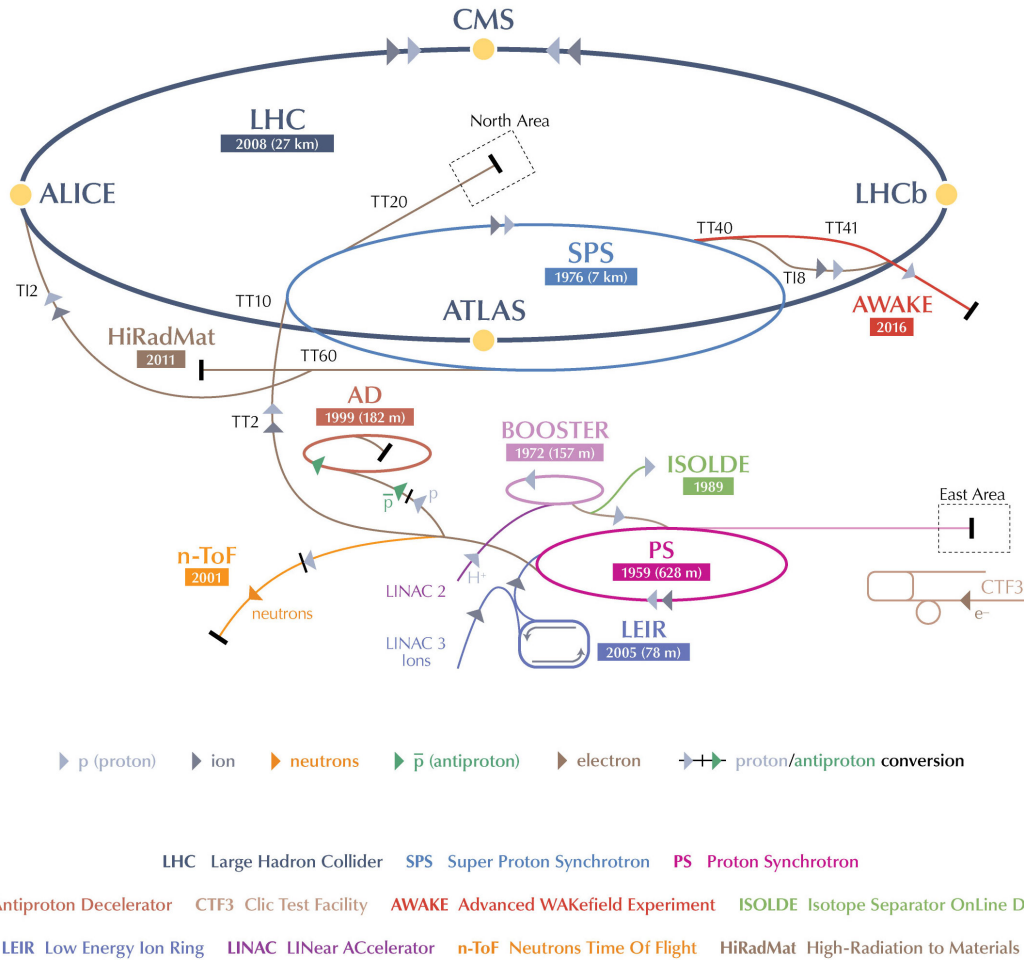


Figure 3.1: The CERN accelerator complex [22]. Protons move from Linac 2 to the Booster, the PS, the SPS, and the LHC with increased momenta at each stage.

beams have an energy of 6.5 TeV. When two protons going in opposite directions collide, the center-of-mass energy is 13 TeV.

3.2 The Compact Muon Solenoid

The Compact Muon Solenoid (CMS) is a general purpose detector. Data from the CMS experiment are used to study SM particles such as the Higgs boson and to search for evidence of BSM physics such as SUSY.

CMS is near Cessy, France and is opposite to ATLAS on the LHC ring. The CMS Technical Design Report (TDR) provides the original design of the CMS detector [23]. The CMS detector is a cylinder that is 21.6 m long, 14.6 m in diameter, and weighs 12,500 tons. A strong magnetic field of 4 T is produced by the superconducting solenoid within CMS, which is 12.9 m long and 5.9 m in diameter. The superconducting solenoid has 2168 turns and carries an electric current of 19.5 kA. The magnetic field enables good momentum resolution of charged particles, which follow a helical trajectory through the detector. CMS is composed of various subdetectors including the silicon trackers, the electromagnetic calorimeter (ECAL), the hadronic calorimeter (HCAL), and the muon chambers as shown in Fig. 3.2. Figure 3.3 is an illustration of a cross section of CMS showing the subdetectors and paths that different types of particles may take through CMS. Figure 3.4 is a picture of one end of the CMS detector taken during a shutdown period.

The tracking system is the innermost detector in CMS and fills a cylinder 5.8 m long with a diameter of 2.6 m. There are three layers of silicon pixel detectors near the interaction region and ten layers of silicon microstrip detectors.

The ECAL uses lead tungstate (PbWO_4) crystals as a scintillating material as it is transparent and has a high density, which results in a short radiation length. ECAL uses avalanche photodiodes (APD) in the barrel region and vacuum phototriodes (VPT) to detect scintillation light.

The HCAL contains alternating layers brass and scintillator. The brass layers cause incident high energy particles to lose energy and produce showers of particles. These showers interact with the scintillator to produce light. A portion of this light is collected by wavelength shifting fibers and transmitted to hybrid photodiodes (HPD).

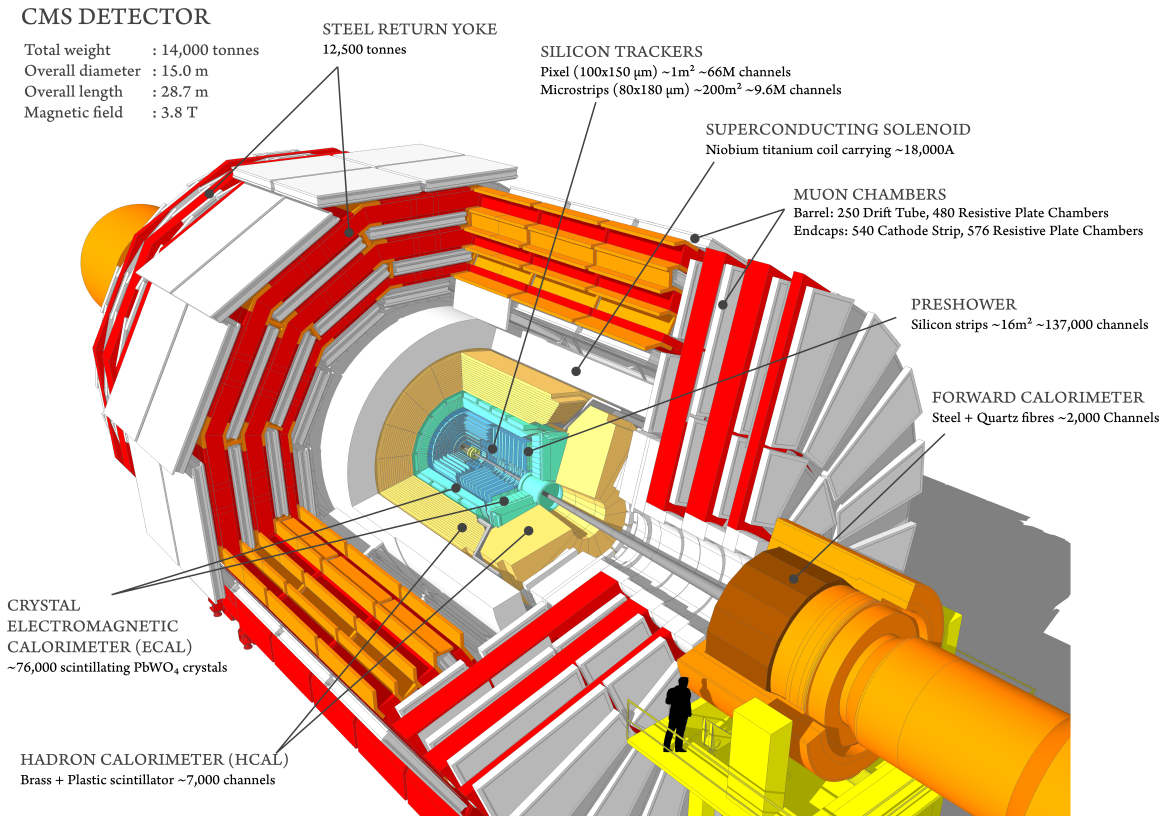


Figure 3.2: An illustration of the CMS detector and subdetectors [24].

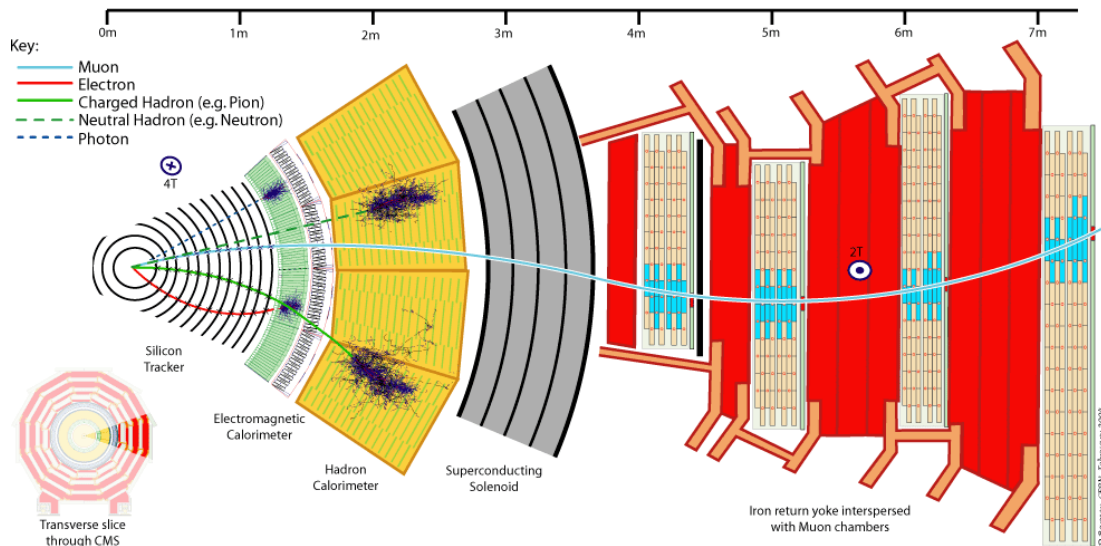


Figure 3.3: A transverse slice of CMS with subdetectors and illustrative particles originating at the collision point [25]. Note the straight trajectories of neutral particles and the curved trajectories of charged particles due to the presence of the magnetic field generated by the superconducting solenoid.

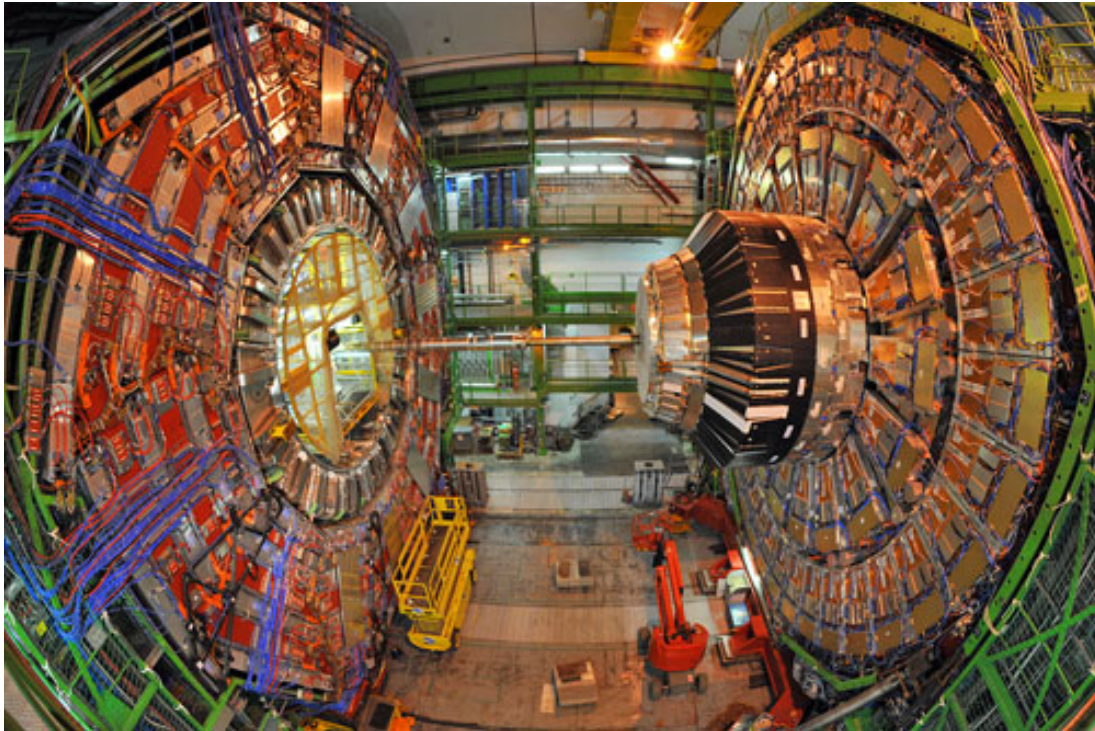


Figure 3.4: One end of the CMS detector during an LHC shutdown period. The endcap is extruded to allow for work on the detector. For normal operation, the endcap is inserted into the barrel.

The amount of light measured by the HPDs is correlated with the energy of particles incident upon HCAL.

The muon chambers are composed of drift tubes (DT) in the barrel region, cathode strip chambers (CSC) in the endcap region, and resistive plate chambers (RPC).

The LHC bunch crossing rate is 40 MHz, and the proton interaction rate is $\mathcal{R} = \sigma\mathcal{L} = 10^9 \text{ s}^{-1}$. However, collision event information can only be recorded for long term storage at a rate of 100 bunch crossings per second, where each bunch crossing has multiple interactions. Therefore, the event rate needs to be reduced by a factor of around 10^6 . Triggers are carefully designed to reduce the event rate in an advantageous way and target events possessing certain characteristics. There are many triggers in CMS that select events containing reconstructed objects above a momentum threshold (e.g. electrons, muons, photons, or jets) or having physics parameters above a specified threshold (e.g. missing transverse energy (p_T^{miss}) or the scalar sum of jet transverse momenta (H_T)). Each data analysis can then select data events using a trigger best suited to the final state(s) of the physics process(es) in the analysis. The CMS trigger system includes the Level 1 (L1) trigger and the High Level Trigger (HLT).

The L1 trigger reduces the event rate by a factor of approximately 10^3 , from the 40 MHz bunch crossing rate to an output rate of 100 kHz. The L1 trigger calculation is performed in the underground service cavern after collecting data from front-end (i.e. on-detector) electronics, and then the L1 trigger decision is sent to front-end and back-end electronics. The total time allotted for data transit and the L1 trigger

calculation is $3.2 \mu\text{s}$, and the portion of time for the L1 calculation is less than $1 \mu\text{s}$. During the total time of $3.2 \mu\text{s}$, detector data from the events are stored in buffers.

The HLT reduces the event rate by a factor of 10^3 , from 100 kHz from the L1 trigger output to 100 Hz for long term storage. Optimized HLT code runs on an above ground processor farm and uses information from all subdetectors in stages. The storage size for each event is about 1.5 MB.

3.3 *CMS Phase 1 Upgrades*

The CMS HCAL Phase 1 upgrade is fully described in [26]. For the HCAL forward (HF), new multi-anode photomultiplier tubes (PMT) were installed. For the HCAL endcap (HE) and HCAL barrel (HB), the hybrid photodiodes (HPD) were replaced with silicon photomultipliers (SiPM). Furthermore, for HF, HE, and HB, new front-end and back-end electronics for data readout and acquisition were installed.

CHAPTER FOUR

Event Reconstruction

The proton-proton collision events collected by the CMS detector tend to have myriad particles. Many particles interact with some portion of the detector, and some have little or no measurable interaction with the detector (e.g. neutrinos). The goal of event reconstruction is to use the data collected by the CMS subdetectors to properly identify different particles present in the event, which can then in turn be used to construct higher-level particles and objects or to calculate physics parameters. CMS event reconstruction is done using an approach called particle flow (PF) reconstruction [27]. PF reconstruction uses signals from channels in the tracker (hits) to construct tracks, representing particle trajectories, and vertices, representing particle starting locations. Calorimeter signals are used to form clusters and superclusters that quantify the energy deposited by particles. Tracks and clusters are matched based on location in the detector. Information from the CMS subdetectors (the inner tracker, ECAL, HCAL, and muon detector) is combined to create a set of PF particles where each particle is identified as a muon, electron, photon, charged hadron, or neutral hadron. The collection of PF particles is then used to form additional objects such as jets, missing transverse energy, and taus. PF particles are also used to measure particle isolation.

4.1 Muons

Muons are identified by compatible tracks from the inner tracker and muon detectors. Since muons are charged, they leave hits in the tracker and muon detectors.

Muons do not deposit much energy in the calorimeters. The large mass of muons compared to electrons enables them to travel through the entirety of the CMS detector without being stopped by the material in the detector.

4.2 Electrons

Electrons are identified by tracks matched to ECAL clusters without matching HCAL clusters. Electrons leave hits in the inner tracker because they possess electric charge. Electrons deposit most of their energy in ECAL and are stopped before reaching HCAL.

4.3 Photons

Photons are identified by ECAL clusters without matching tracks or HCAL clusters. Photons do not leave hits in the inner tracker because they are electrically neutral. Photons deposit most of their energy in ECAL.

4.4 Hadrons

Charged hadrons are identified by tracks matched to HCAL clusters. Neutral hadrons are identified by HCAL clusters without matching tracks. Charged hadrons leave hits in the inner tracker, while neutral hadrons do not. Charged hadrons and neutral hadrons deposit most of their energy in HCAL and are stopped before reaching the muon detectors.

4.5 Jets

High energy inelastic proton-proton collisions result in parton scattering (quarks and gluons). Quarks and gluons hadronize and form hadronic jets of particles due to color confinement as described by quantum chromodynamics (QCD). In order to

reconstruct hadronic jets, the particles produced by the hadronization of a parton need to be associated together (or clustered, in other words) to form a single object. There are a variety of algorithms that can be used to cluster particles into hadronic jets.

Sequential recombination algorithms make use of the distance d_{ij} between entities (particles/pseudojets) i and j and the distance d_{iB} between entity i and the beam. Particles are iteratively clustered into jets by comparing d_{ij} and d_{iB} . If $d_{ij} < d_{iB}$, then entities i and j are combined. If $d_{ij} > d_{iB}$, then entity i is classified as a jet and removed from the collection of entities. The process is repeated until no entities remain. The Cambridge/Aachen, k_T , and anti- k_T algorithms use distance parameters defined as

$$\begin{aligned}
 d_{ij} &= \min(k_{ti}^{2p}, k_{tj}^{2p}) \frac{\Delta_{ij}^2}{R^2}, \\
 d_{iB} &= k_{ti}^{2p}, \\
 \Delta_{ij}^2 &= (y_i - y_j)^2 + (\phi_i - \phi_j)^2,
 \end{aligned}
 \tag{4.1}$$

where k_{ti} , y_i , and ϕ_i are the transverse momentum, rapidity, and azimuthal angle of particle i , respectively [28]. The distance parameter R can be specified to determine the maximum allowed size of clustered jets. The parameter p determines the power applied to the transverse momentum k_{ti} . Setting $p = 0$ results in the Cambridge/Aachen algorithm. The k_T algorithm uses $p = 1$, and the anti- k_T algorithm uses $p = -1$.

For the data analysis in Chapter Five, jets are reconstructed using the anti- k_T algorithm [28]. The anti- k_T algorithm is an infrared and collinear (IRC) safe algorithm in which jet clustering is driven by hard radiation. Soft radiation does not influence

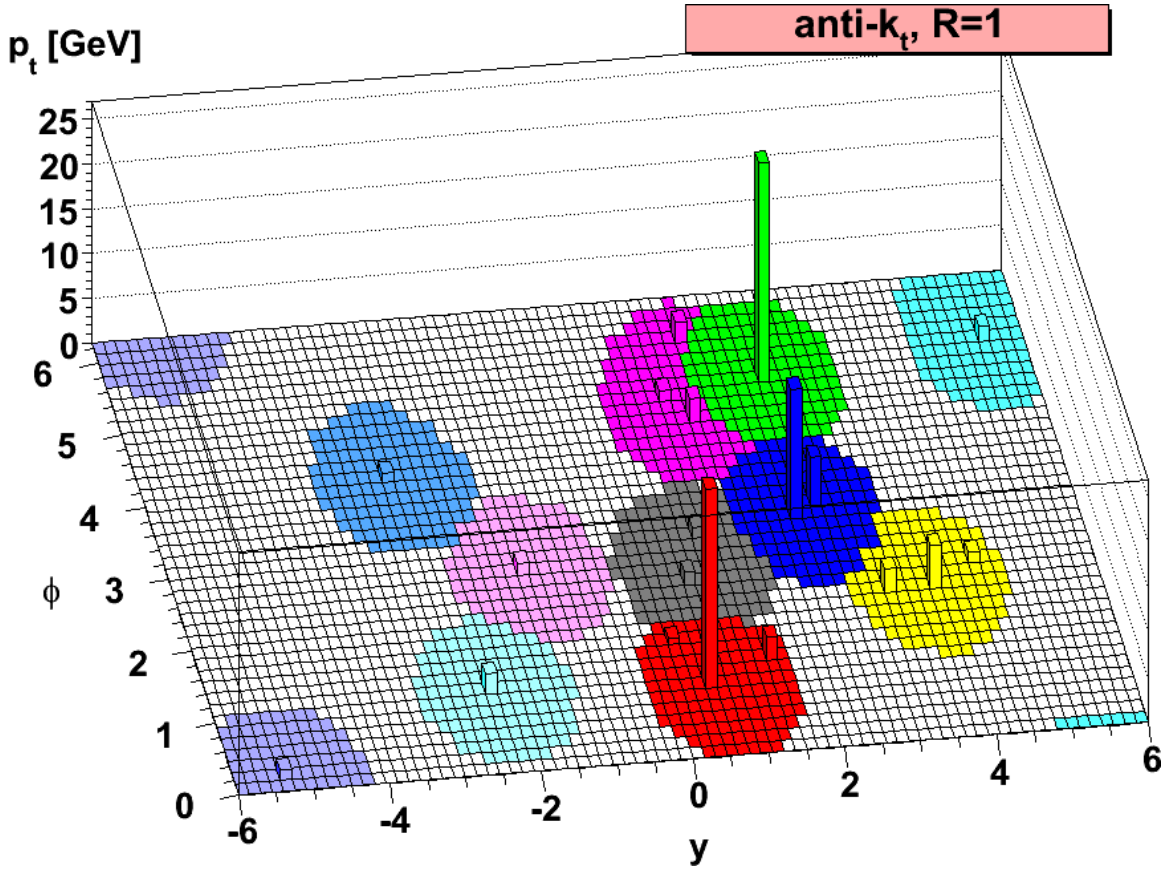


Figure 4.1: Clustering jets using the anti- k_T algorithm with the distance parameter $R = 1$ [28]. The clustered jets are shown in the y - ϕ plane, where y is the rapidity and ϕ is the azimuth. Each color represents a separate jet, and all particles within the colored region are included in that jet. Each jet typically contains many particles, but each particle can be included in at most one jet.

the jet shapes defined by the anti- k_T algorithm. An example of the application of the anti- k_T algorithm is shown in Fig. 4.1.

For CMS data analysis involving jets, the anti- k_T distance parameters $R = 0.4$ and $R = 0.8$ are commonly used, and the resulting jets are referred to as AK4 and AK8 jets, respectively. The SUSY search presented in Chapter Five makes use of both AK4 and AK8 jets.

CHAPTER FIVE

Searching for Supersymmetry

5.1 Overview

Many top squark searches have been performed by the ATLAS [29–39] and CMS [40–51] collaborations using LHC proton-proton collision events at 13 TeV, and lower limits on the top squark mass are beginning to reach the TeV energy scale. This analysis looks for evidence of top squarks in CMS data collected during the years 2016–2018 (referred to as Run 2) corresponding to a total integrated luminosity of 137.0 fb^{-1} of proton-proton collisions at a center-of-mass energy of 13 TeV provided by the LHC.

The CMS collaboration conducts a number of different searches for SUSY using simplified models. The following naming scheme is used in CMS to identify simplified SUSY models. Model names begin with “TX” where X is a positive integer. Odd values (T1, T3, T5) are used in the prefix for models with gluino-pair production, and even values (T2, T4, T6) are used in the prefix for models with squark-antisquark production. T1 and T2 are the main gluino-pair and squark-antisquark series, and T3, T4, T5, and T6 are used when decays are asymmetric/mixed, when there are intermediate particles, etc. This analysis searches for nine different simplified SUSY models. The search targets the six direct top squark production models shown in Fig. 5.1, which are named T2tt, T2bW, T2tb, T2ttC, T2bWC, and T2cc. The results are also interpreted for the three gluino-mediated top squark production models shown in Fig. 5.2, which are named T1tttt, T1ttbb, and T5ttcc. The final states for these

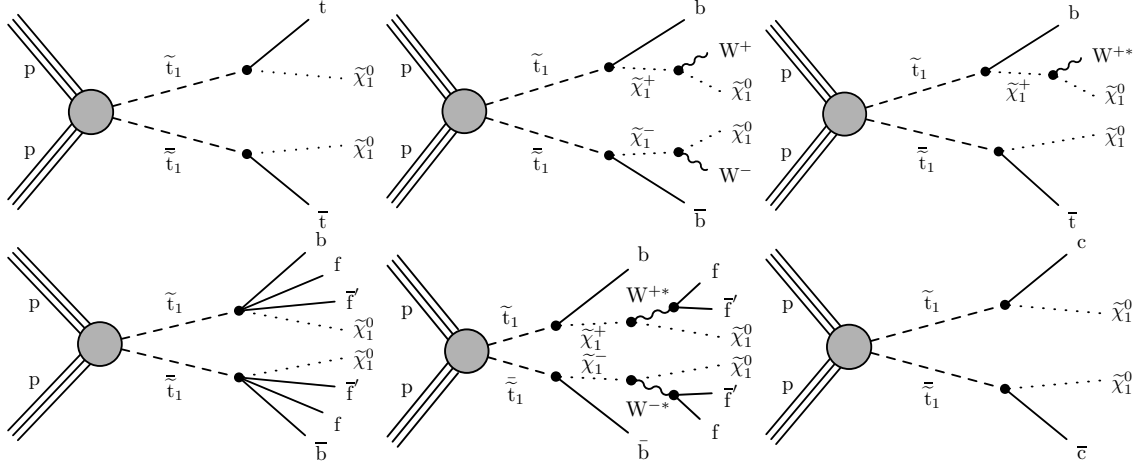


Figure 5.1: From left to right, event diagrams for the direct squark production scenarios considered in this study: the T2tt, T2bW, T2tb, T2ttC, T2bWC, and T2cc simplified model spectra scenarios, with the lightest neutralino $\tilde{\chi}_1^0$ taken to be a weakly interacting LSP.

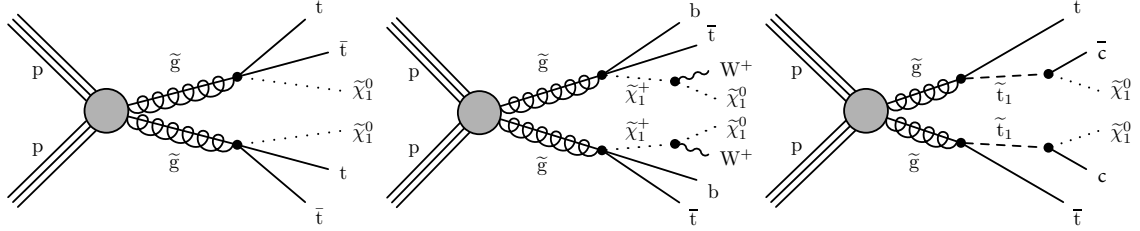


Figure 5.2: From left to right, event diagrams for the direct gluino production scenarios considered in this study: the T1tttt, T1ttbb, and T5ttcc simplified model spectra scenarios, with the lightest neutralino $\tilde{\chi}_1^0$ taken to be a weakly interacting LSP.

SUSY models contain neutralinos, quarks (tops, bottoms, charms, and others) and W bosons. To keep this analysis orthogonal with other SUSY analyses in CMS that select leptonic final states, we choose the all-hadronic decay channel in which the top quarks and W bosons decay to quarks rather than leptons.

5.2 Object Identification

5.2.1 Electrons

In the search region, events with one or more electrons are vetoed. For the electron veto, electrons are required to have $p_T > 5$ GeV, $|\eta| < 2.5$, and pass the veto electron ID. The cut $|\eta| < 2.5$ is used because the CMS tracker does not extend beyond $|\eta| = 2.5$. Furthermore, electrons are required to have a mini-isolation value $r < 0.1$. Mini-isolation is defined as the ratio

$$r = \frac{\sum_i p_T^i}{p_T^{\text{lepton}}}, \quad (5.1)$$

where the numerator is the scalar summation of p_T from Particle Flow (PF) charged hadrons, neutral hadrons, and photons that fall within a cone of size ΔR around the lepton and the denominator is the lepton p_T . For mini-isolation, the cone size ΔR is p_T dependent and is determined by Eq. 5.2.

$$\Delta R = \begin{cases} 0.2 & p_T < 50 \text{ GeV} \\ \frac{10 \text{ GeV}}{p_T} & 50 \text{ GeV} \leq p_T \leq 200 \text{ GeV} \\ 0.05 & p_T > 200 \text{ GeV} \end{cases} \quad (5.2)$$

5.2.2 Muons

Similar to the electron veto, events with one or more muons are vetoed in the search region. Muons must have $p_T > 5$ GeV, $|\eta| < 2.4$, and pass the loose muon ID. The selection $|\eta| < 2.4$ is chosen because the muon detector ends at $|\eta| = 2.4$. Muons are required to have a mini-isolation value $r < 0.2$. See Section 5.2.1 for a description of mini-isolation.

5.2.3 Taus

Events with one or more taus are vetoed in the search region. Taus are required to pass $p_T > 20$ GeV, $|\eta| < 2.4$, and the medium tau ID. Taus must decay hadronically for this veto. In addition, the cut $m_T(\tau, p_T^{\text{miss}}) < 100$ GeV is required, where

$$m_T(\tau, p_T^{\text{miss}}) = \sqrt{2p_T^\tau p_T^{\text{miss}}(1 - \cos \Delta\phi)}. \quad (5.3)$$

5.2.4 Isolated Tracks

To suppress the lost lepton background, events with one or more isolated tracks are vetoed. Isolated tracks are determined using PF candidates near the primary vertex (PV) with $|d_z(\text{PV})| < 0.1$ cm and $|d_{xy}(\text{PV})| < 0.2$ cm. For all isolated tracks, the selection $m_T(\text{tk}, p_T^{\text{miss}}) < 100$ GeV is applied, where

$$m_T(\text{tk}, p_T^{\text{miss}}) = \sqrt{2p_T^{\text{tk}} p_T^{\text{miss}}(1 - \cos \Delta\phi)}. \quad (5.4)$$

Further requirements are placed on isolated tracks that differ according to the type of isolated track (electron, muon, or charged hadron). Requirements are placed on the relative isolation of the track, which is defined as the ratio

$$r = \frac{\sum_i p_T^i}{p_T^{\text{tk}}}, \quad (5.5)$$

where the numerator is the scalar summation of p_T from PF charged hadrons that fall within a cone of size $\Delta R < 0.3$ around the isolated track and the denominator is the isolated track p_T . Electron and muon isolated tracks must have $p_T > 5$ GeV, $|\eta| < 2.5$, and relative isolation value $r < 0.2$. Charged hadron tracks must have $p_T > 10$ GeV, $|\eta| < 2.5$, and relative isolation value $r < 0.1$.

5.2.5 Photons

The $Z \rightarrow \nu\bar{\nu}$ background estimation uses a single photon control region to obtain a data-driven background prediction. In this control region, the photon is required to have $p_T > 220$ GeV and $|\eta| < 1.4442$ (within ECAL barrel) or $1.5660 < |\eta| < 2.5$ (within ECAL endcap). The photon must pass the medium photon ID provided by the EGamma Physics Object Group (POG). The large photon p_T requirement is chosen based on the photon trigger efficiency measurement (Fig. 5.7). In addition, the $Z \rightarrow \nu\bar{\nu}$ background events have large p_T^{miss} due to a boosted Z, and a high- p_T photon better models a high- p_T Z boson.

5.2.6 Jets

Hadronic jets for the analysis (arising from quarks or gluons) are PF jets reconstructed with the anti- k_T algorithm with a distance parameter of 0.4 [28]. These jets are referred to as “AK4 jets.” Charged hadron subtraction is applied to correct pileup effects [52]. Selected AK4 jets are required to have $p_T > 30$ GeV and $|\eta| < 2.4$. Furthermore, AK4 jets are required to pass the tight jet ID provided by the JetMET POG [53–56]. Jet energy corrections (JEC) are applied to better match detector response to true particle energy [57].

5.2.7 *b*-tagging

Jets are identified as b-jets using the DeepCSV algorithm [58]. DeepCSV is a deep neural network with four hidden layers that have 100 nodes each. B-tagged jets are required to satisfy $p_T > 20$ GeV, $|\eta| < 2.4$, and to pass the medium DeepCSV b-tag working point, which has a 68% tagging efficiency [58]. The corresponding misidentification rate for jets from gluons and up, down, and strange quarks is 1%

and for charm quarks is 12% [58]. Additionally, DeepCSV is used when identifying an initial state radiation (ISR) jet (Section 5.2.11). The ISR jet and its two sub-jets are required to fail the loose DeepCSV b-tag working point.

The DeepCSV b-tagging loose and medium working points (WP) for each year of data-taking are provided in Table 5.1.

Table 5.1: Working points used for DeepCSV to tag b quarks in corresponding years [59].

DeepCSV	2016	2017	2018
Loose WP	0.2217	0.1522	0.1241
Medium WP	0.6321	0.4941	0.4184

5.2.8 Soft b-tagging

Some models targeted by this search produce soft (meaning low p_T) bottom or charm quarks. The soft b quarks may have $p_T < 20$ GeV, may not be reconstructed as AK4 jets, or may not pass the DeepCSV medium working point threshold. Soft b-tagging improves discrimination between SUSY signals and SM background processes. The Inclusive Vertex Finder (IVF) algorithm is used to find secondary vertices (SV) that can indicate the presence of b/c quarks. Requirements are placed on candidate SV to reduce the background from light u/d/s quarks. Soft b-tags are constructed to be orthogonal to AK4 jets and b-jets selected for this analysis.

The requirements on each SV to pass the soft b-tagging definition are:

- The distance in the transverse plane between the SV and the PV is less than 3 cm

- The significance of the distance, SIP3D , between the SV and the PV is greater than 4
- The pointing angle, defined as $\cos(\overrightarrow{(\text{PV}, \text{SV})}, \vec{p}_{\text{SV}})$, is greater than 0.98, where \vec{p}_{SV} is the total four-momentum of the tracks associated to the SV
- The number of tracks associated to the SV is greater or equal to three
- The p_{T} of the SV is less than 20 GeV
- The distance to any jet with $p_{\text{T}} > 20$ GeV, $\Delta R(\text{jet}, \vec{p}_{\text{SV}})$, is greater than 0.4 to achieve the orthogonality to the jets and b-tagged jets

The scale factors for soft b-tagging given in Table 5.2 are measured in a $t\bar{t}$ -enriched region that contains one electron, one muon, and one b-tagged jet [60].

Table 5.2: The soft b-tagging data/MC scale factors [60] and fullsim/fastsim scale factors [61] for each year of data-taking.

Scale Factor	2016	2017	2018
Data/MC	1.08 ± 0.03	1.05 ± 0.06	1.19 ± 0.06
Fullsim/Fastsim	0.935 ± 0.062	0.930 ± 0.018	0.932 ± 0.023

5.2.9 Boosted Top- and W-tagging

This analysis relies on identifying hadronically decaying top quarks and W bosons across a large momentum range. Increasing the momentum of top quarks and W bosons decreases the angular separation of their decay products in the CMS detector rest frame. The selections $p_{\text{T}} > 400$ GeV for boosted top quarks and $p_{\text{T}} > 200$ GeV for boosted W bosons are used because in these p_{T} ranges top quarks and W bosons are expected to be contained within an AK8 jet (an anti- k_{T} jet with distance parameter 0.8) [28]. Boosted top quark and boosted W boson tagging is done with

the DeepAK8 algorithm [62], which is a neural network that classifies an AK8 jet in one of five main categories, W/Z/H/t/other.

To reduce fake top quarks and W bosons with minimal effect on tagging efficiency, the cut $|\eta| < 2.0$ is placed on top and W candidates. The top quark and W boson categories are made orthogonal using soft-drop mass cuts of $60 < m_{\text{SD}} < 105$ GeV for W bosons and $m_{\text{SD}} > 105$ GeV for top quarks. The DeepAK8 working points used for each year of data-taking are provided in Table 5.3.

Table 5.3: Working points used for DeepAK8 to tag top quarks and W bosons in corresponding years.

DeepAK8	2016	2017	2018
Top quark	0.937	0.895	0.895
W boson	0.973	0.991	0.991

5.2.10 Resolved Top-tagging

While DeepAK8 can identify boosted top quarks with $p_{\text{T}} > 400$ GeV, the ability to identify lower p_{T} top quarks is also important for this analysis. As top quark momentum decreases, the angular separation of the top quark decay products in the CMS detector rest frame increases. The decay products from hadronically decaying low momentum top quarks can be reconstructed by CMS in three separate AK4 jets (anti- k_{T} jets with distance parameter 0.4) [28]. Hadronically decaying top quarks whose decay products create three separate AK4 jets are called resolved top quarks. Resolved top quarks are tagged using the DeepResolved algorithm [50], which determines whether a trijet combination arises from a top quark decay. The trijet combinations have a few preselection requirements in order to be considered resolved

top quark candidates. When ordered from highest to lowest p_T , the three jets must pass $p_T > 40, 30, 20$ GeV. The trijet invariant mass must be within the range $100 < m < 250$ GeV. To reduce fake top quarks, no more than one of the three jets may be a b-tagged jet, and the trijet must have $|\eta| < 2.0$. Finally, all three AK4 jets must have $\Delta R < 3.14$ compared with the trijet centroid.

DeepResolved is a neural network tasked with differentiating trijet combinations which result from a top quark decay versus those which do not. The neural network uses various input variables from the trijet system. The trijet invariant mass and the dijet pair invariant masses are input to the network. Furthermore, variables for each of the three AK4 jets are used as inputs including the Lorentz vector, DeepCSV heavy-flavor discriminator values, jet shape variables, and detector-level particle multiplicity and energy fraction variables.

The neural network is trained using $t\bar{t}$ and QCD simulation and CMS detector data. The simulation provides the network with examples of signal and background. Data is included in training to prevent the network from learning features present in simulation that are not present in data.

The top quark and W boson tagging efficiencies are shown in Fig. 5.3. The top quark tagging efficiency is as high as 30% for $p_T < 400$ GeV and 50% for $p_T > 400$ GeV. The DeepResolved tagger is most efficient at tagging top quarks in the $p_T < 400$ GeV region, and the DeepAK8 tagger is most efficient at tagging top quarks in the $p_T > 400$ GeV region. The W boson tagging efficiency reaches 45%.

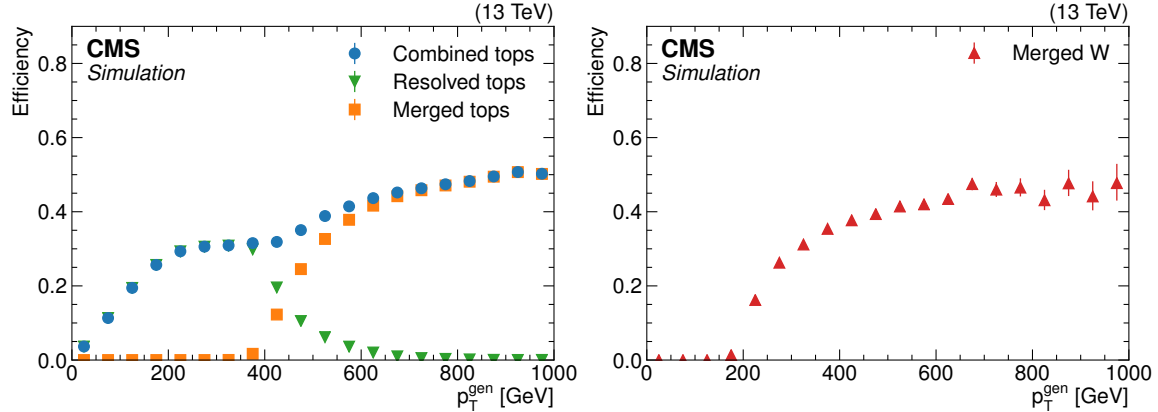


Figure 5.3: Top quark and W boson tagging efficiencies as a function of top quark p_T and W boson p_T , respectively, for the merged and resolved tagging algorithms. The left plot shows the efficiencies as calculated in a sample of simulated $t\bar{t}$ events in which one top quark decays leptonically while the other decays hadronically. The right plot shows the W boson tagging efficiency when calculated in a sample of simulated WW events. In addition to the individual algorithms shown as orange squares (boosted top quarks), green inverted triangles (resolved top quarks), and red triangles (boosted W), the total top quark tagging efficiency is shown as blue dots.

5.2.11 ISR-tagging

Initial state radiation (ISR) jets are reconstructed using the anti- k_T algorithm with a distance parameter of 0.8. These larger radius jets are referred to as “AK8 jets.” This larger radius is used to capture ISR jets which have gluon splitting that results in larger size jets. The ISR jet is the highest p_T AK8 jet in events which do not have boosted top quarks or W bosons tagged by DeepAK8 or resolved top quarks tagged by DeepResolved. In addition, the ISR jet must have $p_T > 200$ GeV and $|\eta| < 2.4$. The ISR jet and its two sub-jets are required to fail the loose b-tagging working point. Finally, the ISR jet must satisfy $\Delta\phi(\vec{p}_T^{\text{miss}}, j_{\text{ISR}}) > 2$. This forces the ISR jet to have opposite ϕ direction from \vec{p}_T^{miss} ; the ISR jet provides boost in one direction, resulting in opposing \vec{p}_T^{miss} .

5.2.12 Missing Transverse Energy

Missing transverse energy (\vec{p}_T^{miss} or MET) is defined as

$$\vec{p}_T^{\text{miss}} = - \sum_i \vec{p}_T^i,$$

where the summation is over all PF candidates. The vector \vec{p}_T^{miss} is in the x-y plane and is perpendicular to the z-axis, where the z-axis is parallel to the LHC beam in CMS. The scalar p_T^{miss} is simply the magnitude of this vector,

$$p_T^{\text{miss}} = |\vec{p}_T^{\text{miss}}|.$$

The variable p_T^{miss} is defined in the transverse direction based on conservation of momentum in the transverse plane. The initial proton-proton collision momentum in the beam direction (z-axis) is unknown because the partons interacting within the protons have unknown fractions of the proton momenta. However, by carefully aligning the proton collisions along the z-axis, the initial transverse momentum is very close to zero, allowing for the application of momentum conservation in the transverse plane. Filters related to p_T^{miss} are applied as recommended by the JetMET POG [63]. In addition, the number of events with fake p_T^{miss} are reduced by requiring that the ratio of p_T^{miss} and CaloMET is less than 5.0 [64].

5.2.13 Level-1 Trigger Prefiring Inefficiency

During data-taking in 2016 and 2017, ECAL had a gradual timing shift that was not properly propagated to Level-1 (L1) trigger primitives (TP). This led to a significant fraction of high- η TP being mistakenly associated with the previous bunch crossing. Since the Level-1 trigger rules forbid two consecutive bunch crossings to fire, the consequence is these events can self-veto if a significant amount of ECAL energy is found in the region $2 < |\eta| < 3$, in addition to not finding the TP in the

bunch crossing. This effect is not described by the simulations. To correct for this issue, a reweighting procedure was provided [65], and the non-prefiring probability of the events is applied to the signal and background Monte Carlo (MC) samples for 2016 and 2017.

5.2.14 HEM 15/16 Failure

On June 30th 2018, two sectors of the HCAL endcap (HE) became unresponsive and eventually un-operational. These two HE modules (a 40 degree sector in ϕ) correspond to the region of $-3.0 < \eta < -1.4$, $-1.57 < \phi < -0.87$ and affect lepton, photon, jet and $p_{\text{T}}^{\text{miss}}$ reconstruction in that region.

The simulation samples produced assume a well-conditioned detector. Therefore, events affected by the failure of the two HE modules are vetoed if there is any AK4 jet with $p_{\text{T}} > 30$ GeV in the affected region ($-3.2 < \eta < -1.2$, $-1.77 < \phi < -0.67$); this is referred to as the ‘‘HEM veto.’’ This wider η - ϕ window is used for AK4 jets which have a radius of $\Delta R = 0.4$, and it is the same η - ϕ window used for the SUSY RA2/b analysis [66]. The HEM veto is applied to affected 2018 data starting from Run 319077 and the corresponding 2018 Monte Carlo (MC) events. The overall effect on signal yield is small and does not affect the search sensitivity.

In addition, lepton and photon control regions are used in order to predict some of the SM backgrounds. The failure of two sectors of HE does not have much impact on muon identification, but there are nonnegligible effects on electron and photon identification. The electron and photon identification depend on the amount of energy measured by ECAL and HCAL. Electromagnetic radiation is expected to deposit a large portion of energy in ECAL and little or no energy in HCAL. The failed

HE modules effectively report zero energy measured in HCAL for their sectors. Thus the portion of the detector with failed HE sectors measures an excess in electrons and photons from misidentified hadronic jets. For electrons and photons, an event veto is defined as follows for the corresponding control regions. Events are vetoed if there is an electron passing the control region requirements ($p_T > 20$ GeV, $|\eta| < 2.5$, and passing the medium electron ID) or a photon passing the control region requirements ($p_T > 220$ GeV, $|\eta| < 1.4442$ or $1.5660 < |\eta| < 2.5$, and passing the medium photon ID) in the region $-3.0 < \eta < -1.4$, $-1.57 < \phi < -0.87$. This ensures that events are not used in the control regions if they contain electrons or photons affected by the two failed HE sectors.

5.3 Search Strategy

The search region is designed to target both low Δm and high Δm regions of phase space. The variable m_T^b is used to separate the search region into a low Δm category and a high Δm category. The definition of m_T^b is

$$m_T^b = \begin{cases} m_T^b(\text{b}, p_T^{\text{miss}}) & N_b = 1 \\ \min [m_T^b(\text{b}_1, p_T^{\text{miss}}), m_T^b(\text{b}_2, p_T^{\text{miss}})] & N_b \geq 2 \end{cases} \quad (5.6)$$

where for $N_b \geq 2$, b_1 and b_2 are the two b-tagged jets with the highest DeepCSV discriminators. Fig. 5.4 shows the m_T^b distribution for the SM backgrounds as well as some mass points for two of the simplified SUSY models, T2tt and T1tttt. Signals with lower mass differences tend to peak for smaller m_T^b , while higher mass difference signals peak for larger m_T^b . The cut $m_T^b < 175$ GeV is chosen for all low Δm search bins and for eight high Δm search bins. The cut $m_T^b > 175$ GeV is chosen for the remaining high Δm search bins.

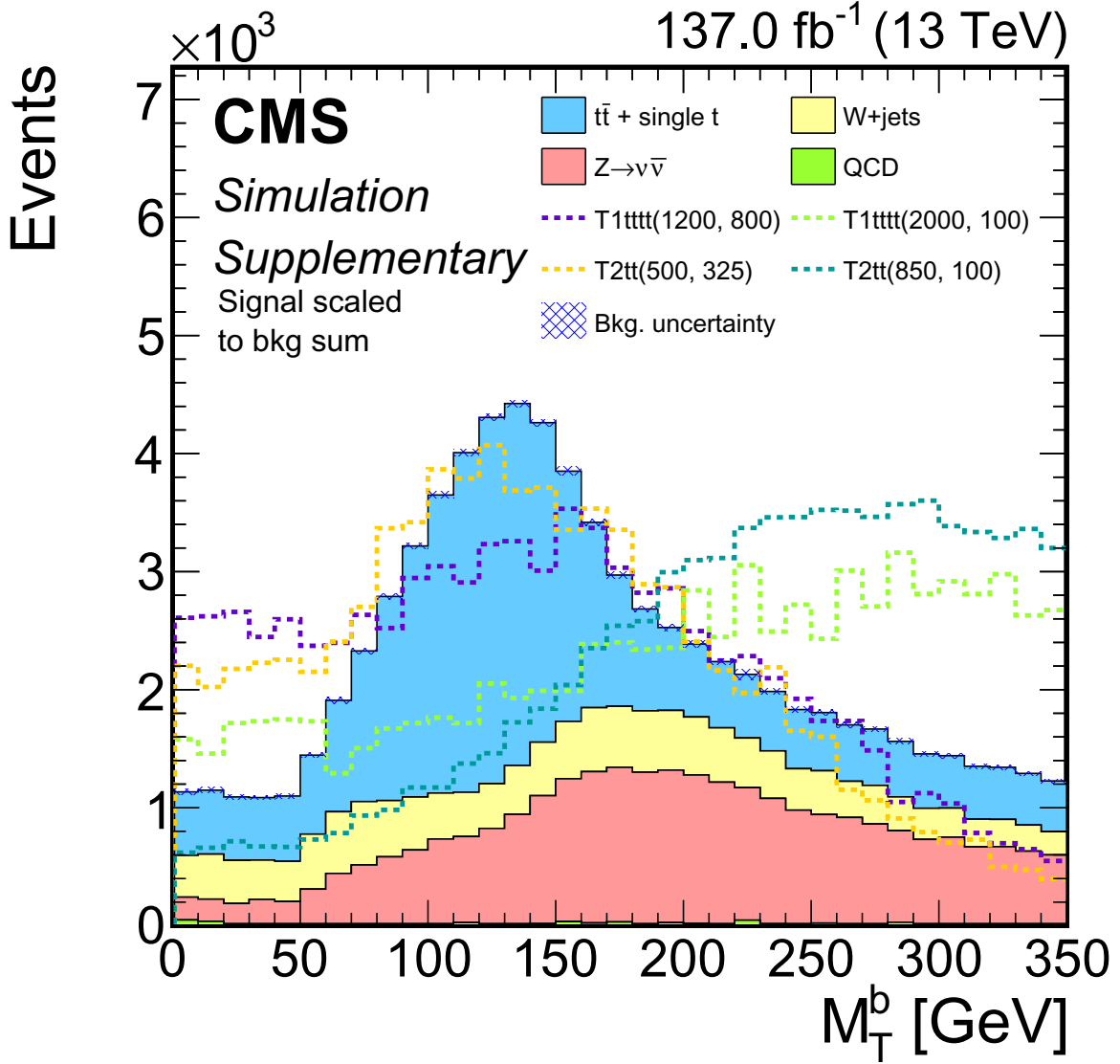


Figure 5.4: The m_T^b distribution for SM backgrounds and some mass points for the T2tt and T1tttt signal models. All Run 2 SM MC is used for the backgrounds, and the T2tt and T1tttt signals are 2017 MC normalized to have the same area as the SM backgrounds. The inclusive baseline selection and the high- Δm $\Delta\phi$ cut $\Delta\phi(\vec{p}_T^{\text{miss}}, j_{1,2,3,4}) > 0.5$ (Table 5.4) are applied.

5.3.1 Triggers

The data used in the search region of the analysis is collected using $p_{\text{T}}^{\text{miss}}$ triggers. For the lepton and photon control regions used for the Z invisible background estimation, electron, muon, and photon triggers are used. Trigger efficiencies for each trigger used are measured and then applied to simulation. Each trigger efficiency is measured using data collected with a reference trigger by observing the fraction of events that pass the trigger in question (the signal trigger) as a function of relevant kinematic variables. The trigger efficiency e is defined as

$$e = \frac{N_{\text{s+r}}}{N_{\text{r}}} \quad (5.7)$$

where N_{r} is the number of events passing the reference trigger and $N_{\text{s+r}}$ is the number of events passing the signal and reference triggers.

The $p_{\text{T}}^{\text{miss}}$ trigger efficiency is measured using the inclusive baseline selection defined in Section 5.3.2. The lepton veto and $p_{\text{T}}^{\text{miss}}$ cut are removed. A loose ID muon veto is applied, and events are required to have at least one medium ID electron. Separate $p_{\text{T}}^{\text{miss}}$ trigger efficiencies are measured for the search region (with the Single Electron data set) and the QCD control region (with the JetHT data set) as $p_{\text{T}}^{\text{miss}}$ in the QCD control region tends to be fake and caused by jet energy mismeasurement. These separate $p_{\text{T}}^{\text{miss}}$ trigger efficiencies are shown in Fig. 5.5. The $p_{\text{T}}^{\text{miss}}$ trigger efficiency from the QCD control region is applied to simulation for the QCD background prediction, and the $p_{\text{T}}^{\text{miss}}$ trigger efficiency from the search region is applied to simulation for all other background predictions.

The lepton trigger efficiencies shown in Fig. 5.6 are measured using the MET data set. For the electron trigger efficiency, a control region is used which has the

baseline selection (without the standard lepton veto and p_T^{miss} cut), a loose ID muon veto, and at least one medium ID electron with $p_T > 40$ GeV. For the muon trigger efficiency, a control region is used which has the baseline selection (without the standard lepton veto and p_T^{miss} cut), a veto ID electron veto, and at least one medium ID muon with $p_T > 50$ GeV.

The lepton trigger efficiencies are applied to simulation in the dilepton control region for the Z invisible background prediction. The efficiency for triggering on either lepton (or both) is considered. Given trigger efficiencies e_1 and e_2 for two leptons, the combined dilepton trigger efficiency is

$$1 - (1 - e_1)(1 - e_2) = e_1 + e_2 - e_1e_2. \quad (5.8)$$

The photon trigger efficiencies are shown in Fig. 5.7. The JetHT data set is used to measure the photon trigger efficiency. For this measurement, a photon control region is defined as follows. The baseline selection is applied without the standard lepton veto and p_T^{miss} cut. Vetoes are applied on veto ID electrons and loose ID muons, but no tau or isolated track vetoes are applied. At least one medium ID photon is required. For the efficiency as a function of photon η , the photons are required to have $p_T > 200$ GeV. The measured photon trigger efficiency is applied to simulation in the photon control region for the Z invisible background prediction.

5.3.2 Event Selection

A large amount of background events are removed using the following pre-selection, which will be referred to as the baseline selection. Lepton vetoes are applied so that this analysis is orthogonal to other CMS top squark searches that use leptonic events. Requirements are placed on the missing transverse energy (p_T^{miss}) defined in

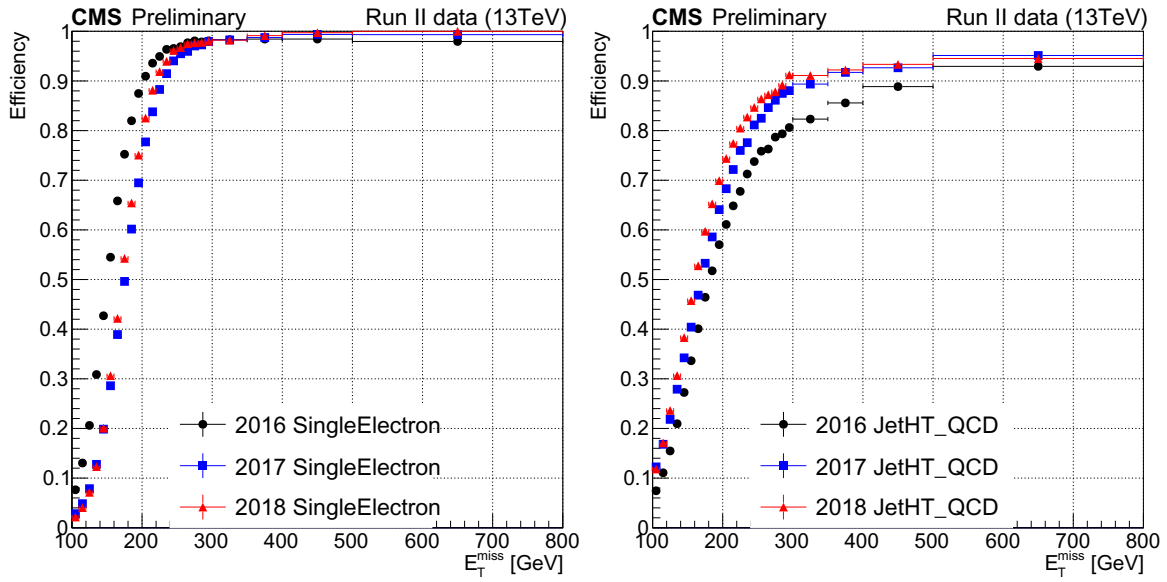


Figure 5.5: MET trigger efficiency in the baseline region as a function of p_T^{miss} . The efficiency in the search region (left) is measured with the Single Electron data set, while the efficiency in the QCD control region (right) is measured with the JetHT data set.

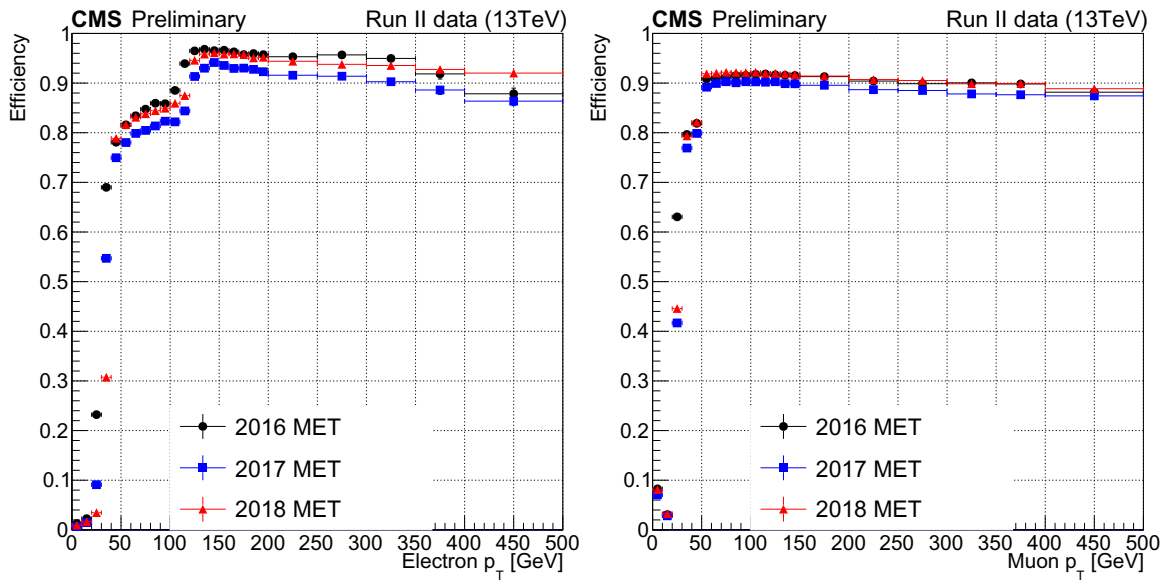


Figure 5.6: Electron (left) and muon (right) trigger efficiencies in the lepton control region as a function of lepton p_T . The lepton trigger efficiencies are measured using the MET data set.

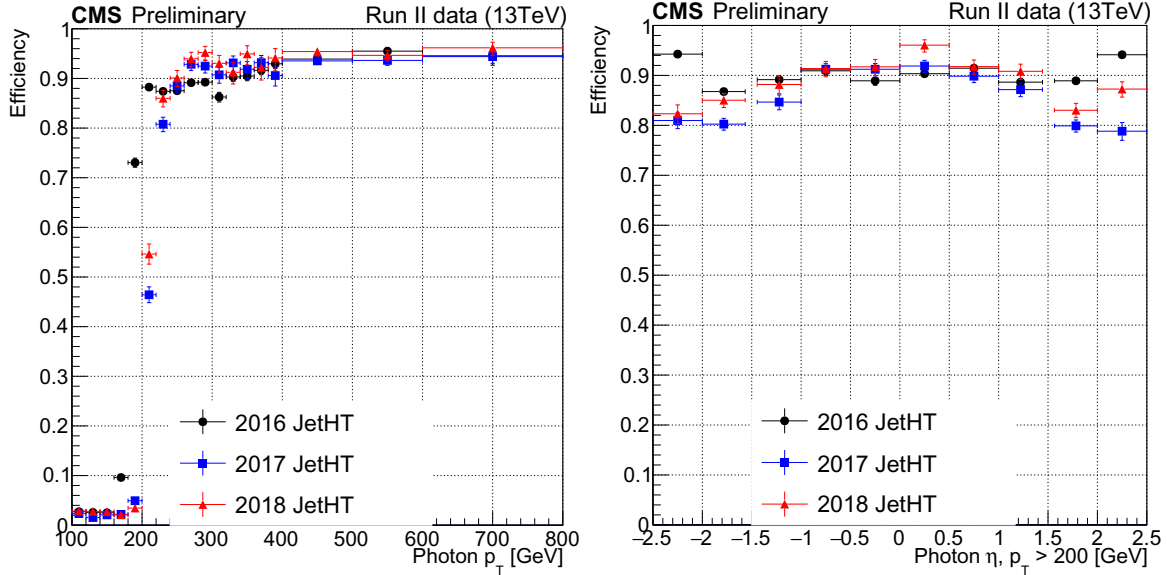


Figure 5.7: Photon trigger efficiency in the photon control region as a function of photon p_T (left) and η (right) using the JetHT data set. For the trigger efficiency as a function of photon η , the photons are required to have $p_T > 200$ GeV.

Section 5.2.12 and on the scalar sum of jet p_T (H_T), which is defined as

$$H_T = \sum_i p_T^i, \quad (5.9)$$

where the summation is over all jets that pass the requirements described in Section 5.2.6. The p_T^{miss} requirement corresponds the p_T^{miss} trigger used to collect the data set and targets SUSY signals that decay to the Lightest Supersymmetric Particle (LSP), which is not detected and results in large p_T^{miss} . The H_T requirement targets high energy events to match the expected kinematics of the signals. The baseline selection is summarized in Table 5.4 and is comprised of the following requirements:

- Events pass the recommended MET filters as detailed in Section 5.2.12.
- $N_{e/\mu} = 0$ ($p_T > 5$ GeV, < 2.5 for e , $|\eta| < 2.4$ for μ) as defined in Sections 5.2.1 and 5.2.2.
- $N_{e/\mu/\pi}^{\text{trk}} = 0$ ($p_T > 5$ GeV for e/μ , 10 GeV for π , $|\eta| < 2.5$, $m_T < 100$ GeV) as defined in Section 5.2.4.

- $N_\tau = 0$ ($p_T > 20$ GeV, $|\eta| < 2.4$, $m_T < 100$ GeV) as defined in Section 5.2.3.
- $N_j \geq 2$, ($p_T > 30$ GeV, $|\eta| < 2.4$).
- $H_T > 300$ GeV to target high energy events.
- $p_T^{\text{miss}} > 250$ GeV to reach the plateau of the trigger efficiency.
- $\Delta\phi(\vec{p}_T^{\text{miss}}, j_1) > 0.5$, $\Delta\phi(\vec{p}_T^{\text{miss}}, j_2) > 0.15$, $\Delta\phi(\vec{p}_T^{\text{miss}}, j_3) > 0.15$ (if applicable) where $j_{1,2,3}$ are three leading jets in p_T with $p_T > 30$ GeV and $|\eta| < 4.7$. The requirements on the azimuthal angles between jets and \vec{p}_T^{miss} reduce the contribution of the QCD multijet background in the final search regions. Here jets from the region $2.4 < |\eta| < 4.7$ are included as they contribute to the p_T^{miss} measurement.
- $\text{PF-}p_T^{\text{miss}}/\text{Calo-}p_T^{\text{miss}} < 5$ to reduce events with an anomalous PF- p_T^{miss} measurement.

Furthermore, the search region is divided into two categories, each with different selections, to target different SUSY models and mass differences between SUSY particles. The low Δm selection targets compressed signals with a small mass difference between the \tilde{t} and $\tilde{\chi}^0$. The high Δm selection targets uncompressed signals with a large mass difference between the \tilde{t} and $\tilde{\chi}^0$. The low Δm and high Δm requirements are provided in Table 5.4.

The low Δm selection adds the following requirements to the baseline selection:

- $N_t = 0$, $N_W = 0$, $N_{\text{res}} = 0$, where N_t and N_W are the numbers of merged top quarks and W bosons, respectively (see Section 5.2.9 for details), and N_{res} is the number of resolved top quarks (see Section 5.2.10 for details).

- $N_j(\text{ISR}) = 1$: $R = 0.8$, $p_T > 200$ GeV, $|\eta| < 2.4$, $\Delta\phi(\vec{p}_T^{\text{miss}}, j_{\text{ISR}}) > 2$ (as defined in Section 5.2.11).
- $p_T^{\text{miss}}/\sqrt{H_T} \geq 10$

The top quark and W boson veto in low Δm reduces the $t\bar{t}$ background and has less effect on low mass difference signals that are unable to produce on-shell top quarks and W bosons. One ISR jet is selected in order to provide momentum imbalance so that events have large p_T^{miss} . For low mass difference signals, the ISR jet boosts the top squark pair so that the neutralinos have sufficient momentum to yield large p_T^{miss} . The $p_T^{\text{miss}}/\sqrt{H_T}$ requirement is added to ensure that the p_T^{miss} is based on the event kinematics and not mismeasurement.

The high Δm selection adds the following requirements to the baseline selection:

- $N_j \geq 5$ ($p_T > 30$ GeV, $|\eta| < 2.4$).
- $N_b \geq 1$ ($p_T > 20$ GeV, $|\eta| < 2.4$), where N_b is the number of selected jets satisfying the DeepCSV medium working point (see Section 5.2.7 for details).
- $\Delta\phi(\vec{p}_T^{\text{miss}}, j_{1,2,3,4}) > 0.5$

The number of jets required is increased to five because high Δm events have more energy available to transfer to SM objects. At least one b-tagged jet is required as high Δm signals tend to have a bottom quark from a stop, gluino, or top decay. The high Δm search bins use top quark and W boson multiplicities as high Δm signals are able to produce on-shell top quarks and W bosons.

Table 5.4: Summary of the preselection requirements (baseline selection) on the reconstructed physics objects for this search, as well as the low Δm and high Δm baseline selections. Here R is the distance parameter of the anti- k_T algorithm. Electron and muon candidates as well as τ_h candidates and isolated tracks are as defined in Sections 5.2.1 to 5.2.4. The i th highest- p_T jet is denoted by j_i .

Baseline selection	
Jets	$N_j \geq 2: R = 0.4, p_T > 30 \text{ GeV}, \eta < 2.4$
H_T	$H_T > 300 \text{ GeV}$
p_T^{miss}	$p_T^{\text{miss}} > 250 \text{ GeV}$ $\Delta\phi(\vec{p}_T^{\text{miss}}, j_1) > 0.5$ $\Delta\phi(\vec{p}_T^{\text{miss}}, j_2) > 0.15$ $\Delta\phi(\vec{p}_T^{\text{miss}}, j_3) > 0.15$ (when applicable)
Veto electron	$p_T > 5 \text{ GeV}, \eta < 2.5, p_T^{\text{sum}} < 0.1 p_T$
Veto muon	$p_T > 5 \text{ GeV}, \eta < 2.4, p_T^{\text{sum}} < 0.2 p_T$
Veto τ_h	$p_T > 20 \text{ GeV}, \eta < 2.4, m_T < 100 \text{ GeV}$
Veto track	PF charged candidates, $ \eta < 2.5, m_T < 100 \text{ GeV}$ $p_T > 5 \text{ GeV}, p_T^{\text{sum}} < 0.2 p_T$ for electron and muon tracks $p_T > 10 \text{ GeV}, p_T^{\text{sum}} < 0.1 p_T$ for charged hadron tracks
Low Δm baseline selection	
N_t, N_W, N_{res}	$N_t = N_W = N_{\text{res}} = 0$
m_T^b	$m_T^b < 175 \text{ GeV}$ (for events with $N_b \geq 1$)
ISR jet	$N_j(\text{ISR}) = 1: R = 0.8, p_T^{\text{ISR}} > 200 \text{ GeV}, \eta < 2.4$ $\Delta\phi(\vec{p}_T^{\text{miss}}, j_{\text{ISR}}) > 2$
p_T^{miss}	$p_T^{\text{miss}} / \sqrt{H_T} > 10 \sqrt{\text{GeV}}$
High Δm baseline selection	
Jets	$N_j \geq 5: R = 0.4, p_T > 30 \text{ GeV}, \eta < 2.4$
b-tagging	$N_b \geq 1$
p_T^{miss}	$\Delta\phi(\vec{p}_T^{\text{miss}}, j_{1,2,3,4}) > 0.5$

5.3.3 Search Region Selection

Events in the search must pass the baseline selection and either the low Δm or high Δm requirements (Table 5.4). The orthogonal low Δm and high Δm regions are further divided into multifarious search bins designed to improve signal sensitivity.

There are 53 disjoint search bins in the low Δm region summarized in Table 5.5. Low Δm search bins with $N_b \geq 1$ are required to have $m_T^b < 175$ GeV because low Δm signals tend to have small m_T^b as seen in Fig. 5.4. The low Δm search bins differ in the number of jets (N_j), b jets (N_b), and soft b jets (N_{SV}), as well as in ISR jet p_T (p_T^{ISR}), p_T^b , and missing transverse energy (p_T^{miss}). The variable p_T^b is defined as

$$p_T^b = \begin{cases} p_T(\text{b}) & N_b = 1 \\ p_T(\text{b}_1) + p_T(\text{b}_2) & N_b \geq 2 \end{cases} \quad (5.10)$$

where for $N_b \geq 2$, b_1 and b_2 are the two b-tagged jets with the highest p_T . The p_T^b binning is designed to benefit from the low b jet p_T spectra present in the low Δm signals.

There are 130 disjoint search bins in the high Δm region summarized in Table 5.6. All search bins in the high Δm region require $N_b \geq 1$ as mandated by the high Δm selection. There are eight high Δm search bins with $m_T^b < 175$ GeV, $N_j \geq 7$ (at least seven jets), and $N_{\text{res}} \geq 1$ (at least one resolved top quark), which are meant to capture signal events which have resolved tops and $m_T^b < 175$ GeV. The other 122 high Δm search bins have $m_T^b > 175$ GeV as high Δm signals generally possess large m_T^b (Fig. 5.4). The high Δm search bins differ in the number of b jets (N_b), merged top quarks (N_t), merged W bosons (N_W), and resolved top quarks (N_{res}), as well as in missing transverse energy (p_T^{miss}) and scalar sum of jet p_T (H_T). These binning

Table 5.5: Summary of the 53 search bins that mainly target low Δm signal models.

For these search bins, events are required to pass the low Δm region selection discussed in Section 5.3.3. Within each row of this table, the bins are ordered by increasing p_T^{miss} requirements. A dash (—) indicates that no requirements are made.

N_j	N_b	N_{SV}	m_T^b [GeV]	p_T^{ISR} [GeV]	p_T^b [GeV]	p_T^{miss} [GeV]	Bin number
2–5	0	0	—	>500	>20	[450, 550, 650, 750, ∞]	0–3
≥ 6	0	0	—	>500	>20	[450, 550, 650, 750, ∞]	4–7
2–5	0	≥ 1	—	>500	>20	[450, 550, 650, 750, ∞]	8–11
≥ 6	0	≥ 1	—	>500	>20	[450, 550, 650, 750, ∞]	12–15
≥ 2	1	0	<175	300–500	20–40	[300, 400, 500, 600, ∞]	16–19
≥ 2	1	0	<175	300–500	40–70	[300, 400, 500, 600, ∞]	20–23
≥ 2	1	0	<175	>500	20–40	[450, 550, 650, 750, ∞]	24–27
≥ 2	1	0	<175	>500	40–70	[450, 550, 650, 750, ∞]	28–31
≥ 2	1	≥ 1	<175	>300	20–40	[300, 400, 500, ∞]	32–34
≥ 2	≥ 2	—	<175	300–500	40–80	[300, 400, 500, ∞]	35–37
≥ 2	≥ 2	—	<175	300–500	80–140	[300, 400, 500, ∞]	38–40
≥ 7	≥ 2	—	<175	300–500	>140	[300, 400, 500, ∞]	41–43
≥ 2	≥ 2	—	<175	>500	40–80	[450, 550, 650, ∞]	44–46
≥ 2	≥ 2	—	<175	>500	80–140	[450, 550, 650, ∞]	47–49
≥ 7	≥ 2	—	<175	>300	>140	[450, 550, 650, ∞]	50–52

variables are chosen to differentiate events based on kinematics favored by the SUSY models targeted by this analysis.

5.3.4 Validation Region Selection

In order to test the SM background predictions, a validation region is defined in a signal depleted phase space that is orthogonal to the search region. The validation region is used to verify that the SM background predictions have good agreement with data. Similar to the search region, the validation region is divided into low Δm and high Δm categories.

There are 19 disjoint validation bins in the low Δm region summarized in Table 5.7. Bins 0–14 use the same low Δm baseline selection as the search region, but the p_T^{miss} binning is 250–300 GeV and 250–400 GeV covering a low p_T^{miss} region

Table 5.6: Summary of the 130 search bins that mainly target high Δm signal models. For these search bins, events are required to pass the high Δm region selection discussed in Section 5.3.3. Within each row of this table, the bins are ordered by increasing p_T^{miss} requirements.

m_T^b [GeV]	N_j	N_b	N_t	N_W	N_{res}	H_T [GeV]	p_T^{miss} [GeV]	Bin number
<175	≥ 7	1	≥ 0	≥ 0	≥ 1	>300	[250, 300, 400, 500, ∞]	53–56
<175	≥ 7	≥ 2	≥ 0	≥ 0	≥ 1	>300	[250, 300, 400, 500, ∞]	57–60
>175	≥ 5	1	0	0	0	>1000	[250, 350, 450, 550, ∞]	61–64
>175	≥ 5	≥ 2	0	0	0	>1000	[250, 350, 450, 550, ∞]	65–68
>175	≥ 5	1	≥ 1	0	0	300–1000	[250, 550, 650, ∞]	69–71
>175	≥ 5	1	≥ 1	0	0	1000–1500	[250, 550, 650, ∞]	72–74
>175	≥ 5	1	≥ 1	0	0	>1500	[250, 550, 650, ∞]	75–77
>175	≥ 5	1	0	≥ 1	0	300–1300	[250, 350, 450, ∞]	78–80
>175	≥ 5	1	0	≥ 1	0	>1300	[250, 350, 450, ∞]	81–83
>175	≥ 5	1	0	0	≥ 1	300–1000	[250, 350, 450, 550, 650, ∞]	84–88
>175	≥ 5	1	0	0	≥ 1	1000–1500	[250, 350, 450, 550, 650, ∞]	89–93
>175	≥ 5	1	0	0	≥ 1	>1500	[250, 350, 450, 550, 650, ∞]	94–98
>175	≥ 5	1	≥ 1	≥ 1	0	>300	[250, 550, ∞]	99–100
>175	≥ 5	1	≥ 1	0	≥ 1	>300	[250, 550, ∞]	101–102
>175	≥ 5	1	0	≥ 1	≥ 1	>300	[250, 550, ∞]	103–104
>175	≥ 5	2	1	0	0	300–1000	[250, 550, 650, ∞]	105–107
>175	≥ 5	2	1	0	0	1000–1500	[250, 550, 650, ∞]	108–110
>175	≥ 5	2	1	0	0	>1500	[250, 550, 650, ∞]	111–113
>175	≥ 5	2	0	1	0	300–1300	[250, 350, 450, ∞]	114–116
>175	≥ 5	2	0	1	0	>1300	[250, 350, 450, ∞]	117–119
>175	≥ 5	2	0	0	1	300–1000	[250, 350, 450, 550, 650, ∞]	120–124
>175	≥ 5	2	0	0	1	1000–1500	[250, 350, 450, 550, 650, ∞]	125–129
>175	≥ 5	2	0	0	1	>1500	[250, 350, 450, 550, 650, ∞]	130–134
>175	≥ 5	2	1	1	0	>300	[250, 550, ∞]	135–136
>175	≥ 5	2	1	0	1	300–1300	[250, 350, 450, ∞]	137–139
>175	≥ 5	2	1	0	1	>1300	[250, 350, 450, ∞]	140–142
>175	≥ 5	2	0	1	1	>300	[250, 550, ∞]	143–144
>175	≥ 5	2	2	0	0	>300	[250, 450, ∞]	145–146
>175	≥ 5	2	0	2	0	>300	>250	147
>175	≥ 5	2	0	0	2	300–1300	[250, 450, ∞]	148–149
>175	≥ 5	2	0	0	2	>1300	[250, 450, ∞]	150–151
>175	≥ 5	2	$N_t + N_W + N_{\text{res}} \geq 3$			>300	>250	152
>175	≥ 5	≥ 3	1	0	0	300–1000	[250, 350, 550, ∞]	153–155
>175	≥ 5	≥ 3	1	0	0	1000–1500	[250, 350, 550, ∞]	156–158
>175	≥ 5	≥ 3	1	0	0	>1500	[250, 350, 550, ∞]	159–161
>175	≥ 5	≥ 3	0	1	0	>300	[250, 350, 550, ∞]	162–164
>175	≥ 5	≥ 3	0	0	1	300–1000	[250, 350, 550, ∞]	165–167
>175	≥ 5	≥ 3	0	0	1	1000–1500	[250, 350, 550, ∞]	168–170
>175	≥ 5	≥ 3	0	0	1	>1500	[250, 350, 550, ∞]	171–173
>175	≥ 5	≥ 3	1	1	0	>300	>250	174
>175	≥ 5	≥ 3	1	0	1	>300	[250, 350, ∞]	175–176
>175	≥ 5	≥ 3	0	1	1	>300	>250	177
>175	≥ 5	≥ 3	2	0	0	>300	>250	178
>175	≥ 5	≥ 3	0	2	0	>300	>250	179
>175	≥ 5	≥ 3	0	0	2	>300	[250, 350, ∞]	180–181
>175	≥ 5	≥ 3	$N_t + N_W + N_{\text{res}} \geq 3$			>300	>250	182

Table 5.7: Summary of the 19 validation bins for low Δm . Bins 0 to 14 use the normal low Δm region selection. Bins 15–18 use a similar selection, but require medium $\Delta\phi$ as discussed in Section 5.3.4. A dash (—) indicates that no requirements are made.

$\Delta\phi$	N_b	N_{SV}	p_T^{ISR} [GeV]	p_T^b [GeV]	N_j	p_T^{miss} [GeV]	Bin number
—	0	0	>500	>20	2–5	250–400	0
—	0	0	>500	>20	≥ 6	250–400	1
—	0	≥ 1	>500	>20	2–5	250–400	2
—	0	≥ 1	>500	>20	≥ 6	250–400	3
—	1	0	300–500	<40	≥ 2	250–300	4
—	1	0	300–500	40–70	≥ 2	250–300	5
—	1	0	>500	<40	≥ 2	250–400	6
—	1	0	>500	40–70	≥ 2	250–400	7
—	1	≥ 1	—	<40	≥ 2	250–300	8
—	≥ 2	—	300–500	<80	≥ 2	250–300	9
—	≥ 2	—	300–500	80–140	≥ 2	250–300	10
—	≥ 2	—	300–500	>140	≥ 7	250–300	11
—	≥ 2	—	>500	<80	≥ 2	250–400	12
—	≥ 2	—	>500	80–140	≥ 2	250–400	13
—	≥ 2	—	>500	>140	≥ 7	250–400	14
medium $\Delta\phi$	0	0	>200	—	≥ 2	≥ 250	15
medium $\Delta\phi$	0	≥ 1	>200	—	≥ 2	≥ 250	16
medium $\Delta\phi$	≥ 1	0	>200	—	≥ 2	≥ 250	17
medium $\Delta\phi$	≥ 1	≥ 1	>200	—	≥ 2	≥ 250	18

that is not included in the search bins. Bins 15–18 use a low Δm selection similar to the low Δm search region selection with the only difference being the $\Delta\phi$ cut between the leading jets and \vec{p}_T^{miss} . The medium- $\Delta\phi$ selection for these low Δm bins is defined as $0.15 < \Delta\phi(\vec{p}_T^{\text{miss}}, j_1) < 0.5$ and $\Delta\phi(\vec{p}_T^{\text{miss}}, j_{2,3}) > 0.15$.

There are 24 disjoint validation bins in the high Δm region summarized in Table 5.8. The high Δm validation region uses a selection similar to the high Δm search region with the only difference being the $\Delta\phi$ cut between the leading jets and \vec{p}_T^{miss} . The medium- $\Delta\phi$ for the high Δm region is defined as $\Delta\phi(\vec{p}_T^{\text{miss}}, j_1) > 0.5$, $\Delta\phi(\vec{p}_T^{\text{miss}}, j_{2,3}) > 0.15$, and one of $\Delta\phi(\vec{p}_T^{\text{miss}}, j_{2,3,4})$ must be less than 0.5.

Table 5.8: Summary of the 24 validation bins for high Δm . These search bins are orthogonal to the high Δm search region because of the $\Delta\phi$ requirements discussed in Section 5.3.4.

m_{T}^{b} [GeV]	N_{b}	N_{j}	N_{t}	N_{W}	N_{res}	$p_{\text{T}}^{\text{miss}}$ [GeV]	Bin number
<175	1	≥ 7	≥ 0	≥ 0	≥ 1	250–400	19
<175	1	≥ 7	≥ 0	≥ 0	≥ 1	>400	20
<175	≥ 2	≥ 7	≥ 0	≥ 0	≥ 1	250–400	21
<175	≥ 2	≥ 7	≥ 0	≥ 0	≥ 1	>400	22
>175	1	≥ 5	0	0	0	250–400	23
>175	1	≥ 5	0	0	0	>400	24
>175	≥ 2	≥ 5	0	0	0	250–400	25
>175	≥ 2	≥ 5	0	0	0	>400	26
>175	1	≥ 5	1	0	0	250–400	27
>175	1	≥ 5	1	0	0	>400	28
>175	1	≥ 5	0	1	0	250–400	29
>175	1	≥ 5	0	1	0	>400	30
>175	1	≥ 5	0	0	1	250–400	31
>175	1	≥ 5	0	0	1	>400	32
>175	1	≥ 5	$N_{\text{t}} + N_{\text{W}} + N_{\text{res}} \geq 2$			250–400	33
>175	1	≥ 5	$N_{\text{t}} + N_{\text{W}} + N_{\text{res}} \geq 2$			>400	34
>175	≥ 2	≥ 5	1	0	0	250–400	35
>175	≥ 2	≥ 5	1	0	0	>400	36
>175	≥ 2	≥ 5	0	1	0	250–400	37
>175	≥ 2	≥ 5	0	1	0	>400	38
>175	≥ 2	≥ 5	0	0	1	250–400	39
>175	≥ 2	≥ 5	0	0	1	>400	40
>175	≥ 2	≥ 5	$N_{\text{t}} + N_{\text{W}} + N_{\text{res}} \geq 2$			250–400	41
>175	≥ 2	≥ 5	$N_{\text{t}} + N_{\text{W}} + N_{\text{res}} \geq 2$			>400	42

5.4 Standard Model Backgrounds

The search regions (Section 5.3.2) are designed to optimize sensitivity to the targeted simplified SUSY models (Section 5.1) so that the presence of SUSY can be differentiated from SM backgrounds. There are various SM background processes that produce events that pass the search region selections. The SM backgrounds are divided into the following categories:

- Lost Lepton
- Z invisible
- QCD
- $t\bar{t}Z$ and Rare

The “Lost Lepton” (LL) background arises from events that have a lepton (electron, muon, or tau) that is not reconstructed. The lepton may fail kinematic cuts (p_T or η), may fall outside the detector acceptance, or may pass through a blind spot (e.g. dead channel) in the detector. The lepton vetoes cannot reject these events. Such events can also have missing transverse energy (p_T^{miss}) from neutrinos, for example from a W decaying to a charged lepton and a neutrino. These events result in a significant background in the search regions. The Lost Lepton background prediction is presented in Section 5.4.1.

The “Z invisible” background is from events containing a Z boson that decays to neutrinos. The neutrinos cannot be reconstructed by the CMS detector and therefore result in missing transverse energy (p_T^{miss}). The Z to neutrinos process is an irreducible background in the search region. These events will typically have a boosted Z boson such that the events pass the $p_T^{\text{miss}} > 250$ GeV selection. The Z

invisible background prediction is introduced in Section 5.4.2 and presented in more detail in Chapter Six.

The QCD background comes from the abundance of events which have many quarks and gluons due to quantum chromodynamics (QCD) physics in high energy proton-proton collisions. The quarks and gluons in QCD events are reconstructed as hadronic jets in the CMS detector. If all jet energies and momenta are measured accurately, the vector sum of transverse momenta should vanish due to momentum conservation in the transverse plane. The majority of QCD events are rejected by the missing transverse energy requirement $p_T^{\text{miss}} > 250$ GeV. However, it is possible that not all jet energies and momenta are accurately measured, which could occur if a jet hits a dead calorimeter cell. Jet energy mismeasurement can result in a nonzero vector sum of transverse momenta which implies missing transverse energy (p_T^{miss}). The QCD process has a high cross section, and there are some QCD events which pass the search region selection. The QCD background prediction is described in Section 5.4.3.

The $t\bar{t}Z$ and Rare backgrounds include other processes which pass the event selection. In the $t\bar{t}Z$ process, if the top quarks decay hadronically and the Z decays to neutrinos, this process can pass the lepton veto and the p_T^{miss} requirement. The $t\bar{t}Z$ and Rare background predictions are discussed in Section 5.4.4.

The relative contribution of each background for different search region selections is shown in Fig. 5.8. The selections cover the entire search region, and the relative fractions are calculated by summing the Run 2 background predictions from the search bins that have the corresponding selection. The Lost Lepton background dominates for selections that require top quarks and/or W bosons. The Z invisible

background is significant for search regions that reject top quarks and W bosons. The QCD background is the largest in high Δm bins that have top quark and W boson vetoes. The $t\bar{t}Z$ and Rare backgrounds have important contributions in high Δm bins that require at least two bottom quarks as well as top quarks and/or W bosons.

5.4.1 Lost Lepton Background

The “Lost Lepton” (LL) background includes the SM processes $t\bar{t}$, W +jets, single top, tW and $t\bar{t}W$. A data-driven background prediction is accomplished by using a single lepton control region (CR). Instead of vetoing leptons as done in the search region (SR), one lepton (an electron or muon) is selected in the control region.

The LL background prediction ($N_{\text{pred}}^{\text{LL}}$) is calculated in each SR using the equation

$$N_{\text{pred}}^{\text{LL}} = TF_{\text{LL}} \cdot N_{\text{data}}(1l) \quad (5.11)$$

where $N_{\text{data}}(1l)$ is the number of data events observed in the corresponding CR. The transfer factor (TF) TF_{LL} is defined as

$$TF_{\text{LL}} = \frac{N_{\text{MC}}(0l)}{N_{\text{MC}}(1l)} \quad (5.12)$$

where $N_{\text{MC}}(0l)$ is the number of simulated events in the corresponding SR and $N_{\text{MC}}(1l)$ is the number of simulated events in the corresponding CR.

Data and simulation comparisons as a function of $p_{\text{T}}^{\text{miss}}$ for different years (2016, 2017, and 2018) as well as all years combined (Run 2) are shown in Figures 5.9 and 5.10. Some differences between data and simulation are apparent, such as for high $p_{\text{T}}^{\text{miss}}$ for the low Δm selection, and this suggests that the corrections to the LL prediction from the CR will be nonnegligible. No striking differences are present in the data/MC ratio for different years.

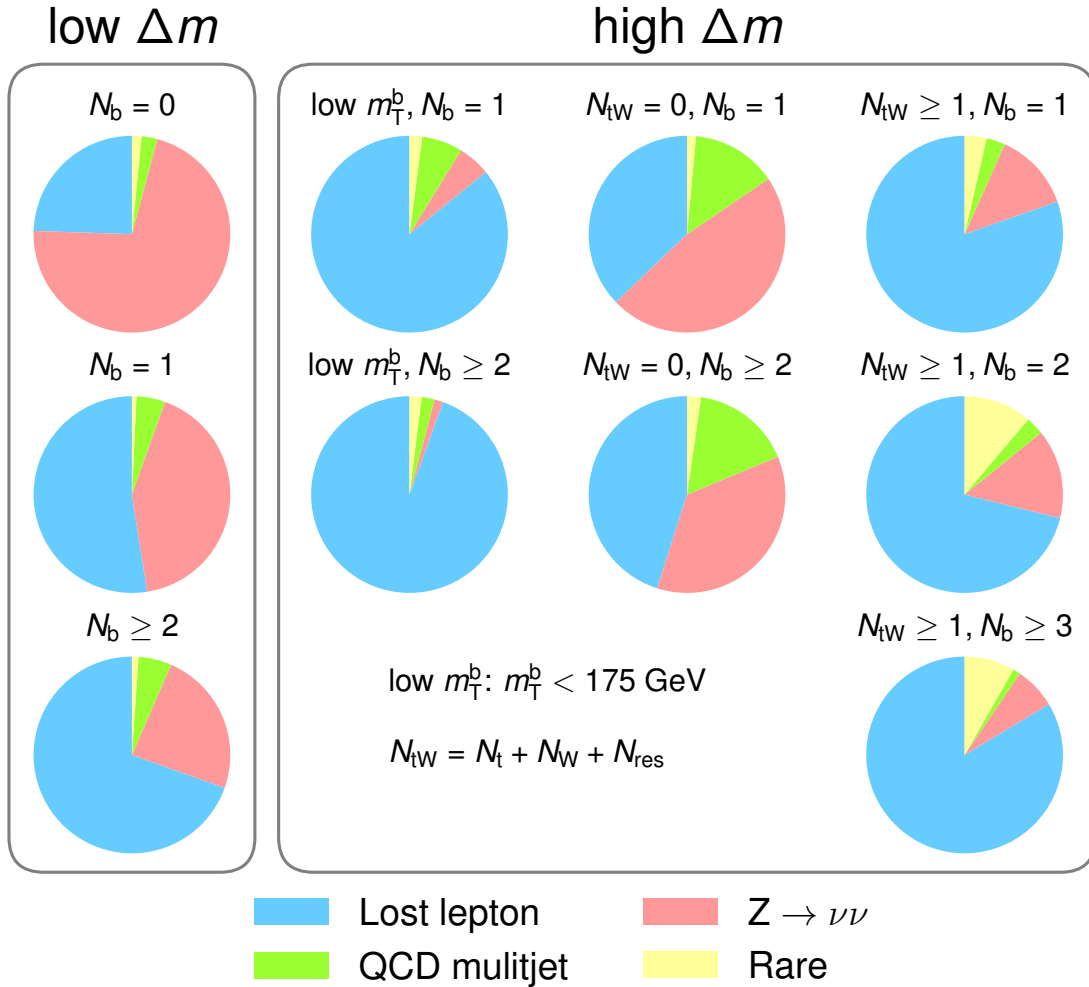


Figure 5.8: Background composition from data-driven background predictions. The pie charts show the background composition for different N_b , m_T^b , and $N_{tW} = N_t + N_W + N_{res}$ selections in the low Δm and high Δm search regions. The relative fractions are calculated by summing the Run 2 background predictions from the search bins that have the corresponding selection.

In high Δm , the CR and TF in Eq. (5.11) are defined such that top quark and W boson multiplicities are not used in the CR. This improves statistics in the CR. Dedicated scale factors (SF) for top quark and W boson tagging are derived and applied to the simulation to account for differences with the data.

The TF in high Δm can be factored into the two terms written in Eq. (5.13).

$$\begin{aligned}
TF_{LL} &= TF_{LL}^{\text{CR-SR}} \times TF_{LL}^{\text{SR-extrap}} \\
&= \frac{N_{\text{MC}}(0l)(N_b, p_T^{\text{miss}}, H_T)}{N_{\text{MC}}(1l)(N_b, p_T^{\text{miss}}, H_T)} \times \frac{N_{\text{MC}}(0l)(N_b, p_T^{\text{miss}}, H_T, N_t, N_{\text{res}}, N_W)}{N_{\text{MC}}(0l)(N_b, p_T^{\text{miss}}, H_T)}
\end{aligned} \tag{5.13}$$

The first term in Eq. (5.13), $TF_{LL}^{\text{CR-SR}}$, addresses event count differences between the zero-lepton search region and the one-lepton control region. The second term in Eq. (5.13), $TF_{LL}^{\text{SR-extrap}}$, accounts for the top quark and W boson multiplicity requirements in the search region. These two TF terms are calculated and plotted separately in Fig. 5.11 for different eras. The total TF, which is the product of these two terms, is plotted in Fig. 5.12 for different eras. The TF distributions are similar for different eras.

Since no significant era dependence is present in the LL CR, the final prediction is calculated by combining data and simulation from all eras.

5.4.2 *Z Invisible Background*

The “Z invisible” background is from the Z to neutrinos SM process. A data-driven approach is used to determine the estimation of Z invisible events in the search region. The Z invisible simulation is correction is split into two terms: a normalization factor with coarse selection and a shape factor with granular selection. Each of these terms is measured in different control region orthogonal to the search region.

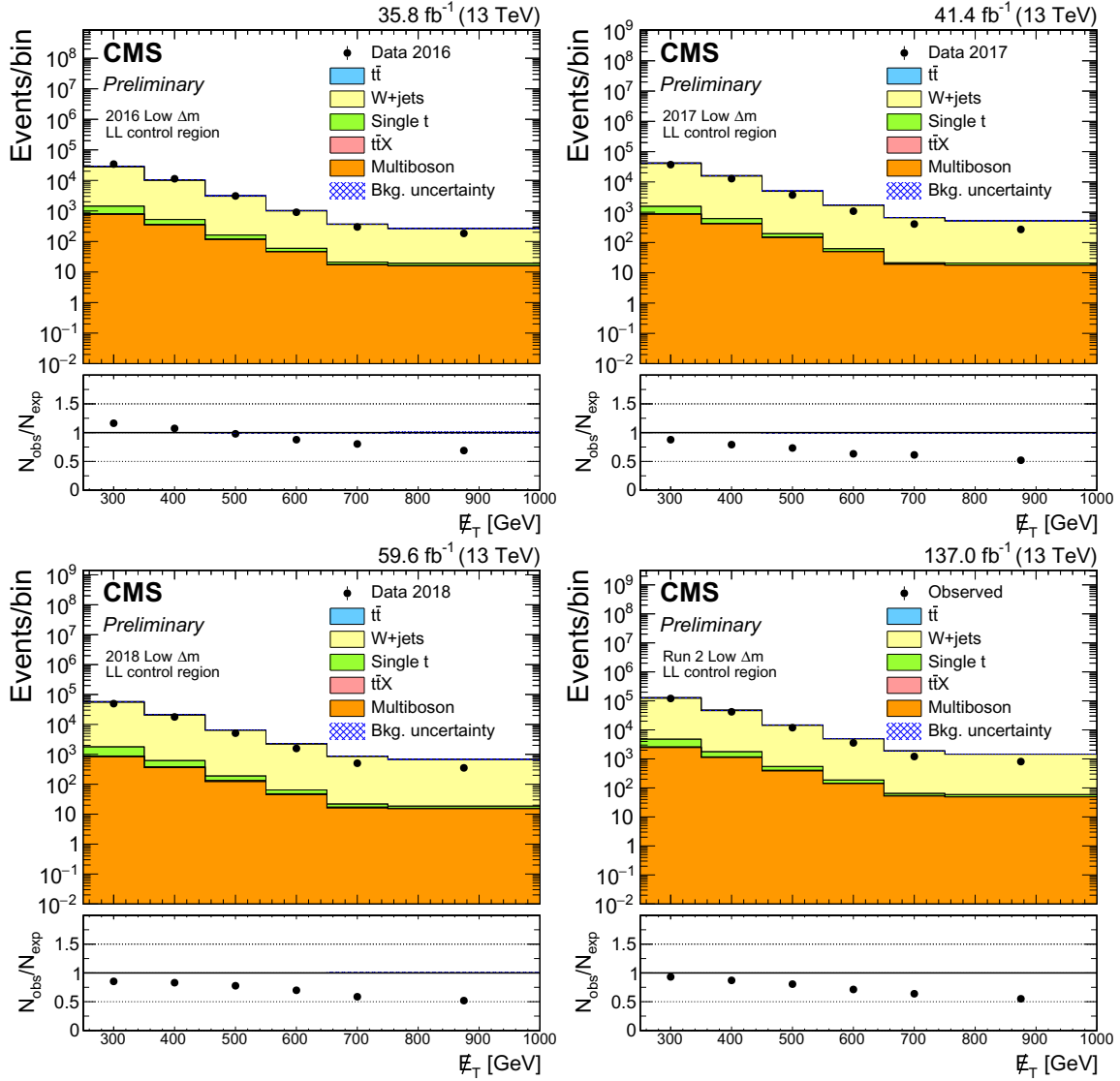


Figure 5.9: Comparison of the data and MC as a function of p_T^{miss} in the single lepton CR for each era: 2016, 2017, 2018, and Run 2 (the combination of all years) in the low Δm inclusive region. There are downward trends in data/MC which appear similar in all eras.

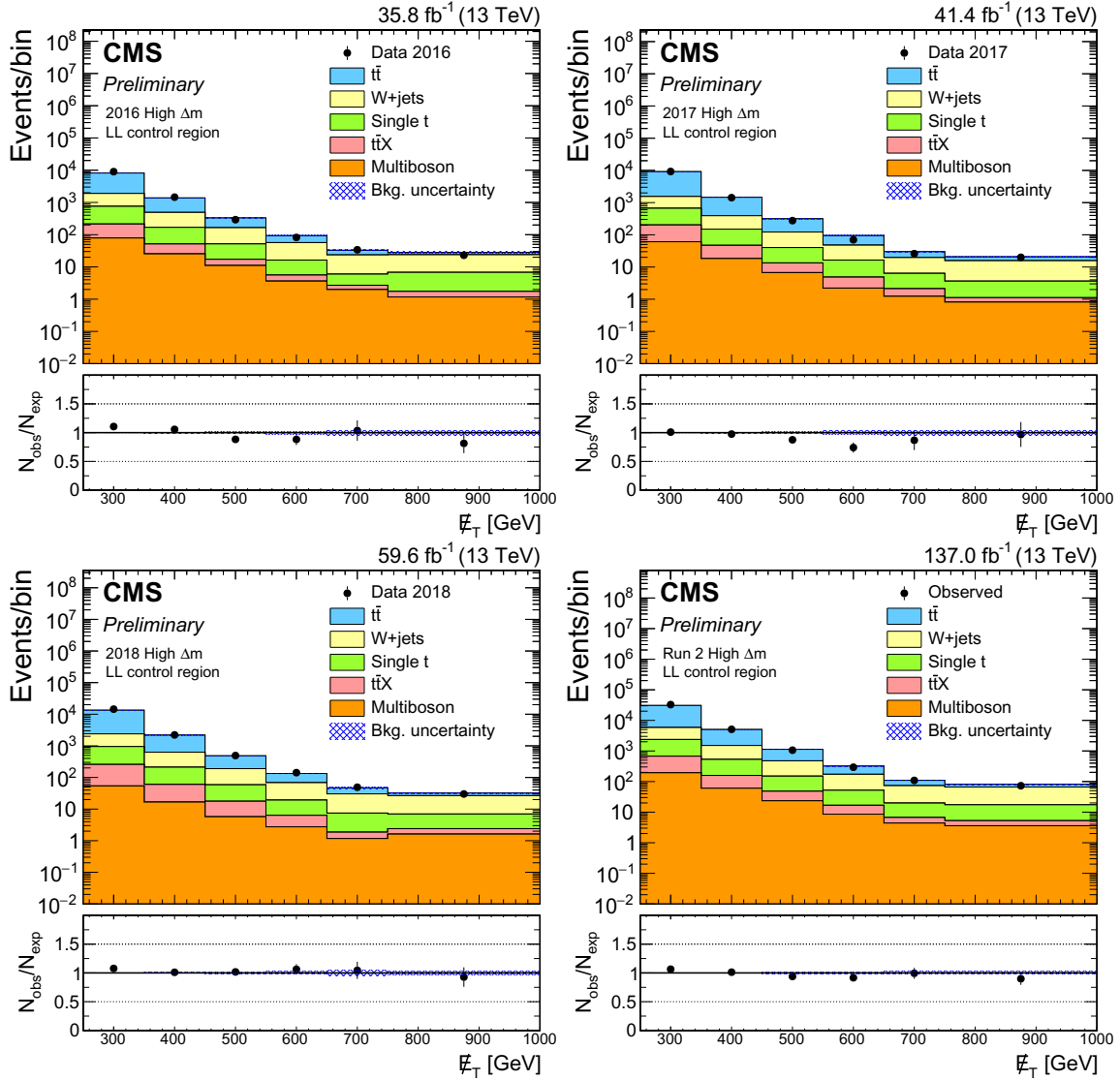


Figure 5.10: Comparison of the data and MC as a function of p_T^{miss} in the single lepton CR for each era: 2016, 2017, 2018, and Run 2 (the combination of all years) in the high Δm inclusive region. Each era shows reasonable agreement between data and MC and some residual trends look similar between different eras.

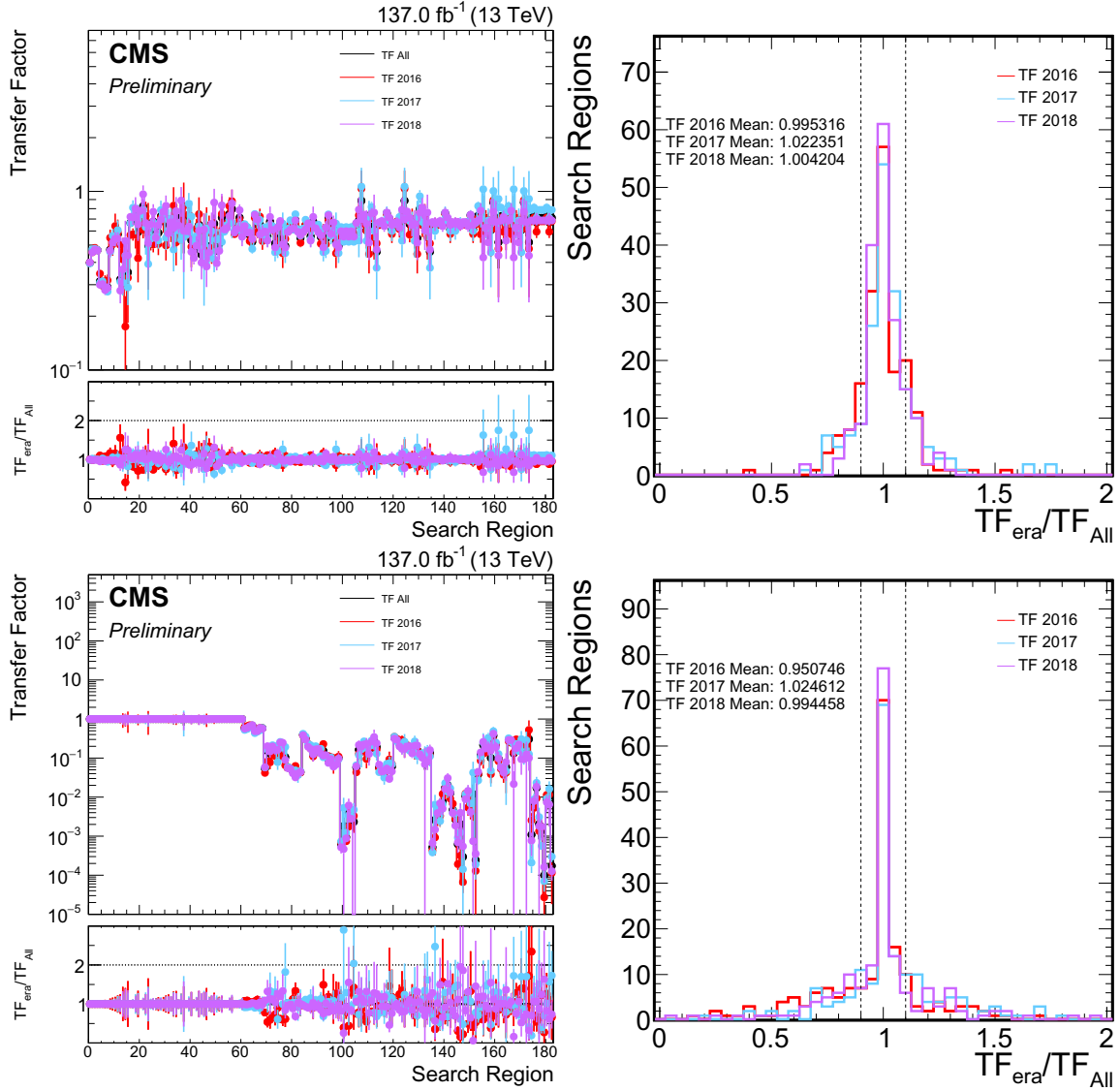


Figure 5.11: Comparisons of the transfer factors, separated into the CR-to-SR (top) and SR-to-extrapolation (bottom), for each era of MC in the low and high Δm regions. The values are shown in their separate bins on the left plot and in a combined form on the right. The mean for each is also shown.

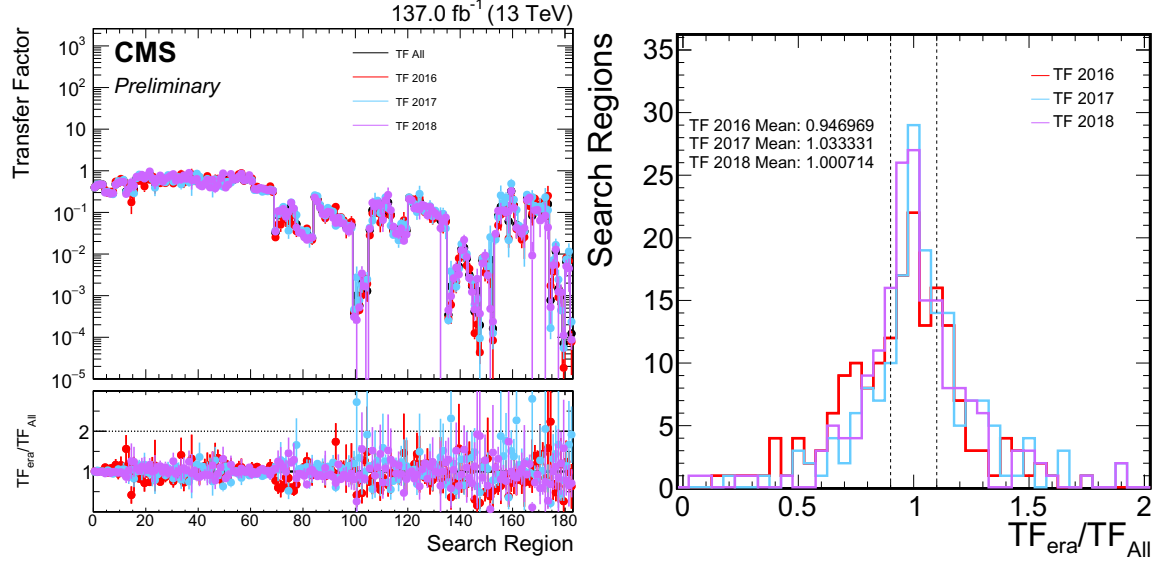


Figure 5.12: Comparisons of the transfer factors for each era of MC in the low and high Δm regions. The values are shown in their separate bins on the left plot and in a combined form on the right. The mean for each is also shown.

The normalization factor for the Z invisible prediction is measured in a dilepton control region (selecting two electrons or two muons) that is tailored for events with a boosted Z boson decaying to two leptons. The small Z to dielectron and dimuon branching ratios limit statistics in the control region. A small number of different selections in bottom quark multiplicity are used to calculate accurate normalization factors while maintaining reasonable statistics. The normalization term corrects for differences between the simulated and measured Z production cross section.

The shape factor for the Z invisible prediction is measured in a photon control region that selects events with one boosted photon and no leptons. The photon control region benefits from a large photon production cross section and has better statistics than the dilepton control region. The shape factor accounts for differences between simulation and data as a function of kinematic variables (p_T^{ISR} , p_T^{b} , m_T^{b} , p_T^{miss} ,

H_T) and object multiplicities (N_j , N_b , N_{SV}). The shape factor is inclusive in top quark and W boson multiplicities to maintain adequate statistics.

The methods used to obtain the Z invisible background prediction and relevant uncertainties are presented in detail in Chapter Six.

5.4.3 QCD Background

The QCD background is estimated using a QCD CR that is orthogonal to the SR. Missing transverse energy (p_T^{miss}) in QCD events can originate from jet p_T mismeasurement or from semi-leptonic heavy flavor decay. Both of these sources of p_T^{miss} will be referred to as mismeasurement. Mismeasurement results in p_T^{miss} that is nearly collinear with one of the jets in the event. To reject QCD background events, the search region includes a veto of events in which at least one of the three leading jets is close in azimuthal angle to the p_T^{miss} (Section 5.3.2). This selection used in the search region is written in Eq. (5.14).

$$\begin{aligned}\Delta\phi(\vec{p}_T^{\text{miss}}, j_1) &> 0.5 \\ \Delta\phi(\vec{p}_T^{\text{miss}}, j_2) &> 0.15 \\ \Delta\phi(\vec{p}_T^{\text{miss}}, j_3) &> 0.15\end{aligned}\tag{5.14}$$

The selection in Eq. (5.14) is inverted for the QCD control region to target QCD events where at least one of the three leading jets is mismeasured. Furthermore, the requirement that at least one of the three leading jets has $\Delta\phi < 0.1$ with the p_T^{miss} is added in the QCD CR to further constrain the p_T^{miss} to have a similar direction with one of the leading jets. The other baseline selections used in the search region (besides the $\Delta\phi$ selection) are unchanged in the QCD CR. Furthermore, the low Δm

selection is unchanged in the QCD CR, and the only change to the high Δm selection is the removal of the high Δm $\Delta\phi$ ($\bar{p}_T^{\text{miss}}, j_{1,2,3,4}$) cuts.

The QCD control region, like the search region, is divided into low Δm and high Δm categories. In low Δm , the control region is binned in N_j , N_b , N_{SV} , p_T^{ISR} , p_T^b , and p_T^{miss} . In high Δm , the control region is binned in N_j , N_b , m_T^b , H_T , and p_T^{miss} . The high Δm control region does not bin in N_t , N_W , and N_{res} to maintain adequate statistics.

The QCD prediction $N_{\text{pred}}^{\text{QCD}}$ is estimated by the equation

$$N_{\text{pred}}^{\text{QCD}} = TF_{\text{QCD}} \cdot \left(N_{\text{data}} - N_{\text{MC}}^{\text{non-QCD}} \right) \quad (5.15)$$

where N_{data} is the number of events in the QCD CR and $N_{\text{MC}}^{\text{non-QCD}}$ is the number of simulated non-QCD events in the CR. The transfer factor TF_{QCD} is the ratio between simulated QCD events in the SR and CR,

$$TF_{\text{QCD}} = \frac{N_{\text{MC}}^{\text{SR}}}{N_{\text{MC}}^{\text{CR}}}. \quad (5.16)$$

Data and simulation are compared in the QCD control region as a function of p_T^{miss} and H_T in Fig. 5.13.

The QCD prediction and uncertainties are shown in the validation bins (Fig. 5.14) defined in Section 5.3.4 and the search bins (Fig. 5.15) defined in Section 5.3.3.

5.4.4 $t\bar{t}Z$ and Rare Backgrounds

The $t\bar{t}Z$ and Rare backgrounds include the diboson (WW, WZ, ZZ) processes, multiboson (WWW, WWZ, WZZ, ZZZ) processes, the associated production with a top quark pair ($t\bar{t}H$, $t\bar{t}\gamma$, $t\bar{t}W$, and $t\bar{t}Z$), and others (tWZ , $WZ\gamma$, $WW\gamma$). As seen in Fig. 5.8, the $t\bar{t}Z$ and Rare backgrounds have the largest contribution to the total SM background in the high Δm search region when requiring at least two bottom

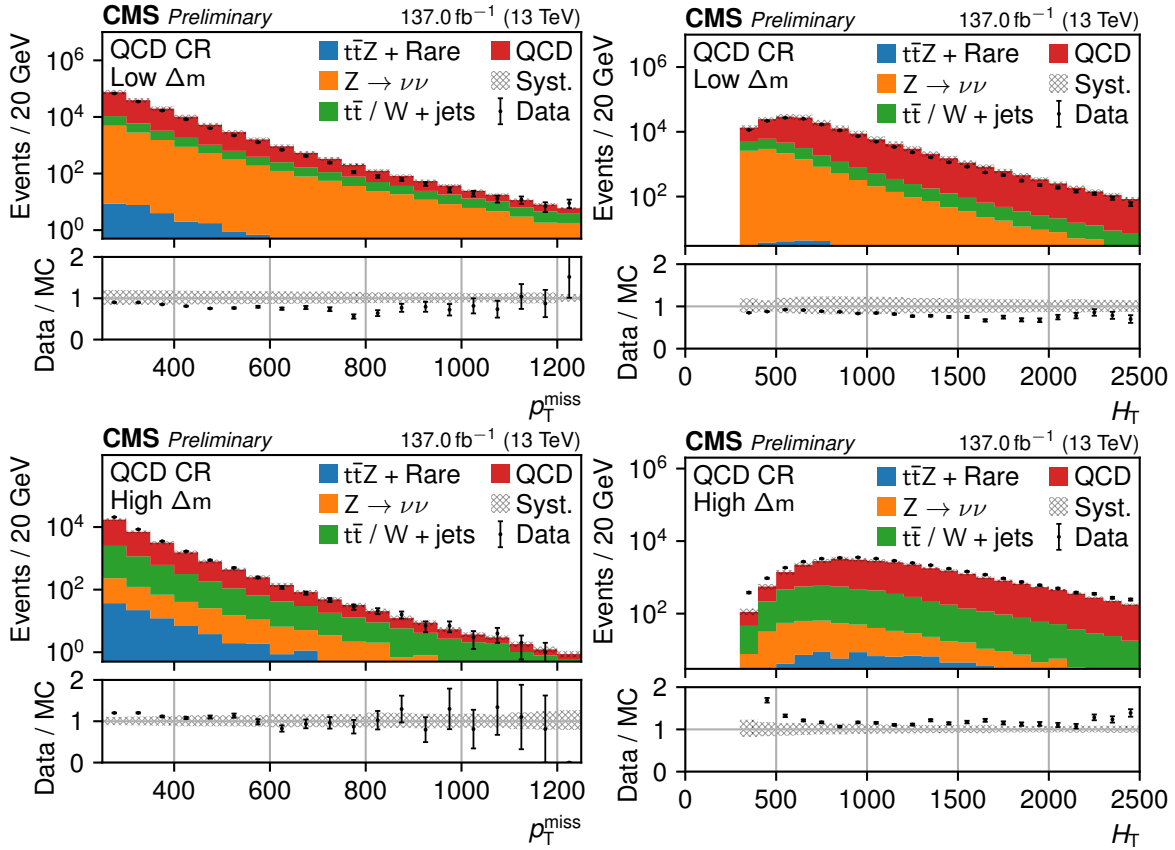


Figure 5.13: Validation of simulation in the QCD control region for the low Δm (top row) and high Δm (bottom row) selections as a function of p_T^{miss} (left column) and H_T (right column). The error bars on the data points show the statistical uncertainty, and the cross-hatched region shows the total systematic uncertainty on the prediction from simulation.

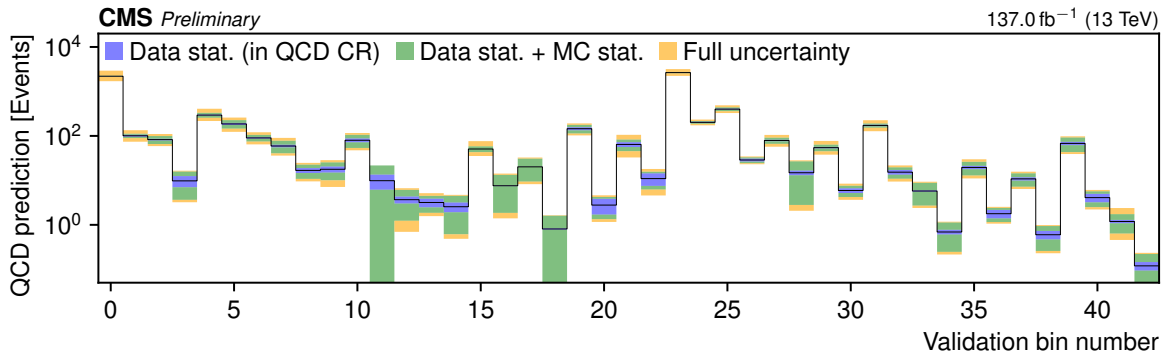


Figure 5.14: The predicted rate of QCD in the validation bins. The uncertainty on the prediction is split into the component arising from the limited statistics of the data in the QCD control region, the limited statistics of the Monte Carlo simulation, and all other systematic uncertainties.

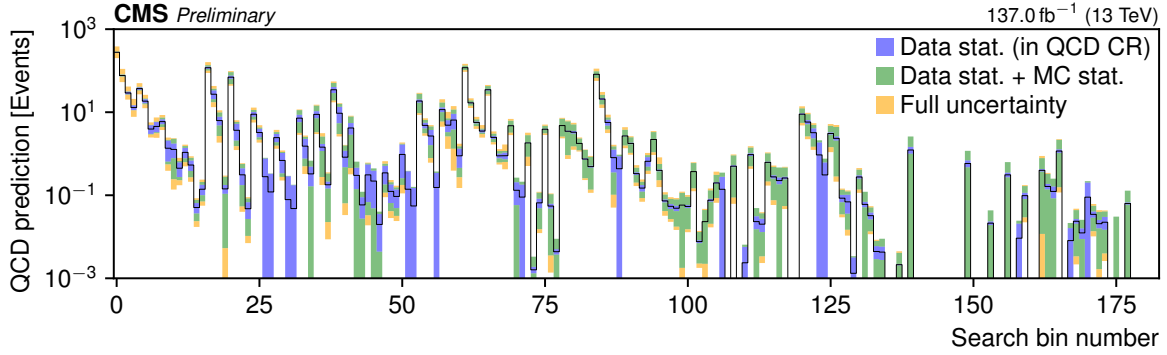


Figure 5.15: The predicted rate of QCD in the search bins. The uncertainty on the prediction is split into the component arising from the limited statistics of the data in the QCD control region, the limited statistics of the Monte Carlo simulation, and all other systematic uncertainties.

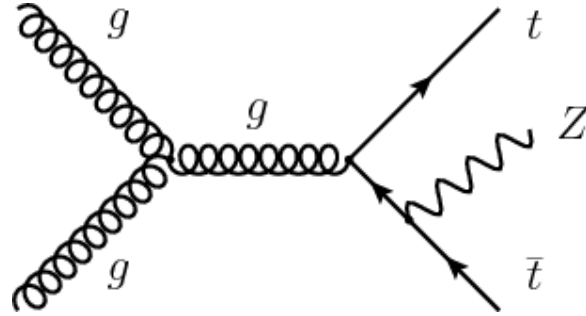


Figure 5.16: Dominant leading-order Feynman diagram for $t\bar{t}Z$ production at the LHC.

quarks and at least one top quark or W boson. The majority of this contribution is from the $t\bar{t}Z$ process, which has a signature that is similar to some of the high Δm signals. The $t\bar{t}Z$ process has the same final state as the T2tt model when the top quarks decay hadronically and the Z boson decays to neutrinos, and for this final state $t\bar{t}Z$ is an irreducible background. The Feynman diagram of the dominant $t\bar{t}Z$ production mode at the LHC is shown in Fig. 5.16.

Even for selections that favor $t\bar{t}Z$, the combined $t\bar{t}Z$ and Rare background contribution in the search region is at most $\approx 10\%$ (Fig. 5.8). Since $t\bar{t}Z$ and Rare are relatively small backgrounds in the search region, these backgrounds are predicted

using simulation rather than with a data-driven approach. An overall normalization scale factor is applied to the $t\bar{t}Z$ simulation as a correction to the production cross section at 13 TeV, which is 0.7826 pb. This normalization factor is obtained using the results from a CMS measurement of the $t\bar{t}Z$ cross section as discussed below.

The $t\bar{t}Z$ background prediction from simulation is validated with data using the three-lepton decay channel. The three-lepton selection used to validate the $t\bar{t}Z$ prediction is as follows:

- Pass all filters that remove detector- and beam-related noise as described in Section 5.2.12.
- Pass the single lepton trigger (Section 5.3.1)
- Have exactly three leptons passing medium ID requirement
 - * Leading lepton, which is a muon or electron required by the trigger, with $p_T > 50$ or 40 GeV respectively
 - * Second and third leading leptons with $p_T > 20$ GeV
- Have one Z boson (reconstructed from two leptons) within the mass window of 81–101 GeV
- Have at least four jets with $p_T > 40$ GeV, $|\eta| < 2.4$
- Have at least two b-tagged jets with $p_T > 30$ GeV, $|\eta| < 2.4$
- $p_T^{\text{miss}} > 30$ GeV

Simulations of the $t\bar{t}Z$ process and other backgrounds are compared to the “Single Muon” (muon-triggered) and “Single Electron” (electron-triggered) data separately using the three-lepton selection in Fig. 5.17. The observed $t\bar{t}Z$ yield is calculated by subtracting the simulated background yields from the data yield. Then a $t\bar{t}Z$ normalization scale factor is obtained by taking the ratio of the observed $t\bar{t}Z$

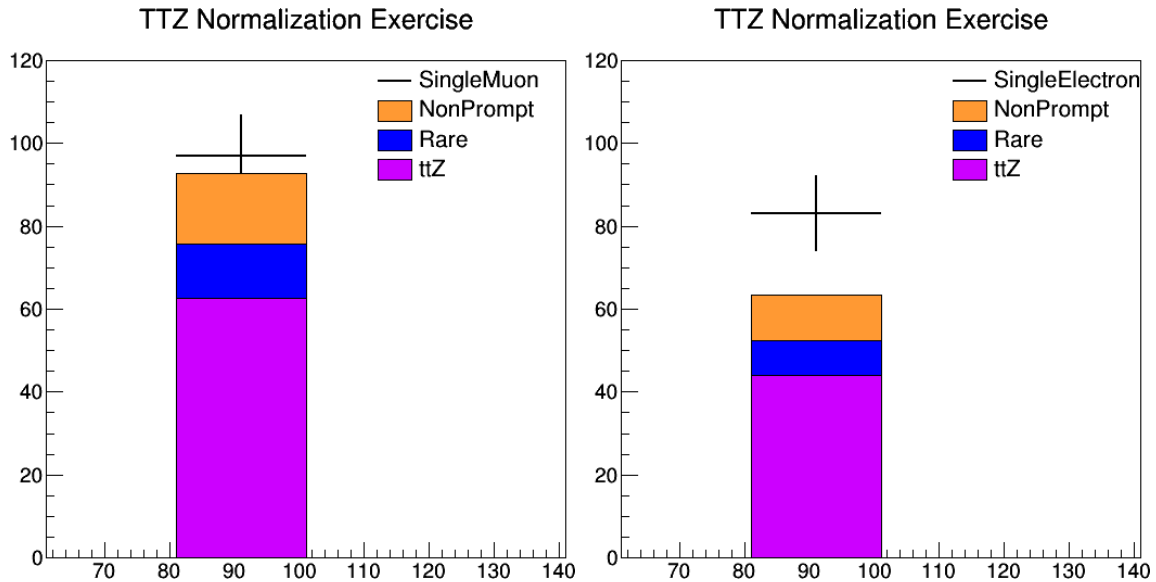


Figure 5.17: $t\bar{t}Z$ validation in the three-lepton channel from Single Muon (left) and Single Electron (right) data. The error bar denotes the statistical uncertainty.

yield and the simulated $t\bar{t}Z$ yield. The uncertainty of this scale factor results from propagating the statistical uncertainties for each term through this calculation. From the Single Muon data set, the derived scale factor is 1.06871 ± 0.15890 , and from the Single Electron data set, the scale factor is 1.44722 ± 0.20910 .

There is a recently published measurement from CMS of the inclusive cross section of $t\bar{t}Z$ [67]. This measurement uses 2016 and 2017 data corresponding to an integrated luminosity of 77.5 fb^{-1} with proton-proton collisions at a center-of-mass energy of 13 TeV provided by the LHC. The measurement selects three and four lepton final states (electrons or muons), and the Z boson is reconstructed using a pair of same-flavor opposite-charge leptons. The production cross section at 13 TeV is measured to be $0.95 \pm 0.05 \text{ (stat.)} \pm 0.06 \text{ (syst.) pb}$, while the $t\bar{t}Z$ cross section used for this SUSY analysis 0.7826 pb . A $t\bar{t}Z$ normalization scale factor can be calculated by taking the ratio of this measured cross section and the cross section used in this

analysis. Combining the statistical and systematic uncertainties and taking this ratio gives

$$(0.95 \pm 0.8 \text{ pb}) / (0.7826 \text{ pb}) = 1.214 \pm 0.100. \quad (5.17)$$

This $t\bar{t}Z$ scale factor is in agreement with the muon and electron scale factors that we measured in the three-lepton final state, and it has a smaller uncertainty, so we choose to use this scale factor derived from the CMS measurement for the $t\bar{t}Z$ prediction.

5.5 *Uncertainties*

There are a number of uncertainties associated with the background predictions and simulated signal samples used in the analysis. The uncertainties fall into two distinct categories: statistical uncertainties and systematic uncertainties.

Statistical uncertainties arise from the sample size (e.g. the number of data events or simulated events) and account for the inherent randomness present in each event. Given a small sample size, statistical fluctuations are more common. As the sample size increases, the results fluctuate less and have less relative statistical uncertainty. The analysis has a large number of search region bins and corresponding control region bins, many of which have fairly restrictive selections. Statistical uncertainties are large in both data and simulation for bins that have few events passing the selection required by the bin.

Systematic uncertainties are associated with possible measurement errors or unknowns that are relevant to the final results. Systematic uncertainties can be estimated by determining a range of likely values for a given parameter, varying the parameter across this range, and measuring the effect on the final results. Systematic

uncertainties are only associated with simulation and not with data. Many data-driven correction factors are applied to the simulation, and many of these correction factors have a corresponding systematic uncertainty. Systematic uncertainties common to signal and backgrounds include those from b- and soft b-tagging scale factors, p_T^{miss} trigger efficiency, pileup reweighting, L1 prefire weight, jet energy scale (JES), corrections from unclustered MET, lepton scale factors, and top- and W-tagging scale factors.

Limited MC statistics in search region bins and control region bins not only result in large statistical uncertainties but can also result in large and poorly determined systematic uncertainties. Three methods are used to address poorly determined systematic uncertainties.

First, if the statistical uncertainty in the predicted yield in a bin is larger than the predicted yield (implying a greater than 100% statistical uncertainty), then all systematic uncertainties are ignored in that bin (set to 0%). The systematic uncertainties cannot be accurately determined because the predicted yield is not well determined. The statistical uncertainty dominates, and there is no need to determine systematic uncertainties as they will be negligible by comparison.

After this first procedure, there are still cases of poorly determined systematics. These cases tend to occur for systematics such as JES and p_T^{miss} resolution that change kinematic variables instead of event weights. Altering kinematic variables allows for events to move from one bin to another as the bin selections are dependent on kinematic variables. In some cases, events moving from one bin to another can result in a very large systematic in one direction. A condition is used to check for extremely

asymmetric systematics,

$$|(|\ln R(\text{Up})|) - (|\ln R(\text{Down})|)| > 0.35, \quad (5.18)$$

where $R(\text{Up})$ is the ratio of the predicted yield for the “Up” systematic variation to the unvaried predicted yield, $R(\text{Down})$ is the ratio of the predicted yield for the “Down” systematic variation to the unvaried predicted yield, and 0.35 is a somewhat arbitrary threshold. When this threshold is exceeded, the direction that results in the larger variation (based on the absolute value of the logarithm of the ratio) is ignored and replaced with the reciprocal of the remaining ratio. For example, suppose $R(\text{Up}) = 0.55$ and $R(\text{Down}) = 1.25$. Their natural logarithms are $\ln R(\text{Up}) = -0.60$ and $\ln R(\text{Down}) = 0.22$, and the difference in the absolute values is 0.37, which exceeds the threshold 0.35. Because -0.60 has a larger absolute value than 0.22, $R(\text{Down})$ is left unchanged, and $R(\text{Up})$ is replaced with $R(\text{Up}) = 1/R(\text{Down}) = 0.8$. Note that the logarithms of the ratios are used to measure the amount of asymmetry because the systematic uncertainties are modeled using the log-normal distribution, so the logarithms of the ratios are Gaussian distributed.

Finally, after applying the first two procedures, the last cases to address are those where both the “Up” and “Down” variations are on the same side of the central prediction, i.e. both are greater than or both are less than the central prediction. Same-side systematics can cause technical difficulties in the fitting procedure. To remedy this, the “Up” and “Down” systematic ratios are divided by their geometric mean, which is used because the systematics are modeled using the log-normal distribution. This symmetrizes the log-normal distribution and centers it on the predicted yield with systematic variations.

5.6 Results

5.6.1 Validation Bins

The validation bins defined in Section 5.3.4 are used to test the background predictions by comparing them with data in a phase space that has low signal contamination. The Run 2 data and SM background predictions for each validation bin are shown in Fig. 5.18. The background predictions are obtained using the methods presented in Sections 5.4.1, 5.4.2, 5.4.3, and 5.4.4. The data generally agrees with the background predictions and falls within the range of the statistical and systematic uncertainties. The data and background prediction comparison can be quantified using the “pull,” which is defined as

$$\text{pull} = \frac{\text{data} - \text{pred}}{\sqrt{\text{pred} + \Delta_{\text{pred}}^2}}$$

where Δ_{pred} takes both statistical and systematic uncertainties into account. The pulls for the validation bins are shown in Fig. 5.19. In the 43 validation bins, the pulls are within the range $-2 < \text{pull} < 2$, and the background predictions agree well with the data. After being validated, these same background prediction methods are used for the search region.

5.6.2 Search Bins

The search bins defined in Section 5.3.3 are used to look for evidence of SUSY models, which would be seen as an excess in data in signal enhanced regions. The search bin definitions, background prediction yields and uncertainties, and observed data are detailed in Tables C.1 to C.7 in Appendix C. The observed Run 2 data, SM background prediction, and example signal model yields for each search bin are shown

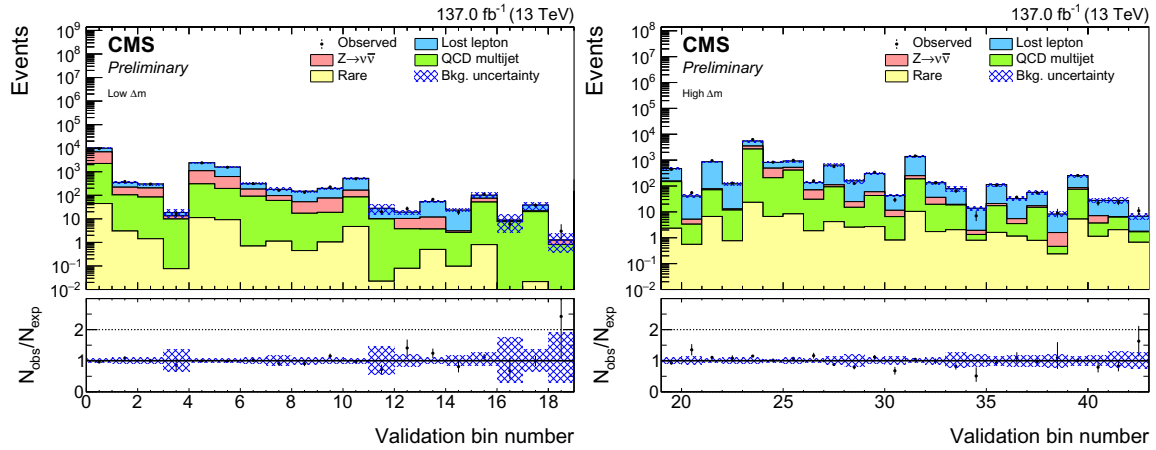


Figure 5.18: Data and background prediction in low Δm (left, defined in Table 5.7) and high Δm (right, defined in Table 5.8) validation bins. The lower pads show the ratio of data and the sum of all background predictions, where the hashed blue band represents the total statistical and systematic uncertainty.

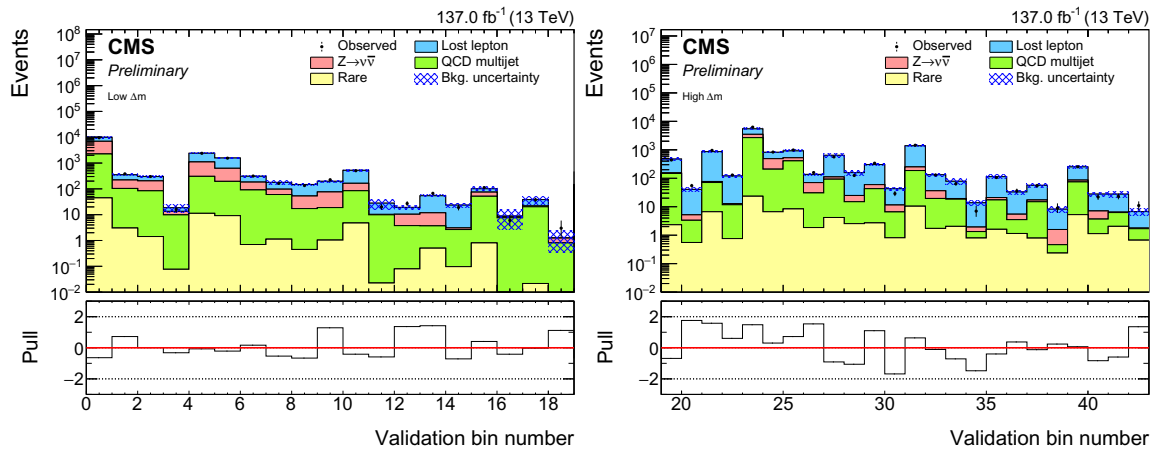


Figure 5.19: Data and background prediction in low Δm (left, defined in Table 5.7) and high Δm (right, defined in Table 5.8) validation bins. The lower pads show the pull of data and the sum of all background predictions, where pull is defined as $\text{pull} = \frac{\text{data} - \text{pred}}{\sqrt{\text{pred} + \Delta_{\text{pred}}^2}}$ and Δ_{pred} takes both statistical and systematic uncertainties into account.

in Figs. 5.20 and 5.21. The observed Run 2 data, postfit SM background prediction, and example signal model yields for each search bin are shown in Figs. 5.22, and 5.23. No significant excesses in data are observed in the search bins, so no evidence is found for the simplified SUSY models described in Section 5.1. Exclusion limits are placed on the production cross section as a function of SUSY particle masses for each simplified SUSY model; these limits are presented in Section 5.6.3. In addition, event displays of interesting selected events that pass the search region selection are shown in Appendix B.

5.6.3 Limits

The exclusion limits for the T2tt, T2bW, and T2tb simplified models are shown as a function of the top squark and LSP masses in Fig. 5.24. For the T2tt model, top squark masses up to 1310 GeV and LSP masses up to 640 GeV are excluded. For the T2bW model, top squark masses up to 1170 GeV and LSP masses up to 550 GeV are excluded. For the T2tb model, top squark masses up to 1150 GeV and LSP masses up to 500 GeV are excluded.

The exclusion limits for the T2ttC, T2bWC, and T2cc simplified models are shown as a function of the top squark mass and the difference between the top squark and LSP masses in Fig. 5.25. For the T2ttC model, top squark masses up to 640 GeV are excluded. For the T2bWC model, top squark masses up to 740 GeV are excluded. For the T2cc model, top squark masses up to 630 GeV are excluded.

The exclusion limits for the T1tttt, T1ttbb, and T5ttcc simplified models are shown as a function of the gluino and LSP masses in Fig. 5.26. For the T1tttt model, gluino masses up to 2260 GeV and LSP masses up to 1410 GeV are excluded. For

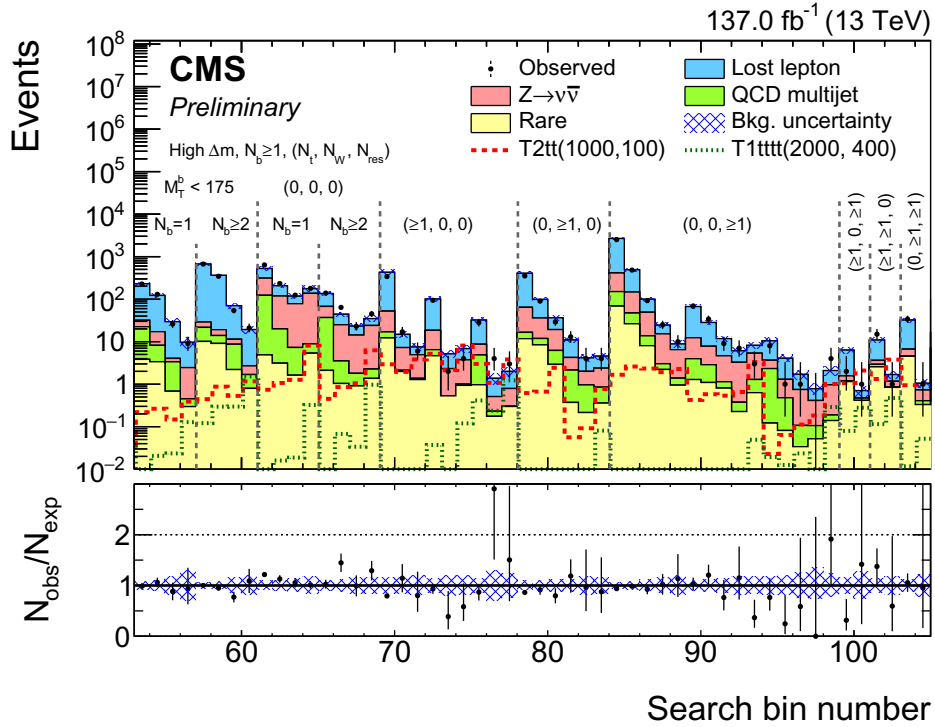
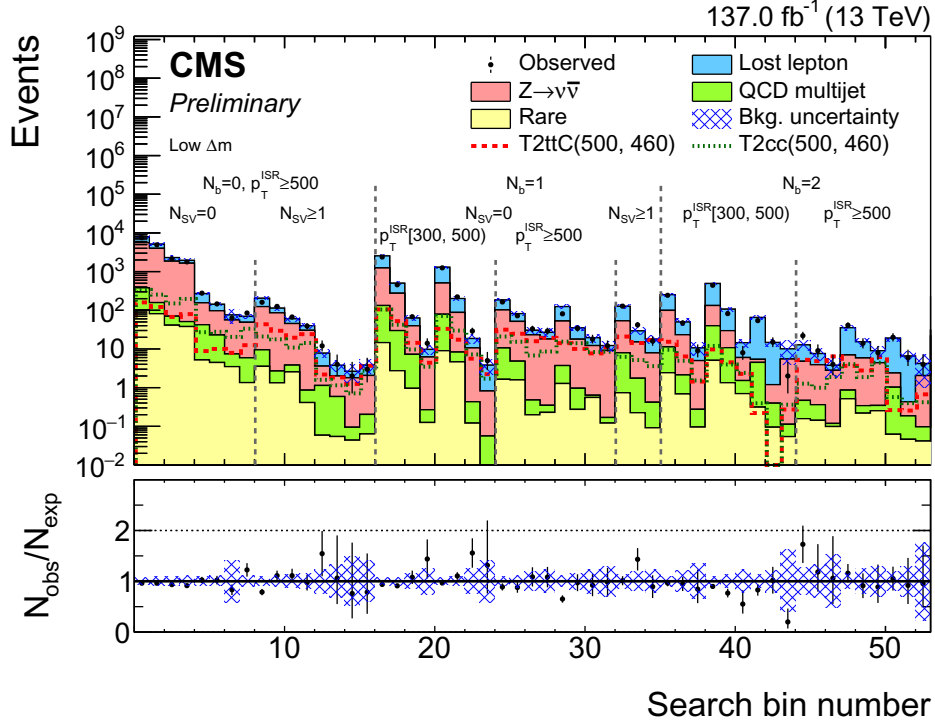


Figure 5.20: Observed data yields (black points), predicted SM background (filled histograms), and example signal models (dashed histograms) in the low Δm bins 0–52 (top) and high Δm bins 53–104 (bottom). The high Δm bins included are the bins which have $m_T^b < 175$ GeV, or $N_t = 0, N_{res} = 0$, and $N_W = 0$, or $N_b = 1$. In both plots, the lower panel shows the ratio of data over the total SM background prediction. The hatched bands represent the total uncertainty in the background prediction.

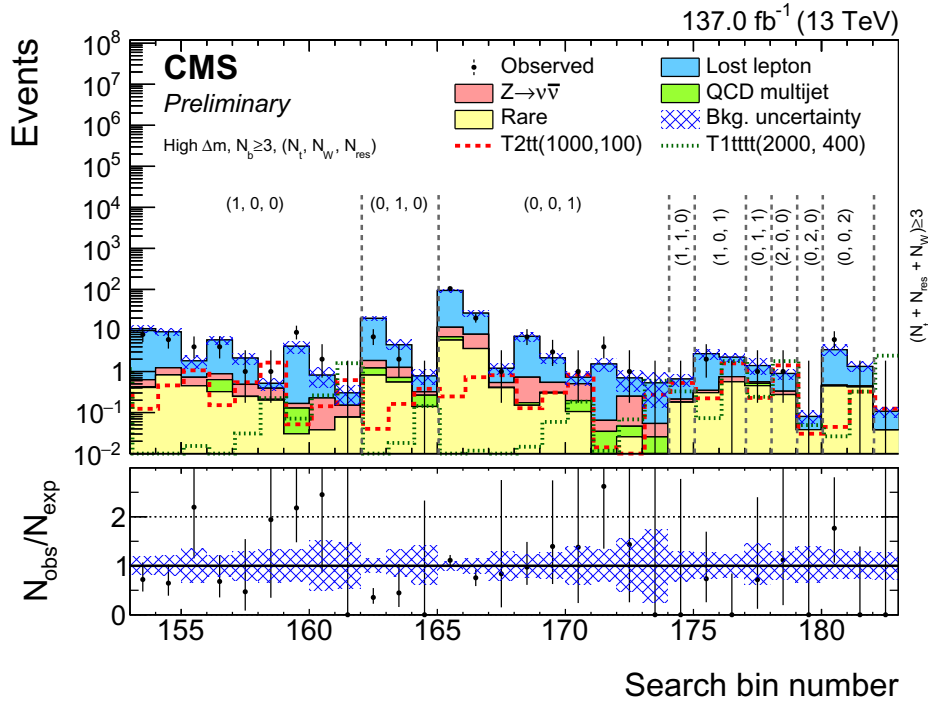
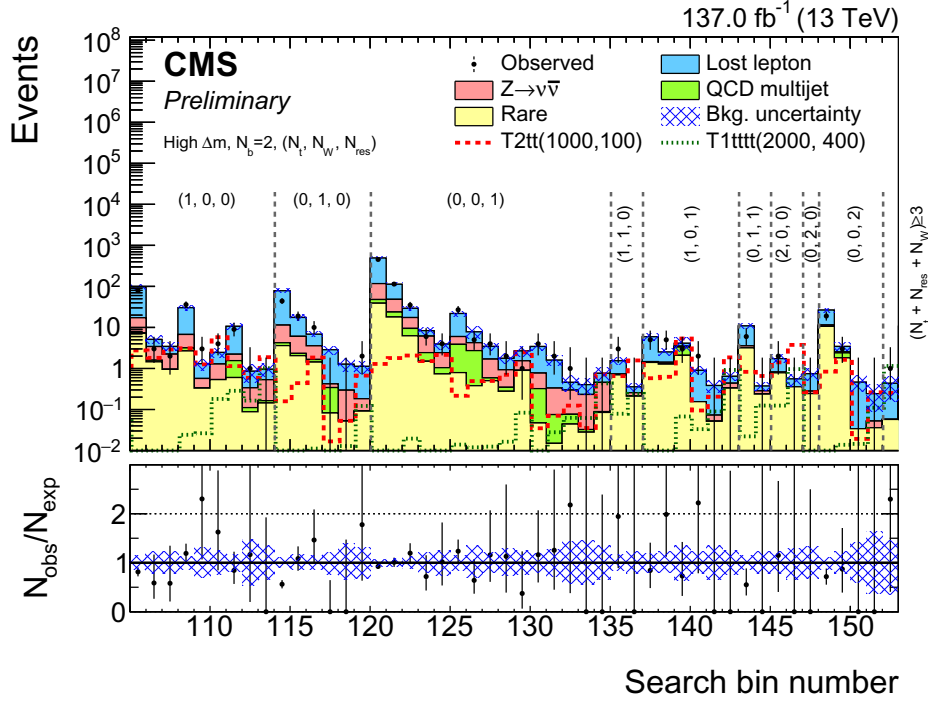


Figure 5.21: Observed data yields (black points), predicted SM background (filled histograms), and example signal models (dashed histograms) in the high Δm bins 105–152 with $N_b = 2$ (top) and high Δm bins 153–182 with $N_b \geq 3$ (bottom). In both plots, the lower panel shows the ratio of data over the total SM background prediction. The hatched bands represent the total uncertainty in the background prediction.

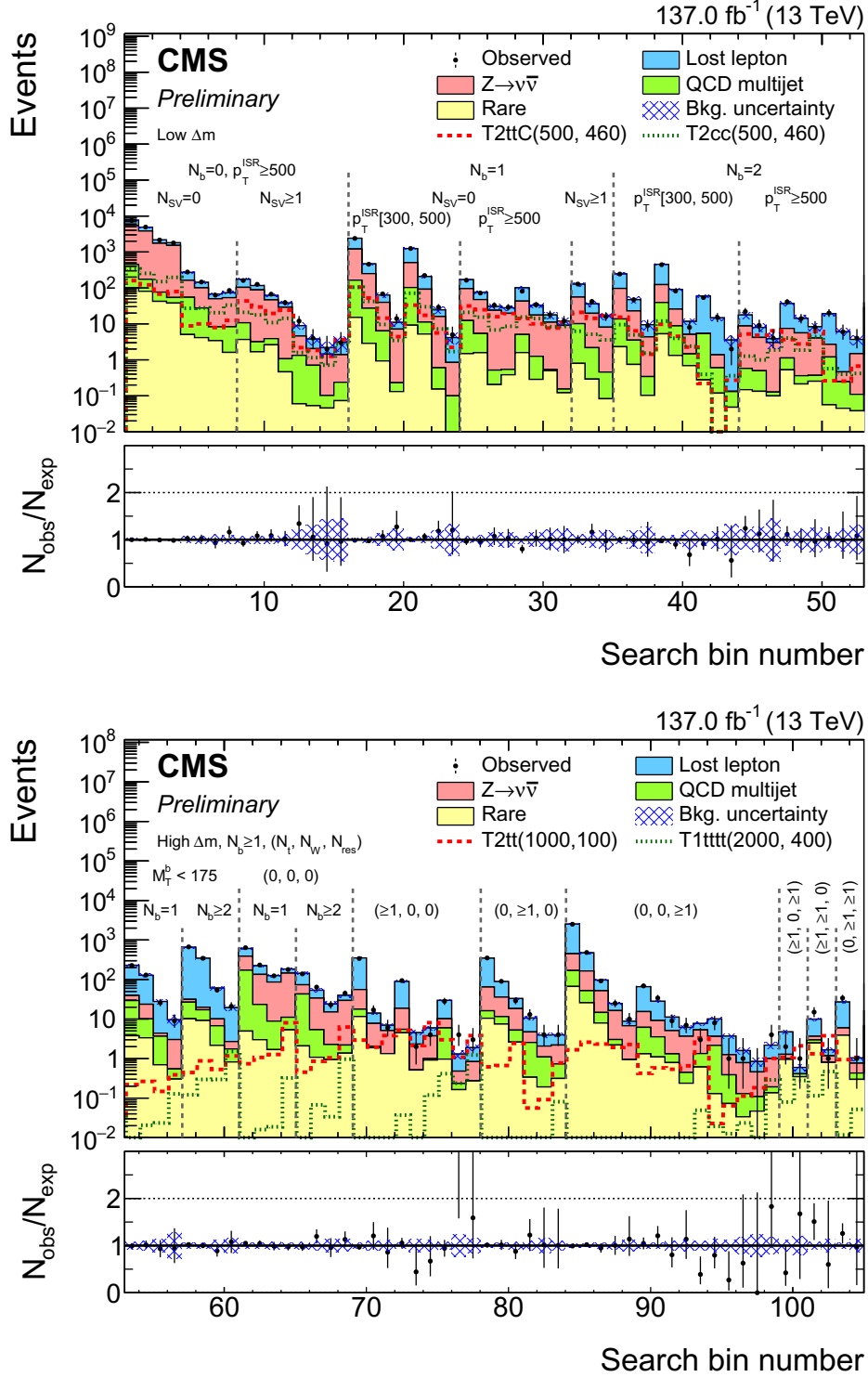


Figure 5.22: Observed data yields (black points), postfit SM background prediction (filled histograms), and example signal models (dashed histograms) in the low Δm bins 0–52 (top) and high Δm bins 53–104 (bottom). The high Δm bins included are the bins which have $m_T^b < 175$ GeV, or $N_t = 0, N_{\text{res}} = 0$, and $N_W = 0$, or $N_b = 1$. In both plots, the lower panel shows the ratio of data over the total SM background prediction. The hatched bands represent the total uncertainty in the background prediction.

the T1ttbb model, gluino masses up to 2250 GeV and LSP masses up to 1400 GeV are excluded. For the T5ttcc model, gluino masses up to 2150 GeV and LSP masses up to 1380 GeV are excluded.

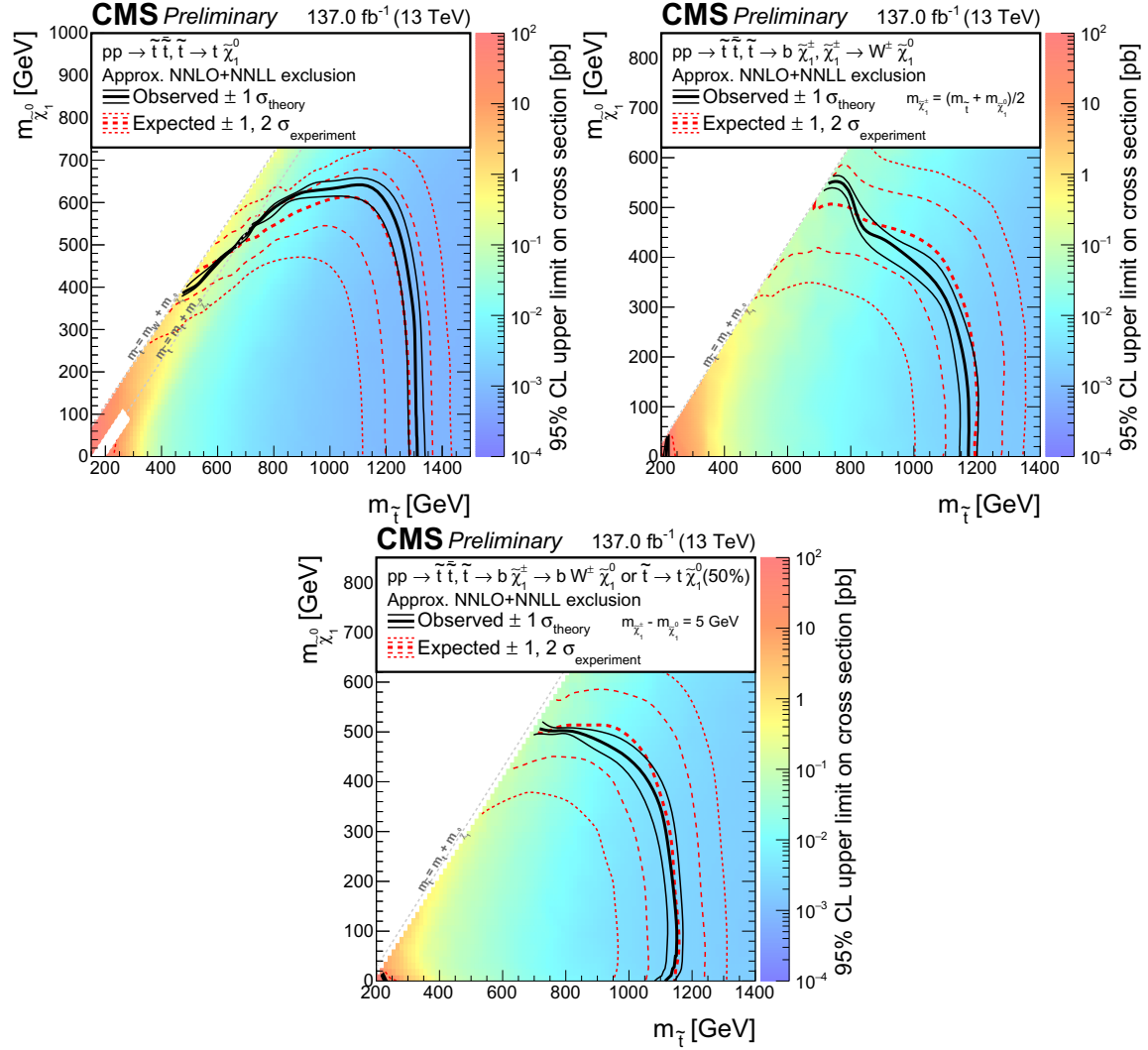


Figure 5.24: The 95% CL upper limit on the production cross section of the T2tt (upper left), T2bW (upper right), and T2tb (bottom) simplified models as a function of the top squark and LSP masses. The solid black curves represent the observed exclusion contour with respect to approximate NNLO+NNLL signal cross sections and the change in this contour due to variation of these cross sections within their theoretical uncertainties [68–78]. The dashed red curves indicate the mean expected exclusion contour and the region containing 68% and 95% of the distribution of expected exclusion limits under the background-only hypothesis. For T2tt, no interpretation is provided for signal models for which $|m_{\tilde{t}} - m_{\tilde{\chi}_1^0} - m_t| \leq 25 \text{ GeV}$ and $m_{\tilde{t}} \leq 275 \text{ GeV}$ because events from such models are essentially indistinguishable from SM $t\bar{t}$ events in this region, rendering the signal event acceptance difficult to model.

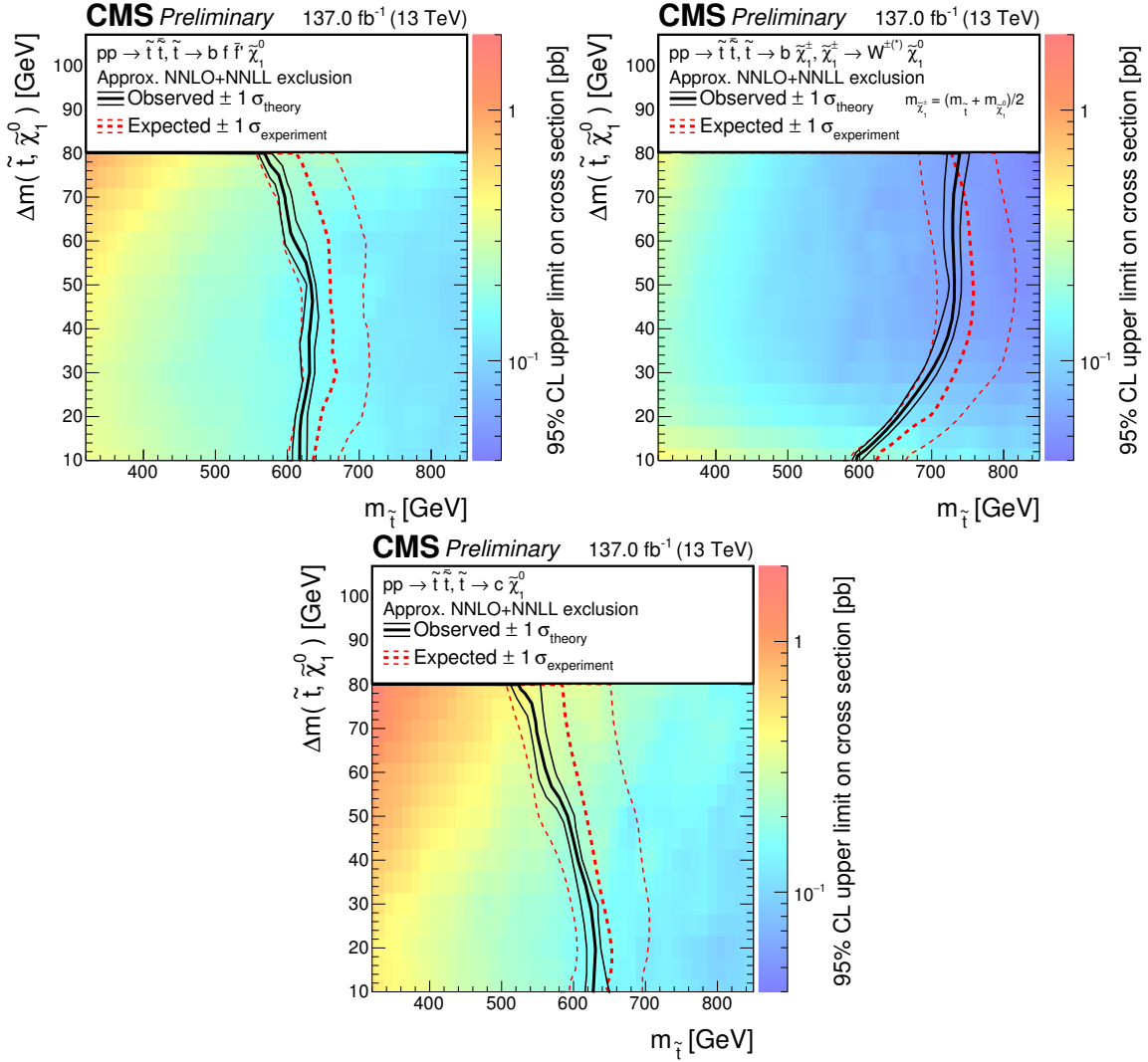


Figure 5.25: The 95% CL upper limit on the production cross section of the T2ttC (upper left), T2bWC (upper right), and T2cc (bottom) simplified models as a function of the top squark mass and the difference between the top squark and LSP masses. The solid black curves represent the observed exclusion contour with respect to approximate NNLO+NNLL signal cross sections and the change in this contour due to variation of these cross sections within their theoretical uncertainties [68–78]. The dashed red curves indicate the mean expected exclusion contour and the region containing 68% of the distribution of expected exclusion limits under the background-only hypothesis.

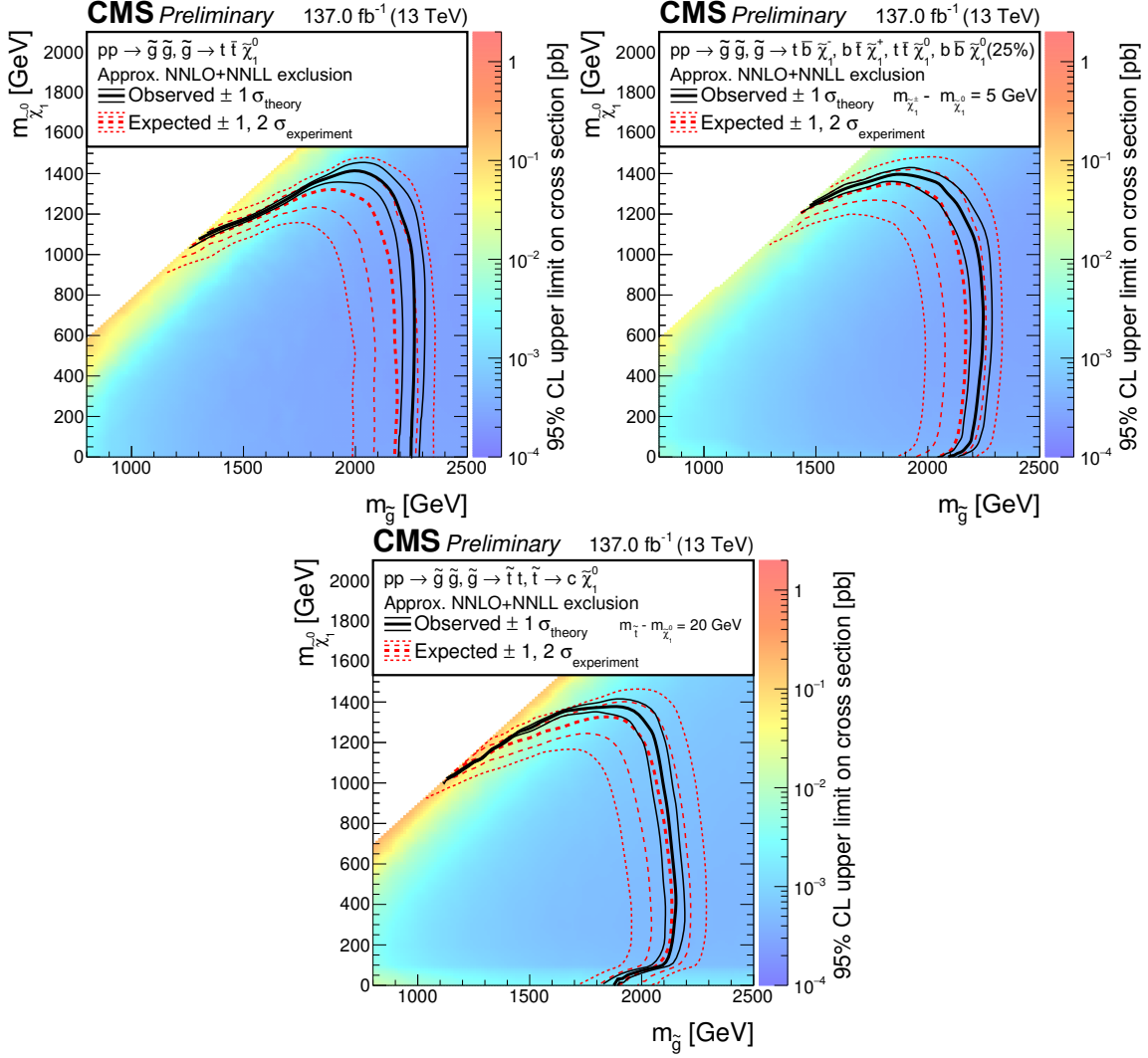


Figure 5.26: The 95% CL upper limit on the production cross section of the T1tttt (upper left), T1ttbb (upper right), and T5ttcc (bottom) simplified models as a function of the gluino and LSP masses. The solid black curves represent the observed exclusion contour with respect to approximate NNLO+NNLL signal cross sections and the change in this contour due to variation of these cross sections within their theoretical uncertainties [68–78]. The dashed red curves indicate the mean expected exclusion contour and the region containing 68% and 95% of the distribution of expected exclusion limits under the background-only hypothesis.

CHAPTER SIX

Z Invisible Background

6.1 Overview

An important SM background process for the all-hadronic stop analysis comes from events which have a Z boson that decays to a neutrino and an antineutrino. The proton-proton collisions inside CMS have unknown initial momentum in the z-axis (parallel to the beam) because interacting partons possess unknown fractions of the proton momenta. However, the initial momentum in the transverse direction (perpendicular to the beam) is zero, and thus the final transverse momentum should also be zero when including all final state particles (whether or not these particles can be detected and reconstructed). However, if only the momenta of visible particles (those which are detected and reconstructed) are summed, then it is possible for nonzero transverse momentum to arise due to invisible particles (those which are not detected or reconstructed). Neutrinos cannot be detected by CMS, and the production of a Z boson with transverse momentum that decays to neutrinos results in an imbalance in transverse momentum, or missing transverse energy (p_T^{miss}). In this case, the amount of p_T^{miss} depends on the transverse component of the momentum of the Z boson. The Z decay to a neutrino-antineutrino pair (of electron, muon, or tau flavor) will be referred to as the “Z invisible” process. The Z invisible process can produce similar signatures to SUSY models that have a weakly interacting and stable LSP. As shown in Fig. 5.8, the Z invisible background is a significant portion of the total SM background for the selections which require no top quarks or W bosons.

Table 6.1: The Z boson branching ratios for “standard” decays [1]. Rare Z decays and limits on unobserved decays are not included.

Z decay mode	Branching ratio (Γ_i/Γ)
$Z \rightarrow e^+e^-$	$(3.3632 \pm 0.0042)\%$
$Z \rightarrow \mu^+\mu^-$	$(3.3662 \pm 0.0066)\%$
$Z \rightarrow \tau^+\tau^-$	$(3.3696 \pm 0.0083)\%$
$Z \rightarrow \nu\bar{\nu}$	$(20.000 \pm 0.055)\%$
$Z \rightarrow q\bar{q}$	$(69.911 \pm 0.056)\%$

The Z mass has been measured with very high precision to be $m_Z = 91.1876 \pm 0.0021$ GeV, and the full Z width is $\Gamma_Z = 2.4952 \pm 0.0023$ GeV [1]. The Z invisible width including all three neutrino flavors is $\Gamma_{\nu\nu} = 499.0 \pm 1.5$ MeV [1]. Taking the ratio of $\Gamma_{\nu\nu}$ and Γ_Z gives the branching ratio, which is the probability for a Z boson to decay to neutrinos.

$$\frac{\Gamma_{\nu\nu}}{\Gamma_Z} = 20\% \tag{6.1}$$

The calculation of Z widths is presented in Appendix A. The Z boson branching ratios for the primary Z decay channels are given in Table 6.1.

6.2 Method

Because the Z invisible background is a significant background for the analysis, it is beneficial to use a data-driven method to predict this background and in this way correct for any mismodeling effects present in the $Z \rightarrow \nu\bar{\nu}$ simulation. One natural control region is a dilepton control region selecting same-flavor opposite-sign charged leptons. When the dilepton invariant mass is near the mass of the Z boson (91 GeV), this control region is dominated by events with a Z decaying to dileptons. The kinematics of events with a Z decaying to neutrinos and a Z decaying to charged leptons should be very similar; the primary difference is in the final state. The Z

decays to electrons, muons, and taus about 10% of the time compared to about 20% of the time for neutrinos (Table 6.1). The CMS detector can efficiently reconstruct electrons and muons using measurements from the tracker, calorimeters, and muon chambers. Taus are more difficult to reconstruct because they have a very short lifetime and decay within the CMS detector. For the Z invisible background prediction, both dielectron and dimuon control regions are used to calculate a normalization factor. The dilepton control region is orthogonal to the search region (which has a lepton veto). Furthermore, the dilepton control region should not have significant SUSY signal contamination because the control region requires a boosted Z boson and targets the Z mass peak region.

Another available control region is a single photon control region. The photon, like the Z boson, is a neutral vector boson that interacts with quarks and charged leptons. The photon does not interact with neutrinos as the Z boson does. However, photon and Z boson production from proton-proton collisions have similar kinematics when the Z and photon momenta are much higher than the Z mass. Photon production has a higher cross section than the Z boson production allowing for more events and better statistics in a photon control region. This analysis has many search bins and corresponding control region bins, and the uncertainty on the Z invisible prediction is driven by statistics. To improve statistics for the data-driven Z invisible prediction, a photon control region is used to estimate a shape correction factor. The photon control region is made orthogonal to the search region by placing the requirement $p_T^{\text{miss}} < 250$ GeV. Signal contamination is limited by selecting a boosted photon.

The Z invisible prediction is given by the equation

$$N_{\text{pred}}^{Z \rightarrow \nu\bar{\nu}} = R_Z \cdot S_\gamma \cdot N_{\text{MC}}^{Z \rightarrow \nu\bar{\nu}} \quad (6.2)$$

where $N_{\text{pred}}^{Z \rightarrow \nu\bar{\nu}}$ is the predicted number of Z invisible events, R_Z is a normalization factor obtained in a dilepton control region, S_γ is a shape factor obtained in a photon control region, and $N_{\text{MC}}^{Z \rightarrow \nu\bar{\nu}}$ is the weighted number of simulated $Z \rightarrow \nu\bar{\nu}$ MC events. The number of $Z \rightarrow \nu\bar{\nu}$ events, $N_{\text{MC}}^{Z \rightarrow \nu\bar{\nu}}$, is rescaled using the $Z \rightarrow \nu\bar{\nu}$ cross-section and the integrated luminosity of 137.0 fb^{-1} for the Run 2 data set. Additional data-driven weights are applied to $N_{\text{MC}}^{Z \rightarrow \nu\bar{\nu}}$ for to account for various effects such as pileup, prefire, soft b-tagging, b-tagging, top-tagging, and W-tagging.

6.3 Normalization Factor

Differences between the theoretical Z boson cross section and the physical cross section can cause normalization differences between simulated events and data. The Z to dilepton process (where the leptons are electrons or muons) is a good candidate to derive corrections for normalization differences. The Z to dilepton decay has as very clear signature in the CMS detector, and the Z production is the same as the Z to neutrinos case; only the decays are different. In the dilepton control region, the main signal process is Drell-Yan (DY), and the main background process is top quark-antiquark ($t\bar{t}$) production decaying to two charged leptons. Even though Z to charged leptons has as different branching ratio than Z to neutrinos (Table 6.1), this factor cancels in data over MC ratios (Eq. (6.3)).

$$\frac{N_{\text{data}}^{Z \rightarrow \nu\bar{\nu}}}{N_{\text{MC}}^{Z \rightarrow \nu\bar{\nu}}} = \frac{N_{\text{data}}^{Z \rightarrow \ell^+ \ell^-}}{N_{\text{MC}}^{Z \rightarrow \ell^+ \ell^-}} \quad (6.3)$$

Rearranging Eq. (6.3) to solve for the term that the method seeks to predict, $N_{\text{data}}^{Z \rightarrow \nu\bar{\nu}}$, gives

$$N_{\text{data}}^{Z \rightarrow \nu\bar{\nu}} = \left(\frac{N_{\text{data}}^{Z \rightarrow \ell^+ \ell^-}}{N_{\text{MC}}^{Z \rightarrow \ell^+ \ell^-}} \right) N_{\text{MC}}^{Z \rightarrow \nu\bar{\nu}}. \quad (6.4)$$

In Eq. (6.4), the $Z \rightarrow \ell^+ \ell^-$ data over MC ratio can be thought of as a normalization term that is applied to $Z \rightarrow \nu\bar{\nu}$ to correct the MC event count so that it matches the data event count for a given selection. However, $t\bar{t}$ and other processes producing two opposite-charge leptons are present in the dilepton control region as can be seen in the dilepton p_T (Fig. 6.1) and mass (Figs. 6.2 to 6.5) distributions. The $t\bar{t}$ contamination is larger for the selections that require at least one b-tagged jet because top quarks decay to bottom quarks. The $t\bar{t}$ background is addressed in a few ways:

- The dilepton p_T cut of $p_T > 200$ GeV is applied to removed $t\bar{t}$ events while keeping DY events (see Fig. 6.1).
- Two separate normalization factors are defined: R_Z for Z processes (such as DY) and R_T for background processes (such as $t\bar{t}$).

The factor R_Z is extracted from the dilepton control regions, simultaneously with a similar factor R_T that accounts for contamination from other processes such as $t\bar{t}$, by solving the matrix equation:

$$\begin{bmatrix} N_{\text{on-Z}}^{\text{Data}} \\ N_{\text{off-Z}}^{\text{Data}} \end{bmatrix} = \begin{bmatrix} N_{\text{on-Z}}^{Z \rightarrow LL} & N_{\text{on-Z}}^{\text{Other}} \\ N_{\text{off-Z}}^{Z \rightarrow LL} & N_{\text{off-Z}}^{\text{Other}} \end{bmatrix} \begin{bmatrix} R_Z \\ R_T \end{bmatrix} \quad (6.5)$$

where “on-Z” refers to the event yield within the Z mass window of $81 < M_{ll} < 101$ GeV and “off-Z” refers to the event yield outside of the Z mass window in the region of $50 < M_{ll} < 81$ GeV and $M_{ll} > 101$ GeV. Here “Data” on the left side of Eq. 6.5 is electron or muon triggered data. On the right hand side of Eq. 6.5, the MC

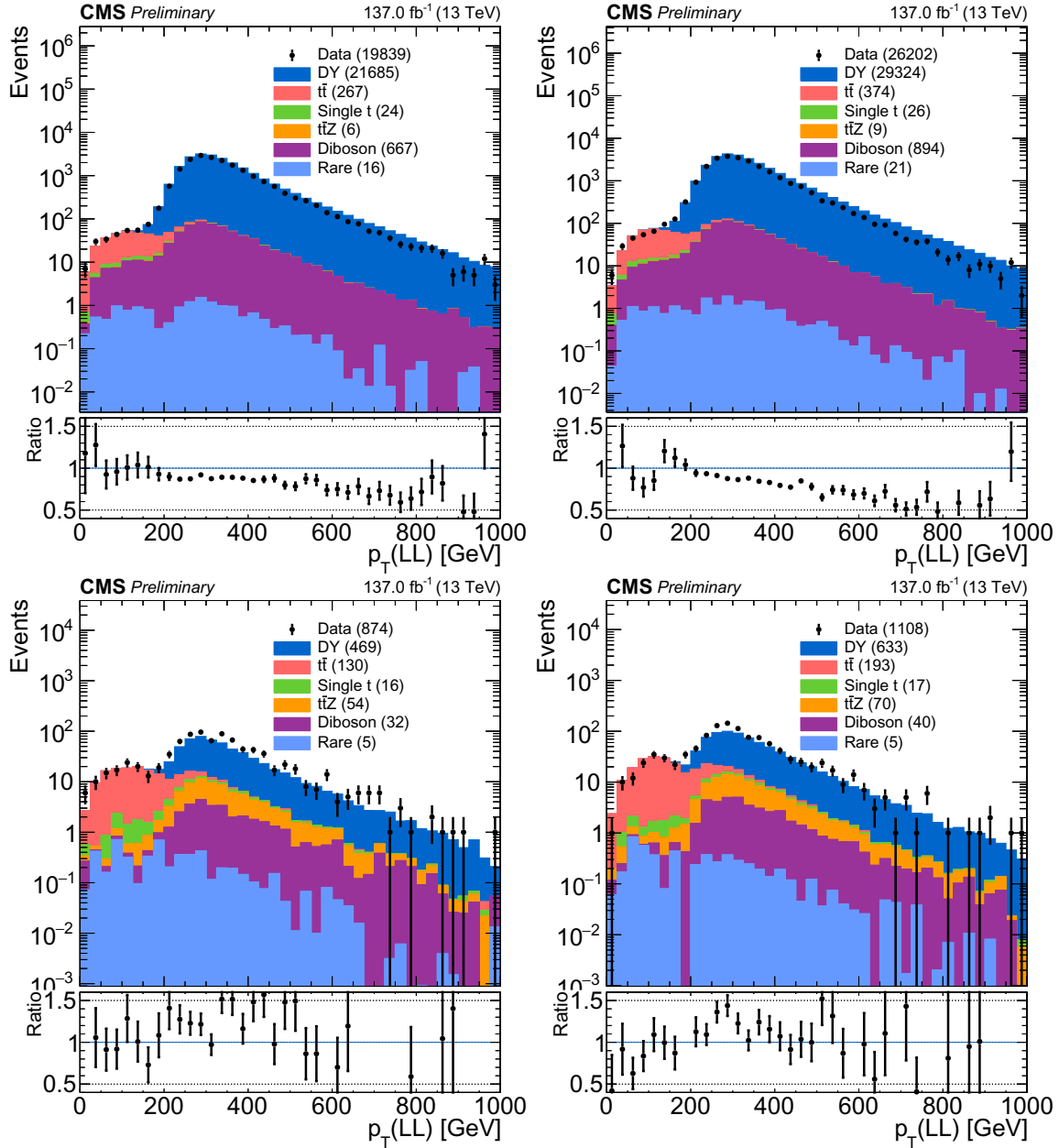


Figure 6.1: The dilepton p_T for the electron (left column) and muon (right column) control regions. The selection is low Δm baseline (top row) and high Δm baseline (bottom row) with the on-Z mass cut of $81 < M_{ll} < 101$ GeV applied. Based on the dilepton p_T distributions, the cut $p_T > 200$ GeV is chosen to reduce the $t\bar{t}$ background while removing very few DY events.

is divided into the categories $Z \rightarrow LL$, which is MC with a Z decaying to charged leptons, and “Other,” which is other MC producing dileptons. The MC samples in these two categories are:

- $Z \rightarrow LL$: DYJetsToLL, TTZToLLNuNu, WZTo3LNu, WZTo2L2Q, ZZTo2L2Nu, ZZTo2L2Q, ZZTo4L, WWZ, WZZ, ZZZ, WZG
- Other: TTbarSingleLepT, TTbarSingleLepTbar, TTbarDiLep, ST_s_lep, ST_t_top, ST_t_antitop, tZq_ll, ST_tWll, ST_tWnuunu, ST_tW_top_NoHad, ST_tW_antitop_NoHad, TTZToQQ, WZTo1L3Nu, WWTo4Q, WWTo2L2Nu, WWToLNuQQ, ZZTo2Q2Nu, TTWJetsToLNu, TTWJetsToQQ, TTGJets, WWW, WWG

To account for potential effects related to heavy flavor production, R_Z and R_T are measured independently for different N_b and N_{SV} requirements of low Δm and high Δm regions as shown in Table 6.2. Figures 6.2, 6.3, 6.4, and 6.5 show example M_{ll} distributions from which the R_Z and R_T factors are extracted. Some search bins have the requirement $N_b \geq 3$. However, there are not enough events in the dilepton control region passing $N_b \geq 3$ to provide a precise normalization value. For the search bins with $N_b \geq 3$, the value of R_Z obtained in the $N_b \geq 2$ region is used, which has an adequate number of events. Furthermore, some search bins require $N_b = 2$, and some require $N_b \geq 2$. In order to use statistically independent R_Z values, the R_Z value obtained with $N_b \geq 2$ is applied to the search bins with $N_b = 2$ and those with $N_b \geq 2$.

Furthermore, R_Z and R_T are calculated independently in the dielectron and dimuon channels. These two channels are statistically independent because for the dielectron selection, a muon veto is applied, and for the dimuon selection, an electron veto is applied. The values of R_Z and R_T are obtained by inverting the matrix in

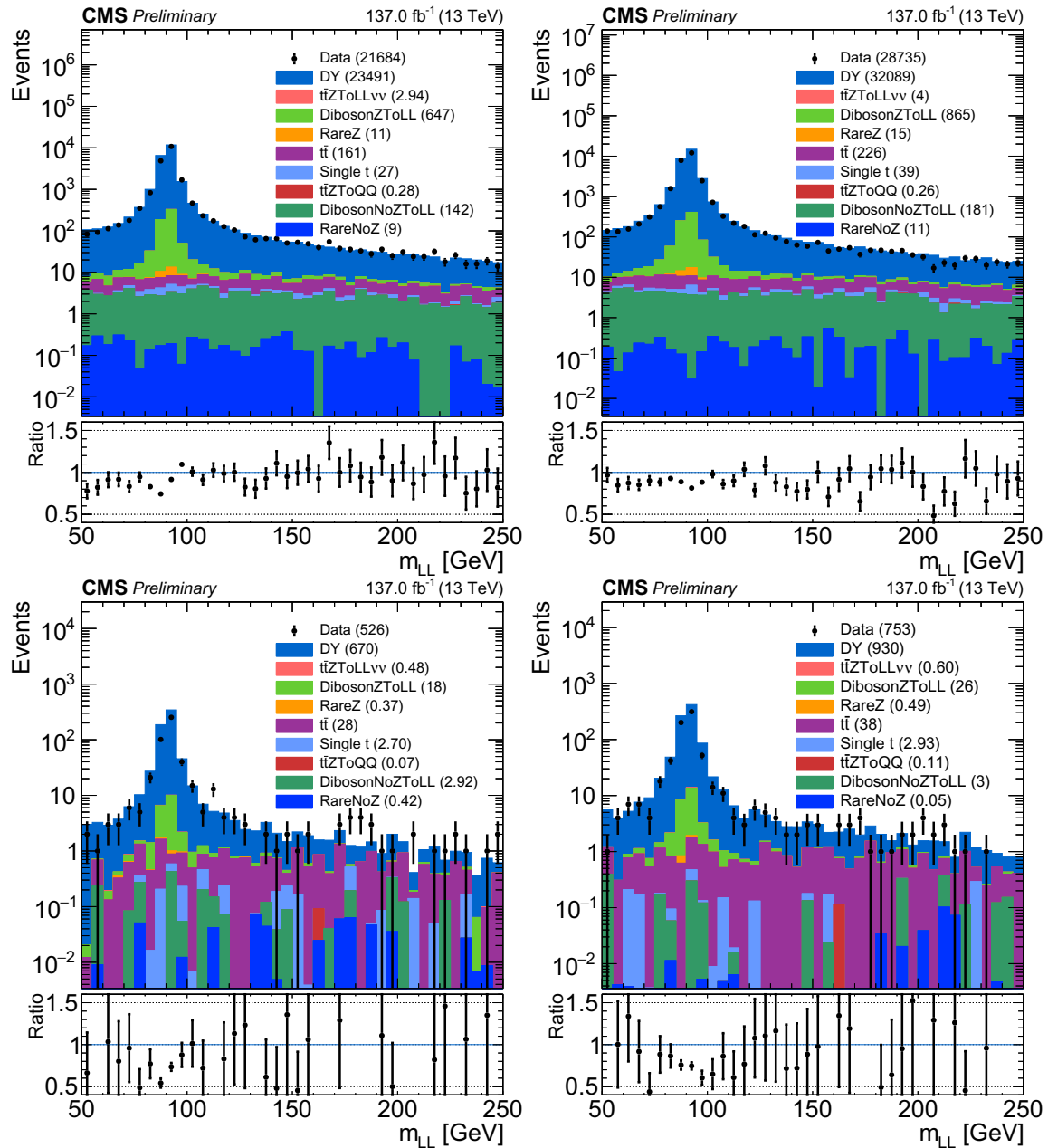


Figure 6.2: The dilepton mass for the electron (left column) and muon (right column) control regions for Run 2 with low Δm baseline applied. The additional selections are $N_b = 0$, $N_{SV} = 0$ (top row) and $N_b = 0$, $N_{SV} \geq 1$ (bottom row). The stacked MC has the $Z \rightarrow LL$ processes on top (from DY to RareZ) and the other processes on the bottom (from $t\bar{t}$ to RareNoZ).

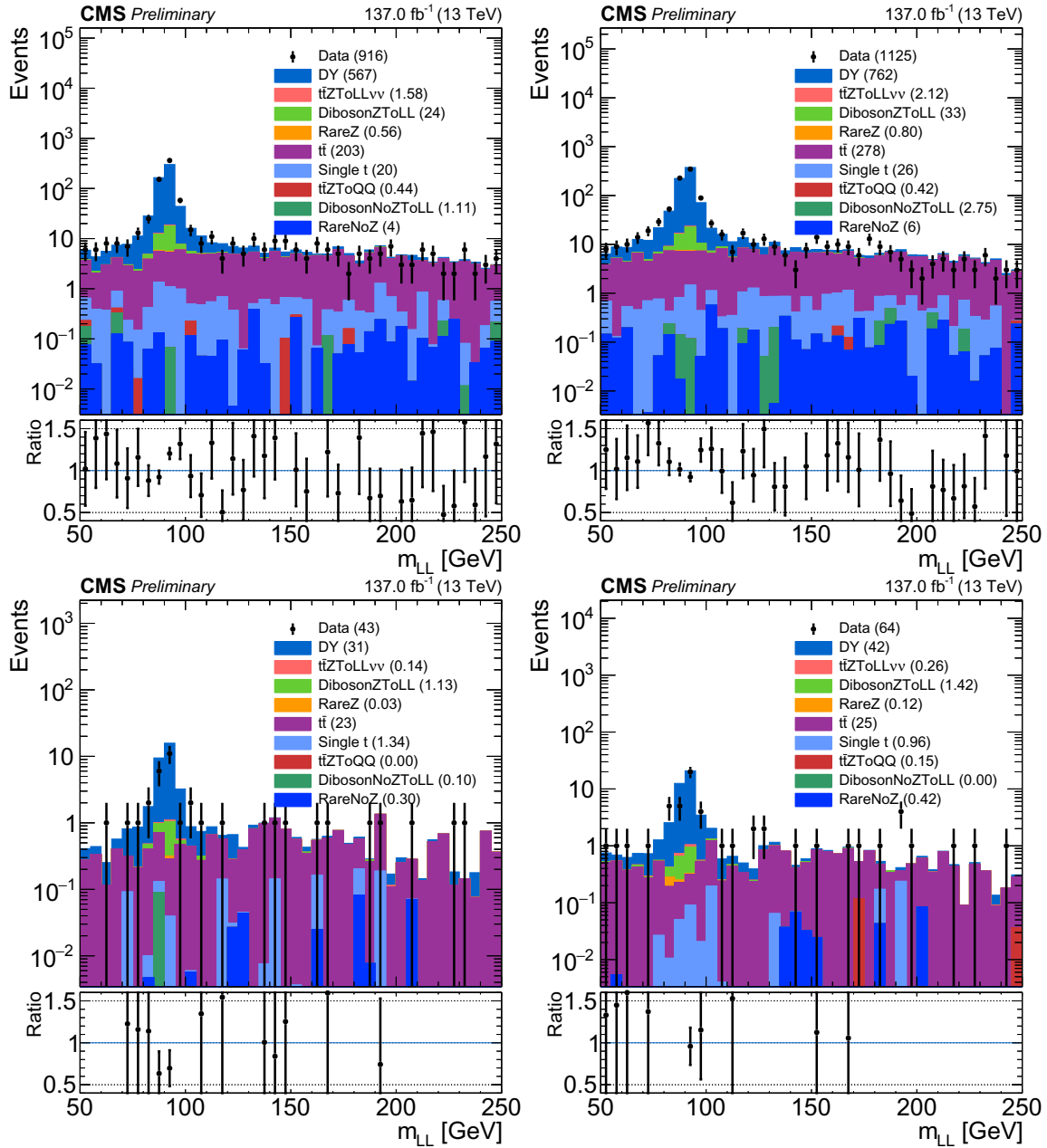


Figure 6.3: The dilepton mass for the electron (left column) and muon (right column) control regions for Run 2 with low Δm baseline applied. The additional selections are $N_b = 1$, $N_{SV} = 0$ (top row) and $N_b = 1$, $N_{SV} \geq 1$ (bottom row). The stacked MC has the $Z \rightarrow LL$ processes on top (from DY to RareZ) and the other processes on the bottom (from $t\bar{t}$ to RareNoZ).

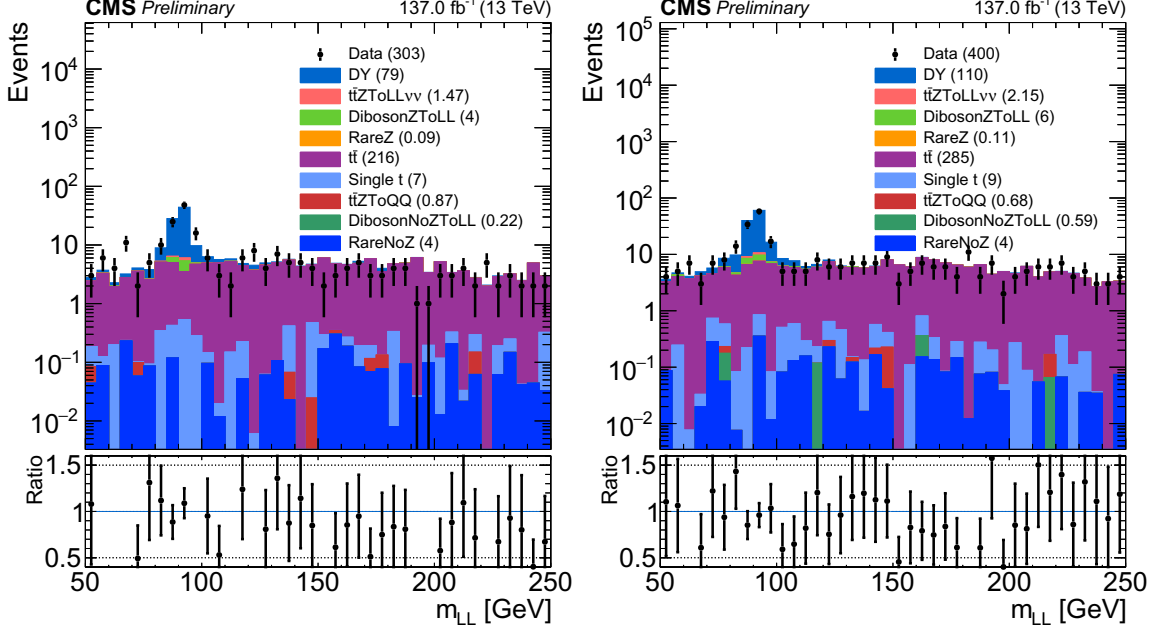


Figure 6.4: The dilepton mass for the electron (left) and muon (right) control regions for Run 2 with low Δm baseline and $N_b \geq 2$ applied. The stacked MC has the $Z \rightarrow LL$ processes on top (from DY to RareZ) and the other processes on the bottom (from $t\bar{t}$ to RareNoZ).

Eq. 6.5. The statistical uncertainties for R_Z and R_T are derived by propagating the statistical uncertainties in MC and data throughout the calculation in Eq. 6.5. The R_Z value used for the Z invisible prediction is the weighted average of the dielectron normalization R_Z^{ee} and the dimuon normalization $R_Z^{\mu\mu}$. The equation for the weighted average is

$$\langle x \rangle = \frac{\sum w_i x_i}{\sum w_i}, \quad (6.6)$$

and the weights are set to $w_i = 1/\sigma_i^2$, where σ_i are the statistical uncertainties on R_Z^{ee} and $R_Z^{\mu\mu}$. Then the R_Z weighted average is

$$\langle R_Z \rangle = \frac{R_Z^{ee}/\sigma_{ee}^2 + R_Z^{\mu\mu}/\sigma_{\mu\mu}^2}{1/\sigma_{ee}^2 + 1/\sigma_{\mu\mu}^2}. \quad (6.7)$$

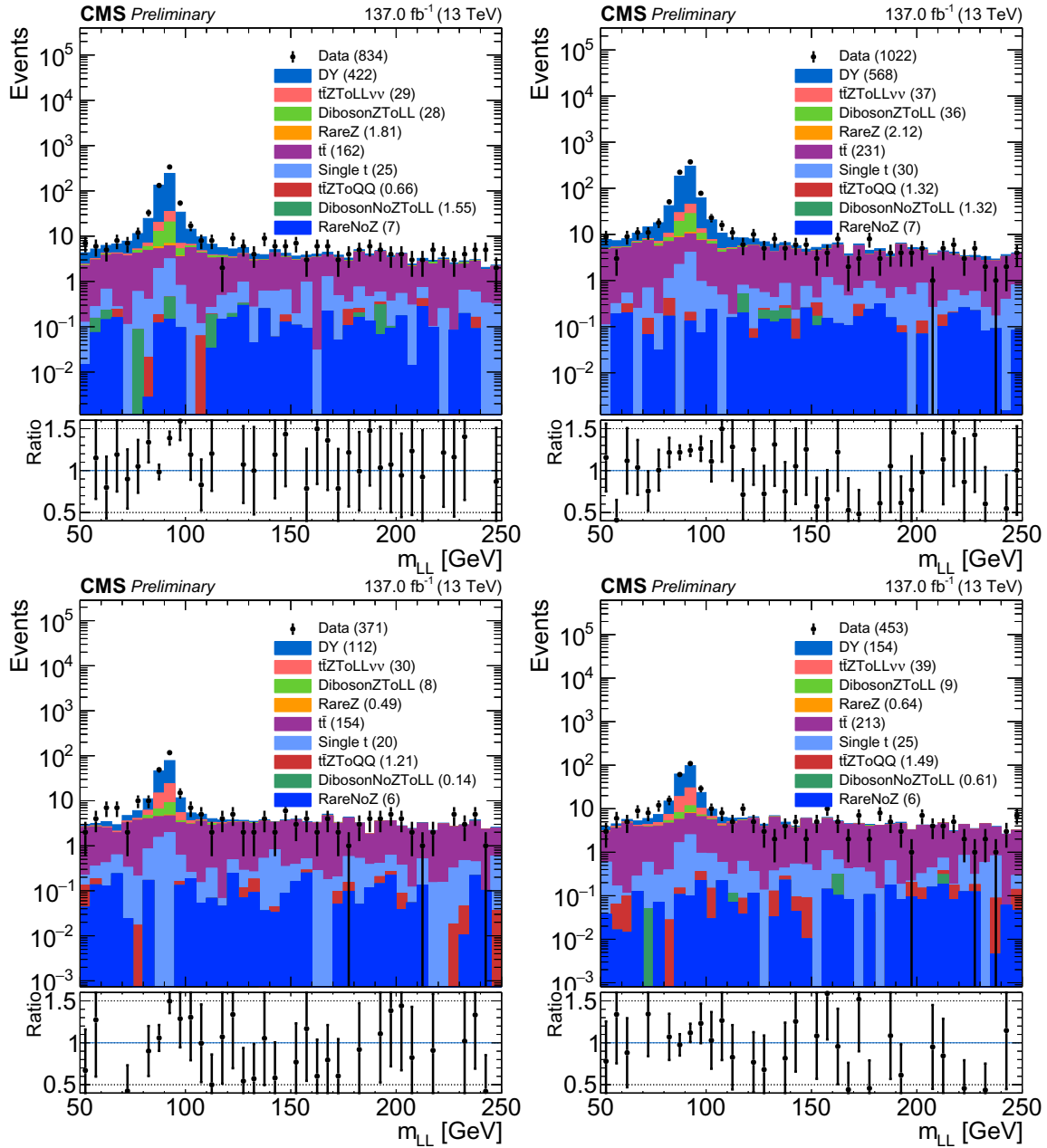


Figure 6.5: The dilepton mass for the electron (left column) and muon (right column) control regions for Run 2 with high Δm baseline applied. The additional selections are $N_b = 1$ (top row) and $N_b \geq 2$ (bottom row). The stacked MC has the $Z \rightarrow LL$ processes on top (from DY to RareZ) and the other processes on the bottom (from $t\bar{t}$ to RareNoZ).

Table 6.2: The normalization values R_Z calculated for various N_b and N_{SV} selections in low and high Δm . The R_Z factors from the dielectron and dimuon control regions for the full Run 2 data set are shown, as well as the weighted average $\langle R_Z \rangle$, all with statistical uncertainties. An additional systematic uncertainty is obtained to account for differences in R_Z for different eras as shown in Figs. 6.13–6.15, and the full uncertainty is listed in the last column. The R_Z value obtained with $N_b \geq 2$ is used for search bins that require $N_b = 2$, $N_b \geq 2$, and $N_b \geq 3$.

N_b	N_{SV}	R_Z^{ee}	$R_Z^{\mu\mu}$	$\langle R_Z \rangle$ (with stat. unc.)	$\langle R_Z \rangle$ (with full unc.)
low Δm regions					
0	0	0.870 ± 0.028	0.849 ± 0.024	0.858 ± 0.019	0.858 ± 0.063
0	≥ 1	0.679 ± 0.078	0.737 ± 0.077	0.709 ± 0.055	0.709 ± 0.072
1	0	1.105 ± 0.065	0.991 ± 0.052	1.036 ± 0.041	1.036 ± 0.041
1	≥ 1	0.683 ± 0.188	0.857 ± 0.187	0.770 ± 0.133	0.770 ± 0.133
≥ 2	–	1.108 ± 0.151	1.007 ± 0.125	1.048 ± 0.097	1.048 ± 0.097
high Δm regions					
1	–	1.283 ± 0.078	1.252 ± 0.066	1.265 ± 0.051	1.265 ± 0.142
≥ 2	–	1.359 ± 0.125	1.103 ± 0.099	1.202 ± 0.077	1.202 ± 0.087

Since R_Z^{ee} and $R_Z^{\mu\mu}$ are statistically independent, the statistical uncertainty of the weighted average $\langle R_Z \rangle$ is obtained through applying uncorrelated uncertainty propagation in Eq. 6.7. The values and statistical uncertainties of R_Z^{ee} , $R_Z^{\mu\mu}$, $\langle R_Z \rangle$ are shown in Table 6.2.

6.4 Shape Factor

The photon control region has more events and better statistics than the lepton control regions due to the large photon cross section and the small Z to dielectron and Z to dimuon branching ratios (Table 6.1). The Z boson kinematics in the Z invisible background process are comparable with photon kinematics at large momentum that is well above the mass of the Z boson. The photon control region is used to estimate a shape correction factor in control region bins which map to the search bins and

do not bin in the number of top quarks or W bosons. Removing top quark and W boson binning reduces the number of control region bins and improves statistics. Mismodeling for top quark and W boson tagging is corrected by dedicated scale factors which are applied to the $Z \rightarrow \nu\bar{\nu}$ simulation.

In the control region, one photon is selected with $p_T > 220$ GeV and $|\eta| < 1.4442$ or $1.5660 < |\eta| < 2.5$. The photon p_T cut is chosen based on the photon trigger efficiency measurement from Section 5.3.1. The photon η cuts are defined such that the photon will be contained within the ECAL barrel or endcap and will not be in the gap that exists between them. The photon must pass the medium photon ID. Any hadronic jet that is matched to the photon is removed from the jet collection so that matching jets are not used to calculate analysis variables (H_T , N_j , etc.). Similarly to the lepton jet cleaning applied in the dilepton control region, AK4 (AK8) jets with $\Delta R < 0.2$ ($\Delta R < 0.4$) compared to a photon are considered matched. In addition, the selected photon is treated as p_T^{miss} to mimic the $Z \rightarrow \nu\bar{\nu}$ decay. The photon four-vector is added to the p_T^{miss} from the event, and then the transverse component of the result gives the modified $p_T^{\text{miss}(\gamma)}$. The selection $p_T^{\text{miss}} < 250$ GeV is placed on the original p_T^{miss} from the event to make the photon control region orthogonal to the search region.

The detector reconstructed photon (reco photon for short) selected in the single photon control region can come from various sources. The following photon categories are defined in order to describe the different processes that can produce reco photons passing the photon selection. Generator level (gen level for short) information from the simulated events is used to differentiate the photon categories. For gen-reco photon matching, the requirements are $\Delta R(\text{gen photon}, \text{reco photon}) < 0.1$

and $0.5 < p_{\text{T}}^{\text{reco}}/p_{\text{T}}^{\text{gen}} < 2.0$ such that a gen and reco photon are matched if they have a similar direction and momentum. The shorthand $\Delta R_{\gamma p}$ is used to represent $\Delta R(\text{gen photon, gen parton})$. The photon categories are direct, fragmentation (parton-to-photon fragmentation), nonprompt (photons from hadron decays), and fake, and they are defined by the following requirements:

- Direct
 - * gen matched to prompt status 1 gen photon
 - * $\Delta R_{\gamma p} > 0.4$ for all prompt status 23 gen partons
- Fragmentation
 - * gen matched to prompt status 1 gen photon
 - * $\Delta R_{\gamma p} < 0.4$ for at least one prompt status 23 gen parton
- Nonprompt
 - * gen matched to nonprompt status 1 gen photon
- Fake
 - * not gen matched to any status 1 gen photon

Both $\gamma + \text{jets}$ and QCD MC are considered for the photon control region. For the sake of efficient computing resource usage, the MADGRAPH $\gamma + \text{jets}$ sample has the requirement $\Delta R_{\gamma p} > 0.4$ on prompt generator level photons compared to all generator level hard partons. The QCD MC also has events with prompt-photons in this phase space. In order to avoid double counting in this phase space, QCD events are rejected if they have at least one generator level photon that is prompt, matched to the selected reco photon passing the photon selection, and passes the $\Delta R_{\gamma p} > 0.4$ requirement. This QCD event veto is referred to as the “QCD overlap cut.” For the QCD overlap cut, generated photons are selected with PDG ID 22, PYTHIA status 1 (stable), and

status flag 1 (prompt), and generated partons are selected with PDG $\pm 1-6$ (quarks), 9 or 21 (gluons), PYTHIA status 23 (outgoing from hardest subprocess), and status flag 1 (prompt).

Data and simulation in the photon control region are shown as a function of $p_T^{\text{miss}(\gamma)}$ (Fig. 6.6) and H_T (Fig. 6.7) with QCD separated into the various photon categories defined above. The effect of potential mismodeling of fragmentation, non-prompt, and fake photons can be measured. To do this, each of these contributions is independently varied by $\pm 50\%$ to represent a large amount of mismodeling. Then the shape factor is recalculated and compared to the nominal shape factor. The results are shown in Figs. 6.8 and 6.9. The photon control region is dominated by $\gamma + \text{jets}$ events, and the fragmentation, nonprompt, and fake photons from QCD have only a small contribution to the shape factor. When the different QCD photon categories are varied by $\pm 50\%$, the change in the shape factor is small (1–5%). Therefore no dedicated correction factors or additional uncertainties are required regarding different photon categories. For the shape factor used for the $Z \rightarrow \nu\bar{\nu}$ prediction, QCD is not separated into different photon categories.

The shape factors S_γ^{low} and S_γ^{high} for low Δm and high Δm regions are defined by

$$S_\gamma^{\text{low}} \left(N_j, N_b, N_{\text{SV}}, p_T^{\text{ISR}}, p_T^{\text{b}}, p_T^{\text{miss}(\gamma)} \right) = \frac{N^{\text{data}} \left(N_j, N_b, N_{\text{SV}}, p_T^{\text{ISR}}, p_T^{\text{b}}, p_T^{\text{miss}(\gamma)} \right)}{Q \cdot N^{\text{MC}} \left(N_j, N_b, N_{\text{SV}}, p_T^{\text{ISR}}, p_T^{\text{b}}, p_T^{\text{miss}(\gamma)} \right)} \quad (6.8)$$

$$S_\gamma^{\text{high}} \left(N_j, N_b, m_T^{\text{b}}, H_T, p_T^{\text{miss}(\gamma)} \right) = \frac{N^{\text{data}} \left(N_j, N_b, m_T^{\text{b}}, H_T, p_T^{\text{miss}(\gamma)} \right)}{Q \cdot N^{\text{MC}} \left(N_j, N_b, m_T^{\text{b}}, H_T, p_T^{\text{miss}(\gamma)} \right)} \quad (6.9)$$

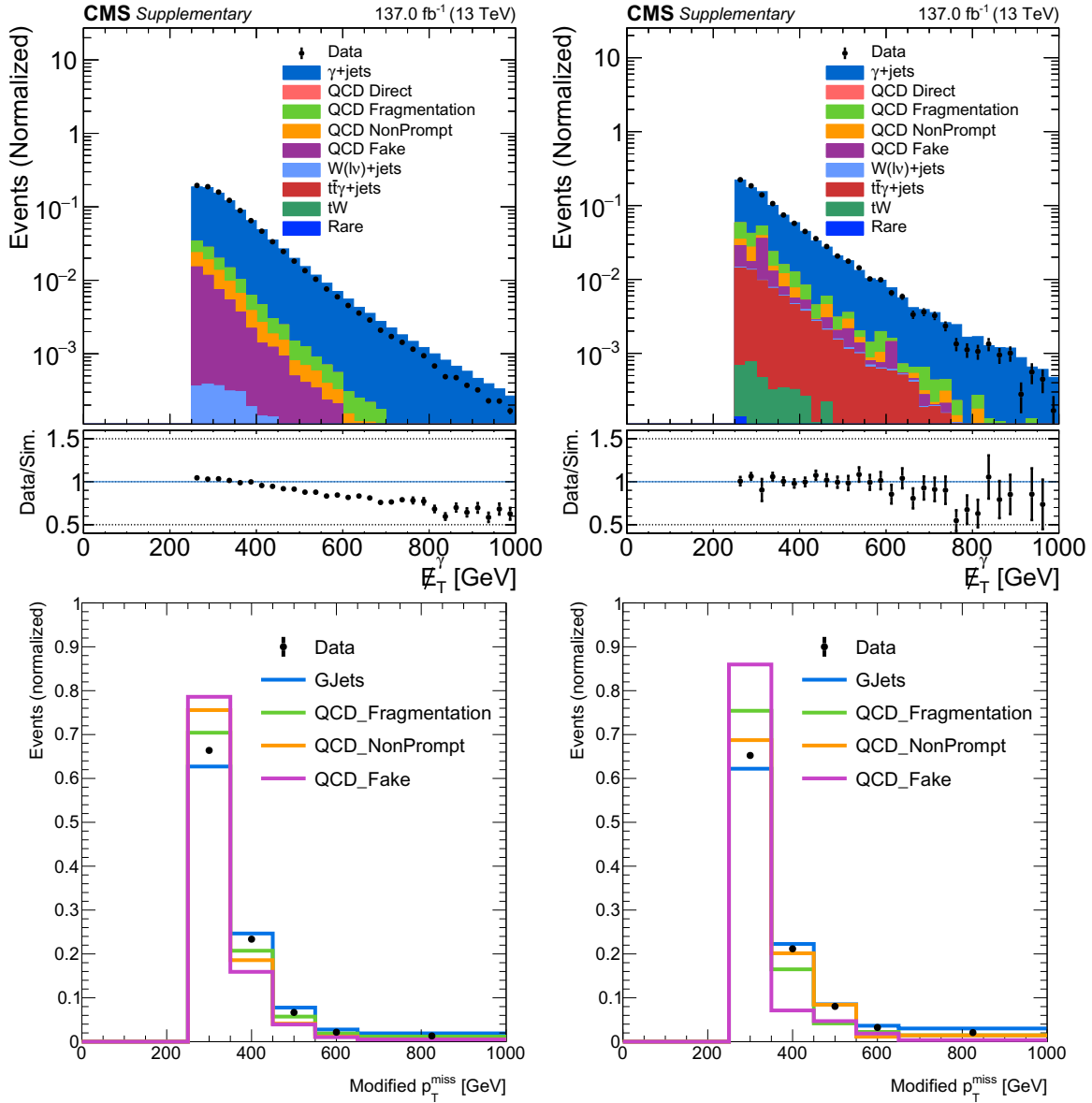


Figure 6.6: Modified $p_T^{\text{miss}(\gamma)}$ distributions in the photon control region with low Δm (left) and high Δm (right) baseline selections applied and the QCD simulation separated by photon category. In the data simulation comparisons (top), the data and the total MC stack are normalized to unit area. The shape comparisons (bottom) have each distribution normalized to unit area.

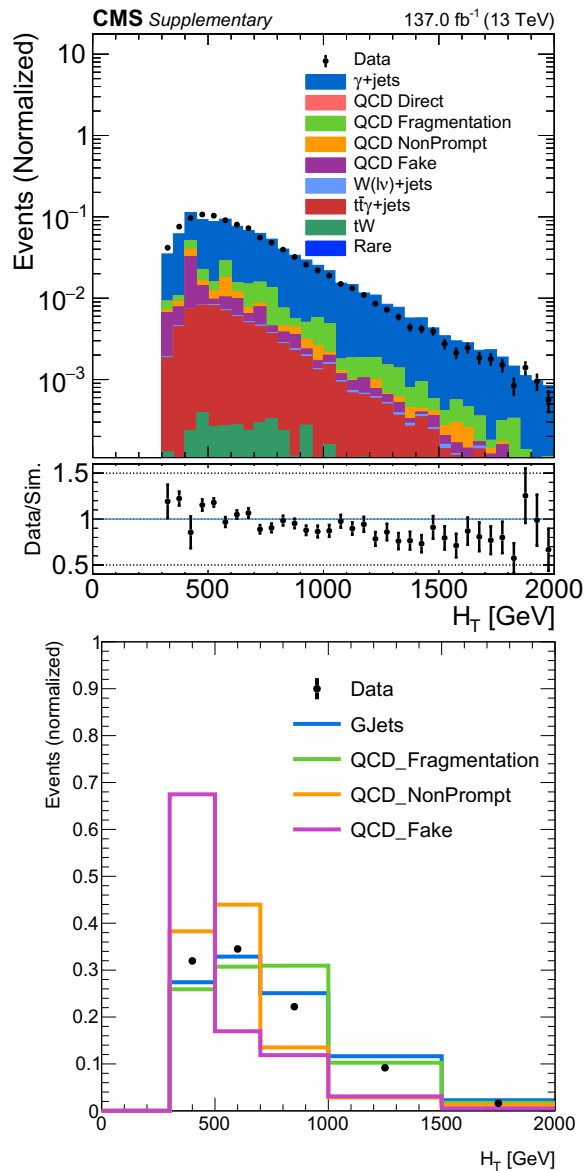


Figure 6.7: H_T distributions in the photon control region with the high Δm baseline selection applied and the QCD simulation separated by photon category. In the data simulation comparison (top), the data and the total MC stack are normalized to unit area. The shape comparison (bottom) has each distribution normalized to unit area.

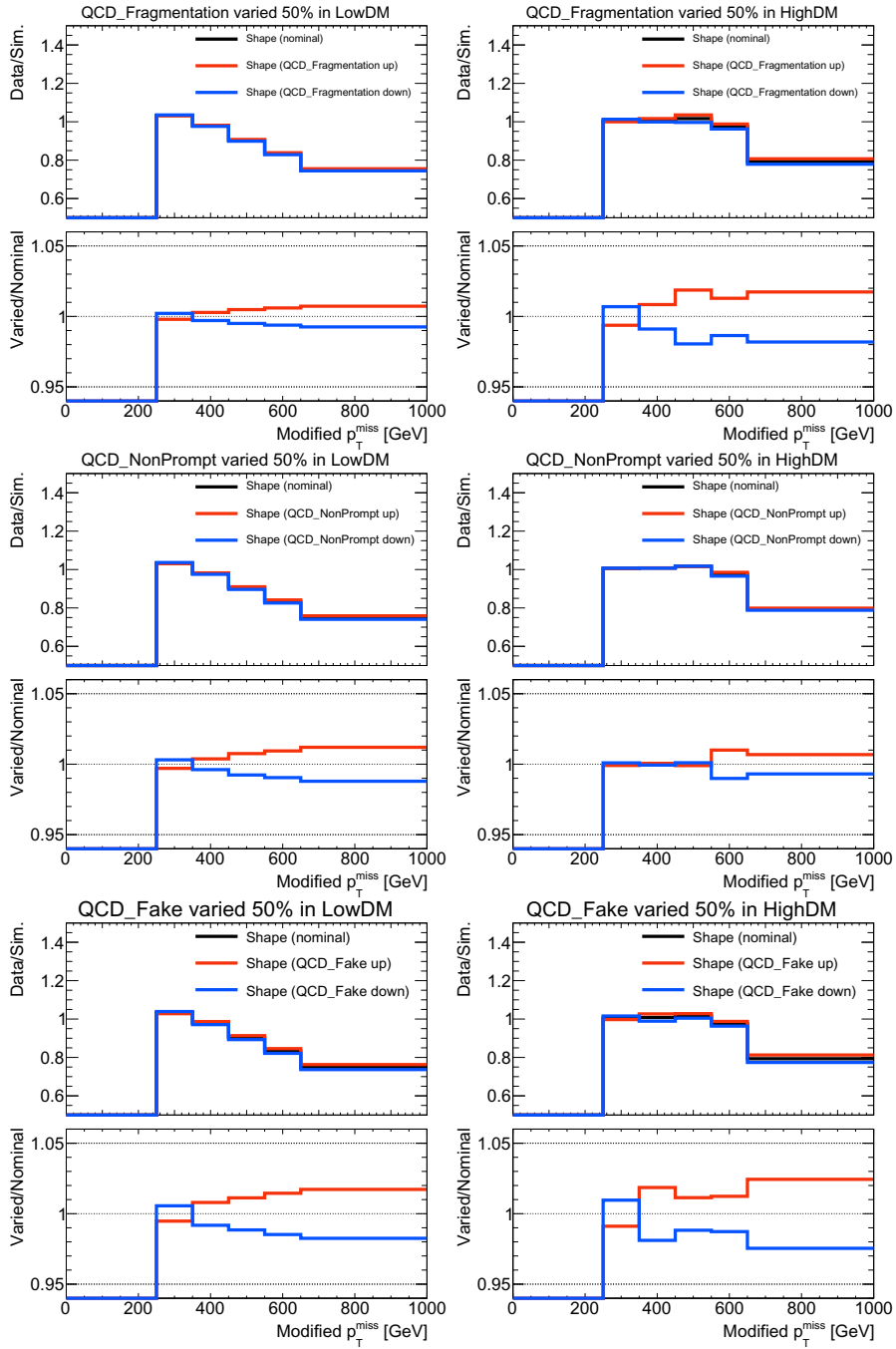


Figure 6.8: Modified $p_T^{\text{miss}(\gamma)}$ shape (data over simulation) distributions in the photon control region with low Δm (left) and high Δm (right) baseline selections applied. The nominal shape factor is compared to shape factors recalculated after QCD components are varied by $\pm 50\%$. In addition, the ratios between the varied shape factors and the nominal shape factor are shown. This is done for fragmentation photons (top two rows), nonprompt photons (middle two rows), and fake photons (bottom two rows).

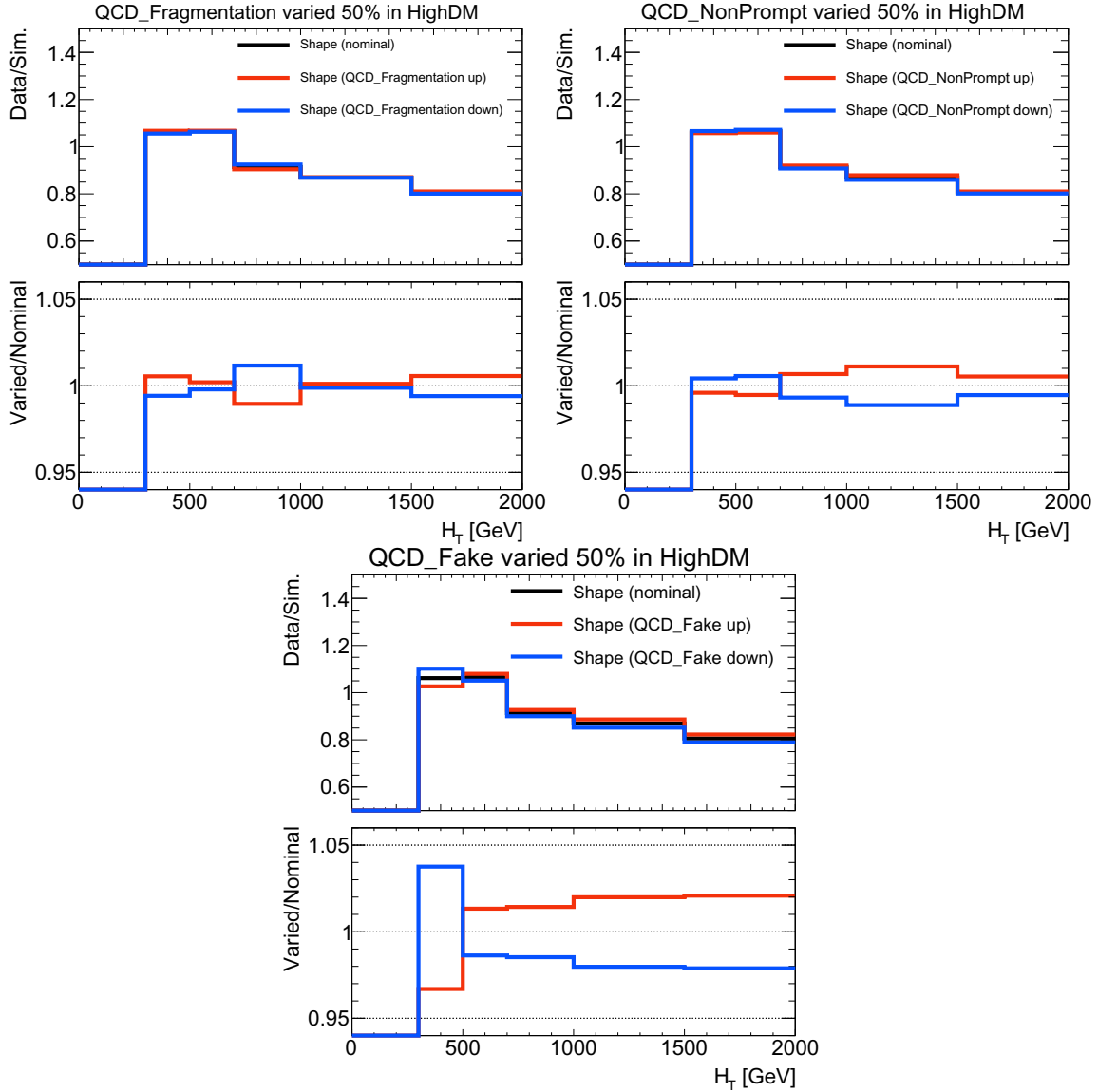


Figure 6.9: H_T shape (data over simulation) distributions in the photon control region with the high Δm baseline selection applied. The nominal shape factor is compared to shape factors recalculated after QCD components are varied by $\pm 50\%$. In addition, the ratios between the varied shape factors and the nominal shape factor are shown. This is done for fragmentation photons (top left), nonprompt photons (top right), and fake photons (bottom).

where Q is a data/MC normalization term as a function of N_b and N_j given by

$$Q(N_b, N_j) = \frac{N^{\text{data}}(N_b, N_j)}{N^{\text{MC}}(N_b, N_j)}. \quad (6.10)$$

There is an implied integration over search bin variables not listed in Eqs. (6.8), (6.9), and (6.10); for example the number of top quarks and W bosons are integrated over when calculating S_γ^{high} . The shape factor used for the final predictions is calculated in control region bins that have no top quark or W boson requirements in high Δm to increase the number of events per control region bin and improve statistical precision. Dedicated data-driven top quark and W boson tagging scale factors are applied to the $Z \rightarrow \nu\bar{\nu}$ simulation to correct for top quark and W boson related mismodeling.

Figures 6.10, 6.11 and 6.12 show some examples of data and simulation comparison as a function of $p_T^{\text{miss}(\gamma)}$ with low Δm and high Δm baseline selections, as well as different N_b and N_j requirements. There is a clear trend in the data over simulation ratio for certain selections as seen in Fig. 6.10. The shape factor rectifies this disagreement between data and simulation by applying the data over simulation ratios from the control region to the search region.

6.5 Combining Eras

The CMS Run 2 data set used for this analysis includes three years of data-taking, 2016, 2017, and 2018, and each year will also be referred to as an era or run period. For the Z invisible background prediction, the normalization and shape factors in different eras are examined to determine if there are any important differences that need to be accounted for. The era dependence of measured R_Z values is shown in Figs. 6.13 to 6.15. The R_Z factor is generally stable over different run periods, so the R_Z factor from the full Run 2 data period is used for the background prediction. For

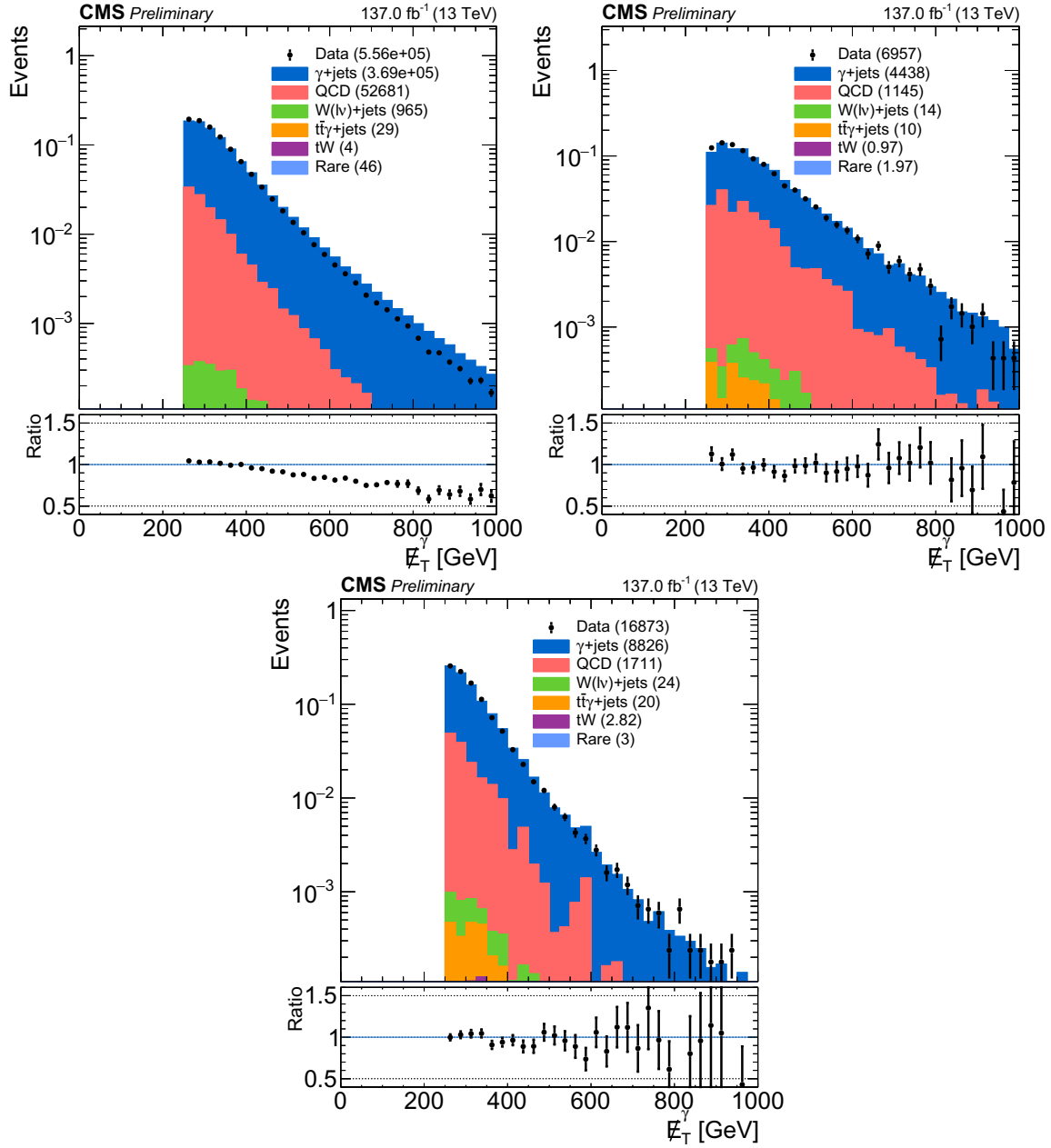


Figure 6.10: The modified $p_T^{\text{miss}(\gamma)}$ for the photon control region for Run 2 with low Δm baseline applied. The additional selections are $N_b = 0, N_j \leq 5$ (top left), $N_b = 0, N_j \geq 6$ (top right), and $N_b = 1$ (bottom). Both data and total MC are normalized to unit area in order to compare the shapes of the data and MC $p_T^{\text{miss}(\gamma)}$ distributions.

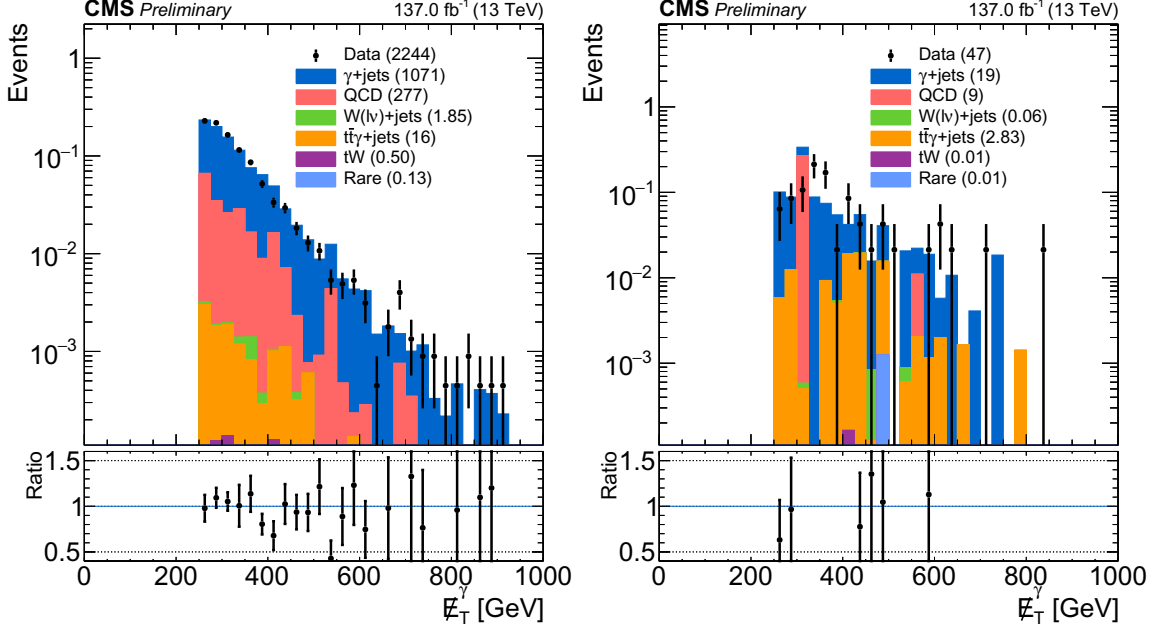


Figure 6.11: The modified $p_T^{\text{miss}(\gamma)}$ for the photon control region for Run 2 with low Δm baseline applied. The additional selections are $N_b \geq 2$ (left) and $N_b \geq 2, N_j \geq 7$ (right). Both data and total MC are normalized to unit area in order to compare the shapes of the data and MC $p_T^{\text{miss}(\gamma)}$ distributions.

some regions where the measurement has small statistical uncertainties (e.g. low Δm , $N_b = 0$, and $N_{SV} = 0$), variations of R_Z are larger than statistical fluctuations, and additional systematic uncertainties are assigned to cover the variations (Section 6.6).

The era dependence of measured S_γ distributions is shown in Figs. 6.16 to 6.18. The distributions are generally stable over different run periods, so a set of S_γ shape correction factors from the full Run 2 data period is used for the background prediction.

6.6 Uncertainties

Several sources of uncertainty are considered in the estimation of the $Z \rightarrow \nu\bar{\nu}$ background including the statistical uncertainties in the photon control region data (up to 100%) and simulated event samples (up to 110%), the photon identification

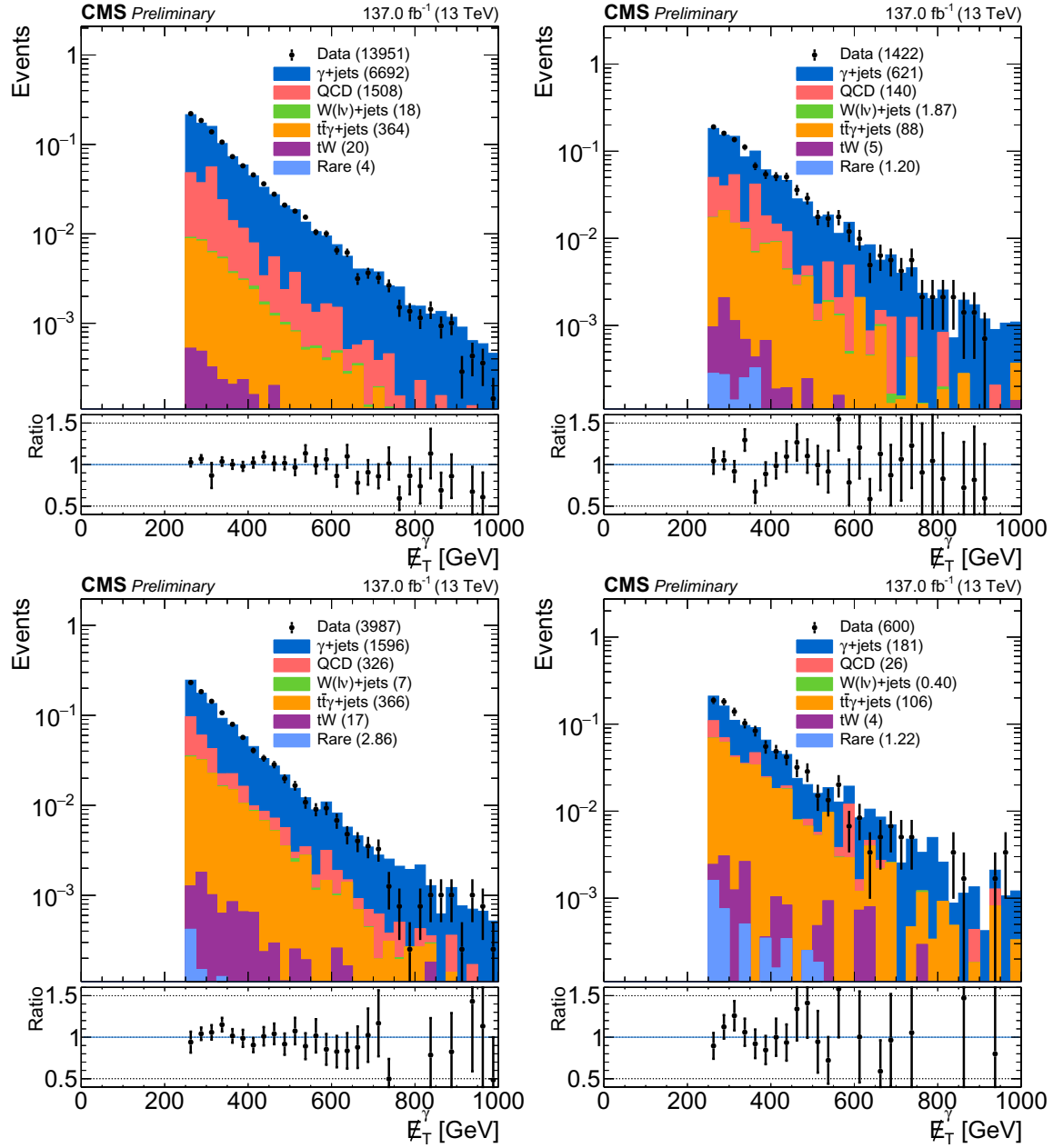


Figure 6.12: The modified $p_T^{\text{miss}(\gamma)}$ for the photon control region for Run 2 with high Δm baseline applied. The additional selections are $N_b = 1$ (top row), $N_b \geq 2$ (bottom row), and $N_j \geq 7$ (right column). Both data and total MC are normalized to unit area in order to compare the shapes of the data and MC $p_T^{\text{miss}(\gamma)}$ distributions.

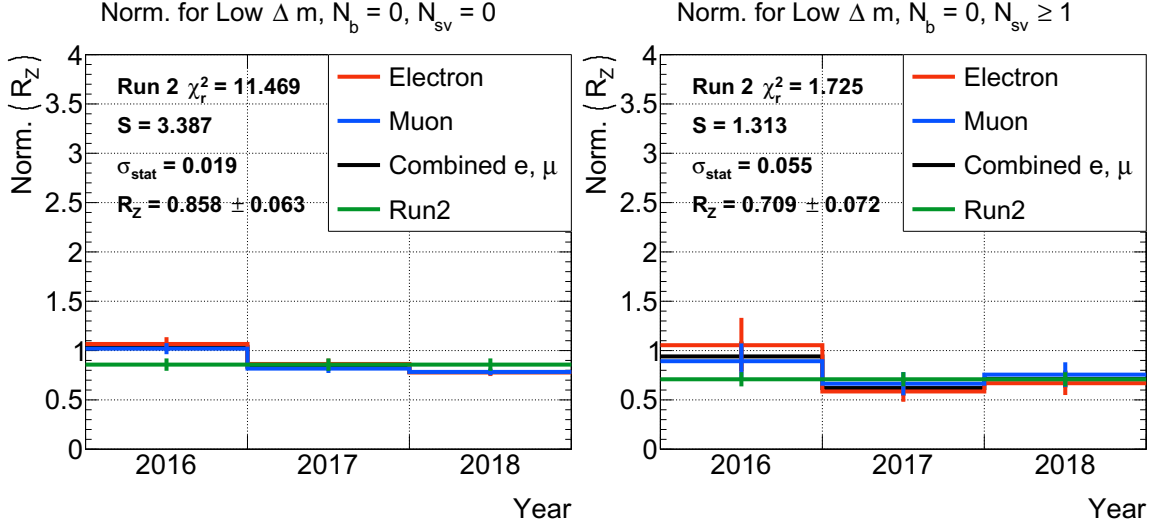


Figure 6.13: Normalization factors, R_Z , for different Run 2 years for events passing low Δm baseline. The additional requirements are $N_b = 0$, as well as $N_{SV} = 0$ (left) and $N_{SV} \geq 1$ (right).

efficiencies (5–13%), the photon trigger efficiency (up to 2%), the pileup reweighting (up to 40%), the jet energy scale corrections (up to 41%), the p_T^{miss} energy resolution (up to 35%), the PDF uncertainty (up to 59%), the b tagging efficiencies for heavy-flavor jets (up to 5%) and misidentification rates for light jets (up to 16%), the soft-b tagging efficiencies (up to 1%), and the top quark and W boson misidentification rates (up to 34%). In addition, two more sources of systematic uncertainty for the $Z \rightarrow \nu\bar{\nu}$ prediction are described below.

First, an additional systematic uncertainty is applied to the normalization factor, R_Z , to cover differences seen between different run eras which are not covered by the statistical uncertainties of the factor as seen in Figs. 6.13 to 6.15. The central value of R_Z is derived by summing the three eras discussed in Section 6.5. The additional uncertainty is then estimated by taking the $S = \chi^2/\text{NDOF}$ between the central value and the three individual eras and scaling the statistical uncertainty on the central value by \sqrt{S} . This method is based on the approach described in Sec. 5.2.2

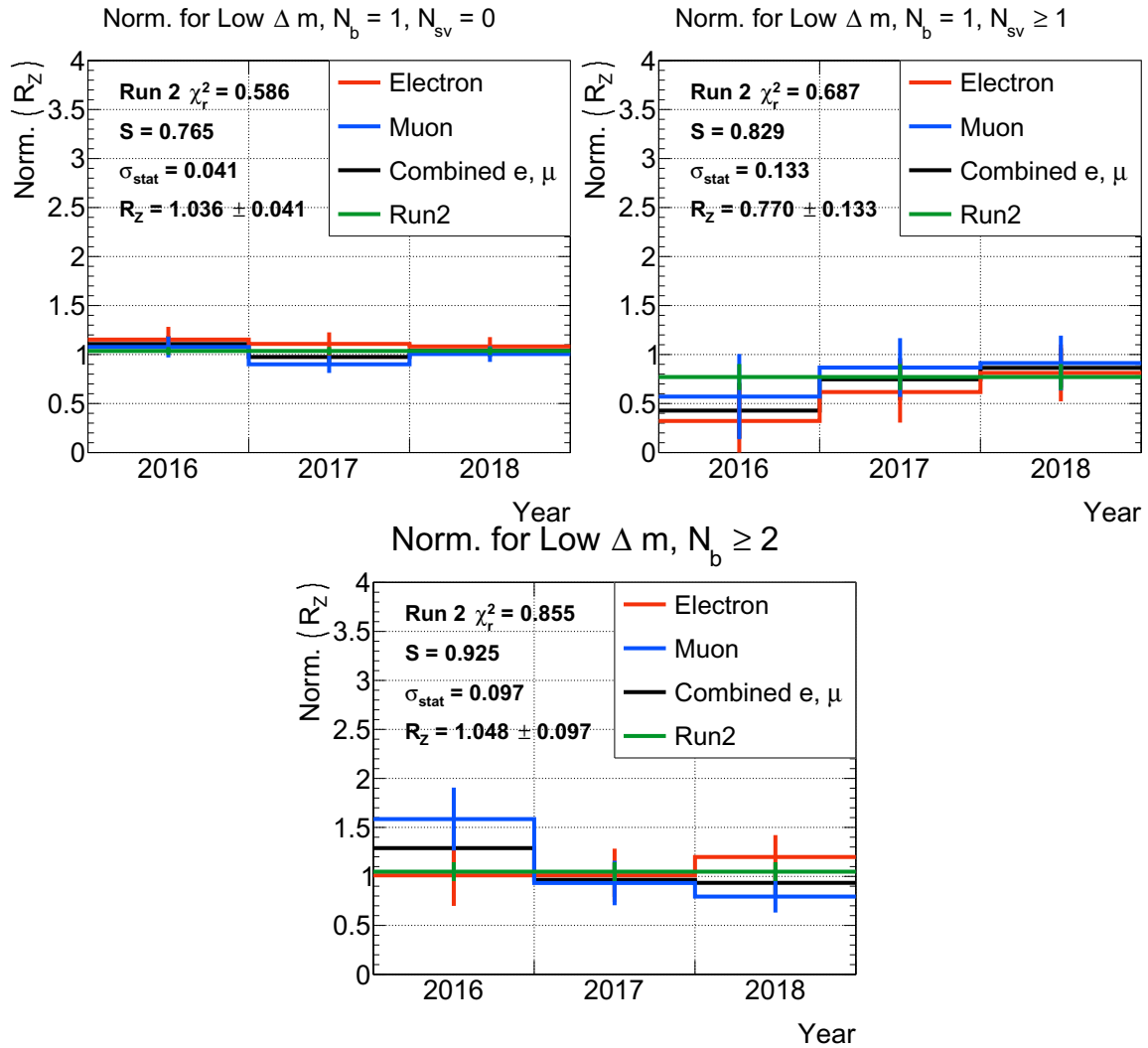


Figure 6.14: Normalization factors, R_Z , for different Run 2 years for events passing low Δm baseline. The additional requirements are $N_b = 1$ and $N_{sv} = 0$ (top left), $N_b = 1$ and $N_{sv} \geq 1$ (top right), and $N_b \geq 2$ (bottom).

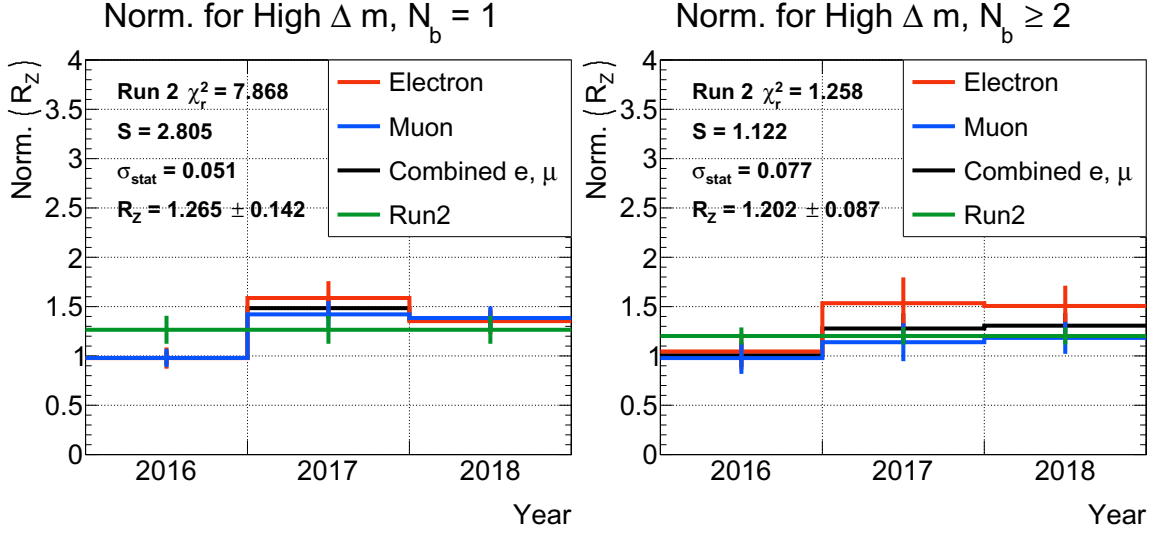


Figure 6.15: Normalization factors, R_Z , for different Run 2 years for events passing high Δm baseline. The additional requirements are $N_b = 1$ (left) and $N_b \geq 2$ (right).

of Ref. [1]. The R_Z normalization factor uncertainties are 4–14% and are propagated to the $Z \rightarrow \nu\bar{\nu}$ prediction in the search regions.

The second additional $Z \rightarrow \nu\bar{\nu}$ systematic is designed to cover any residual differences between the modeling of Z +jets events and γ +jets events. This systematic is derived by looking at the double ratio between data and simulation in the dilepton control region and photon control region as a function of p_T^{miss} , shown in Fig. 6.19. In order to make the best use of the low statistics in the dilepton control region, the inclusive low Δm and high Δm selections are used for this comparison. Any deviation from unity is considered to be due to modeling differences between the Z +jets and γ +jets processes in the control regions. The larger of either the absolute deviation of the ratio from unity or the statistical uncertainty (up to 16%) is assigned as a systematic uncertainty for the $Z \rightarrow \nu\bar{\nu}$ prediction as a function of modified p_T^{miss} .

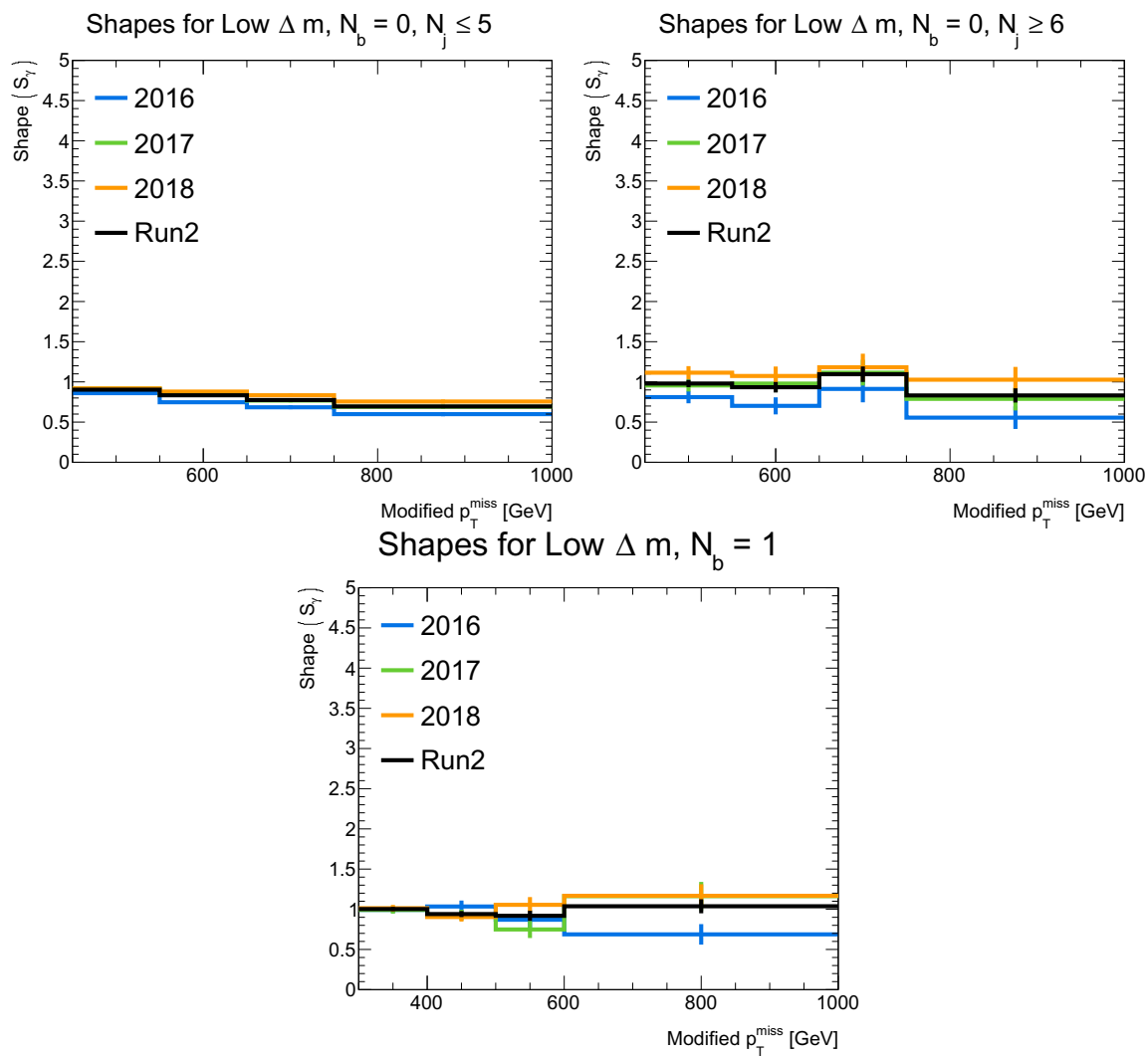


Figure 6.16: Shape factors, S_γ , for different Run 2 eras for events passing the low Δm baseline and with different N_b and N_j selections.

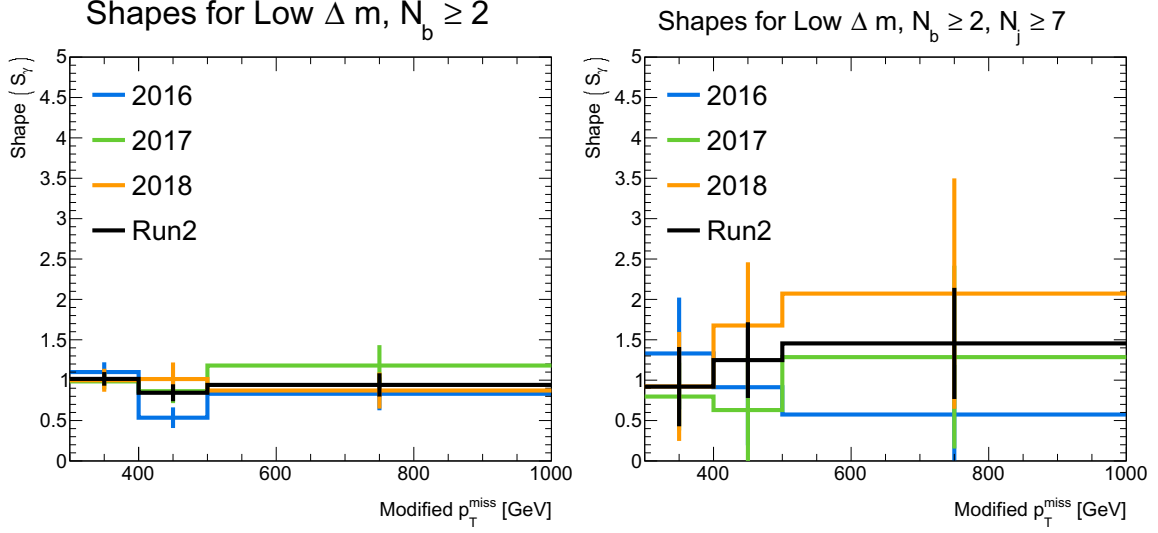


Figure 6.17: Shape factors, S_γ , for different Run 2 eras for events passing the low Δm baseline and with different N_b and N_j selections.

6.7 Results

The Z invisible predictions for Run 2 are shown in the validation bins (Fig. 6.20) and search bins (Fig. 6.21). The normalization factor R_Z , shape factor S_γ , number of $Z \rightarrow \nu\bar{\nu}$ simulation (MC) events $N_{\text{MC}}^{Z \rightarrow \nu\bar{\nu}}$, and the background prediction $N_{\text{pred}}^{Z \rightarrow \nu\bar{\nu}}$ including statistical uncertainties are provided for each search bin in Tables D.1 to D.7 in Appendix D. The uncertainty for the prediction $N_{\text{pred}}^{Z \rightarrow \nu\bar{\nu}}$ is calculated by propagating the statistical uncertainties of R_Z , S_γ , and $N_{\text{MC}}^{Z \rightarrow \nu\bar{\nu}}$ through the calculation in Eq. (6.2).

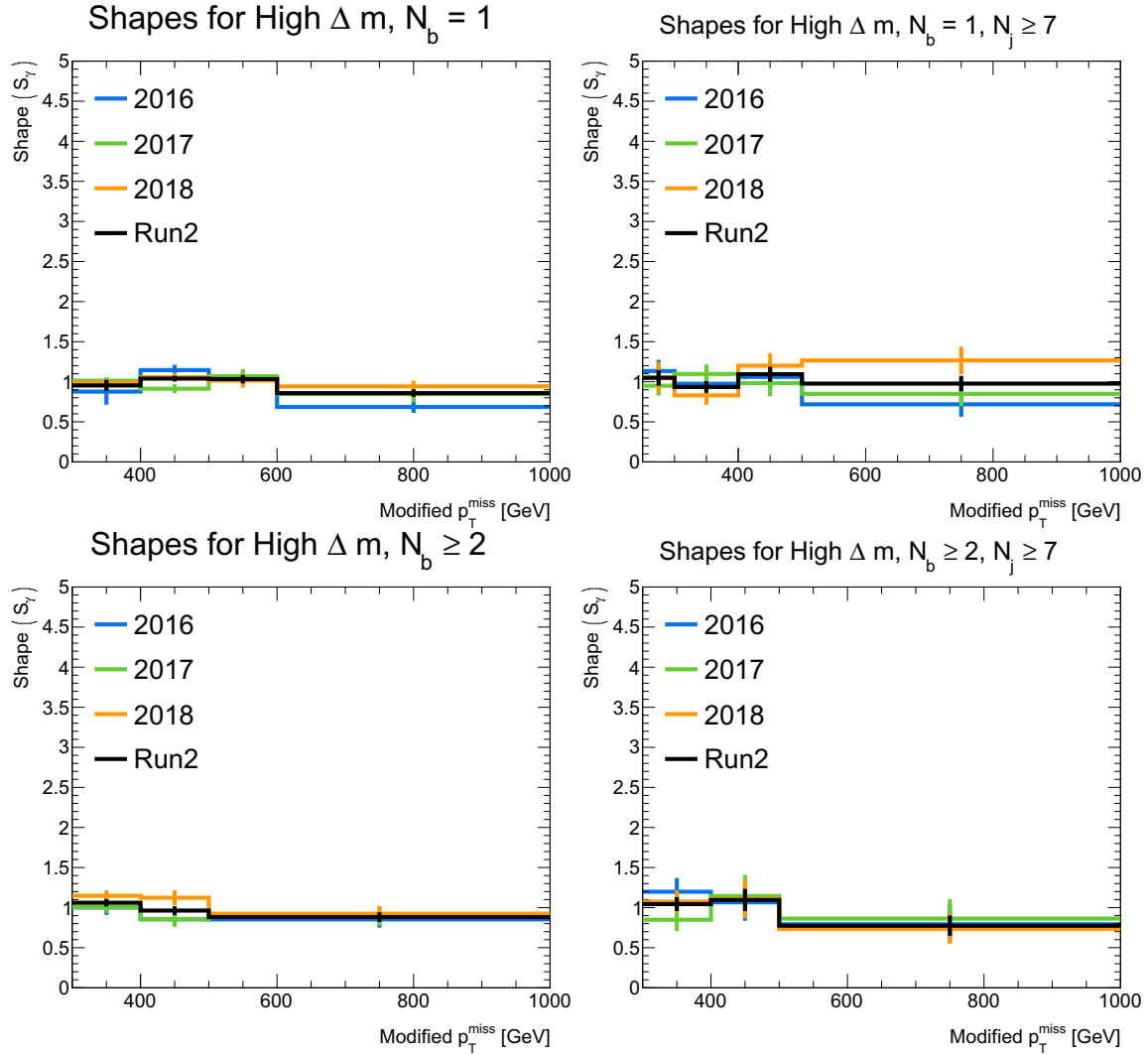


Figure 6.18: Shape factors, S_γ , for different Run 2 eras for events passing the high Δm baseline selection and with different N_b and N_j selections.

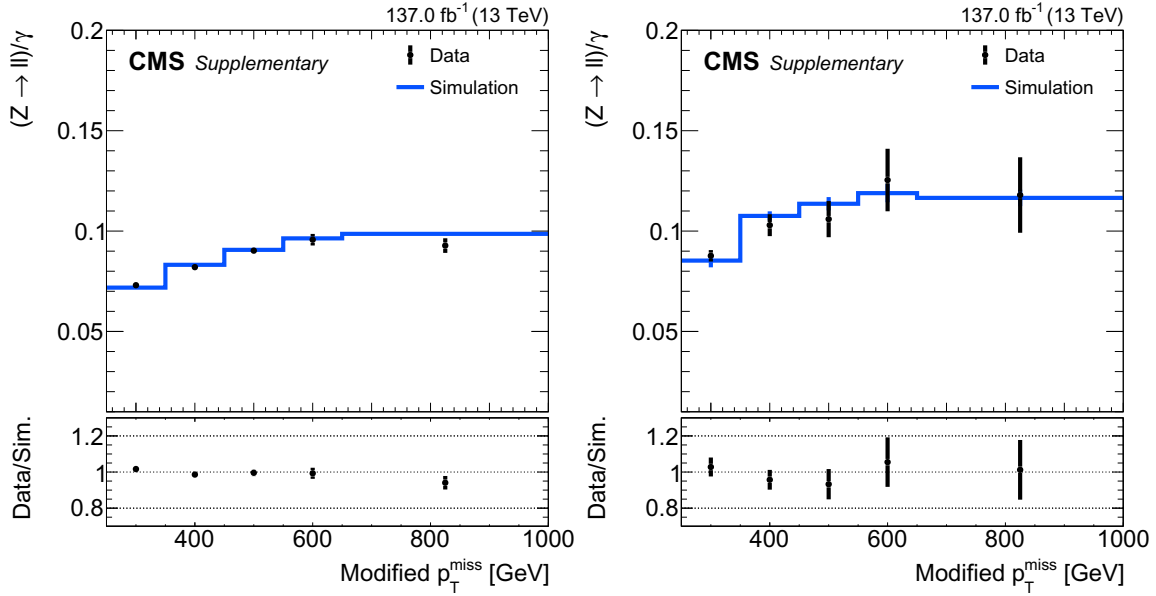


Figure 6.19: A comparison of the modified p_T^{miss} distributions for the low Δm (left) and high Δm (right) lepton and photon control regions. For each control region, the simulation is normalized such that the simulation has the same number of events as data. The modified p_T^{miss} includes the four-vector of the reconstructed Z or photon for the respective control region to mimic the Z to neutrinos decay. The upper panel shows the ratio of Z and photon data (black points) and the ratio of Z and photon simulation (blue histogram). The bottom panel shows the ratio of the two distributions in the upper panel, the data ratio divided by the simulation ratio.

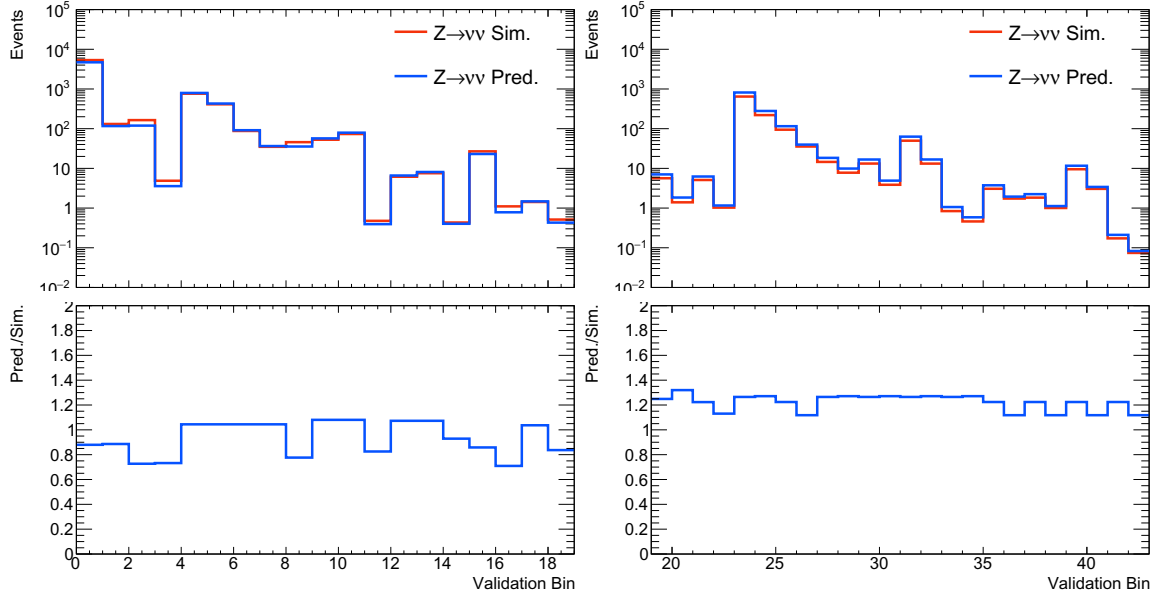


Figure 6.20: The $Z \rightarrow \nu\bar{\nu}$ simulation and Z invisible prediction in the low Δm (left) and high Δm (right) validation bins for Run 2. The $Z \rightarrow \nu\bar{\nu}$ simulation has various weights applied to account for effects such as pileup, prefire, soft b-tagging, b-tagging, top-tagging, and W-tagging. For the Z invisible prediction, the R_Z and S_γ factors have been multiplied with the $Z \rightarrow \nu\bar{\nu}$ simulation as prescribed by Eq. (6.2). Additionally, the lower plots have the ratio $N_{\text{pred}}^{Z \rightarrow \nu\bar{\nu}} / N_{\text{MC}}^{Z \rightarrow \nu\bar{\nu}}$, which shows the cumulative effect of R_Z and S_γ on the prediction for each validation bin.

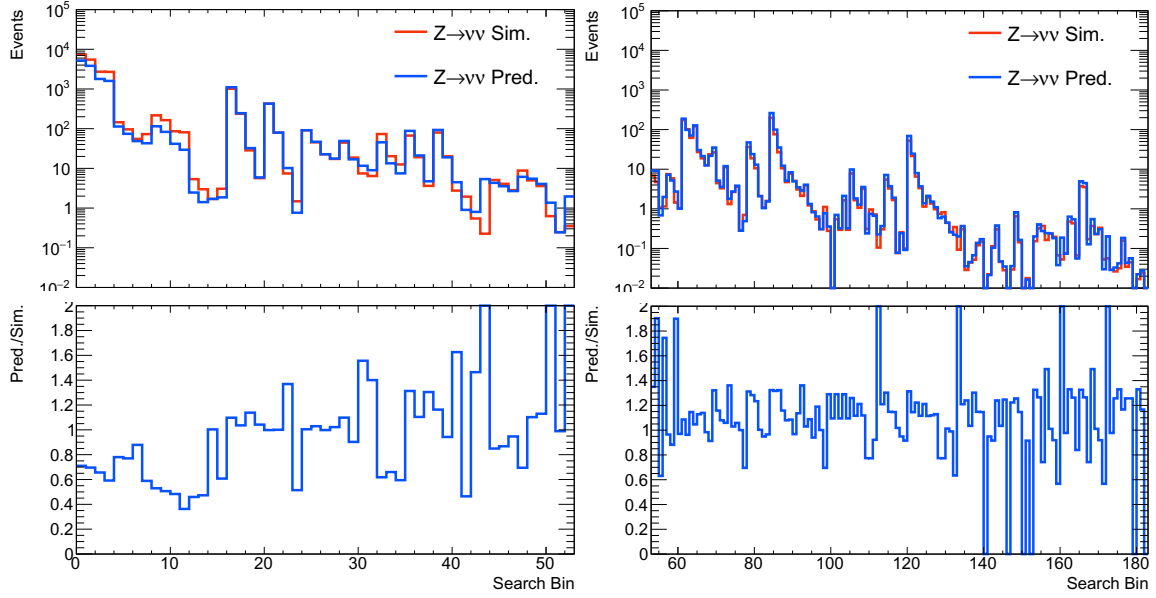


Figure 6.21: The $Z \rightarrow \nu\bar{\nu}$ simulation and Z invisible prediction in the low Δm (left) and high Δm (right) search bins for Run 2. The $Z \rightarrow \nu\bar{\nu}$ simulation has various weights applied to account for effects such as pileup, prefire, soft b-tagging, b-tagging, top-tagging, and W-tagging. For the Z invisible prediction, the R_Z and S_γ factors have been multiplied with the $Z \rightarrow \nu\bar{\nu}$ simulation as prescribed by Eq. (6.2). Additionally, the lower plots have the ratio $N_{\text{pred}}^{Z \rightarrow \nu\bar{\nu}} / N_{\text{MC}}^{Z \rightarrow \nu\bar{\nu}}$, which shows the cumulative effect of R_Z and S_γ on the prediction for each search bin.

CHAPTER SEVEN

Conclusion

The Large Hadron Collider (LHC) and the Compact Muon Solenoid (CMS) provide proton-proton collision data that is used for myriad measurements of Standard Model (SM) physics and searches for new physics. This dissertation presents a search for supersymmetry (SUSY), which is an extension of the SM and predicts many new particles. This search is done using the CMS Run 2 data set, which was collected during the years 2016–2018. The analysis selects all-hadronic final state events and targets direct and gluino-mediated top squark (stop) pair production models.

Unfortunately, the all-hadronic stop search did not find any evidence for SUSY in the CMS Run 2 data set. There are no statistically significant data excesses in the 183 search bins used in the analysis. However, the analysis was able to increase existing ATLAS and CMS mass exclusion limits for various simplified SUSY models. The direct top squark production models fall into two categories based on the mass difference between the top squark \tilde{t} and the LSP $\tilde{\chi}_1^0$. When the mass difference between the \tilde{t} and the $\tilde{\chi}_1^0$ is larger than the mass of the W boson, the top squark (LSP) mass is excluded below an upper limit ranging from 1150 GeV to 1310 GeV (500 GeV to 640 GeV), depending on the top squark decay channel. When the mass difference between the \tilde{t} and the $\tilde{\chi}_1^0$ is smaller than the mass of the W boson, the top squark mass is excluded below an upper limit ranging from 630 GeV to 740 GeV, depending on the top squark decay channel. For gluino mediated top squark production models, the gluino (LSP) mass is excluded below an upper limit ranging from 2150 GeV to

2260 GeV (1380 GeV to 1410 GeV), depending on the gluino decay channel. The improvements in the exclusion limits are attributed to an increased amount of data, an optimized search bin design, and object tagging improvements.

APPENDICES

APPENDIX A

Decay Rate Calculations

In this appendix, decay rates for the W and Z bosons are calculated using parameters from the SM. The Fermi coupling constant is [1]

$$G_F = 1.1663787 \times 10^{-5} \text{ GeV}^{-2},$$

and the W and Z boson masses are

$$m_W = 80.379 \text{ GeV}$$

$$m_Z = 91.1876 \text{ GeV}.$$

The strong coupling constant at the Z mass energy has a value of [1]

$$\alpha_s(m_Z) = 0.1181,$$

and the weak mixing angle is

$$\sin^2 \theta_W = 0.23155$$

$$\theta_W = 0.50202 \text{ rad}.$$

To begin, the coupling constants g_W and g_Z will be determined. The relation between G_F and g_W is

$$\frac{G_F}{\sqrt{2}} = \frac{g_W^2}{8m_W^2}. \tag{A.1}$$

Solving for g_W gives

$$g_W = \sqrt{\frac{8G_F m_W^2}{\sqrt{2}}}$$

$$g_W = 0.65291.$$

The coupling constant g_W and the weak mixing angle θ_W are used to find g_Z .

$$g_Z = \frac{g_W}{\cos \theta_W}$$

$$g_Z = 0.74480.$$

The weak fine structure constant α_W is then

$$\alpha_W = \frac{g_W^2}{4\pi}$$

$$\alpha_W = 0.033923$$

$$\alpha_W = \frac{1}{29.479}.$$

The weak neutral-current for the interaction of the Z boson and fermions is

$$j_Z^\mu = g_Z (c_L \bar{u}_L \gamma^\mu u_L + c_R \bar{u}_R \gamma^\mu u_R) \quad (\text{A.2})$$

where u_L, u_R and \bar{u}_L, \bar{u}_R are spinors and adjoint spinors for left-handed and right-handed chiral states. The coefficients c_L and c_R are the Z boson couplings to left- and right-handed chiral states.

$$c_L = I_W^{(3)} - Q_f \sin^2 \theta_W \quad (\text{A.3})$$

$$c_R = -Q_f \sin^2 \theta_W$$

The weak neutral-current can also be expressed in terms of the vector and axial-vector Z couplings c_V and c_A .

$$j_Z^\mu = \frac{1}{2} g_Z \bar{u} (c_V \gamma^\mu - c_A \gamma^\mu \gamma^5) u \quad (\text{A.4})$$

The vector and axial vector couplings in terms of c_L and c_R are

$$c_V = c_L + c_R \tag{A.5}$$

$$c_A = c_L - c_R,$$

and using Eq. (A.3), these become

$$c_V = I_W^{(3)} - 2Q_f \sin^2 \theta_W \tag{A.6}$$

$$c_A = I_W^{(3)}.$$

In order to calculate W and Z boson decay rates, consider the generic two-body particle decay $1 \rightarrow 2 + 3$. Energy and momentum conservation are applied by equating the sums of initial and final state four-momenta.

$$p_1 = p_2 + p_3 \tag{A.7}$$

In the rest frame of the mother particle 1, $\vec{p}_1 = 0$, and the Einstein energy-momentum relationship $E^2 = |\vec{p}|^2 + m^2$ gives

$$E_1^2 = m_1^2$$

$$E_1 = m_1.$$

Then the four-momenta for the two-body decay are

$$p_1 = (m_1, \vec{0})$$

$$p_2 = (E_2, \vec{p}_2)$$

$$p_3 = (E_3, \vec{p}_3).$$

In the rest frame of particle 1, Eq. (A.7) becomes

$$m_1 = E_2 + E_3 \tag{A.8}$$

$$\vec{0} = \vec{p}_2 + \vec{p}_3.$$

Therefore, $\vec{p}_2 = -\vec{p}_3$, and the momenta of particles 2 and 3 are equal in magnitude and opposite in direction. The magnitude of this momentum in the center-of-mass frame is defined as

$$p^* \equiv |\vec{p}_2| = |\vec{p}_3|. \quad (\text{A.9})$$

To determine p^* , each side of the energy relation in Eq. (A.8) is squared, and then the Einstein energy-momentum relationship is applied.

$$\begin{aligned} m_1^2 &= E_2^2 + E_3^2 + 2E_2E_3 \\ m_1^2 &= p^{*2} + m_2^2 + p^{*2} + m_3^2 + 2\sqrt{(p^{*2} + m_2^2)(p^{*2} + m_3^2)} \end{aligned}$$

Rearranging gives

$$(p^{*2} + m_2^2)(p^{*2} + m_3^2) = \frac{1}{4}(m_1^2 - m_2^2 - m_3^2 - 2p^{*2})^2.$$

Solving for p^{*2} and manipulating the resulting expression gives

$$\begin{aligned} p^{*2} &= \frac{1}{4m_1^2} \left((m_1^2 - m_2^2 - m_3^2)^2 - 4m_2^2m_3^2 \right) \\ &= \frac{1}{4m_1^2} \left(m_1^4 - 2m_1^2(m_2^2 + m_3^2) + m_2^4 + m_3^4 - 2m_2^2m_3^2 \right) \\ &= \frac{1}{4m_1^2} \left(m_1^4 - 2m_1^2(m_2^2 + m_3^2) + (m_2^2 - m_3^2)^2 \right) \\ &= \frac{1}{4m_1^2} \left(m_1^4 - m_1^2(m_2 + m_3)^2 - m_1^2(m_2 - m_3)^2 + (m_2 + m_3)^2(m_2 - m_3)^2 \right) \\ p^{*2} &= \frac{1}{4m_1^2} [m_1^2 - (m_2 + m_3)^2] [m_1^2 - (m_2 - m_3)^2]. \end{aligned}$$

Thus momenta of particles 2 and 3 is

$$p^* = \frac{1}{2m_1} \sqrt{[m_1^2 - (m_2 + m_3)^2] [m_1^2 - (m_2 - m_3)^2]}. \quad (\text{A.10})$$

The decay rate for a two-body decay is given by

$$\Gamma(1 \rightarrow 2 + 3) = \frac{p^*}{32\pi^2 m_1^2} \int |\mathcal{M}_{fi}|^2 d\Omega \quad (\text{A.11})$$

where p^* is the magnitude of the momenta of the final-state particles in the center-of-mass frame from Eq. (A.10). If the mass of the mother particle is much larger than the masses of the daughter particles ($m_1 \gg m_2, m_3$), then the momentum p^* is approximately

$$p^* \approx \frac{m_1}{2},$$

and the decay rate becomes

$$\Gamma(1 \rightarrow 2 + 3) \approx \frac{1}{64\pi^2 m_1} \int |\mathcal{M}_{fi}|^2 d\Omega.$$

Inserting the spin-averaged matrix element squared $\langle |\mathcal{M}_{fi}|^2 \rangle$ and performing the $d\Omega$ integral results in

$$\Gamma(1 \rightarrow 2 + 3) \approx \frac{1}{16\pi m_1} \langle |\mathcal{M}_{fi}|^2 \rangle. \quad (\text{A.12})$$

For the $W^- \rightarrow e^- \bar{\nu}_e$ decay, the spin-averaged matrix element squared is

$$\langle |\mathcal{M}_{fi}|^2 \rangle = \frac{1}{3} g_W^2 m_W^2,$$

and substituting this into Eq. (A.12) with $m_1 = m_W$ gives the decay rate

$$\Gamma(W^- \rightarrow e^- \bar{\nu}_e) = \frac{g_W^2 m_W}{48\pi}. \quad (\text{A.13})$$

For the $Z \rightarrow f \bar{f}$ decay, the spin-averaged matrix element squared is

$$\langle |\mathcal{M}_{fi}|^2 \rangle = \frac{1}{3} g_Z^2 m_Z^2 (c_V^2 + c_A^2),$$

and substituting this into Eq. (A.12) with $m_1 = m_Z$ gives the decay rate

$$\Gamma(Z \rightarrow f \bar{f}) = \frac{g_Z^2 m_Z}{48\pi} (c_V^2 + c_A^2). \quad (\text{A.14})$$

The total decay rate of the Z boson Γ_Z is the sum the decay rates from all possible Z decays.

$$\Gamma_Z = \sum_f \Gamma(Z \rightarrow f\bar{f}) \quad (\text{A.15})$$

Expanding Eq. (A.15) with the decay rates from all Z decays gives

$$\begin{aligned} \Gamma_Z &= \Gamma(Z \rightarrow \nu\bar{\nu}) + \Gamma(Z \rightarrow l^+l^-) + \kappa_{QCD}\Gamma(Z \rightarrow q\bar{q}) \\ \Gamma_Z &= 3\Gamma(Z \rightarrow \nu_e\bar{\nu}_e) + 3\Gamma(Z \rightarrow e^+e^-) \\ &\quad + 3 \times 2\kappa_{QCD}\Gamma(Z \rightarrow u\bar{u}) + 3 \times 3\kappa_{QCD}\Gamma(Z \rightarrow d\bar{d}). \end{aligned}$$

The factors of three for the leptonic decays are due to the three lepton flavors where different flavors have equal decay rates. The factors of three for the hadronic decays are for the three colors in the strong force. The up-type quark decays have an additional factor of two because the Z can decay to an up quark-antiquark pair or a charm quark-antiquark pair, but not a top quark-antiquark pair as the mass of the top quark exceeds the mass of the Z. The three down-type quarks all have much smaller masses than the Z, so the down-type quark decays have an additional factor of three applied. Furthermore, the hadronic Z decays have been multiplied by the factor κ_{QCD} to account for the enhancement of these decays due to gluon radiation.

The expression for κ_{QCD} is

$$\kappa_{QCD} = \left(1 + \frac{\alpha_S(Q^2)}{\pi}\right) \quad (\text{A.16})$$

where $\alpha_S(Q^2)$ is the strong force coupling. Evaluating Eq. (A.16) with $\alpha_s(m_Z) = 0.1181$ gives $\kappa_{QCD} = 1.038$.

Table A.1: Fermion couplings to the Z boson [4]. Q_f is the electric charge. $I_W^{(3)}$ is the third component of weak isospin for left handed particles. Note that $I_W^{(3)} = 0$ for right-handed particles and left-handed antiparticles. Y_L and Y_R are the weak hypercharge for left- and right-handed chiral states. c_L and c_R are the Z couplings to left- and right-handed chiral states expressed in Eq. (A.3). c_V and c_A are the vector and axial-vector Z couplings given in Eq. (A.6).

fermion	Q_f	$I_W^{(3)}$	Y_L	Y_R	c_L	c_R	c_V	c_A
ν_e, ν_μ, ν_τ	0	$+\frac{1}{2}$	-1	0	$+\frac{1}{2}$	0	$+\frac{1}{2}$	$+\frac{1}{2}$
e^-, μ^-, τ^-	-1	$-\frac{1}{2}$	-1	-2	-0.27	+0.23	-0.04	$-\frac{1}{2}$
u, c, t	$+\frac{2}{3}$	$+\frac{1}{2}$	$+\frac{1}{3}$	$+\frac{4}{3}$	+0.35	-0.15	+0.19	$+\frac{1}{2}$
d, s, b	$-\frac{1}{3}$	$-\frac{1}{2}$	$+\frac{1}{3}$	$-\frac{2}{3}$	-0.42	+0.08	-0.35	$-\frac{1}{2}$

The various Z decay rates are calculated using Eq. (A.14) with the corresponding c_V and c_A values from Table A.1.

$$\Gamma(Z \rightarrow \nu\bar{\nu}) = 503.18 \text{ MeV}$$

$$\Gamma(Z \rightarrow l^+l^-) = 252.96 \text{ MeV}$$

$$\Gamma(Z \rightarrow q\bar{q}) = 1692.23 \text{ MeV}$$

The total Z decay rate is then

$$\Gamma_Z = 2511.98 \text{ MeV}$$

which is consistent with the current measured value $2495.2 \pm 2.3 \text{ MeV}$ [1]. After determining the decay rates, branching ratios are found by the ratio of a specific decay rate over the total decay rate.

$$Br(Z \rightarrow f\bar{f}) = \frac{\Gamma(Z \rightarrow f\bar{f})}{\Gamma_Z}$$

For example, the Z to neutrinos branching ratio is

$$Br(Z \rightarrow \nu\bar{\nu}) = \frac{\Gamma(Z \rightarrow \nu\bar{\nu})}{\Gamma_Z}$$

$$Br(Z \rightarrow \nu\bar{\nu}) = 0.20031$$

which agrees with the measured value $20.000 \pm 0.055\%$ [1].

APPENDIX B

Event Displays

Event displays of selected CMS events passing the search region requirements are provided in this appendix. Events are chosen to illustrate different types of object tagging used in the analysis.

The CMS event 471815433 is shown in Fig. B.1 the x-y plane; the z-axis is in the direction of the proton beam. This is one of the two data events in search bin 145 and has two tagged merged top quarks. The momentum of each top quark is large enough that the decay products of the top quark are contained within one AK8 jet. The AK8 jet for each top quark is shown.

An event display of CMS event 448246125 is shown in Fig. B.2. This is one of the seven data events in search bin 180 and has two tagged resolved top quarks. The momentum of each top quark is relatively small, and the decay products of each top quark have large angular separation and are reconstructed in separate AK4 jets. The three AK4 jet decay products for each top quark are shown.

An event display of CMS event 371464374 is shown in Fig. B.3. This is one of the two data events in search bin 140 and has one tagged merged top quark and one tagged resolved top quark. The AK8 jet for the merged top quark and the three AK4 jets for the resolved top quark are shown.

An event display of CMS event 621760811 is shown in Fig. B.4. This is one of the two data events in search bin 119 and has one tagged W boson. The AK8 jet for the W boson and two AK4 jets tagged as bottom quarks are shown.

An event display of CMS event 1887015358 is shown in Fig. B.5. This is one of the four data events in search bin 46 and has one ISR jet. The AK8 jet for the ISR jet two AK4 jets tagged as bottom quarks are shown.

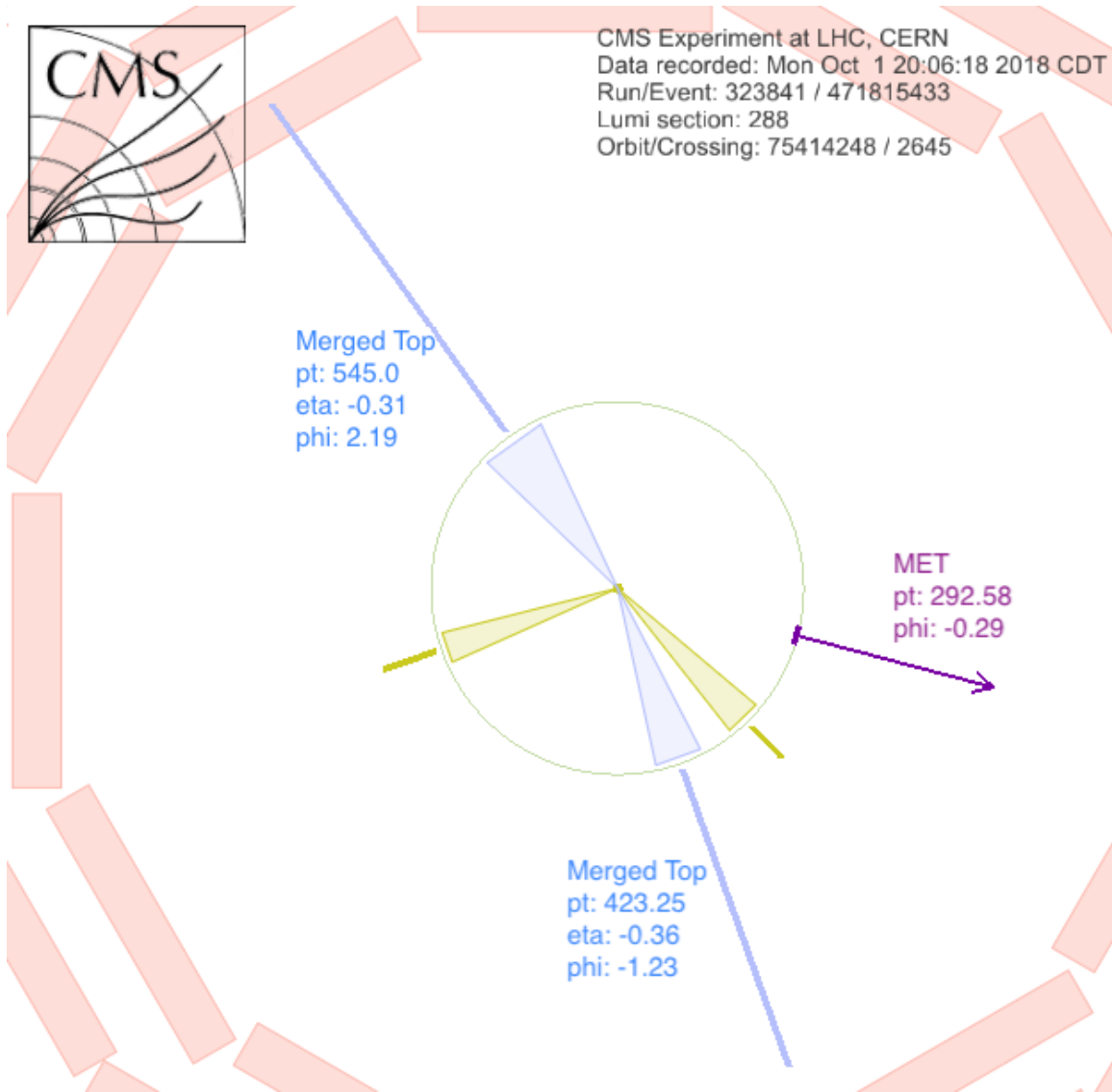


Figure B.1: Event display of event 471815433, which is a data event in search bin 145 and has two tagged merged top quarks. The AK8 jets tagged as merged top quarks are colored blue. Additional AK4 jets in the event are colored yellow, and the missing transverse energy is colored purple.

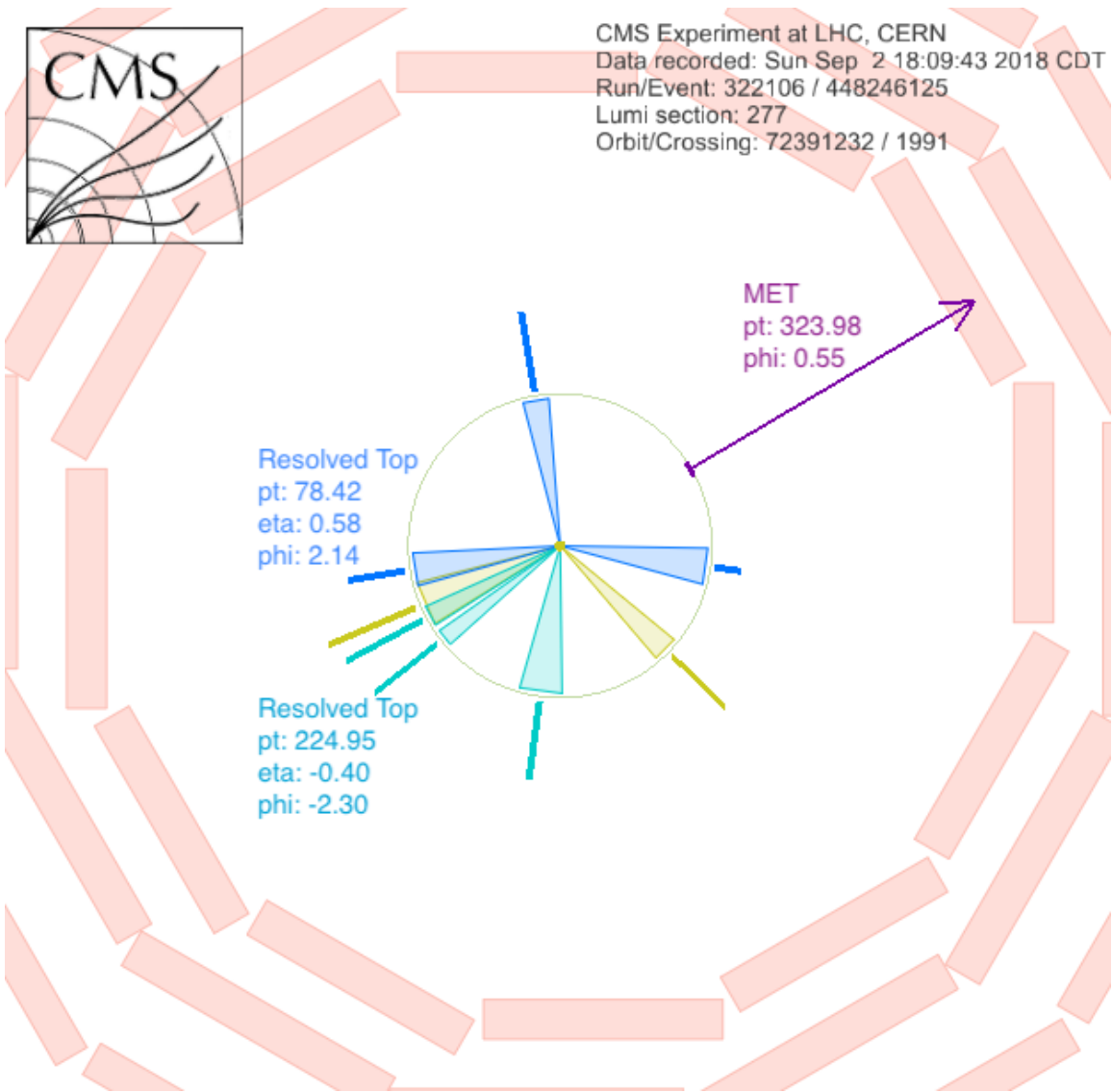


Figure B.2: Event display of event 448246125, which is a data event in search bin 180 and has two tagged resolved top quarks. Each tagged resolved top quark has three AK4 jet constituents, the decay products of the top quark, which are colored cyan and blue. Additional AK4 jets in the event are colored yellow, and the missing transverse energy is colored purple.

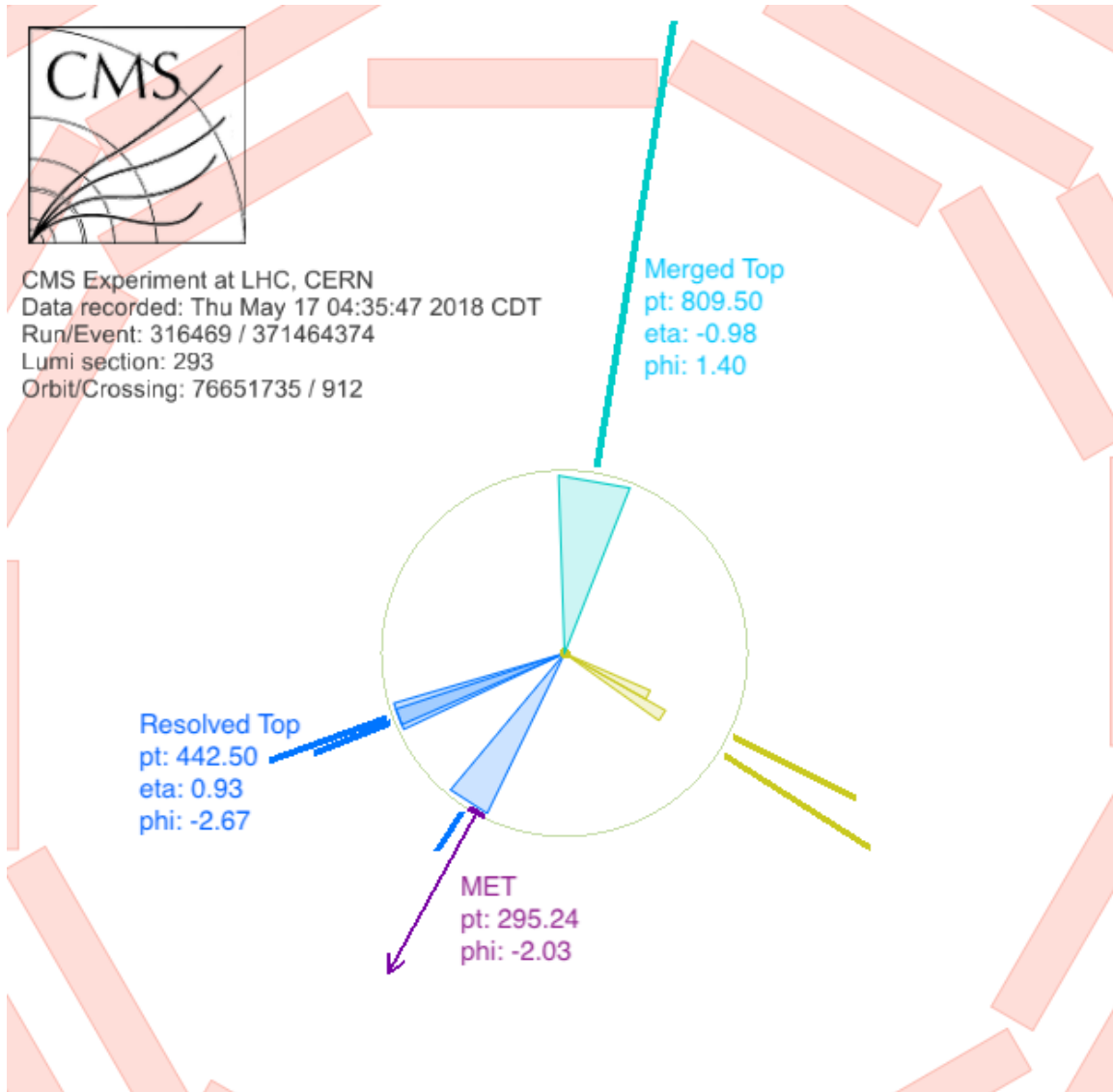


Figure B.3: Event display of event 371464374, which is a data event in search bin 140 and has one tagged merged top quark and one tagged resolved top quark. The AK8 jet that is tagged as a merged top quark is colored cyan. The three AK4 jet constituents of the resolved top quark are colored blue. Additional AK4 jets in the event are colored yellow, and the missing transverse energy is colored purple.

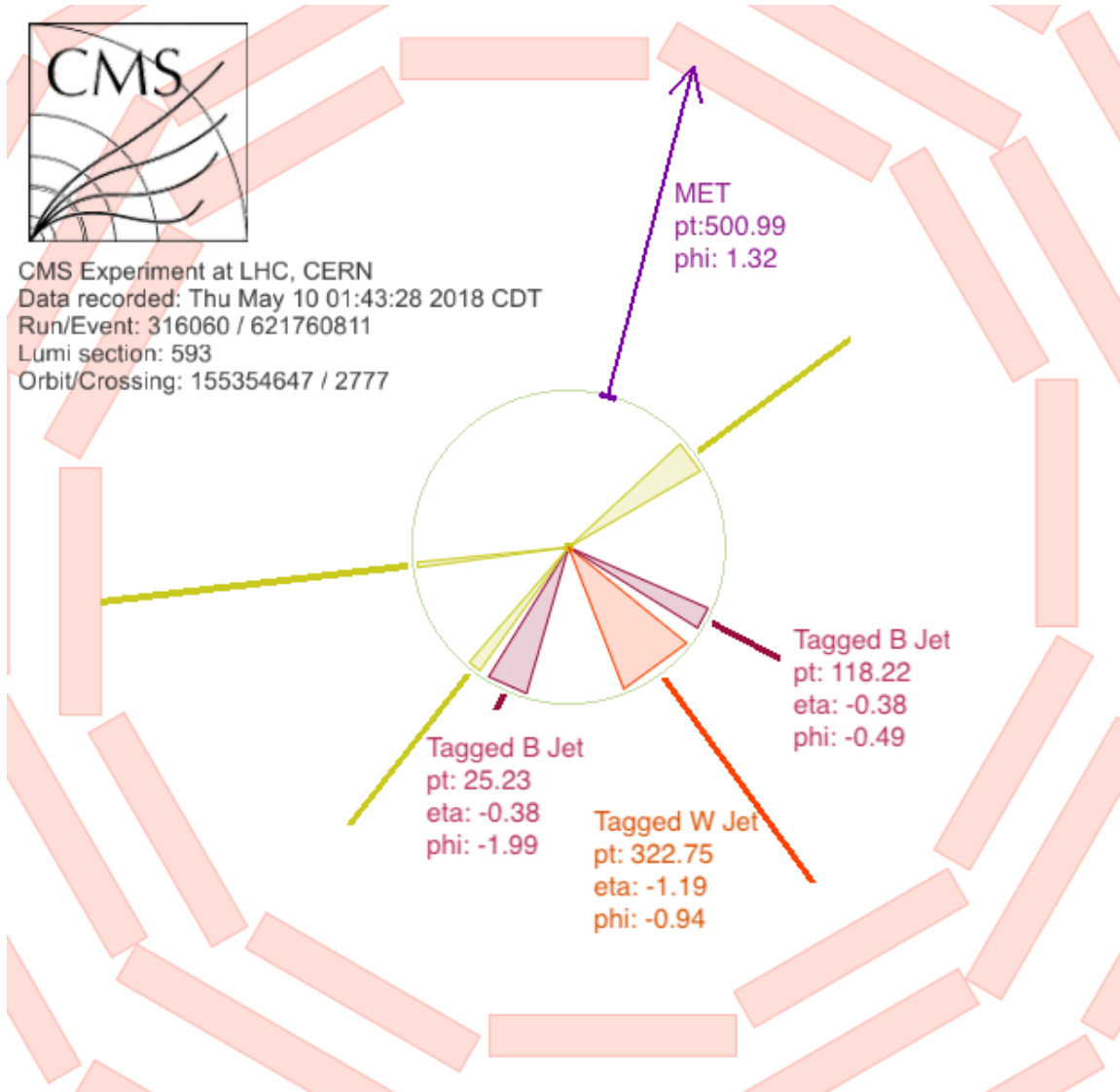


Figure B.4: Event display of event 621760811, which is a data event in search bin 119 and has one tagged W boson. The AK8 jet that is tagged as a W boson is colored orange. There are two AK4 jets that are tagged as bottom quarks, which are colored red. Additional AK4 jets in the event are colored yellow, and the missing transverse energy is colored purple.

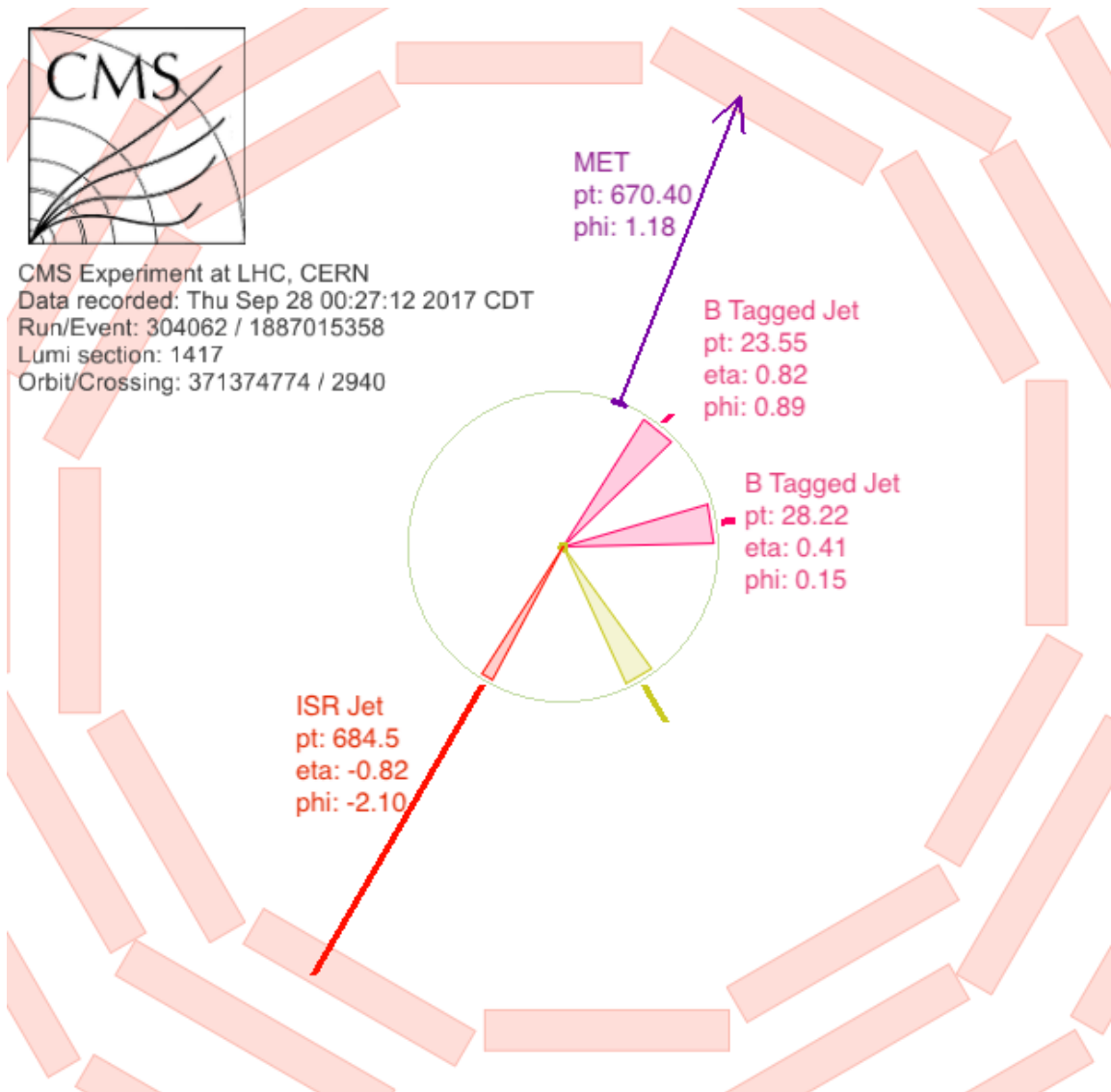


Figure B.5: Event display of event 1887015358, which is a data event in search bin 46 and has one ISR jet. The AK8 jet that is identified as the ISR jet is colored orange. There are two AK4 jets that are tagged as bottom quarks, which are colored red. An additional AK4 jet in the event is colored yellow, and the missing transverse energy is colored purple.

APPENDIX C

Background Predictions

This appendix presents the SM background predictions and observed data in the 183 search bins in Tables C.1 to C.7.

Table C.1: Observed number of events and SM background predictions in search bins 0–27.

Search bin	p_T^{miss} [GeV]	Lost lepton	$Z \rightarrow \nu\bar{\nu}$	Rare	QCD multijet	Total SM	N_{data}
Low Δm , $N_b = 0$, $N_{\text{SV}} = 0$, $p_T^{\text{ISR}} > 500$ GeV, $2 \leq N_j \leq 5$							
0	450–550	2240 ⁺¹⁶⁰ ₋₁₅₀	5220 ⁺⁵⁹⁰ ₋₅₂₀	103 ⁺¹¹ ₋₁₀	280 ⁺¹¹⁰ ₋₈₀	7840 ⁺⁶²⁰ ₋₅₅₀	7538
1	550–650	1128 ⁺⁷⁵ ₋₇₀	3830 ⁺⁴⁴⁰ ₋₃₉₀	81 ± 10	77 ⁺³⁴ ₋₂₃	5120 ⁺⁴⁵⁰ ₋₄₀₀	4920
2	650–750	446 ⁺³² ₋₃₀	1790 ⁺²³⁰ ₋₂₀₀	41.1 ± 5.5	29 ⁺¹² ₋₉	2300 ⁺²³⁰ ₋₂₁₀	2151
3	> 750	301 ± 23	1600 ⁺²⁰⁰ ₋₁₈₀	38.0 ± 5.0	12.9 ^{+8.0} _{-5.2}	1950 ⁺²⁰⁰ ₋₁₈₀	1780
Low Δm , $N_b = 0$, $N_{\text{SV}} = 0$, $p_T^{\text{ISR}} > 500$ GeV, $N_j \geq 6$							
4	450–550	115 ⁺¹² ₋₁₁	113 ⁺¹⁶ ₋₁₅	5.2 ^{+1.6} _{-1.8}	37 ⁺¹³ ₋₁₀	270 ⁺²⁵ ₋₂₂	277
5	550–650	45.7 ^{+5.8} _{-5.5}	74 ⁺¹¹ ₋₁₀	4.5 ^{+1.8} _{-1.6}	18.5 ^{+7.8} _{-6.0}	143 ⁺¹⁵ ₋₁₃	146
6	650–750	19.5 ± 3.0	49 ± 31	3.5 ± 1.6	3.9 ^{+1.8} _{-1.5}	76 ± 32	63
7	> 750	20.6 ^{+3.3} _{-3.1}	42.9 ^{+7.3} _{-6.8}	1.35 ^{+0.38} _{-0.44}	4.5 ^{+2.9} _{-2.1}	69.4 ^{+8.5} _{-7.9}	85
Low Δm , $N_b = 0$, $N_{\text{SV}} \geq 1$, $p_T^{\text{ISR}} > 500$ GeV, $2 \leq N_j \leq 5$							
8	450–550	80.1 ± 8.9	115 ⁺¹⁷ ₋₁₆	3.5 ^{+1.3} _{-1.1}	5.9 ^{+2.6} _{-2.2}	205 ⁺²⁰ ₋₁₈	161
9	550–650	27.7 ± 4.4	83 ⁺¹³ ₋₁₂	1.33 ^{+0.49} _{-0.45}	1.4 ^{+1.1} _{-1.0}	113 ⁺¹⁴ ₋₁₃	126
10	650–750	14.9 ± 3.1	41.6 ^{+7.6} _{-7.1}	2.5 ± 1.2	1.3 ± 1.1	60.3 ± 8.2	67
11	> 750	9.7 ± 2.5	29.4 ^{+5.7} _{-5.3}	0.41 ± 0.10	0.45 ^{+0.35} _{-0.27}	40.0 ± 6.1	39
Low Δm , $N_b = 0$, $N_{\text{SV}} \geq 1$, $p_T^{\text{ISR}} > 500$ GeV, $N_j \geq 6$							
12	450–550	4.2 ± 1.3	2.5 ± 1.2	0.06 ± 0.03	1.08 ± 0.58	7.8 ^{+1.8} _{-1.9}	12
13	550–650	1.77 ± 0.84	1.41 ± 0.81	0.05 ± 0.03	0.53 ± 0.33	3.8 ± 1.2	4
14	650–750	0.84 ± 0.63	1.7 ± 1.1	0.04 ± 0.02	0.05 ± 0.03	2.6 ± 1.3	2
15	> 750	1.75 ± 0.85	1.9 ± 1.3	0.06 ± 0.04	0.14 ^{+0.10} _{-0.08}	3.8 ^{+1.6} _{-1.5}	3
Low Δm , $N_b = 1$, $N_{\text{SV}} = 0$, $m_T^b < 175$ GeV, $300 < p_T^{\text{ISR}} < 500$ GeV, $p_T^b < 40$ GeV							
16	300–400	1302 ⁺⁹² ₋₈₆	1110 ⁺¹³⁰ ₋₁₁₀	14.6 ± 2.3	118 ⁺⁴³ ₋₃₀	2540 ⁺¹⁸⁰ ₋₁₅₀	2383
17	400–500	226 ± 22	246 ⁺³² ₋₂₉	2.7 ^{+1.1} _{-0.5}	27 ⁺¹⁶ ₋₁₄	501 ⁺⁴³ ₋₃₉	456
18	500–600	23.4 ± 5.1	32.4 ± 6.2	0.96 ^{+0.58} _{-0.66}	6.3 ^{+4.8} _{-4.4}	63.0 ± 9.7	68
19	> 600	3.5 ± 1.5	5.9 ± 2.0	0.13 ^{+0.10} _{-0.03}	0.14 ± 0.15	9.7 ± 2.5	14
Low Δm , $N_b = 1$, $N_{\text{SV}} = 0$, $m_T^b < 175$ GeV, $300 < p_T^{\text{ISR}} < 500$ GeV, $40 < p_T^b < 70$ GeV							
20	300–400	789 ⁺⁶⁵ ₋₅₉	427 ± 51	9.0 ^{+1.7} _{-1.6}	70 ⁺²⁸ ₋₂₆	1295 ⁺⁹¹ ₋₈₄	1250
21	400–500	113 ± 15	80 ⁺¹² ₋₁₁	4.6 ^{+1.9} _{-2.2}	3.7 ^{+2.7} _{-2.4}	201 ± 21	222
22	500–600	8.0 ± 2.7	10.2 ± 3.7	0.12 ± 0.05	0.31 ± 0.28	18.6 ± 4.7	29
23	> 600	3.0 ± 1.4	0.76 ± 0.60	0.01 ± 0.02	0.05 ± 0.04	3.8 ± 1.6	5
Low Δm , $N_b = 1$, $N_{\text{SV}} = 0$, $m_T^b < 175$ GeV, $p_T^{\text{ISR}} > 500$ GeV, $p_T^b < 40$ GeV							
24	450–550	82.6 ± 9.9	91 ± 13	1.64 ± 0.98	8.9 ^{+4.0} _{-3.3}	185 ± 17	164
25	550–650	30.5 ± 5.5	46.7 ± 8.1	1.58 ± 0.97	3.2 ^{+1.6} _{-1.4}	82 ± 10	72
26	650–750	7.2 ± 2.2	22.7 ± 5.3	0.20 ± 0.06	0.28 ± 0.52	30.4 ± 5.9	33
27	> 750	8.8 ± 2.4	17.7 ^{+5.5} _{-5.2}	0.23 ^{+0.15} _{-0.11}	0.12 ± 0.21	26.8 ^{+6.1} _{-5.8}	29

Table C.2: Observed number of events and SM background predictions in search bins 28–52.

Search bin	p_T^{miss} [GeV]	Lost lepton	$Z \rightarrow \nu\bar{\nu}$	Rare	QCD multijet	Total SM	N_{data}
Low Δm , $N_b = 1$, $N_{\text{SV}} = 0$, $m_T^b < 175$ GeV, $p_T^{\text{ISR}} > 500$ GeV, $40 < p_T^b < 70$ GeV							
28	450–550	72 ± 10	49.0 ± 8.3	$1.28_{-0.52}^{+0.56}$	$2.4_{-1.1}^{+1.3}$	125 ± 13	81
29	550–650	17.2 ± 4.0	16.9 ± 4.0	$0.27_{-0.06}^{+0.07}$	$0.69_{-0.46}^{+0.51}$	35.0 ± 5.7	34
30	650–750	7.3 ± 2.5	11.6 ± 3.8	$0.56_{-0.42}^{+0.69}$	0.08 ± 0.21	19.5 ± 4.5	18
31	> 750	$3.1_{-1.4}^{+1.5}$	9.0 ± 3.3	0.12 ± 0.04	0.05 ± 0.13	12.2 ± 3.7	12
Low Δm , $N_b = 1$, $N_{\text{SV}} \geq 1$, $m_T^b < 175$ GeV, $p_T^{\text{ISR}} > 300$ GeV, $p_T^b < 40$ GeV							
32	300–400	73 ± 11	45 ± 13	0.74 ± 0.14	7.2 ± 4.3	127 ± 19	128
33	400–500	$14.2_{-3.7}^{+3.9}$	13.4 ± 3.8	$0.22_{-0.09}^{+0.15}$	1.5 ± 1.2	$29.3_{-5.4}^{+5.8}$	42
34	> 500	10.0 ± 3.1	7.5 ± 2.6	0.09 ± 0.05	0.33 ± 0.35	17.9 ± 4.2	16
Low Δm , $N_b \geq 2$, $m_T^b < 175$ GeV, $300 < p_T^{\text{ISR}} < 500$ GeV, $p_T^{\text{b}12} < 80$ GeV							
35	300–400	154 ± 17	88_{-16}^{+17}	$2.43_{-0.65}^{+0.81}$	$8.9_{-5.9}^{+6.3}$	253_{-24}^{+26}	244
36	400–500	26.5 ± 5.8	21.2 ± 8.4	$0.69_{-0.10}^{+0.11}$	$1.4_{-1.3}^{+1.7}$	50 ± 11	47
37	> 500	5.6 ± 2.6	4.7 ± 2.6	0.10 ± 0.04	$0.18_{-0.17}^{+0.18}$	10.6 ± 3.8	9
Low Δm , $N_b \geq 2$, $m_T^b < 175$ GeV, $300 < p_T^{\text{ISR}} < 500$ GeV, $80 < p_T^{\text{b}12} < 140$ GeV							
38	300–400	360 ± 31	93 ± 21	$5.07_{-0.42}^{+0.46}$	35_{-17}^{+20}	493_{-40}^{+46}	443
39	400–500	77 ± 11	19.0 ± 4.7	$1.34_{-0.18}^{+0.16}$	9.4 ± 6.9	107 ± 14	82
40	> 500	8.5 ± 2.5	$4.5_{-1.9}^{+2.0}$	0.70 ± 0.44	0.83 ± 0.80	14.5 ± 3.3	8
Low Δm , $N_b \geq 2$, $m_T^b < 175$ GeV, $300 < p_T^{\text{ISR}} < 500$ GeV, $p_T^{\text{b}12} > 140$ GeV, $N_j \geq 7$							
41	300–400	59.7 ± 7.4	0.90 ± 0.82	$0.31_{-0.09}^{+0.08}$	4.2 ± 4.0	65.1 ± 8.4	54
42	400–500	13.5 ± 3.1	0.80 ± 0.57	0.09 ± 0.05	0.30 ± 0.34	14.7 ± 3.2	15
43	> 500	4.6 ± 1.9	5.4 ± 5.9	0.05 ± 0.03	0.06 ± 0.06	10.0 ± 6.2	2
Low Δm , $N_b \geq 2$, $m_T^b < 175$ GeV, $p_T^{\text{ISR}} > 500$ GeV, $p_T^{\text{b}12} < 80$ GeV							
44	450–550	7.9 ± 2.3	4.3 ± 2.5	$0.16_{-0.06}^{+0.07}$	0.31 ± 0.29	12.7 ± 3.5	22
45	550–650	$3.7_{-1.7}^{+1.6}$	3.5 ± 1.9	0.14 ± 0.04	0.22 ± 0.22	7.6 ± 2.5	9
46	> 650	0.98 ± 0.71	$2.7_{-1.8}^{+1.9}$	0.10 ± 0.04	0.02 ± 0.02	3.8 ± 2.0	4
Low Δm , $N_b \geq 2$, $m_T^b < 175$ GeV, $p_T^{\text{ISR}} > 500$ GeV, $80 < p_T^{\text{b}12} < 140$ GeV							
47	450–550	$28.4_{-4.8}^{+5.1}$	6.1 ± 2.2	0.52 ± 0.09	$0.35_{-0.26}^{+0.32}$	$35.4_{-5.3}^{+5.7}$	41
48	550–650	9.5 ± 2.8	5.5 ± 2.5	$0.22_{-0.07}^{+0.06}$	$0.12_{-0.10}^{+0.11}$	$15.4_{-3.6}^{+3.8}$	14
49	> 650	4.6 ± 1.9	4.1 ± 1.9	$0.25_{-0.07}^{+0.06}$	$0.09_{-0.07}^{+0.08}$	9.0 ± 2.7	8
Low Δm , $N_b \geq 2$, $m_T^b < 175$ GeV, $p_T^{\text{ISR}} > 500$ GeV, $p_T^{\text{b}12} > 140$ GeV, $N_j \geq 7$							
50	450–550	16.6 ± 3.3	1.4 ± 1.1	0.06 ± 0.04	$0.96_{-0.85}^{+0.91}$	19.0 ± 3.6	20
51	550–650	6.1 ± 1.9	$0.25_{-0.32}^{+0.38}$	0.05 ± 0.02	0.14 ± 0.25	$6.5_{-1.9}^{+2.0}$	6
52	> 650	2.1 ± 1.3	2.0 ± 2.9	0.04 ± 0.03	0.06 ± 0.10	4.2 ± 3.2	4

Table C.3: Observed number of events and SM background predictions in search bins 53–80.

Search bin	p_T^{miss} [GeV]	Lost lepton	$Z \rightarrow \nu\bar{\nu}$	Rare	QCD multijet	Total SM	N_{data}
High Δm , $N_b = 1$, $m_T^b < 175$ GeV, $N_j \geq 7$, $N_{\text{res}} \geq 1$							
53	250–300	199^{+17}_{-16}	9.3 ± 3.0	$3.83^{+0.53}_{-0.61}$	19^{+11}_{-10}	231 ± 21	227
54	300–400	105 ± 11	9.0 ± 3.0	3.37 ± 0.62	$4.8^{+2.3}_{-2.1}$	122 ± 12	130
55	400–500	25.4 ± 5.0	$0.68^{+0.46}_{-0.41}$	$0.68^{+0.16}_{-0.15}$	2.7 ± 2.2	29.5 ± 5.5	26
56	> 500	7.2 ± 2.6	2.0 ± 1.3	$0.30^{+0.08}_{-0.09}$	0.15 ± 0.22	9.7 ± 2.9	9
High Δm , $N_b \geq 2$, $m_T^b < 175$ GeV, $N_j \geq 7$, $N_{\text{res}} \geq 1$							
57	250–300	639 ± 42	$7.3^{+1.9}_{-2.0}$	10.1 ± 1.6	$11.6^{+9.0}_{-7.1}$	668 ± 44	669
58	300–400	344 ± 25	$5.2^{+1.6}_{-1.5}$	$9.1^{+1.5}_{-1.3}$	$4.9^{+5.3}_{-3.6}$	363 ± 26	345
59	400–500	58.6 ± 7.8	2.7 ± 1.4	$2.21^{+0.32}_{-0.36}$	$6.5^{+7.6}_{-6.1}$	70^{+11}_{-10}	54
60	> 500	16.6 ± 3.5	1.01 ± 0.54	$0.79^{+0.18}_{-0.15}$	$0.89^{+0.85}_{-0.74}$	19.3 ± 3.7	21
High Δm , $N_b = 1$, $m_T^b > 175$ GeV, $N_t = 0$, $N_{\text{res}} = 0$, $N_W = 0$, $H_T > 1000$ GeV							
61	250–350	214^{+21}_{-19}	189^{+35}_{-33}	4.9 ± 1.0	118^{+28}_{-24}	526^{+50}_{-47}	639
62	350–450	$88.0^{+9.8}_{-9.0}$	98^{+19}_{-18}	$3.12^{+0.61}_{-0.58}$	$16.8^{+4.8}_{-4.1}$	206 ± 22	233
63	450–550	39.5 ± 5.2	71^{+15}_{-14}	$1.62^{+0.35}_{-0.30}$	$5.7^{+2.0}_{-1.7}$	118^{+16}_{-15}	124
64	> 550	$40.1^{+5.2}_{-4.9}$	128^{+29}_{-27}	$5.3^{+1.1}_{-1.2}$	$3.5^{+1.4}_{-1.1}$	177^{+30}_{-28}	179
High Δm , $N_b \geq 2$, $m_T^b > 175$ GeV, $N_t = 0$, $N_{\text{res}} = 0$, $N_W = 0$, $H_T > 1000$ GeV							
65	250–350	68.1 ± 7.8	$30.4^{+5.7}_{-5.4}$	2.11 ± 0.40	35^{+11}_{-10}	135 ± 15	139
66	350–450	19.3 ± 3.1	21.4 ± 4.2	$1.04^{+0.19}_{-0.16}$	$2.48^{+0.97}_{-0.80}$	$44.2^{+5.6}_{-5.3}$	64
67	450–550	8.9 ± 2.2	$12.5^{+3.2}_{-3.0}$	0.91 ± 0.16	$0.89^{+0.40}_{-0.34}$	$23.2^{+4.0}_{-3.7}$	23
68	> 550	10.8 ± 2.3	$21.8^{+5.2}_{-4.9}$	1.37 ± 0.21	$0.90^{+0.77}_{-0.48}$	$34.8^{+6.0}_{-5.5}$	45
High Δm , $N_b = 1$, $m_T^b > 175$ GeV, $N_t \geq 1$, $N_{\text{res}} = 0$, $N_W = 0$, $H_T < 1000$ GeV							
69	250–550	376 ± 65	$35.3^{+7.6}_{-6.9}$	12.2 ± 1.8	$4.7^{+2.2}_{-1.9}$	428 ± 68	340
70	550–650	7.6 ± 1.8	$5.1^{+1.4}_{-1.3}$	1.99 ± 0.32	0.13 ± 0.13	14.9 ± 2.5	17
71	> 650	2.57 ± 0.86	$3.6^{+1.1}_{-1.0}$	$1.28^{+0.25}_{-0.23}$	0.09 ± 0.12	$7.5^{+1.5}_{-1.4}$	6
High Δm , $N_b = 1$, $m_T^b > 175$ GeV, $N_t \geq 1$, $N_{\text{res}} = 0$, $N_W = 0$, $1000 < H_T < 1500$ GeV							
72	250–550	82^{+13}_{-14}	$12.0^{+2.5}_{-2.3}$	4.66 ± 0.70	$1.8^{+1.4}_{-1.3}$	101^{+14}_{-15}	94
73	550–650	2.84 ± 0.84	$1.79^{+0.58}_{-0.55}$	0.53 ± 0.12	< 0.01	$5.2^{+1.1}_{-1.0}$	2
74	> 650	$3.13^{+0.99}_{-0.94}$	$2.74^{+0.81}_{-0.76}$	0.94 ± 0.17	$0.07^{+0.06}_{-0.05}$	$6.9^{+1.4}_{-1.3}$	4
High Δm , $N_b = 1$, $m_T^b > 175$ GeV, $N_t \geq 1$, $N_{\text{res}} = 0$, $N_W = 0$, $H_T > 1500$ GeV							
75	250–550	23.5 ± 4.5	$3.84^{+0.91}_{-0.86}$	$0.97^{+0.20}_{-0.19}$	3.9 ± 1.1	32.2 ± 5.0	28
76	550–650	0.87 ± 0.36	$0.28^{+0.17}_{-0.16}$	$0.18^{+0.06}_{-0.05}$	$0.05^{+0.06}_{-0.05}$	1.38 ± 0.42	4
77	> 650	1.20 ± 0.41	$0.49^{+0.22}_{-0.20}$	0.30 ± 0.08	< 0.01	1.99 ± 0.48	3
High Δm , $N_b = 1$, $m_T^b > 175$ GeV, $N_t = 0$, $N_{\text{res}} = 0$, $N_W \geq 1$, $H_T < 1300$ GeV							
78	250–350	342 ± 35	$47.6^{+9.6}_{-9.1}$	$11.8^{+1.7}_{-1.6}$	4.8 ± 2.5	406 ± 39	351
79	350–450	62.4 ± 7.1	$24.1^{+5.2}_{-4.8}$	8.4 ± 1.7	$3.5^{+2.9}_{-2.7}$	98^{+11}_{-10}	90
80	> 450	$17.1^{+2.7}_{-2.5}$	$13.0^{+2.8}_{-2.6}$	2.92 ± 0.46	$3.3^{+2.3}_{-2.0}$	$36.4^{+5.2}_{-4.8}$	29

Table C.4: Observed number of events and SM background predictions in search bins 81–107.

Search bin	p_T^{miss} [GeV]	Lost lepton	$Z \rightarrow \nu\bar{\nu}$	Rare	QCD multijet	Total SM	N_{data}
High Δm , $N_b = 1$, $m_T^b > 175$ GeV, $N_t = 0$, $N_{\text{res}} = 0$, $N_W \geq 1$, $H_T > 1300$ GeV							
81	250–350	6.71 ± 0.98	$2.10^{+0.54}_{-0.51}$	0.37 ± 0.10	$1.77^{+0.69}_{-0.64}$	$11.0^{+1.5}_{-1.4}$	13
82	350–450	$2.16^{+0.46}_{-0.41}$	$1.04^{+0.32}_{-0.30}$	$0.22^{+0.07}_{-0.06}$	0.75 ± 0.52	$4.16^{+0.84}_{-0.79}$	4
83	> 450	2.18 ± 0.47	1.53 ± 0.41	0.36 ± 0.09	$0.49^{+0.40}_{-0.38}$	4.56 ± 0.81	4
High Δm , $N_b = 1$, $m_T^b > 175$ GeV, $N_t = 0$, $N_{\text{res}} \geq 1$, $N_W = 0$, $H_T < 1000$ GeV							
84	250–350	2260^{+160}_{-170}	262^{+51}_{-47}	$68.5^{+8.7}_{-9.2}$	82^{+30}_{-25}	2670^{+180}_{-190}	2506
85	350–450	343^{+30}_{-33}	100^{+20}_{-18}	26.3 ± 3.8	$20.8^{+9.9}_{-8.1}$	490 ± 42	483
86	450–550	$50.5^{+6.8}_{-6.4}$	$35.4^{+7.7}_{-7.1}$	$8.0^{+1.4}_{-1.2}$	$5.7^{+3.1}_{-2.5}$	100^{+12}_{-11}	92
87	550–650	9.2 ± 1.6	$12.2^{+3.1}_{-2.8}$	$2.22^{+0.34}_{-0.38}$	$0.81^{+0.84}_{-0.75}$	24.4 ± 3.8	25
88	> 650	2.34 ± 0.66	$5.1^{+1.4}_{-1.3}$	$0.95^{+0.18}_{-0.16}$	0.44 ± 0.51	$8.8^{+1.7}_{-1.6}$	10
High Δm , $N_b = 1$, $m_T^b > 175$ GeV, $N_t = 0$, $N_{\text{res}} \geq 1$, $N_W = 0$, $1000 < H_T < 1500$ GeV							
89	250–350	54.6 ± 6.0	$8.4^{+2.0}_{-1.8}$	$1.28^{+0.28}_{-0.24}$	$2.7^{+1.7}_{-1.3}$	67.0 ± 7.3	69
90	350–450	20.4 ± 3.1	$4.9^{+1.2}_{-1.1}$	$1.09^{+0.20}_{-0.23}$	1.77 ± 0.85	28.2 ± 4.0	34
91	450–550	7.2 ± 1.3	$3.50^{+0.97}_{-0.89}$	0.81 ± 0.29	$0.33^{+0.20}_{-0.17}$	11.8 ± 1.8	9
92	550–650	2.83 ± 0.68	$2.89^{+0.88}_{-0.81}$	0.23 ± 0.07	$0.15^{+0.09}_{-0.08}$	$6.1^{+1.2}_{-1.1}$	7
93	> 650	2.85 ± 0.60	$4.1^{+1.2}_{-1.1}$	$0.63^{+0.12}_{-0.14}$	$0.66^{+0.39}_{-0.33}$	$8.2^{+1.6}_{-1.5}$	3
High Δm , $N_b = 1$, $m_T^b > 175$ GeV, $N_t = 0$, $N_{\text{res}} \geq 1$, $N_W = 0$, $H_T > 1500$ GeV							
94	250–350	$6.8^{+1.1}_{-1.2}$	$1.33^{+0.46}_{-0.41}$	0.12 ± 0.06	2.2 ± 1.3	10.5 ± 2.1	8
95	350–450	$2.77^{+0.62}_{-0.58}$	$0.82^{+0.31}_{-0.29}$	0.08 ± 0.04	$0.40^{+0.42}_{-0.24}$	$4.07^{+0.97}_{-0.79}$	1
96	450–550	0.96 ± 0.32	0.64 ± 0.27	0.03 ± 0.03	$0.07^{+0.05}_{-0.04}$	1.70 ± 0.45	1
97	550–650	0.37 ± 0.14	$0.31^{+0.23}_{-0.14}$	0.05 ± 0.03	$0.05^{+0.04}_{-0.03}$	$0.78^{+0.30}_{-0.21}$	0
98	> 650	1.12 ± 0.39	$0.78^{+0.29}_{-0.27}$	0.14 ± 0.05	$0.05^{+0.04}_{-0.03}$	2.09 ± 0.52	4
High Δm , $N_b = 1$, $m_T^b > 175$ GeV, $N_t \geq 1$, $N_{\text{res}} = 0$, $N_W \geq 1$							
99	250–550	4.8 ± 1.0	0.36 ± 0.15	1.15 ± 0.21	0.06 ± 0.06	6.3 ± 1.1	2
100	> 550	0.24 ± 0.15	< 0.03	$0.42^{+0.10}_{-0.09}$	$0.05^{+0.05}_{-0.04}$	$0.71^{+0.22}_{-0.20}$	1
High Δm , $N_b = 1$, $m_T^b > 175$ GeV, $N_t \geq 1$, $N_{\text{res}} \geq 1$, $N_W = 0$							
101	250–550	7.3 ± 1.3	0.70 ± 0.24	2.56 ± 0.42	0.37 ± 0.25	$10.9^{+1.7}_{-1.6}$	15
102	> 550	0.51 ± 0.19	$0.32^{+0.17}_{-0.14}$	$0.84^{+0.18}_{-0.19}$	0.01 ± 0.01	1.68 ± 0.34	1
High Δm , $N_b = 1$, $m_T^b > 175$ GeV, $N_t = 0$, $N_{\text{res}} \geq 1$, $N_W \geq 1$							
103	250–550	25.5 ± 3.6	$2.12^{+0.63}_{-0.59}$	4.51 ± 0.78	0.02 ± 0.02	32.2 ± 4.2	34
104	> 550	0.32 ± 0.13	$0.32^{+0.15}_{-0.14}$	0.33 ± 0.08	$0.08^{+0.07}_{-0.06}$	$1.05^{+0.23}_{-0.28}$	1
High Δm , $N_b = 2$, $m_T^b > 175$ GeV, $N_t = 1$, $N_{\text{res}} = 0$, $N_W = 0$, $H_T < 1000$ GeV							
105	250–550	80^{+15}_{-14}	$9.9^{+1.9}_{-1.7}$	7.2 ± 1.1	$0.20^{+0.17}_{-0.13}$	97^{+16}_{-15}	79
106	550–650	1.69 ± 0.60	1.84 ± 0.88	1.45 ± 0.24	0.14 ± 0.21	$5.1^{+1.2}_{-1.1}$	3
107	> 650	1.21 ± 0.57	1.28 ± 0.46	$0.95^{+0.18}_{-0.19}$	< 0.01	3.45 ± 0.78	2

Table C.5: Observed number of events and SM background predictions in search bins 108–136.

Search bin	p_T^{miss} [GeV]	Lost lepton	$Z \rightarrow \nu\bar{\nu}$	Rare	QCD multijet	Total SM	N_{data}
High Δm , $N_b = 2$, $m_T^b > 175$ GeV, $N_t = 1$, $N_{\text{res}} = 0$, $N_W = 0$, $1000 < H_T < 1500$ GeV							
108	250–550	23.5 ± 4.0	$3.57^{+0.87}_{-0.71}$	2.67 ± 0.46	0.50 ± 0.45	30.2 ± 4.3	36
109	550–650	0.73 ± 0.36	$0.24^{+0.15}_{-0.13}$	0.33 ± 0.08	< 0.01	1.30 ± 0.41	3
110	> 650	$1.18^{+0.52}_{-0.49}$	0.75 ± 0.28	0.53 ± 0.12	< 0.01	$2.46^{+0.64}_{-0.60}$	4
High Δm , $N_b = 2$, $m_T^b > 175$ GeV, $N_t = 1$, $N_{\text{res}} = 0$, $N_W = 0$, $H_T > 1500$ GeV							
111	250–550	8.4 ± 1.8	$0.67^{+0.23}_{-0.25}$	0.60 ± 0.13	$0.95^{+0.57}_{-0.52}$	$10.7^{+1.9}_{-2.0}$	9
112	550–650	0.52 ± 0.35	0.23 ± 0.20	0.09 ± 0.04	0.02 ± 0.03	0.86 ± 0.41	1
113	> 650	0.43 ± 0.25	0.37 ± 0.21	$0.14^{+0.04}_{-0.05}$	0.02 ± 0.02	0.96 ± 0.34	0
High Δm , $N_b = 2$, $m_T^b > 175$ GeV, $N_t = 0$, $N_{\text{res}} = 0$, $N_W = 1$, $H_T < 1300$ GeV							
114	250–350	67.0 ± 8.0	$7.2^{+1.6}_{-1.5}$	3.61 ± 0.55	0.62 ± 0.46	78.4 ± 8.7	44
115	350–450	$11.4^{+2.5}_{-2.0}$	$3.7^{+1.1}_{-1.3}$	2.05 ± 0.37	$0.28^{+0.24}_{-0.22}$	$17.5^{+3.1}_{-2.8}$	19
116	> 450	3.27 ± 0.72	$1.91^{+0.47}_{-0.44}$	$1.43^{+0.28}_{-0.26}$	0.23 ± 0.24	$6.8^{+1.1}_{-1.0}$	10
High Δm , $N_b = 2$, $m_T^b > 175$ GeV, $N_t = 0$, $N_{\text{res}} = 0$, $N_W = 1$, $H_T > 1300$ GeV							
117	250–350	$2.44^{+0.55}_{-0.63}$	0.08 ± 0.05	0.08 ± 0.04	0.26 ± 0.21	$2.86^{+0.62}_{-0.69}$	0
118	350–450	$0.98^{+0.48}_{-0.42}$	$0.24^{+0.14}_{-0.13}$	0.05 ± 0.03	< 0.01	$1.27^{+0.51}_{-0.45}$	0
119	> 450	0.94 ± 0.35	$0.09^{+0.07}_{-0.06}$	0.09 ± 0.04	< 0.01	$1.13^{+0.38}_{-0.36}$	2
High Δm , $N_b = 2$, $m_T^b > 175$ GeV, $N_t = 0$, $N_{\text{res}} = 1$, $N_W = 0$, $H_T < 1000$ GeV							
120	250–350	374^{+29}_{-32}	69^{+12}_{-11}	38.9 ± 5.5	$9.0^{+4.9}_{-4.2}$	492^{+37}_{-40}	454
121	350–450	64.6 ± 6.8	$24.6^{+4.6}_{-4.3}$	17.9 ± 2.6	$5.8^{+3.9}_{-3.6}$	113 ± 11	114
122	450–550	11.8 ± 2.0	$8.0^{+1.9}_{-1.6}$	$6.2^{+1.0}_{-1.1}$	$3.2^{+2.2}_{-2.0}$	$29.3^{+4.5}_{-3.6}$	35
123	550–650	2.21 ± 0.78	3.7 ± 1.0	1.50 ± 0.28	0.9 ± 1.2	8.3 ± 1.8	6
124	> 650	1.50 ± 0.75	1.38 ± 0.47	0.74 ± 0.14	0.31 ± 0.45	3.9 ± 1.0	4
High Δm , $N_b = 2$, $m_T^b > 175$ GeV, $N_t = 0$, $N_{\text{res}} = 1$, $N_W = 0$, $1000 < H_T < 1500$ GeV							
125	250–350	$15.9^{+2.4}_{-2.7}$	$2.13^{+0.62}_{-0.58}$	$0.79^{+0.15}_{-0.18}$	3.1 ± 2.0	$21.9^{+3.8}_{-4.0}$	27
126	350–450	3.56 ± 0.85	$1.52^{+0.44}_{-0.41}$	$0.38^{+0.11}_{-0.12}$	$2.3^{+2.6}_{-2.1}$	$7.8^{+3.1}_{-2.4}$	5
127	450–550	1.76 ± 0.55	$1.10^{+0.40}_{-0.38}$	0.50 ± 0.11	0.09 ± 0.06	$3.45^{+0.76}_{-0.71}$	4
128	550–650	0.84 ± 0.37	$0.58^{+0.32}_{-0.28}$	$0.28^{+0.09}_{-0.08}$	0.07 ± 0.06	1.77 ± 0.51	2
129	> 650	1.14 ± 0.43	0.64 ± 0.23	0.90 ± 0.46	< 0.01	2.68 ± 0.69	1
High Δm , $N_b = 2$, $m_T^b > 175$ GeV, $N_t = 0$, $N_{\text{res}} = 1$, $N_W = 0$, $H_T > 1500$ GeV							
130	250–350	2.67 ± 0.61	$0.45^{+0.22}_{-0.20}$	0.05 ± 0.04	$0.28^{+0.18}_{-0.16}$	3.44 ± 0.71	4
131	350–450	1.26 ± 0.40	0.26 ± 0.14	$0.01^{+0.04}_{-0.03}$	0.06 ± 0.06	1.59 ± 0.45	2
132	450–550	$0.16^{+0.13}_{-0.12}$	$0.22^{+0.15}_{-0.14}$	0.04 ± 0.03	0.03 ± 0.02	$0.46^{+0.22}_{-0.20}$	1
133	550–650	0.17 ± 0.11	0.20 ± 0.14	0.03 ± 0.02	< 0.01	0.40 ± 0.18	0
134	> 650	$0.31^{+0.19}_{-0.17}$	$0.37^{+0.20}_{-0.19}$	0.08 ± 0.04	< 0.01	0.76 ± 0.28	0
High Δm , $N_b = 2$, $m_T^b > 175$ GeV, $N_t = 1$, $N_{\text{res}} = 0$, $N_W = 1$							
135	250–550	0.81 ± 0.23	0.04 ± 0.04	0.70 ± 0.13	< 0.01	1.54 ± 0.29	3
136	> 550	0.10 ± 0.05	0.05 ± 0.04	0.21 ± 0.05	< 0.01	0.36 ± 0.09	0

Table C.6: Observed number of events and SM background predictions in search bins 137–161.

Search bin	p_T^{miss} [GeV]	Lost lepton	$Z \rightarrow \nu\bar{\nu}$	Rare	QCD multijet	Total SM	N_{data}
High Δm , $N_b = 2$, $m_T^b > 175$ GeV, $N_t = 1$, $N_{\text{res}} = 1$, $N_W = 0$, $H_T < 1300$ GeV							
137	250–350	$4.5^{+1.1}_{-1.2}$	$0.07^{+0.06}_{-0.05}$	$1.40^{+0.25}_{-0.23}$	< 0.01	$5.9^{+1.2}_{-1.3}$	5
138	350–450	$1.10^{+0.50}_{-0.43}$	$0.14^{+0.10}_{-0.09}$	$1.28^{+0.24}_{-0.22}$	< 0.01	$2.52^{+0.59}_{-0.52}$	5
139	> 450	$0.62^{+0.27}_{-0.24}$	0.17 ± 0.10	2.09 ± 0.39	1.2 ± 1.4	4.1 ± 1.5	3
High Δm , $N_b = 2$, $m_T^b > 175$ GeV, $N_t = 1$, $N_{\text{res}} = 1$, $N_W = 0$, $H_T > 1300$ GeV							
140	250–350	0.75 ± 0.19	< 0.01	$0.16^{+0.06}_{-0.05}$	< 0.01	0.90 ± 0.20	2
141	350–450	0.31 ± 0.12	0.02 ± 0.02	0.05 ± 0.04	< 0.01	0.38 ± 0.13	0
142	> 450	$0.21^{+0.11}_{-0.10}$	0.10 ± 0.08	0.33 ± 0.08	< 0.01	$0.64^{+0.17}_{-0.16}$	0
High Δm , $N_b = 2$, $m_T^b > 175$ GeV, $N_t = 0$, $N_{\text{res}} = 1$, $N_W = 1$							
143	250–550	$7.3^{+1.4}_{-1.3}$	0.40 ± 0.16	$3.18^{+0.62}_{-0.58}$	< 0.01	10.9 ± 1.7	6
144	> 550	0.09 ± 0.03	0.05 ± 0.05	$0.24^{+0.07}_{-0.06}$	< 0.01	0.37 ± 0.09	0
High Δm , $N_b = 2$, $m_T^b > 175$ GeV, $N_t = 2$, $N_{\text{res}} = 0$, $N_W = 0$							
145	250–450	$0.92^{+0.37}_{-0.33}$	0.04 ± 0.04	0.78 ± 0.16	< 0.01	$1.74^{+0.44}_{-0.41}$	2
146	> 450	$0.20^{+0.13}_{-0.17}$	< 0.01	0.36 ± 0.09	< 0.01	$0.56^{+0.17}_{-0.21}$	0
High Δm , $N_b = 2$, $m_T^b > 175$ GeV, $N_t = 0$, $N_{\text{res}} = 0$, $N_W = 2$							
147	> 250	0.46 ± 0.23	0.04 ± 0.04	0.24 ± 0.06	< 0.01	0.74 ± 0.26	0
High Δm , $N_b = 2$, $m_T^b > 175$ GeV, $N_t = 0$, $N_{\text{res}} = 2$, $N_W = 0$, $H_T < 1300$ GeV							
148	250–450	$15.1^{+2.2}_{-2.9}$	0.82 ± 0.35	10.6 ± 1.9	< 0.01	$26.5^{+3.5}_{-4.3}$	19
149	> 450	0.89 ± 0.29	$0.16^{+0.09}_{-0.08}$	$1.81^{+0.44}_{-0.35}$	0.58 ± 0.59	$3.45^{+0.85}_{-0.79}$	3
High Δm , $N_b = 2$, $m_T^b > 175$ GeV, $N_t = 0$, $N_{\text{res}} = 2$, $N_W = 0$, $H_T > 1300$ GeV							
150	250–450	$0.43^{+0.19}_{-0.18}$	< 0.01	0.03 ± 0.03	< 0.01	$0.46^{+0.20}_{-0.18}$	0
151	> 450	0.19 ± 0.15	0.02 ± 0.02	$0.04^{+0.03}_{-0.02}$	< 0.01	0.24 ± 0.15	0
High Δm , $N_b = 2$, $m_T^b > 175$ GeV, $(N_t + N_{\text{res}} + N_W) \geq 3$							
152	> 250	$0.38^{+0.20}_{-0.28}$	< 0.01	$0.06^{+0.04}_{-0.03}$	< 0.01	$0.44^{+0.21}_{-0.29}$	1
High Δm , $N_b \geq 3$, $m_T^b > 175$ GeV, $N_t = 1$, $N_{\text{res}} = 0$, $N_W = 0$, $H_T < 1000$ GeV							
153	250–350	$10.5^{+2.2}_{-2.0}$	$0.20^{+0.11}_{-0.14}$	0.41 ± 0.08	0.02 ± 0.02	11.1 ± 2.2	8
154	350–550	8.1 ± 1.9	$0.41^{+0.15}_{-0.16}$	0.82 ± 0.15	< 0.01	9.3 ± 1.9	6
155	> 550	1.10 ± 0.60	0.27 ± 0.15	$0.45^{+0.12}_{-0.10}$	< 0.01	1.82 ± 0.65	4
High Δm , $N_b \geq 3$, $m_T^b > 175$ GeV, $N_t = 1$, $N_{\text{res}} = 0$, $N_W = 0$, $1000 < H_T < 1500$ GeV							
156	250–350	5.0 ± 1.2	0.24 ± 0.14	$0.32^{+0.08}_{-0.09}$	0.31 ± 0.32	5.9 ± 1.3	4
157	350–550	1.64 ± 0.61	$0.24^{+0.14}_{-0.15}$	$0.25^{+0.07}_{-0.06}$	< 0.01	$2.13^{+0.67}_{-0.63}$	1
158	> 550	0.12 ± 0.12	0.18 ± 0.12	0.20 ± 0.05	0.01 ± 0.02	0.52 ± 0.18	1
High Δm , $N_b \geq 3$, $m_T^b > 175$ GeV, $N_t = 1$, $N_{\text{res}} = 0$, $N_W = 0$, $H_T > 1500$ GeV							
159	250–350	$4.0^{+1.4}_{-1.3}$	$0.04^{+0.05}_{-0.06}$	0.03 ± 0.03	0.10 ± 0.08	4.1 ± 1.4	9
160	350–550	0.59 ± 0.33	0.19 ± 0.24	0.04 ± 0.03	< 0.01	0.82 ± 0.42	2
161	> 550	0.15 ± 0.10	$0.07^{+0.10}_{-0.09}$	0.08 ± 0.04	< 0.01	$0.30^{+0.15}_{-0.14}$	0

Table C.7: Observed number of events and SM background predictions in search bins 162–182.

Search bin	p_T^{miss} [GeV]	Lost lepton	$Z \rightarrow \nu\bar{\nu}$	Rare	QCD multijet	Total SM	N_{data}
High Δm , $N_b \geq 3$, $m_T^b > 175$ GeV, $N_t = 0$, $N_{\text{res}} = 0$, $N_W = 1$							
162	250–350	$17.9^{+2.7}_{-2.5}$	$0.64^{+0.27}_{-0.39}$	0.82 ± 0.16	$0.40^{+0.49}_{-0.41}$	$19.8^{+2.9}_{-2.7}$	7
163	350–550	$3.22^{+0.80}_{-0.90}$	$0.5^{+1.3}_{-0.2}$	$0.55^{+0.10}_{-0.11}$	$0.16^{+0.18}_{-0.17}$	$4.5^{+1.4}_{-1.1}$	2
164	> 550	0.46 ± 0.28	0.06 ± 0.05	0.14 ± 0.04	0.12 ± 0.13	0.78 ± 0.33	0
High Δm , $N_b \geq 3$, $m_T^b > 175$ GeV, $N_t = 0$, $N_{\text{res}} = 1$, $N_W = 0$, $H_T < 1000$ GeV							
165	250–350	82.5 ± 7.8	$5.0^{+1.5}_{-2.6}$	5.83 ± 0.92	$1.2^{+1.1}_{-1.0}$	94.4 ± 8.9	105
166	350–550	$18.4^{+3.5}_{-3.8}$	4.5 ± 1.3	$3.62^{+0.59}_{-0.63}$	< 0.01	$26.5^{+4.1}_{-4.5}$	20
167	> 550	0.66 ± 0.34	0.13 ± 0.08	0.40 ± 0.09	0.01 ± 0.01	1.20 ± 0.36	1
High Δm , $N_b \geq 3$, $m_T^b > 175$ GeV, $N_t = 0$, $N_{\text{res}} = 1$, $N_W = 0$, $1000 < H_T < 1500$ GeV							
168	250–350	6.5 ± 1.6	0.55 ± 0.27	0.15 ± 0.06	0.02 ± 0.02	7.2 ± 1.7	7
169	350–550	1.61 ± 0.56	$0.23^{+0.13}_{-0.14}$	$0.30^{+0.08}_{-0.07}$	0.01 ± 0.01	2.15 ± 0.61	3
170	> 550	0.22 ± 0.18	0.31 ± 0.17	$0.11^{+0.05}_{-0.04}$	0.09 ± 0.13	0.73 ± 0.29	1
High Δm , $N_b \geq 3$, $m_T^b > 175$ GeV, $N_t = 0$, $N_{\text{res}} = 1$, $N_W = 0$, $H_T > 1500$ GeV							
171	250–350	1.46 ± 0.50	0.03 ± 0.04	< 0.01	$0.03^{+0.03}_{-0.02}$	1.53 ± 0.51	4
172	350–550	0.45 ± 0.29	$0.20^{+0.27}_{-0.23}$	0.03 ± 0.02	0.02 ± 0.02	$0.70^{+0.39}_{-0.37}$	1
173	> 550	0.47 ± 0.39	0.03 ± 0.03	< 0.02	0.02 ± 0.02	0.53 ± 0.40	0
High Δm , $N_b \geq 3$, $m_T^b > 175$ GeV, $N_t = 1$, $N_{\text{res}} = 0$, $N_W = 1$							
174	> 250	$0.45^{+0.19}_{-0.21}$	$0.03^{+0.03}_{-0.04}$	0.18 ± 0.05	< 0.01	0.66 ± 0.21	0
High Δm , $N_b \geq 3$, $m_T^b > 175$ GeV, $N_t = 1$, $N_{\text{res}} = 1$, $N_W = 0$							
175	250–350	2.37 ± 0.71	0.04 ± 0.04	$0.30^{+0.08}_{-0.07}$	< 0.03	2.72 ± 0.73	2
176	> 350	1.48 ± 0.49	0.18 ± 0.09	0.56 ± 0.12	< 0.01	2.23 ± 0.55	0
High Δm , $N_b \geq 3$, $m_T^b > 175$ GeV, $N_t = 0$, $N_{\text{res}} = 1$, $N_W = 1$							
177	> 250	$0.84^{+0.63}_{-0.52}$	0.04 ± 0.05	$0.45^{+0.11}_{-0.10}$	0.06 ± 0.07	$1.39^{+0.66}_{-0.56}$	1
High Δm , $N_b \geq 3$, $m_T^b > 175$ GeV, $N_t = 2$, $N_{\text{res}} = 0$, $N_W = 0$							
178	> 250	0.56 ± 0.23	0.06 ± 0.06	0.27 ± 0.07	< 0.01	0.90 ± 0.27	1
High Δm , $N_b \geq 3$, $m_T^b > 175$ GeV, $N_t = 0$, $N_{\text{res}} = 0$, $N_W = 2$							
179	> 250	0.04 ± 0.02	< 0.01	0.04 ± 0.02	< 0.01	0.08 ± 0.03	0
High Δm , $N_b \geq 3$, $m_T^b > 175$ GeV, $N_t = 0$, $N_{\text{res}} = 2$, $N_W = 0$							
180	250–350	$2.9^{+1.1}_{-0.9}$	$0.02^{+0.02}_{-0.03}$	$0.44^{+0.13}_{-0.11}$	< 0.01	$3.4^{+1.2}_{-1.0}$	6
181	> 350	$0.88^{+0.36}_{-0.33}$	$0.03^{+0.03}_{-0.02}$	0.42 ± 0.12	< 0.01	$1.33^{+0.42}_{-0.37}$	0
High Δm , $N_b \geq 3$, $m_T^b > 175$ GeV, $(N_t + N_{\text{res}} + N_W) \geq 3$							
182	> 250	0.07 ± 0.02	< 0.01	0.04 ± 0.02	< 0.01	0.11 ± 0.03	0

APPENDIX D

Z Invisible Predictions

This appendix presents the Z invisible background predictions in the 183 search bins for the analysis. The normalization factor R_Z , shape factor S_γ , number of $Z \rightarrow \nu\bar{\nu}$ MC events $N_{\text{MC}}^{Z \rightarrow \nu\bar{\nu}}$, and the background prediction $N_{\text{pred}}^{Z \rightarrow \nu\bar{\nu}}$ including statistical uncertainties are provided for each search bin in Tables D.1 to D.7. The uncertainty for the prediction $N_{\text{pred}}^{Z \rightarrow \nu\bar{\nu}}$ is calculated by propagating the statistical uncertainties of R_Z , S_γ , and $N_{\text{MC}}^{Z \rightarrow \nu\bar{\nu}}$ through the calculation in Eq. (6.2).

Table D.1: Prediction for the Z invisible background ($N_{\text{pred}}^{Z \rightarrow \nu\bar{\nu}}$) with statistical uncertainty in low Δm search bins 0–27. The normalization factor (R_Z), shape factor (S_γ), and number of Z $\rightarrow \nu\bar{\nu}$ MC events ($N_{\text{MC}}^{Z \rightarrow \nu\bar{\nu}}$) are also shown for each search bin including their statistical uncertainties.

Search region	$p_{\text{T}}^{\text{miss}}$ [GeV]	R_Z	S_γ	N_{MC}	N_{pred}
low Δm , $N_{\text{b}} = 0$, $N_{\text{SV}} = 0$, $p_{\text{T}}^{\text{ISR}} \geq 500$ GeV, $2 \leq N_{\text{j}} \leq 5$					
0	450–550	0.858 ± 0.019	0.828 ± 0.010	7351.704 ± 25.359	5220.633 ± 63.439
1	550–650	0.858 ± 0.019	0.811 ± 0.011	5501.338 ± 18.526	3828.691 ± 52.439
2	650–750	0.858 ± 0.019	0.765 ± 0.014	2723.384 ± 10.098	1787.470 ± 33.927
3	> 750	0.858 ± 0.019	0.690 ± 0.014	2696.482 ± 10.565	1595.827 ± 31.922
low Δm , $N_{\text{b}} = 0$, $N_{\text{SV}} = 0$, $p_{\text{T}}^{\text{ISR}} \geq 500$ GeV, $N_{\text{j}} \geq 6$					
4	450–550	0.858 ± 0.019	0.910 ± 0.072	145.270 ± 2.429	113.356 ± 9.205
5	550–650	0.858 ± 0.019	0.898 ± 0.081	96.295 ± 1.953	74.159 ± 6.854
6	650–750	0.858 ± 0.019	1.024 ± 0.109	55.380 ± 1.468	48.664 ± 5.332
7	> 750	0.858 ± 0.019	0.686 ± 0.074	72.912 ± 1.768	42.929 ± 4.762
low Δm , $N_{\text{b}} = 0$, $N_{\text{SV}} \geq 1$, $p_{\text{T}}^{\text{ISR}} \geq 500$ GeV, $2 \leq N_{\text{j}} \leq 5$					
8	450–550	0.709 ± 0.055	0.747 ± 0.060	217.038 ± 4.377	114.940 ± 9.489
9	550–650	0.709 ± 0.055	0.714 ± 0.062	163.992 ± 3.301	83.026 ± 7.408
10	650–750	0.709 ± 0.055	0.682 ± 0.081	86.060 ± 1.933	41.587 ± 5.021
11	> 750	0.709 ± 0.055	0.512 ± 0.069	81.084 ± 1.974	29.423 ± 4.030
low Δm , $N_{\text{b}} = 0$, $N_{\text{SV}} \geq 1$, $p_{\text{T}}^{\text{ISR}} \geq 500$ GeV, $N_{\text{j}} \geq 6$					
12	450–550	0.709 ± 0.055	0.648 ± 0.287	5.355 ± 0.503	2.460 ± 1.114
13	550–650	0.709 ± 0.055	0.667 ± 0.362	2.986 ± 0.369	1.412 ± 0.786
14	650–750	0.709 ± 0.055	1.416 ± 0.842	1.696 ± 0.306	1.702 ± 1.058
15	> 750	0.709 ± 0.055	0.857 ± 0.564	3.061 ± 0.390	1.859 ± 1.246
low Δm , $N_{\text{b}} = 1$, $N_{\text{SV}} = 0$, $m_{\text{T}}^{\text{b}} < 175$ GeV, $300 \leq p_{\text{T}}^{\text{ISR}} < 500$ GeV, $p_{\text{T}}^{\text{b}} < 40$ GeV					
16	300–400	1.036 ± 0.041	1.059 ± 0.048	1008.596 ± 15.060	1107.049 ± 52.709
17	400–500	1.036 ± 0.041	1.000 ± 0.071	236.986 ± 6.466	245.526 ± 18.728
18	500–600	1.036 ± 0.041	1.098 ± 0.173	28.445 ± 1.558	32.380 ± 5.403
19	> 600	1.036 ± 0.041	1.006 ± 0.309	5.681 ± 0.460	5.919 ± 1.883
low Δm , $N_{\text{b}} = 1$, $N_{\text{SV}} = 0$, $m_{\text{T}}^{\text{b}} < 175$ GeV, $300 \leq p_{\text{T}}^{\text{ISR}} < 500$ GeV, $40 < p_{\text{T}}^{\text{b}} < 70$ GeV					
20	300–400	1.036 ± 0.041	0.963 ± 0.057	428.005 ± 9.286	427.233 ± 26.736
21	400–500	1.036 ± 0.041	0.965 ± 0.096	79.570 ± 3.406	79.603 ± 8.636
22	500–600	1.036 ± 0.041	1.321 ± 0.443	7.443 ± 0.624	10.190 ± 3.522
23	> 600	1.036 ± 0.041	0.496 ± 0.378	1.482 ± 0.227	0.762 ± 0.592
low Δm , $N_{\text{b}} = 1$, $N_{\text{SV}} = 0$, $m_{\text{T}}^{\text{b}} < 175$ GeV, $p_{\text{T}}^{\text{ISR}} \geq 500$ GeV, $p_{\text{T}}^{\text{b}} < 40$ GeV					
24	450–550	1.036 ± 0.041	0.970 ± 0.101	90.978 ± 2.869	91.408 ± 9.924
25	550–650	1.036 ± 0.041	0.993 ± 0.137	45.351 ± 1.508	46.675 ± 6.626
26	650–750	1.036 ± 0.041	0.963 ± 0.200	22.723 ± 0.990	22.682 ± 4.813
27	> 750	1.036 ± 0.041	0.986 ± 0.223	17.284 ± 0.863	17.667 ± 4.083

Table D.2: Prediction for the Z invisible background ($N_{\text{pred}}^{Z \rightarrow \nu\bar{\nu}}$) with statistical uncertainty in low Δm search bins 28–52. The normalization factor (R_Z), shape factor (S_γ), and number of Z $\rightarrow \nu\bar{\nu}$ MC events ($N_{\text{MC}}^{Z \rightarrow \nu\bar{\nu}}$) are also shown for each search bin including their statistical uncertainties.

Search region	$p_{\text{T}}^{\text{miss}}$ [GeV]	R_Z	S_γ	N_{MC}	N_{pred}
low Δm , $N_{\text{b}} = 1$, $N_{\text{SV}} = 0$, $m_{\text{T}}^{\text{b}} < 175$ GeV, $p_{\text{T}}^{\text{ISR}} \geq 500$ GeV, $40 < p_{\text{T}}^{\text{b}} < 70$ GeV					
28	450–550	1.036 ± 0.041	1.060 ± 0.145	44.599 ± 1.946	48.983 ± 7.016
29	550–650	1.036 ± 0.041	0.871 ± 0.185	18.702 ± 0.854	16.884 ± 3.670
30	650–750	1.036 ± 0.041	1.502 ± 0.454	7.454 ± 0.550	11.601 ± 3.610
31	> 750	1.036 ± 0.041	1.352 ± 0.457	6.417 ± 0.529	8.988 ± 3.128
low Δm , $N_{\text{b}} = 1$, $N_{\text{SV}} \geq 1$, $m_{\text{T}}^{\text{b}} < 175$ GeV, $p_{\text{T}}^{\text{ISR}} \geq 300$ GeV, $p_{\text{T}}^{\text{b}} < 40$ GeV					
32	300–400	0.770 ± 0.133	0.802 ± 0.143	73.375 ± 4.332	45.342 ± 8.528
33	400–500	0.770 ± 0.133	0.857 ± 0.181	20.304 ± 1.632	13.399 ± 3.031
34	> 500	0.770 ± 0.133	0.772 ± 0.224	12.583 ± 0.970	7.483 ± 2.243
low Δm , $N_{\text{b}} \geq 2$, $m_{\text{T}}^{\text{b}} < 175$ GeV, $300 \leq p_{\text{T}}^{\text{ISR}} < 500$ GeV, $p_{\text{T}}^{\text{b}12} < 80$ GeV					
35	300–400	1.048 ± 0.097	1.253 ± 0.157	67.050 ± 3.766	88.044 ± 12.117
36	400–500	1.048 ± 0.097	1.053 ± 0.383	19.158 ± 1.899	21.150 ± 7.980
37	> 500	1.048 ± 0.097	1.245 ± 0.598	3.624 ± 0.794	4.728 ± 2.499
low Δm , $N_{\text{b}} \geq 2$, $m_{\text{T}}^{\text{b}} < 175$ GeV, $300 \leq p_{\text{T}}^{\text{ISR}} < 500$ GeV, $80 < p_{\text{T}}^{\text{b}12} < 140$ GeV					
38	300–400	1.048 ± 0.097	1.109 ± 0.178	79.896 ± 3.599	92.915 ± 15.457
39	400–500	1.048 ± 0.097	0.899 ± 0.173	20.115 ± 1.627	18.961 ± 3.955
40	> 500	1.048 ± 0.097	1.551 ± 0.624	2.754 ± 0.328	4.478 ± 1.877
low Δm , $N_{\text{b}} \geq 2$, $m_{\text{T}}^{\text{b}} < 175$ GeV, $300 \leq p_{\text{T}}^{\text{ISR}} < 500$ GeV, $p_{\text{T}}^{\text{b}12} \geq 140$ GeV, $N_{\text{j}} \geq 7$					
41	300–400	1.048 ± 0.097	0.443 ± 0.393	1.940 ± 0.281	0.901 ± 0.810
42	400–500	1.048 ± 0.097	1.397 ± 0.910	0.546 ± 0.124	0.800 ± 0.552
43	> 500	1.048 ± 0.097	22.685 ± 22.151	0.226 ± 0.085	5.377 ± 5.623
low Δm , $N_{\text{b}} \geq 2$, $m_{\text{T}}^{\text{b}} < 175$ GeV, $p_{\text{T}}^{\text{ISR}} \geq 500$ GeV, $p_{\text{T}}^{\text{b}12} < 80$ GeV					
44	450–550	1.048 ± 0.097	0.810 ± 0.430	5.087 ± 0.429	4.320 ± 2.323
45	550–650	1.048 ± 0.097	0.828 ± 0.410	4.085 ± 0.387	3.544 ± 1.787
46	> 650	1.048 ± 0.097	0.903 ± 0.594	2.831 ± 0.319	2.681 ± 1.789
low Δm , $N_{\text{b}} \geq 2$, $m_{\text{T}}^{\text{b}} < 175$ GeV, $p_{\text{T}}^{\text{ISR}} \geq 500$ GeV, $80 < p_{\text{T}}^{\text{b}12} < 140$ GeV					
47	450–550	1.048 ± 0.097	0.663 ± 0.210	8.801 ± 0.628	6.113 ± 1.982
48	550–650	1.048 ± 0.097	1.052 ± 0.432	4.985 ± 0.539	5.495 ± 2.332
49	> 650	1.048 ± 0.097	1.078 ± 0.452	3.588 ± 0.381	4.054 ± 1.756
low Δm , $N_{\text{b}} \geq 2$, $m_{\text{T}}^{\text{b}} < 175$ GeV, $p_{\text{T}}^{\text{ISR}} \geq 500$ GeV, $p_{\text{T}}^{\text{b}12} \geq 140$ GeV, $N_{\text{j}} \geq 7$					
50	450–550	1.048 ± 0.097	2.079 ± 1.509	0.625 ± 0.169	1.363 ± 1.056
51	550–650	1.048 ± 0.097	0.944 ± 1.092	0.248 ± 0.093	0.245 ± 0.298
52	> 650	1.048 ± 0.097	5.331 ± 7.595	0.350 ± 0.138	1.955 ± 2.889

Table D.3: Prediction for the Z invisible background ($N_{\text{pred}}^{Z \rightarrow \nu\bar{\nu}}$) with statistical uncertainty in high Δm search bins 53–80. The normalization factor (R_Z), shape factor (S_γ), and number of $Z \rightarrow \nu\bar{\nu}$ MC events ($N_{\text{MC}}^{Z \rightarrow \nu\bar{\nu}}$) are also shown for each search bin including their statistical uncertainties.

Search region	$p_{\text{T}}^{\text{miss}}$ [GeV]	R_Z	S_γ	N_{MC}	N_{pred}
high Δm , $N_{\text{b}} = 1$, $m_{\text{T}}^{\text{b}} < 175$ GeV, $N_{\text{j}} \geq 7$, $N_{\text{res}} \geq 1$					
53	250–300	1.265 ± 0.051	1.067 ± 0.247	6.906 ± 0.801	9.319 ± 2.417
54	300–400	1.265 ± 0.051	1.505 ± 0.398	4.724 ± 0.468	8.994 ± 2.541
55	400–500	1.265 ± 0.051	0.498 ± 0.267	1.084 ± 0.173	0.683 ± 0.382
56	> 500	1.265 ± 0.051	1.379 ± 0.801	1.147 ± 0.241	2.002 ± 1.237
high Δm , $N_{\text{b}} \geq 2$, $m_{\text{T}}^{\text{b}} < 175$ GeV, $N_{\text{j}} \geq 7$, $N_{\text{res}} \geq 1$					
57	250–300	1.202 ± 0.077	0.803 ± 0.152	7.521 ± 0.894	7.256 ± 1.625
58	300–400	1.202 ± 0.077	0.734 ± 0.164	5.890 ± 0.814	5.194 ± 1.366
59	400–500	1.202 ± 0.077	1.581 ± 0.721	1.436 ± 0.203	2.728 ± 1.303
60	> 500	1.202 ± 0.077	0.806 ± 0.367	1.040 ± 0.187	1.008 ± 0.493
high Δm , $N_{\text{b}} = 1$, $m_{\text{T}}^{\text{b}} \geq 175$ GeV, $N_{\text{t}} = 0$, $N_{\text{res}} = 0$, $N_{\text{W}} = 0$, $H_{\text{T}} \geq 1000$					
61	250–350	1.265 ± 0.051	0.859 ± 0.048	173.789 ± 2.617	188.755 ± 10.870
62	350–450	1.265 ± 0.051	0.761 ± 0.053	102.281 ± 2.001	98.443 ± 7.078
63	450–550	1.265 ± 0.051	0.906 ± 0.078	61.826 ± 1.578	70.881 ± 6.333
64	> 550	1.265 ± 0.051	0.827 ± 0.054	122.228 ± 2.273	127.902 ± 8.745
high Δm , $N_{\text{b}} \geq 2$, $m_{\text{T}}^{\text{b}} \geq 175$ GeV, $N_{\text{t}} = 0$, $N_{\text{res}} = 0$, $N_{\text{W}} = 0$, $H_{\text{T}} \geq 1000$					
65	250–350	1.202 ± 0.077	0.939 ± 0.110	26.978 ± 1.018	30.434 ± 3.746
66	350–450	1.202 ± 0.077	0.948 ± 0.129	18.807 ± 0.836	21.425 ± 3.073
67	450–550	1.202 ± 0.077	0.818 ± 0.158	12.680 ± 0.696	12.472 ± 2.509
68	> 550	1.202 ± 0.077	0.759 ± 0.106	23.833 ± 0.967	21.754 ± 3.152
high Δm , $N_{\text{b}} = 1$, $m_{\text{T}}^{\text{b}} \geq 175$ GeV, $N_{\text{t}} \geq 1$, $N_{\text{res}} = 0$, $N_{\text{W}} = 0$, $H_{\text{T}} < 1000$					
69	250–550	1.265 ± 0.051	1.045 ± 0.023	26.668 ± 1.502	35.252 ± 2.129
70	550–650	1.265 ± 0.051	0.915 ± 0.073	4.442 ± 0.464	5.143 ± 0.675
71	> 650	1.265 ± 0.051	0.853 ± 0.086	3.292 ± 0.414	3.554 ± 0.574
high Δm , $N_{\text{b}} = 1$, $m_{\text{T}}^{\text{b}} \geq 175$ GeV, $N_{\text{t}} \geq 1$, $N_{\text{res}} = 0$, $N_{\text{W}} = 0$, $1000 \leq H_{\text{T}} < 1500$					
72	250–550	1.265 ± 0.051	0.837 ± 0.037	11.313 ± 0.702	11.979 ± 0.909
73	550–650	1.265 ± 0.051	1.076 ± 0.126	1.317 ± 0.244	1.794 ± 0.394
74	> 650	1.265 ± 0.051	0.814 ± 0.079	2.660 ± 0.361	2.738 ± 0.457
high Δm , $N_{\text{b}} = 1$, $m_{\text{T}}^{\text{b}} \geq 175$ GeV, $N_{\text{t}} \geq 1$, $N_{\text{res}} = 0$, $N_{\text{W}} = 0$, $H_{\text{T}} \geq 1500$					
75	250–550	1.265 ± 0.051	0.837 ± 0.069	3.625 ± 0.422	3.839 ± 0.547
76	550–650	1.265 ± 0.051	0.791 ± 0.192	0.281 ± 0.112	0.281 ± 0.131
77	> 650	1.265 ± 0.051	0.550 ± 0.096	0.702 ± 0.213	0.488 ± 0.170
high Δm , $N_{\text{b}} = 1$, $m_{\text{T}}^{\text{b}} \geq 175$ GeV, $N_{\text{t}} = 0$, $N_{\text{res}} = 0$, $N_{\text{W}} \geq 1$, $H_{\text{T}} < 1300$					
78	250–350	1.265 ± 0.051	1.037 ± 0.029	36.291 ± 2.102	47.616 ± 3.056
79	350–450	1.265 ± 0.051	1.014 ± 0.033	18.803 ± 1.692	24.120 ± 2.305
80	> 450	1.265 ± 0.051	0.975 ± 0.034	10.561 ± 0.731	13.032 ± 1.011

Table D.4: Prediction for the Z invisible background ($N_{\text{pred}}^{Z \rightarrow \nu\bar{\nu}}$) with statistical uncertainty in high Δm search bins 81–107. The normalization factor (R_Z), shape factor (S_γ), and number of $Z \rightarrow \nu\bar{\nu}$ MC events ($N_{\text{MC}}^{Z \rightarrow \nu\bar{\nu}}$) are also shown for each search bin including their statistical uncertainties.

Search region	$p_{\text{T}}^{\text{miss}}$ [GeV]	R_Z	S_γ	N_{MC}	N_{pred}
high Δm , $N_{\text{b}} = 1$, $m_{\text{T}}^{\text{b}} \geq 175$ GeV, $N_{\text{t}} = 0$, $N_{\text{res}} = 0$, $N_{\text{W}} \geq 1$, $H_{\text{T}} \geq 1300$					
81	250–350	1.265 ± 0.051	0.793 ± 0.069	2.094 ± 0.302	2.100 ± 0.353
82	350–450	1.265 ± 0.051	0.750 ± 0.082	1.097 ± 0.219	1.040 ± 0.237
83	> 450	1.265 ± 0.051	0.763 ± 0.064	1.589 ± 0.264	1.534 ± 0.286
high Δm , $N_{\text{b}} = 1$, $m_{\text{T}}^{\text{b}} \geq 175$ GeV, $N_{\text{t}} = 0$, $N_{\text{res}} \geq 1$, $N_{\text{W}} = 0$, $H_{\text{T}} < 1000$					
84	250–350	1.265 ± 0.051	1.046 ± 0.030	197.916 ± 6.195	261.981 ± 11.200
85	350–450	1.265 ± 0.051	1.041 ± 0.036	75.922 ± 3.122	99.940 ± 5.359
86	450–550	1.265 ± 0.051	1.046 ± 0.056	26.764 ± 1.453	35.411 ± 2.690
87	550–650	1.265 ± 0.051	0.915 ± 0.073	10.564 ± 0.656	12.233 ± 1.234
88	> 650	1.265 ± 0.051	0.853 ± 0.086	4.724 ± 0.374	5.099 ± 0.655
high Δm , $N_{\text{b}} = 1$, $m_{\text{T}}^{\text{b}} \geq 175$ GeV, $N_{\text{t}} = 0$, $N_{\text{res}} \geq 1$, $N_{\text{W}} = 0$, $1000 \leq H_{\text{T}} < 1500$					
89	250–350	1.265 ± 0.051	0.858 ± 0.054	7.729 ± 0.517	8.390 ± 0.771
90	350–450	1.265 ± 0.051	0.765 ± 0.059	5.088 ± 0.425	4.925 ± 0.562
91	450–550	1.265 ± 0.051	0.898 ± 0.086	3.084 ± 0.333	3.504 ± 0.507
92	550–650	1.265 ± 0.051	1.076 ± 0.126	2.121 ± 0.273	2.888 ± 0.503
93	> 650	1.265 ± 0.051	0.814 ± 0.079	3.949 ± 0.397	4.064 ± 0.568
high Δm , $N_{\text{b}} = 1$, $m_{\text{T}}^{\text{b}} \geq 175$ GeV, $N_{\text{t}} = 0$, $N_{\text{res}} \geq 1$, $N_{\text{W}} = 0$, $H_{\text{T}} \geq 1500$					
94	250–350	1.265 ± 0.051	0.861 ± 0.099	1.220 ± 0.226	1.328 ± 0.290
95	350–450	1.265 ± 0.051	0.743 ± 0.113	0.872 ± 0.189	0.819 ± 0.217
96	450–550	1.265 ± 0.051	0.941 ± 0.175	0.539 ± 0.142	0.641 ± 0.207
97	550–650	1.265 ± 0.051	0.791 ± 0.192	0.307 ± 0.093	0.307 ± 0.119
98	> 650	1.265 ± 0.051	0.550 ± 0.096	1.119 ± 0.196	0.778 ± 0.192
high Δm , $N_{\text{b}} = 1$, $m_{\text{T}}^{\text{b}} \geq 175$ GeV, $N_{\text{t}} \geq 1$, $N_{\text{res}} = 0$, $N_{\text{W}} \geq 1$					
99	250–550	1.265 ± 0.051	1.020 ± 0.020	0.277 ± 0.101	0.357 ± 0.130
100	> 550	1.265 ± 0.051	0.865 ± 0.039	0.001 ± 0.001	0.001 ± 0.001
high Δm , $N_{\text{b}} = 1$, $m_{\text{T}}^{\text{b}} \geq 175$ GeV, $N_{\text{t}} \geq 1$, $N_{\text{res}} \geq 1$, $N_{\text{W}} = 0$					
101	250–550	1.265 ± 0.051	1.020 ± 0.020	0.545 ± 0.148	0.704 ± 0.192
102	> 550	1.265 ± 0.051	0.865 ± 0.039	0.294 ± 0.107	0.322 ± 0.119
high Δm , $N_{\text{b}} = 1$, $m_{\text{T}}^{\text{b}} \geq 175$ GeV, $N_{\text{t}} = 0$, $N_{\text{res}} \geq 1$, $N_{\text{W}} \geq 1$					
103	250–550	1.265 ± 0.051	1.020 ± 0.020	1.647 ± 0.324	2.125 ± 0.420
104	> 550	1.265 ± 0.051	0.865 ± 0.039	0.295 ± 0.106	0.323 ± 0.116
high Δm , $N_{\text{b}} = 2$, $m_{\text{T}}^{\text{b}} \geq 175$ GeV, $N_{\text{t}} = 1$, $N_{\text{res}} = 0$, $N_{\text{W}} = 0$, $H_{\text{T}} < 1000$					
105	250–550	1.202 ± 0.077	1.048 ± 0.041	7.832 ± 0.712	9.865 ± 0.977
106	550–650	1.202 ± 0.077	0.928 ± 0.148	1.646 ± 0.671	1.837 ± 0.804
107	> 650	1.202 ± 0.077	1.008 ± 0.213	1.059 ± 0.204	1.283 ± 0.367

Table D.5: Prediction for the Z invisible background ($N_{\text{pred}}^{Z \rightarrow \nu\bar{\nu}}$) with statistical uncertainty in high Δm search bins 108–136. The normalization factor (R_Z), shape factor (S_γ), and number of $Z \rightarrow \nu\bar{\nu}$ MC events ($N_{\text{MC}}^{Z \rightarrow \nu\bar{\nu}}$) are also shown for each search bin including their statistical uncertainties.

Search region	$p_{\text{T}}^{\text{miss}}$ [GeV]	R_Z	S_γ	N_{MC}	N_{pred}
high Δm , $N_{\text{b}} = 2$, $m_{\text{T}}^{\text{b}} \geq 175$ GeV, $N_{\text{t}} = 1$, $N_{\text{res}} = 0$, $N_{\text{W}} = 0$, $1000 \leq H_{\text{T}} < 1500$					
108	250–550	1.202 ± 0.077	0.931 ± 0.092	3.189 ± 0.353	3.567 ± 0.529
109	550–650	1.202 ± 0.077	0.644 ± 0.216	0.309 ± 0.101	0.239 ± 0.112
110	> 650	1.202 ± 0.077	0.643 ± 0.136	0.966 ± 0.192	0.746 ± 0.217
high Δm , $N_{\text{b}} = 2$, $m_{\text{T}}^{\text{b}} \geq 175$ GeV, $N_{\text{t}} = 1$, $N_{\text{res}} = 0$, $N_{\text{W}} = 0$, $H_{\text{T}} \geq 1500$					
111	250–550	1.202 ± 0.077	0.767 ± 0.148	0.724 ± 0.176	0.668 ± 0.207
112	550–650	1.202 ± 0.077	1.796 ± 0.791	0.105 ± 0.080	0.226 ± 0.199
113	> 650	1.202 ± 0.077	1.006 ± 0.334	0.304 ± 0.118	0.368 ± 0.187
high Δm , $N_{\text{b}} = 2$, $m_{\text{T}}^{\text{b}} \geq 175$ GeV, $N_{\text{t}} = 0$, $N_{\text{res}} = 0$, $N_{\text{W}} = 1$, $H_{\text{T}} < 1300$					
114	250–350	1.202 ± 0.077	1.084 ± 0.054	5.501 ± 0.812	7.167 ± 1.117
115	350–450	1.202 ± 0.077	0.955 ± 0.064	3.255 ± 0.770	3.737 ± 0.919
116	> 450	1.202 ± 0.077	0.954 ± 0.066	1.663 ± 0.235	1.906 ± 0.300
high Δm , $N_{\text{b}} = 2$, $m_{\text{T}}^{\text{b}} \geq 175$ GeV, $N_{\text{t}} = 0$, $N_{\text{res}} = 0$, $N_{\text{W}} = 1$, $H_{\text{T}} \geq 1300$					
117	250–350	1.202 ± 0.077	0.847 ± 0.176	0.076 ± 0.043	0.078 ± 0.047
118	350–450	1.202 ± 0.077	0.790 ± 0.197	0.256 ± 0.117	0.243 ± 0.127
119	> 450	1.202 ± 0.077	0.762 ± 0.139	0.100 ± 0.050	0.092 ± 0.049
high Δm , $N_{\text{b}} = 2$, $m_{\text{T}}^{\text{b}} \geq 175$ GeV, $N_{\text{t}} = 0$, $N_{\text{res}} = 1$, $N_{\text{W}} = 0$, $H_{\text{T}} < 1000$					
120	250–350	1.202 ± 0.077	1.093 ± 0.057	52.679 ± 3.194	69.205 ± 5.544
121	350–450	1.202 ± 0.077	0.953 ± 0.068	21.501 ± 1.678	24.616 ± 2.595
122	450–550	1.202 ± 0.077	1.017 ± 0.096	6.516 ± 0.592	7.967 ± 1.044
123	550–650	1.202 ± 0.077	0.928 ± 0.148	3.320 ± 0.358	3.704 ± 0.713
124	> 650	1.202 ± 0.077	1.008 ± 0.213	1.138 ± 0.187	1.378 ± 0.369
high Δm , $N_{\text{b}} = 2$, $m_{\text{T}}^{\text{b}} \geq 175$ GeV, $N_{\text{t}} = 0$, $N_{\text{res}} = 1$, $N_{\text{W}} = 0$, $1000 \leq H_{\text{T}} < 1500$					
125	250–350	1.202 ± 0.077	0.927 ± 0.134	1.913 ± 0.249	2.131 ± 0.414
126	350–450	1.202 ± 0.077	0.932 ± 0.152	1.356 ± 0.199	1.519 ± 0.333
127	450–550	1.202 ± 0.077	0.940 ± 0.221	0.976 ± 0.176	1.102 ± 0.327
128	550–650	1.202 ± 0.077	0.644 ± 0.216	0.752 ± 0.163	0.582 ± 0.233
129	> 650	1.202 ± 0.077	0.643 ± 0.136	0.825 ± 0.155	0.637 ± 0.181
high Δm , $N_{\text{b}} = 2$, $m_{\text{T}}^{\text{b}} \geq 175$ GeV, $N_{\text{t}} = 0$, $N_{\text{res}} = 1$, $N_{\text{W}} = 0$, $H_{\text{T}} \geq 1500$					
130	250–350	1.202 ± 0.077	0.843 ± 0.231	0.443 ± 0.130	0.449 ± 0.180
131	350–450	1.202 ± 0.077	0.823 ± 0.274	0.260 ± 0.092	0.257 ± 0.125
132	450–550	1.202 ± 0.077	0.527 ± 0.255	0.348 ± 0.134	0.221 ± 0.136
133	550–650	1.202 ± 0.077	1.796 ± 0.791	0.093 ± 0.045	0.200 ± 0.130
134	> 650	1.202 ± 0.077	1.006 ± 0.334	0.305 ± 0.100	0.368 ± 0.172
high Δm , $N_{\text{b}} = 2$, $m_{\text{T}}^{\text{b}} \geq 175$ GeV, $N_{\text{t}} = 1$, $N_{\text{res}} = 0$, $N_{\text{W}} = 1$					
135	250–550	1.202 ± 0.077	1.032 ± 0.037	0.029 ± 0.029	0.035 ± 0.035
136	> 550	1.202 ± 0.077	0.861 ± 0.084	0.044 ± 0.031	0.045 ± 0.033

Table D.6: Prediction for the Z invisible background ($N_{\text{pred}}^{Z \rightarrow \nu\bar{\nu}}$) with statistical uncertainty in high Δm search bins 137–161. The normalization factor (R_Z), shape factor (S_γ), and number of $Z \rightarrow \nu\bar{\nu}$ MC events ($N_{\text{MC}}^{Z \rightarrow \nu\bar{\nu}}$) are also shown for each search bin including their statistical uncertainties.

Search region	$p_{\text{T}}^{\text{miss}}$ [GeV]	R_Z	S_γ	N_{MC}	N_{pred}
high Δm , $N_{\text{b}} = 2$, $m_{\text{T}}^{\text{b}} \geq 175$ GeV, $N_{\text{t}} = 1$, $N_{\text{res}} = 1$, $N_{\text{W}} = 0$, $H_{\text{T}} < 1300$					
137	250–350	1.202 ± 0.077	1.084 ± 0.054	0.052 ± 0.038	0.067 ± 0.050
138	350–450	1.202 ± 0.077	0.955 ± 0.064	0.121 ± 0.070	0.139 ± 0.081
139	> 450	1.202 ± 0.077	0.954 ± 0.066	0.150 ± 0.079	0.172 ± 0.091
high Δm , $N_{\text{b}} = 2$, $m_{\text{T}}^{\text{b}} \geq 175$ GeV, $N_{\text{t}} = 1$, $N_{\text{res}} = 1$, $N_{\text{W}} = 0$, $H_{\text{T}} \geq 1300$					
140	250–350	1.202 ± 0.077	0.847 ± 0.176	0.000 ± 0.000	0.000 ± 0.000
141	350–450	1.202 ± 0.077	0.790 ± 0.197	0.022 ± 0.022	0.021 ± 0.022
142	> 450	1.202 ± 0.077	0.762 ± 0.139	0.114 ± 0.067	0.104 ± 0.065
high Δm , $N_{\text{b}} = 2$, $m_{\text{T}}^{\text{b}} \geq 175$ GeV, $N_{\text{t}} = 0$, $N_{\text{res}} = 1$, $N_{\text{W}} = 1$					
143	250–550	1.202 ± 0.077	1.032 ± 0.037	0.307 ± 0.114	0.381 ± 0.142
144	> 550	1.202 ± 0.077	0.861 ± 0.084	0.046 ± 0.045	0.047 ± 0.046
high Δm , $N_{\text{b}} = 2$, $m_{\text{T}}^{\text{b}} \geq 175$ GeV, $N_{\text{t}} = 2$, $N_{\text{res}} = 0$, $N_{\text{W}} = 0$					
145	250–450	1.202 ± 0.077	1.037 ± 0.041	0.028 ± 0.028	0.035 ± 0.035
146	> 450	1.202 ± 0.077	0.929 ± 0.060	0.000 ± 0.000	0.000 ± 0.000
high Δm , $N_{\text{b}} = 2$, $m_{\text{T}}^{\text{b}} \geq 175$ GeV, $N_{\text{t}} = 0$, $N_{\text{res}} = 0$, $N_{\text{W}} = 2$					
147	> 250	1.202 ± 0.077	1.018 ± 0.035	0.029 ± 0.029	0.036 ± 0.036
high Δm , $N_{\text{b}} = 2$, $m_{\text{T}}^{\text{b}} \geq 175$ GeV, $N_{\text{t}} = 0$, $N_{\text{res}} = 2$, $N_{\text{W}} = 0$, $H_{\text{T}} < 1300$					
148	250–450	1.202 ± 0.077	1.045 ± 0.042	0.652 ± 0.244	0.819 ± 0.309
149	> 450	1.202 ± 0.077	0.954 ± 0.066	0.143 ± 0.064	0.164 ± 0.074
high Δm , $N_{\text{b}} = 2$, $m_{\text{T}}^{\text{b}} \geq 175$ GeV, $N_{\text{t}} = 0$, $N_{\text{res}} = 2$, $N_{\text{W}} = 0$, $H_{\text{T}} \geq 1300$					
150	250–450	1.202 ± 0.077	0.823 ± 0.131	0.000 ± 0.000	0.000 ± 0.000
151	> 450	1.202 ± 0.077	0.762 ± 0.139	0.018 ± 0.018	0.016 ± 0.017
high Δm , $N_{\text{b}} = 2$, $m_{\text{T}}^{\text{b}} \geq 175$ GeV, $N_{\text{t}} + N_{\text{res}} + N_{\text{W}} \geq 3$					
152	> 250	1.202 ± 0.077	1.018 ± 0.035	0.000 ± 0.000	0.000 ± 0.000
high Δm , $N_{\text{b}} \geq 3$, $m_{\text{T}}^{\text{b}} \geq 175$ GeV, $N_{\text{t}} = 1$, $N_{\text{res}} = 0$, $N_{\text{W}} = 0$, $H_{\text{T}} < 1000$					
153	250–350	1.202 ± 0.077	1.103 ± 0.150	0.152 ± 0.069	0.201 ± 0.095
154	350–550	1.202 ± 0.077	1.052 ± 0.157	0.321 ± 0.100	0.406 ± 0.140
155	> 550	1.202 ± 0.077	0.617 ± 0.238	0.370 ± 0.126	0.275 ± 0.141
high Δm , $N_{\text{b}} \geq 3$, $m_{\text{T}}^{\text{b}} \geq 175$ GeV, $N_{\text{t}} = 1$, $N_{\text{res}} = 0$, $N_{\text{W}} = 0$, $1000 \leq H_{\text{T}} < 1500$					
156	250–350	1.202 ± 0.077	1.242 ± 0.373	0.163 ± 0.073	0.244 ± 0.131
157	350–550	1.202 ± 0.077	0.841 ± 0.287	0.237 ± 0.086	0.239 ± 0.119
158	> 550	1.202 ± 0.077	0.765 ± 0.289	0.197 ± 0.095	0.181 ± 0.111
high Δm , $N_{\text{b}} \geq 3$, $m_{\text{T}}^{\text{b}} \geq 175$ GeV, $N_{\text{t}} = 1$, $N_{\text{res}} = 0$, $N_{\text{W}} = 0$, $H_{\text{T}} \geq 1500$					
159	250–350	1.202 ± 0.077	0.471 ± 0.507	0.067 ± 0.060	0.038 ± 0.053
160	350–550	1.202 ± 0.077	2.979 ± 2.145	0.053 ± 0.053	0.188 ± 0.232
161	> 550	1.202 ± 0.077	0.813 ± 0.628	0.075 ± 0.074	0.073 ± 0.092

Table D.7: Prediction for the Z invisible background ($N_{\text{pred}}^{Z \rightarrow \nu\bar{\nu}}$) with statistical uncertainty in high Δm search bins 162–182. The normalization factor (R_Z), shape factor (S_γ), and number of Z $\rightarrow \nu\bar{\nu}$ MC events ($N_{\text{MC}}^{Z \rightarrow \nu\bar{\nu}}$) are also shown for each search bin including their statistical uncertainties.

Search region	$p_{\text{T}}^{\text{miss}}$ [GeV]	R_Z	S_γ	N_{MC}	N_{pred}
high Δm , $N_{\text{b}} \geq 3$, $m_{\text{T}}^{\text{b}} \geq 175$ GeV, $N_{\text{t}} = 0$, $N_{\text{res}} = 0$, $N_{\text{W}} = 1$					
162	250–350	1.202 ± 0.077	1.106 ± 0.139	0.478 ± 0.160	0.636 ± 0.228
163	350–550	1.202 ± 0.077	1.050 ± 0.141	0.430 ± 0.122	0.543 ± 0.170
164	> 550	1.202 ± 0.077	0.699 ± 0.178	0.066 ± 0.047	0.056 ± 0.042
high Δm , $N_{\text{b}} \geq 3$, $m_{\text{T}}^{\text{b}} \geq 175$ GeV, $N_{\text{t}} = 0$, $N_{\text{res}} = 1$, $N_{\text{W}} = 0$, $H_{\text{T}} < 1000$					
165	250–350	1.202 ± 0.077	1.103 ± 0.150	3.741 ± 0.738	4.961 ± 1.189
166	350–550	1.202 ± 0.077	1.052 ± 0.157	3.527 ± 0.673	4.462 ± 1.081
167	> 550	1.202 ± 0.077	0.617 ± 0.238	0.171 ± 0.069	0.127 ± 0.071
high Δm , $N_{\text{b}} \geq 3$, $m_{\text{T}}^{\text{b}} \geq 175$ GeV, $N_{\text{t}} = 0$, $N_{\text{res}} = 1$, $N_{\text{W}} = 0$, $1000 \leq H_{\text{T}} < 1500$					
168	250–350	1.202 ± 0.077	1.242 ± 0.373	0.369 ± 0.109	0.551 ± 0.232
169	350–550	1.202 ± 0.077	0.841 ± 0.287	0.230 ± 0.080	0.232 ± 0.113
170	> 550	1.202 ± 0.077	0.765 ± 0.289	0.333 ± 0.113	0.306 ± 0.155
high Δm , $N_{\text{b}} \geq 3$, $m_{\text{T}}^{\text{b}} \geq 175$ GeV, $N_{\text{t}} = 0$, $N_{\text{res}} = 1$, $N_{\text{W}} = 0$, $H_{\text{T}} \geq 1500$					
171	250–350	1.202 ± 0.077	0.471 ± 0.507	0.053 ± 0.033	0.030 ± 0.037
172	350–550	1.202 ± 0.077	2.979 ± 2.145	0.057 ± 0.040	0.203 ± 0.205
173	> 550	1.202 ± 0.077	0.813 ± 0.628	0.029 ± 0.025	0.029 ± 0.033
high Δm , $N_{\text{b}} \geq 3$, $m_{\text{T}}^{\text{b}} \geq 175$ GeV, $N_{\text{t}} = 1$, $N_{\text{res}} = 0$, $N_{\text{W}} = 1$					
174	> 250	1.202 ± 0.077	1.045 ± 0.091	0.026 ± 0.026	0.033 ± 0.033
high Δm , $N_{\text{b}} \geq 3$, $m_{\text{T}}^{\text{b}} \geq 175$ GeV, $N_{\text{t}} = 1$, $N_{\text{res}} = 1$, $N_{\text{W}} = 0$					
175	250–350	1.202 ± 0.077	1.106 ± 0.139	0.032 ± 0.032	0.042 ± 0.042
176	> 350	1.202 ± 0.077	0.970 ± 0.114	0.158 ± 0.071	0.185 ± 0.085
high Δm , $N_{\text{b}} \geq 3$, $m_{\text{T}}^{\text{b}} \geq 175$ GeV, $N_{\text{t}} = 0$, $N_{\text{res}} = 1$, $N_{\text{W}} = 1$					
177	> 250	1.202 ± 0.077	1.045 ± 0.091	0.034 ± 0.034	0.043 ± 0.043
high Δm , $N_{\text{b}} \geq 3$, $m_{\text{T}}^{\text{b}} \geq 175$ GeV, $N_{\text{t}} = 2$, $N_{\text{res}} = 0$, $N_{\text{W}} = 0$					
178	> 250	1.202 ± 0.077	1.045 ± 0.091	0.045 ± 0.045	0.057 ± 0.057
high Δm , $N_{\text{b}} \geq 3$, $m_{\text{T}}^{\text{b}} \geq 175$ GeV, $N_{\text{t}} = 0$, $N_{\text{res}} = 0$, $N_{\text{W}} = 2$					
179	> 250	1.202 ± 0.077	1.045 ± 0.091	0.000 ± 0.000	0.000 ± 0.000
high Δm , $N_{\text{b}} \geq 3$, $m_{\text{T}}^{\text{b}} \geq 175$ GeV, $N_{\text{t}} = 0$, $N_{\text{res}} = 2$, $N_{\text{W}} = 0$					
180	250–350	1.202 ± 0.077	1.106 ± 0.139	0.017 ± 0.017	0.022 ± 0.022
181	> 350	1.202 ± 0.077	0.970 ± 0.114	0.024 ± 0.019	0.028 ± 0.022
high Δm , $N_{\text{b}} \geq 3$, $m_{\text{T}}^{\text{b}} \geq 175$ GeV, $N_{\text{t}} + N_{\text{res}} + N_{\text{W}} \geq 3$					
182	> 250	1.202 ± 0.077	1.045 ± 0.091	0.000 ± 0.000	0.000 ± 0.000

BIBLIOGRAPHY

- [1] Particle Data Group Collaboration, “Review of particle physics”, *Phys. Rev. D* **98** (Aug, 2018) 030001, doi:10.1103/PhysRevD.98.030001.
- [2] https://en.wikipedia.org/wiki/File:Standard_Model_of_Elementary_Particles.svg.
- [3] https://commons.wikimedia.org/wiki/File:Standard_Model_Feynman_Diagram_Vertices.png.
- [4] M. Thomson, “Modern Particle Physics”. Cambridge University Press, 2013. doi:10.1017/CB09781139525367.
- [5] D. Croon et al., “GUT physics in the era of the LHC”, *Frontiers in Physics* **7** (Jun, 2019) doi:10.3389/fphy.2019.00076.
- [6] S. Weinberg, “A model of leptons”, *Phys. Rev. Lett.* **19** (Nov, 1967) 1264–1266, doi:10.1103/PhysRevLett.19.1264.
- [7] A. Salam, “Elementary particle theory”, *Prog. Of the Nobel Symposium, 1968, Stockholm, Sweden* **367** (1968).
- [8] CMS Collaboration, “Observation of a new boson at a mass of 125 GeV with the CMS experiment at the LHC”, *Phys. Lett. B* **716** (2012) 30, doi:10.1016/j.physletb.2012.08.021, arXiv:1207.7235.
- [9] R. Barbieri and G. F. Giudice, “Upper bounds on supersymmetric particle masses”, *Nucl. Phys. B* **306** (1988) 63, doi:10.1016/0550-3213(88)90171-X.
- [10] V. C. Rubin and W. K. Ford, Jr., “Rotation of the Andromeda nebula from a spectroscopic survey of emission regions”, *Astrophys. J.* **159** (1970) 379, doi:10.1086/150317.
- [11] J. Wess and B. Zumino, “A Lagrangian model invariant under supergauge transformations”, *Phys. Lett. B* **49** (1974) 52, doi:10.1016/0370-2693(74)90578-4.
- [12] P. Fayet and S. Ferrara, “Supersymmetry”, *Phys. Rept.* **32** (1977) 249, doi:10.1016/0370-1573(77)90066-7.
- [13] R. Barbieri, S. Ferrara, and C. A. Savoy, “Gauge models with spontaneously broken local supersymmetry”, *Phys. Lett. B* **119** (1982) 343, doi:10.1016/0370-2693(82)90685-2.

- [14] H. P. Nilles, “Supersymmetry, supergravity and particle physics”, *Phys. Rept.* **110** (1984) 1, doi:10.1016/0370-1573(84)90008-5.
- [15] H. E. Haber and G. L. Kane, “The search for supersymmetry: probing physics beyond the standard model”, *Phys. Rept.* **117** (1985) 75, doi:10.1016/0370-1573(85)90051-1.
- [16] S. P. Martin, “A supersymmetry primer”, in *Perspectives on supersymmetry. Vol.2*, G. L. Kane, ed., volume 21, p. 1. 2010. arXiv:hep-ph/9709356. doi:10.1142/9789812839657_0001.
- [17] B. de Carlos and J. A. Casas, “One-loop analysis of the electroweak breaking in supersymmetric models and the fine tuning problem”, *Phys. Lett. B* **309** (1993) 320, doi:10.1016/0370-2693(93)90940-J, arXiv:hep-ph/9303291.
- [18] S. Dimopoulos and G. F. Giudice, “Naturalness constraints in supersymmetric theories with nonuniversal soft terms”, *Phys. Lett. B* **357** (1995) 573, doi:10.1016/0370-2693(95)00961-J, arXiv:hep-ph/9507282.
- [19] M. Francis, “A sort of particle-free supersymmetry found in exotic materials”, 2014. <https://arstechnica.com/science/2014/04/a-sort-of-particle-free-supersymmetry-found-in-exotic-materials/>.
- [20] T. Grover, D. N. Sheng, and A. Vishwanath, “Emergent space-time supersymmetry at the boundary of a topological phase”, *Science* **344** (2014), no. 6181, 280–283, doi:10.1126/science.1248253.
- [21] <https://home.cern/science/accelerators/accelerator-complex>.
- [22] <https://cds.cern.ch/images/OPEN-PHO-ACCEL-2013-056-1>.
- [23] CMS Collaboration, G. Bayatian et al., “CMS Physics: Technical Design Report Volume 1: Detector Performance and Software”. Technical Design Report CMS. 2006.
- [24] L. Taylor, “CMS detector design”, 2011. <http://cms.web.cern.ch/news/cms-detector-design>.
- [25] W. Waltenberger, “Development of Vertex Finding and Vertex Fitting Algorithms for CMS”. PhD thesis, Institut für Hochenergiephysik Wien, Jan, 2004.
- [26] CMS Collaboration, “CMS Technical Design Report for the Phase 1 Upgrade of the Hadron Calorimeter”, Technical Report CERN-LHCC-2012-015. CMS-TDR-10, Sep, 2012.
- [27] CMS Collaboration, “Particle-flow reconstruction and global event description with the CMS detector”, *JINST* **12** (2017), no. 10, P10003, doi:10.1088/1748-0221/12/10/P10003, arXiv:1706.04965.

- [28] M. Cacciari, G. P. Salam, and G. Soyez, “The anti- k_t jet clustering algorithm”, *Journal of High Energy Physics* **2008** (2008), no. 04, 063, doi:10.1088/1126-6708/2008/04/063.
- [29] ATLAS Collaboration, “Search for top squarks in final states with one isolated lepton, jets, and missing transverse momentum in $\sqrt{s} = 13$ TeV pp collisions with the ATLAS detector”, *Phys. Rev. D* **94** (2016) 052009, doi:10.1103/PhysRevD.94.052009, arXiv:1606.03903.
- [30] ATLAS Collaboration, “Search for direct top squark pair production in events with a Higgs or Z boson, and missing transverse momentum in $\sqrt{s} = 13$ TeV pp collisions with the ATLAS detector”, *JHEP* **08** (2017) 006, doi:10.1007/JHEP08(2017)006, arXiv:1706.03986.
- [31] ATLAS Collaboration, “Search for direct top squark pair production in final states with two leptons in $\sqrt{s} = 13$ TeV pp collisions with the ATLAS detector”, *Eur. Phys. J. C* **77** (2017) 898, doi:10.1140/epjc/s10052-017-5445-x, arXiv:1708.03247.
- [32] ATLAS Collaboration, “Search for a scalar partner of the top quark in the jets plus missing transverse momentum final state at $\sqrt{s} = 13$ TeV with the ATLAS detector”, *JHEP* **12** (2017) 085, doi:10.1007/JHEP12(2017)085, arXiv:1709.04183.
- [33] ATLAS Collaboration, “Search for $B - L$ R -parity-violating top squarks in $\sqrt{s} = 13$ TeV pp collisions with the ATLAS experiment”, *Phys. Rev. D* **97** (2018) 032003, doi:10.1103/PhysRevD.97.032003, arXiv:1710.05544.
- [34] ATLAS Collaboration, “A search for pair-produced resonances in four-jet final states at $\sqrt{s} = 13$ TeV with the ATLAS detector”, *Eur. Phys. J. C* **78** (2018) 250, doi:10.1140/epjc/s10052-018-5693-4, arXiv:1710.07171.
- [35] ATLAS Collaboration, “Search for top-squark pair production in final states with one lepton, jets, and missing transverse momentum using 36 fb^{-1} of $\sqrt{s} = 13$ TeV pp collision data with the ATLAS detector”, *JHEP* **06** (2018) 108, doi:10.1007/JHEP06(2018)108, arXiv:1711.11520.
- [36] ATLAS Collaboration, “Search for top squarks decaying to tau sleptons in pp collisions at $\sqrt{s} = 13$ TeV with the ATLAS detector”, *Phys. Rev. D* **98** (2018) 032008, doi:10.1103/PhysRevD.98.032008, arXiv:1803.10178.
- [37] ATLAS Collaboration, “Search for supersymmetry in final states with charm jets and missing transverse momentum in 13 TeV pp collisions with the ATLAS detector”, *JHEP* **09** (2018) 050, doi:10.1007/JHEP09(2018)050, arXiv:1805.01649.
- [38] ATLAS Collaboration, “Search for heavy charged long-lived particles in proton-proton collisions at $\sqrt{s} = 13$ TeV using an ionisation measurement with the ATLAS detector”, *Phys. Lett. B* **788** (2019) 96, doi:10.1016/j.physletb.2018.10.055, arXiv:1808.04095.

- [39] ATLAS Collaboration, “Search for heavy charged long-lived particles in the ATLAS detector in 36.1 fb^{-1} of proton-proton collision data at $\sqrt{s} = 13 \text{ TeV}$ ”, *Phys. Rev. D* **99** (2019) 092007, doi:10.1103/PhysRevD.99.092007, arXiv:1902.01636.
- [40] CMS Collaboration, “Searches for pair production of third-generation squarks in $\sqrt{s} = 13 \text{ TeV}$ pp collisions”, *Eur. Phys. J. C* **77** (2017) 327, doi:10.1140/epjc/s10052-017-4853-2, arXiv:1612.03877.
- [41] CMS Collaboration, “Search for supersymmetry in the all-hadronic final state using top quark tagging in pp collisions at $\sqrt{s} = 13 \text{ TeV}$ ”, *Phys. Rev. D* **96** (2017) 012004, doi:10.1103/PhysRevD.96.012004, arXiv:1701.01954.
- [42] CMS Collaboration, “Search for top squark pair production in pp collisions at $\sqrt{s} = 13 \text{ TeV}$ using single lepton events”, *JHEP* **10** (2017) 019, doi:10.1007/JHEP10(2017)019, arXiv:1706.04402.
- [43] CMS Collaboration, “Search for direct production of supersymmetric partners of the top quark in the all-jets final state in proton-proton collisions at $\sqrt{s} = 13 \text{ TeV}$ ”, *JHEP* **10** (2017) 005, doi:10.1007/JHEP10(2017)005, arXiv:1707.03316.
- [44] CMS Collaboration, “Search for supersymmetry in proton-proton collisions at 13 TeV using identified top quarks”, *Phys. Rev. D* **97** (2018) 012007, doi:10.1103/PhysRevD.97.012007, arXiv:1710.11188.
- [45] CMS Collaboration, “Search for the pair production of third-generation squarks with two-body decays to a bottom or charm quark and a neutralino in proton-proton collisions at $\sqrt{s} = 13 \text{ TeV}$ ”, *Phys. Lett. B* **778** (2018) 263, doi:10.1016/j.physletb.2018.01.012, arXiv:1707.07274.
- [46] CMS Collaboration, “Search for top squarks and dark matter particles in opposite-charge dilepton final states at $\sqrt{s} = 13 \text{ TeV}$ ”, *Phys. Rev. D* **97** (2018) 032009, doi:10.1103/PhysRevD.97.032009, arXiv:1711.00752.
- [47] CMS Collaboration, “Search for new physics in events with two soft oppositely charged leptons and missing transverse momentum in proton-proton collisions at $\sqrt{s} = 13 \text{ TeV}$ ”, *Phys. Lett. B* **782** (2018) 440, doi:10.1016/j.physletb.2018.05.062, arXiv:1801.01846.
- [48] CMS Collaboration, “Search for pair-produced resonances decaying to quark pairs in proton-proton collisions at $\sqrt{s} = 13 \text{ TeV}$ ”, *Phys. Rev. D* **98** (2018) 112014, doi:10.1103/PhysRevD.98.112014, arXiv:1808.03124.
- [49] CMS Collaboration, “Search for the pair production of light top squarks in the $e^\pm \mu^\mp$ final state in proton-proton collisions at $\sqrt{s} = 13 \text{ TeV}$ ”, *JHEP* **03** (2019) 101, doi:10.1007/JHEP03(2019)101, arXiv:1901.01288.
- [50] CMS Collaboration, “Search for direct top squark pair production in events with one lepton, jets, and missing transverse momentum at 13 TeV with the

- CMS experiment”, *JHEP* **05** (2020) 032, doi:10.1007/JHEP05(2020)032, arXiv:1912.08887.
- [51] CMS Collaboration, “Search for top squark pair production using dilepton final states in pp collision data collected at $\sqrt{s} = 13$ TeV”, arXiv:2008.05936.
- [52] CMS Collaboration, “Pileup Removal Algorithms”, Technical Report CMS-PAS-JME-14-001, CERN, Geneva, 2014.
- [53] M. Diamantopoulou, D. Karasavvas, N. Saoulidou and E. Tziaferi, “Performance of the particle-flow jet identification criteria using proton-proton collisions at 13 tev for run2017 data”, (2018).
http://cms.cern.ch/iCMS/jsp/db_notes/noteInfo.jsp?cmsnoteid=CMS%20AN-2018/093.
- [54] <https://twiki.cern.ch/twiki/bin/viewauth/CMS/JetID13TeVRun2016>.
- [55] <https://twiki.cern.ch/twiki/bin/viewauth/CMS/JetID13TeVRun2017>.
- [56] <https://twiki.cern.ch/twiki/bin/view/CMS/JetID13TeVRun2018>.
- [57] <https://twiki.cern.ch/twiki/bin/view/CMS/IntroToJEC>.
- [58] CMS Collaboration, “Identification of heavy-flavour jets with the CMS detector in pp collisions at 13 TeV”, *JINST* **13** (2018) P05011, doi:10.1088/1748-0221/13/05/P05011, arXiv:1712.07158.
- [59] <https://twiki.cern.ch/twiki/bin/viewauth/CMS/BtagRecommendation2016Legacy>,
<https://twiki.cern.ch/twiki/bin/viewauth/CMS/BtagRecommendation94X>,
<https://twiki.cern.ch/twiki/bin/viewauth/CMS/BtagRecommendation102X>.
- [60] <https://indico.cern.ch/event/823731/contributions/3446301/>.
- [61] <https://indico.cern.ch/event/828647/contributions/3468642/>.
- [62] CMS Collaboration, “Identification of heavy, energetic, hadronically decaying particles using machine-learning techniques”, *JINST* **15** (2020) P06005, doi:10.1088/1748-0221/15/06/P06005, arXiv:2004.08262.
- [63] <https://twiki.cern.ch/twiki/bin/view/CMS/MissingETOptionalFiltersRun2>.
- [64] <https://twiki.cern.ch/twiki/bin/viewauth/CMS/SUSRecommendationsICHEP16>.
- [65] <https://twiki.cern.ch/twiki/bin/viewauth/CMS/L1ECALPrefiringWeightRecipe>.
- [66] S. Bein et al., “Search for supersymmetry in proton-proton collisions at 13 TeV in final states with missing transverse momentum and jets”, *CMS Analysis Note AN-18-271* (2019).
- [67] CMS Collaboration, “Measurement of top quark pair production in association with a Z boson in proton-proton collisions at $\sqrt{s} = 13$ TeV”, arXiv:1907.11270.

- [68] W. Beenakker et al., “NNLL-fast: predictions for coloured supersymmetric particle production at the LHC with threshold and Coulomb resummation”, *JHEP* **12** (2016) 133, doi:10.1007/JHEP12(2016)133, arXiv:1607.07741.
- [69] W. Beenakker, R. Höpker, M. Spira, and P. M. Zerwas, “Squark and gluino production at hadron colliders”, *Nucl. Phys. B* **492** (1997) 51, doi:10.1016/S0550-3213(97)80027-2, arXiv:hep-ph/9610490.
- [70] A. Kulesza and L. Motyka, “Threshold resummation for squark-antisquark and gluino-pair production at the LHC”, *Phys. Rev. Lett.* **102** (2009) 111802, doi:10.1103/PhysRevLett.102.111802, arXiv:0807.2405.
- [71] A. Kulesza and L. Motyka, “Soft gluon resummation for the production of gluino-gluino and squark-antisquark pairs at the LHC”, *Phys. Rev. D* **80** (2009) 095004, doi:10.1103/PhysRevD.80.095004, arXiv:0905.4749.
- [72] W. Beenakker et al., “Soft-gluon resummation for squark and gluino hadroproduction”, *JHEP* **12** (2009) 041, doi:10.1088/1126-6708/2009/12/041, arXiv:0909.4418.
- [73] W. Beenakker et al., “NNLL resummation for squark-antisquark pair production at the LHC”, *JHEP* **01** (2012) 076, doi:10.1007/JHEP01(2012)076, arXiv:1110.2446.
- [74] W. Beenakker et al., “Towards NNLL resummation: hard matching coefficients for squark and gluino hadroproduction”, *JHEP* **10** (2013) 120, doi:10.1007/JHEP10(2013)120, arXiv:1304.6354.
- [75] W. Beenakker et al., “NNLL resummation for squark and gluino production at the LHC”, *JHEP* **12** (2014) 023, doi:10.1007/JHEP12(2014)023, arXiv:1404.3134.
- [76] W. Beenakker et al., “Stop production at hadron colliders”, *Nucl. Phys. B* **515** (1998) 3, doi:10.1016/S0550-3213(98)00014-5, arXiv:hep-ph/9710451.
- [77] W. Beenakker et al., “Supersymmetric top and bottom squark production at hadron colliders”, *JHEP* **08** (2010) 098, doi:10.1007/JHEP08(2010)098, arXiv:1006.4771.
- [78] W. Beenakker et al., “NNLL resummation for stop pair-production at the LHC”, *JHEP* **05** (2016) 153, doi:10.1007/JHEP05(2016)153, arXiv:1601.02954.